

Study of metal interactions with biomolecules and π -acceptor systems: A detailed investigation of structural aspects, electrochemical properties and spectroscopic features

Von der Fakultät Chemie der Universität Stuttgart
Zur Erlangung der Würde eines
Doktors der Naturwissenschaften (Dr. rer. nat.)
genehmigte Abhandlung

vorgelegt von
Rajkumar Jana
aus Ghatal (Indien)

Hauptberichter:	Prof. Dr. W. Kaim
Mitberichter:	Prof. Dr. D. Gudat
Tag der mündlichen Prüfung:	22nd March 2011

Institut für Anorganische Chemie der Universität Stuttgart
2011

"For all the people who made this possible"

Acknowledgements

This work was continued from September 2008 to January 2011 at the Institute of Inorganic Chemistry, University of Stuttgart, Germany. The completion of the work and the final writing would not have been possible without the help of various people.

It is a great pleasure and proud privilege to express my deep sense of gratitude and everlasting indebtedness to my research supervisor, Prof. Dr. Wolfgang Kaim. I am grateful to my supervisor for giving me the opportunity to carry out this thesis work in his group, for all his ideas, discussions, his patience and guidance throughout my research work. Without his active guidance it would not have been possible for me to complete the work in such a small time span.

My profound gratitude to Prof. Anil Jacob Elias at the Indian Institute of Technology, Delhi, India for training me in the field of synthetic organometallic chemistry in his working group since two years. I am very much thankful to Prof. Goutam Kumar Lahiri, Indian Institute of Technology, Bombay, India and Mr. Bholanath Mukherjee for their continuous inspirations, motivation and mental support. I am grateful to Dr. B. Sarkar, Dr. S. Roy and Dr. A. K. Das for their continuous help, fruitful scientific discussions and initial helps in Stuttgart.

I am thankful to Dr. J. Fiedler for (spectro)electrochemical measurements, Dr. F. Lissner, Dr. I. Hartenbach, Dr. Sabine Strobel, Mr. Denis Bubrin from University of Stuttgart and Dr. S. M. Mobin from Indian Institute of Technology, Bombay, India for crystallographic data collection and solving crystal structures, Dr. B. Sarkar and Dr. B. Schwederski for the EPR measurements, Ms. B. Förtsch for elemental analysis, Ms. K. Török for NMR measurements. I am also thankful to Ms. A. Winkelmann and Ms. Sumati Panicker-Otto for helping me out with bureaucratic problems, Dr. B. Schwederski for translating the summary.

I also thank to Swagata Biswas, Anupam Kumar Chakravarty, Dr. Ameeya Kumar Nayak, Niladri Patra, Sebastian Plebst, Asamanjoy Bhunia and Hari Sankar Das, with whom I shared a lot of things, which also helped me to keep the tempo high. I also owe a great deal to all my friends for their support, co-operation and sincere help in various ways.

I express my sincere thank with gratitude to my parents and other family members, whom I missed all the time, for their support and encouragement without which this thesis would not have been possible.

Finally I would like to thank all the members of Institut für Anorganische Chemie, Universität Stuttgart, especially, the group members of Prof. Kaim's and Dr. Sarkar's research group.

Contents

1. Introduction	1-7
2. Structural, electrochemical and spectroscopic investigations of organometallic copper(I) complexes with lumazine, alloxazine and pterin ligands	8-43
2.1 Introduction	8
2.2 Synthesis and characterization	11
2.3 Crystal structure	14
2.4 Infrared spectroscopy	19
2.5 Electrochemistry	21
2.6 IR-spectroelectrochemistry	33
2.7 UV-vis spectroelectrochemistry	37
2.8 EPR spectroscopy	41
2.9 Conclusion	43
3. Variable metal binding of the unsymmetrical α-iminoketo chelate function in biomolecules: Structures of complexes between heterodinuclear (Cu, Fe) organometallics and purine bases	44-62
3.1 Introduction	44
3.2 Synthesis and characterization	46
3.3 Crystal structure	50
3.4 Cyclic voltammetry	59
3.5 UV-vis spectroscopy	61
3.6 Conclusion	62
4. Structural comparison and spectroscopy of electrochemically generated radical and non-radical bridged heterotetranuclear complexes	63-80
4.1 Introduction	63
4.2 Synthesis and characterization	65
4.3 Crystal structures	68
4.4 Electrochemistry	73
4.5 UV-Vis-NIR spectroelectrochemistry	75
4.6 EPR spectroscopy	80
4.7 Conclusion	80

5. Facilitated reduction and oxidation of {[Ru(NH₃)₅]₄(μ₄-TCNX)}⁸⁺ by changing from TCNX = TCNQ to TCNQF₄ 81-89

5.1 Introduction	81
5.2 Synthesis and characterization	81
5.3 Cyclic voltammetry	82
5.4 IR-Spectroelectrochemistry	83
5.5 UV-Vis-NIR spectroscopy	85
5.6 EPR spectroscopy	89
5.7 Conclusion	89

6. Exploring various coordination modes of redox-innocent TCNB in discrete and polymeric copper(I) complexes: A structural, electrochemical and spectroscopic study

90-104

6.1 Introduction	90
6.2 Synthesis and characterization	92
6.3 Crystal structure	94
6.4 Cyclic voltammetry	100
6.5 IR & UV-Vis spectroelectrochemistry	101
6.6 EPR spectroscopy	102
6.7 Conclusion and outlook	103

7. Structure, electrochemistry and spectroscopy of a new diacylhydrazido-bridged diruthenium complex with a strongly near-infrared absorbing Ru^{III}Ru^{II} 105-111

7.1 Introduction	105
7.2 Synthesis and characterization	106
7.3 Crystal structure	106
7.4 Cyclic voltammetry	108
7.5 UV-Vis-NIR spectroelectrochemistry	109
7.6 EPR spectroscopy	111
7.7 Conclusion	111

8. Experimental section	112-141
8.1 Instrumentation	112
8.2 Solvents and working conditions	113
8.3 Syntheses	113-124
8.3.1 Synthesis of N2-pivaloyl-, 9-methylguanine (P-9MG)	114
8.3.2 Synthesis of copper(I) precursors	114
8.3.3 Synthesis of copper(I)-lumazine complexes	116
8.3.4 Synthesis of copper(I)-alloxazine complexes	117
8.3.5 Synthesis of copper(I)-pterin complexes	118
8.3.6 Synthesis of copper(I)-purine complexes	119
8.3.7 Synthesis of abcp- and abpy-bridged heteronuclear complexes	120
8.3.8 Synthesis of [$\{\text{Ru}(\text{NH}_3)_5\}(\mu_4\text{-TCNQF}_4)\](\text{PF}_6)_8$	122
8.3.9 Synthesis of copper(I)-TCNB complexes	123
8.3.10 Synthesis of [$\{(\text{bpy})_2\text{Ru}\}_2(\mu\text{-adc-CF}_3)\](\text{PF}_6)_2$	123
8.4 Crystallography	125-141
8.4.1 $[\text{Cu}(\text{dppf})(\text{DML})](\text{BF}_4)$	127
8.4.2 $[\text{Cu}(\text{dippf})(\text{DML})](\text{BF}_4)$	128
8.4.3 $[\text{Cu}(\text{dppf})(\text{TMA})](\text{BF}_4)$	129
8.4.4 $[\text{Cu}_3(\text{dppf})(\mu_2\text{-dppf})(\text{PP})(\text{PP}^-)]_2(\text{BF}_4)_4$	130
8.4.5 $[\text{Cu}(\text{dppf})(\text{P-9MG})](\text{BF}_4)$	131
8.4.6 $[\text{Cu}_3(\text{P9MG}^-)_2(\mu\text{-dppf})_2](\text{BF}_4)_2$	132
8.4.7 $[\text{Cu}(\text{dppf})(\text{TMX})](\text{BF}_4)$	133
8.4.8 $[\text{Cu}(\text{dippf})(\text{TMX})](\text{PF}_6)$	134
8.4.9 $[\text{Cu}(\text{dchpf})(\text{TMX})](\text{PF}_6)$	135
8.4.10 $\{(\mu\text{-abcp})[\text{Cu}(\text{dppf})]_2\}(\text{BF}_4)_2$	136
8.4.11 $\{(\mu\text{-abcp})[\text{Cu}(\text{dppf})]_2\}(\text{BF}_4)$	137
8.4.12 $\{(\mu\text{-abpy})\text{Cu}(\text{dippf})\}(\text{BF}_4)$	138
8.4.13 $\{(\mu\text{-TCNB})[\text{Cu}(\text{dppf})]_2\}(\text{BF}_4)_2$	139
8.4.14 $\{[(\mu_2\text{-TCNB})\text{Cu}(\text{dppf})]_n(\text{BF}_4)_2\}_n$	140
8.4.15 $[\{(\text{bpy})_2\text{Ru}\}_2(\mu\text{-adc-CF}_3)](\text{PF}_6)_2$	141

9. Summary 142-150

10. Zusammenfassung 151-159

Appendix

Bibliography

Abbreviations

Curriculum Vitae.

Chapter 1

Introduction

Copper is an essential bio-element present (in ppm concentration range) in most living systems^[1]. It plays a crucial role in the key functions of several enzymes in the energy metabolism, including cytochrome c oxidase^[2], superoxide dismutase^[3,4], and NO reductase^[5,6]. Copper is also involved in electron transfer from blue copper proteins and in the reduction of molecular oxygen^[7]. The essential role of copper cofactors in biological electron transfer reactions has been well established by spectroscopic techniques^[8-14]. The *in vitro* study of enzyme-model complexes provides informations for the understanding of *in vivo* functional mechanisms and the structure-function relationship of cofactors^[11,15]. In biological systems, copper can exist in two relevant oxidation states, +I and +II, and they are characterized by spectroscopic methods. The active site structures contain copper coordination spheres involving nitrogen, oxygen or sulphur donors from the amino acid residues in protein chain. Copper(I) in its d^{10} electronic configuration has no extra stabilization due to the Jahn-Teller effect and as a result, it can adopt two, three or four coordinated geometry, including the energy minimum intermediates. The coordination chemistry of copper(I) to biochemically relevant ligand systems can not only provide information on metal-binding modes, but can also allow studies of various interesting structural aspects.

Pteridine heterocycles (Figure 1.1) are found as the core structure of flavin adenine dinucleotide (FAD) and folic acid, and can also function as cofactors in electron transfer enzymes involved in amino acid biosynthesis^[16-18], NO metabolism^[5,6], redox mediation^[19] and in molecular switches during cell signalling process^[20-22]. The usefulness of pteridine derivatives in anticancer drugs such as methotrexate^[23] is also found. The 1,4-dioxo- and 2-amino,4-oxo- pteridine derivatives (Figure 1.1) are famous for the metal coordination through N,O chelation. A coordination chemistry review^[24] on the metal complexes of pteridine, alloxazine and flavin ligands has demonstrated their metal binding properties through structural elucidation and spectroscopic measurements.

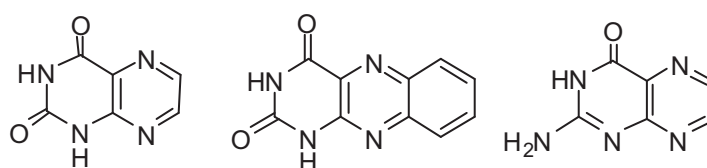


Figure 1.1. The lumazine (left), alloxazine (middle) and pterin (right) bio-heterocycles.

Another biochemically important heterocycle is purine. Purine bases are present in nucleic acids as a source of hydrogen bonding interactions between complementary base pairs to stabilize the antiparallel duplex structure of polynucleotide chains (DNA and RNA). Transition metal coordination chemistry of the purine bases has become of interest after the discovery of the anticancer activity of *cis*-platin^[25]. This complex shows its activity through the inhibition of cell division by cross-linking of the polynucleotide chains. The cross-linking involves metal coordination through the neutral N⁷ nitrogen donor of the guanine base. After this discovery, the metal-purine base coordination chemistry was boosted for the search of better water-soluble cytotoxic metal drugs. The modes of metal coordination by nucleobases have been reviewed by B. Lippert^[26]. This review includes various possible binding modes of purine bases, evidenced through crystal structure determination. Guanine (Figure 1.2), one of the five classical nucleobases, has attracted recent attention for the formation of tetramers in telomeres. Xanthine (Figure 1.2), also a purine base, is found in most human body tissues, fluids and in other organisms.

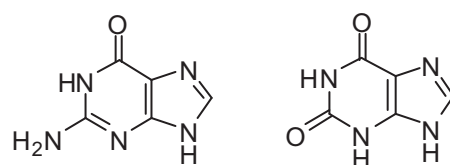


Figure 1.2. The purine bases guanine and xanthine.

Isolation of radical copper complexes and their spectroscopic studies is relevant to understanding the role of copper enzyme and cuproproteins as they also produce radical intermediates in the biological systems^[27]. The coordination chemistry of the azo ligands abcp and abpy (Figure 1.3) is well known for the formation of radical bridged metal complexes, metal-metal interactions at a shorter distance, long-wavelength charge transfer transitions, and the study of the mixed valent intermediates^[28-31].

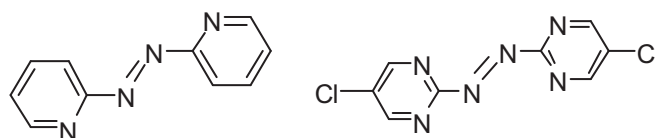


Figure 1.3. The abpy (left) and abcp (right) ligands.

These ligands undergo two-step reduction processes, involving azo anion radical (AAR) and dianionic hydrazido forms, during electrochemical processes. Metal complexes of these two ligands can be isolated either in the radical form or in the diamagnetic form depending on the electronic property of the metal ions. The radical intermediates are characterized by charge transfer transitions in the UV-Vis-NIR spectrum. The metal coordination to the azo ligand is

also indicated by an increase of azo bond length and metal- to -ligand charge transfer transitions.

The first part of this thesis contains the study of soft metal interactions with substituted pteridine and purine heterocycles. Copper complexes with biomolecules have been studied for the investigation of structural aspects and to understand the role of metal ions in various biological functions. The proper choice of ligand systems and the necessary modifications are the key to metal-complex synthesis. All biomolecules have been modified and then reacted with organometallic fragments, $[\text{Cu}(\text{dopf})]^+$, in aprotic media (dopf = 1,1'-bis(diorgano-phosphino)ferrocene). Two types of biomolecules were studied in the course of this doctoral work. Purine nucleobases such as guanine or xanthine (Figure 1.2) and pteridine heterocycles such as lumazine, alloxazine or pterin (Figure 1.1) were modified and their binding to Cu^{I} centres was studied. The structural features have been analyzed and studied spectroscopically, wherever possible. The labile coordination of biomolecules and their equilibria in solution were also investigated. The heteronuclear metal complexes of the non-innocent bridging ligands abpy and abcp (Figure 1.3) have also been synthesized to study the diamagnetic and paramagnetic forms. To enable the isolation of the complexes, I have utilized various organometallic diphosphines as scaffolding chelates (Figure 1.4) which not only stabilize copper(I) but also provides an extra redox-active unit^[32,33].

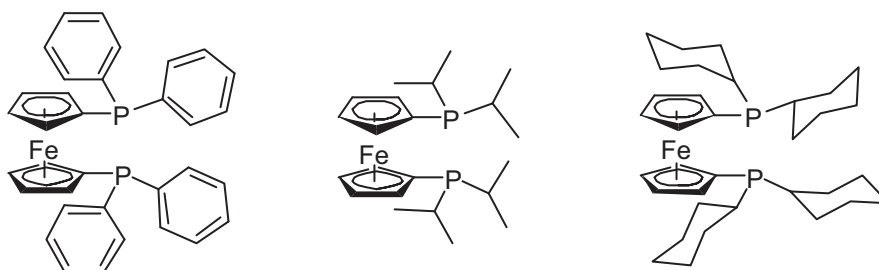


Figure 1.4. The diphosphine ligands dppf (left), dippf (middle) and dchpf (right).

Chapter 2 describes the copper coordination to pteridine-related heterocycles 1,3-dimethylalumazine (DML), 1,3-dimethylalloxazine (DMA), 1,3,7,8-tetramethylalloxazine (TMA) and 2-pivaloylpterin (PP). Infrared spectroscopic measurements, particularly in the carbonyl stretching region, were carried out to infer the metal chelation sites. The crystallographic characterization of the complexes was carried out to establish the N,O chelation of these biomolecules. The reversible electron uptake property of these complexes was studied by cyclic voltammetry under various experimental conditions, polarography, bulk electrolysis, a.c. cyclic voltammetry, and EPR spectroscopy. Spectroelectrochemical methods

were used to observe the UV-Vis and IR spectroscopic changes during the oxidation or reduction processes.

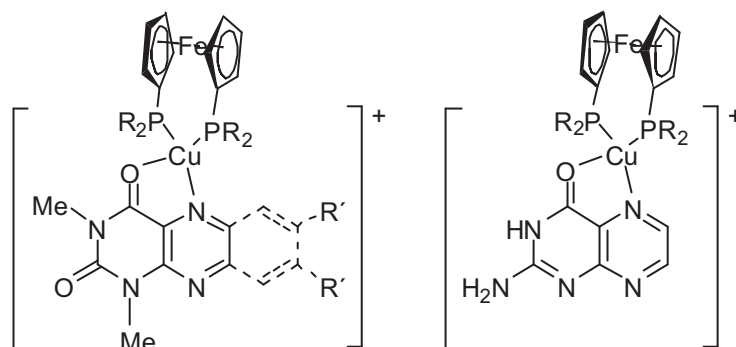


Figure 1.5. Molecular formulae of the $\text{Cu}^{\text{I}}\text{Fe}^{\text{II}}$ -(benzo)pteridine complex cations.

Chapter 3 deals with $[\text{Cu}(\text{dopf})]^+$ binding to the substituted purine nucleobases N2-pivaloyl-9-methylguanine (P-9MG) and 1,3,9-trimethylxanthine (TMX). The discrete and cluster complexes of P-9MG and TMX were synthesized and characterized by infrared spectroscopic measurements. The three organometallic diphosphines (dppf, dippf and dchpf) were used to fine-tune the variable binding property of TMX towards the Cu^{I} centre. Single crystal X-ray structure determination was carried out to investigate the possible binding patterns in these purine complexes. The factors governing the metal binding property of various biomolecules have been established in this chapter. In addition to the structural studies, cyclic voltammetry and UV-Vis spectroscopy has been performed.

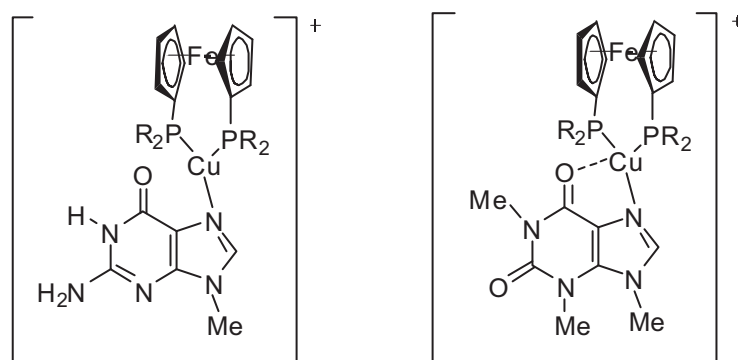


Figure 1.6. Molecular formulae of the $\text{Cu}^{\text{I}}\text{Fe}^{\text{II}}$ -(P-9MG) and $\text{Cu}^{\text{I}}\text{Fe}^{\text{II}}$ -TMX complex cations.

Chapter 4 describes the synthesis and structural characterization of non-innocent radical and non-radical bridged heteronuclear $\text{Cu}^{\text{I}}\text{Fe}^{\text{II}}$ complexes (Figure 1.7). The abcp and abpy ligands (Figure 1.3) were used as bis-chelating, π -electron deficient bridges for soft metal centres.

The spectroscopic investigations include cyclic voltammetry, bulk electrolysis, polarography UV-Vis spectroelectrochemistry, and EPR spectroscopy.

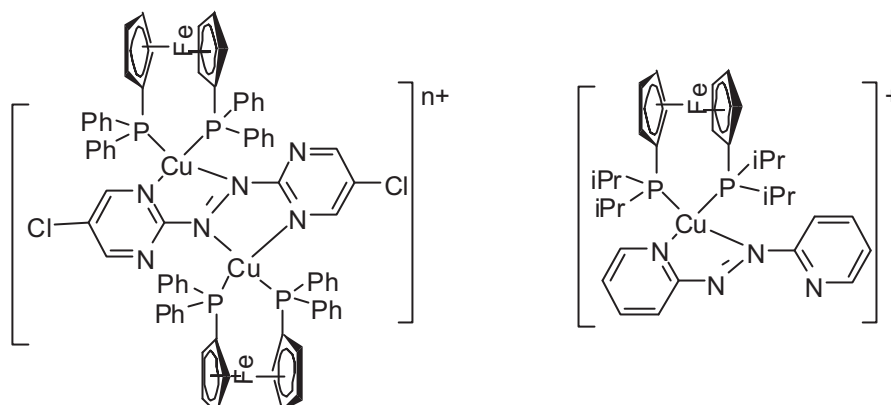


Figure 1.7. Molecular formulae of the complex cations $[(\mu\text{-abcp})\{\text{Cu}(\text{dppf})\}_2]^{2+}$ ($n = 2, 1$) (right) and $[(\mu\text{-abpy})\{\text{Cu}(\text{dppf})\}]^+$ (right).

The thesis also discusses metal-metal interactions via σ -donor and/or π -acceptor bridging ligands. The TCNX (TCNE = tetracyanoethene, TCNQ = 7,7,8,8-tetracyanoquinodimethane, TCNB = 1,2,4,5-tetracyanobenzene) ligand systems are famous for their capability in bridging metal centres, for the isolation of radical complexes, stabilization of mixed-valent intermediates, and the study of unusual electronic and magnetic properties^[34,35]. These ligands can bind up to four metal centres through the cyano nitrogen atoms, and they can undergo electron transfer from the metals to the ligand in ground state, leading to ambiguous oxidation states for metals and ligands. The transition metal-TCNX chemistry of ruthenium^[36-37], osmium^[39], rhenium^[40-42], manganese^[43], iron^[44,45], copper^[46-52] and vanadium^[53] has been investigated for their interesting magnetic properties, anisotropic electrical conductivities, ferromagnetism, NIR absorption and non-linear optical behaviour. The TCNX ligands TCNQF₄ and TCNB (Figure 1.8) are the less employed systems in this area.

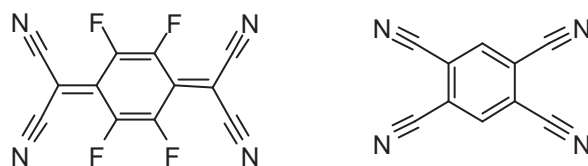


Figure 1.8. The 2,3,5,6-tetrafluoro-7,7,8,8-tetracyano-*p*-benzoquinodimethane (TCNQF₄) (left) and 1,2,4,5-tetracyanobenzene (TCNB) ligands.

Azodicarboxylic esters and their anions and dianions as well as related molecular ions are special ligands in coordination chemistry because of their quinone type two-step redox behaviour, a π conjugated bis-chelate function, a small 6 π center system of which 4 centers are coordinating, a radical intermediate stable against disproportionation, resonance stabilization of the dianionic form, an “S frame” conformation *s-cis*/*E/s-cis* which allows for a rather short metal-metal distance despite molecule bridging, a tuning potential through the substituents R at the non-coordinating carbon π centers, and the possibility to introduce additionally coordinating groups R, leading to bis-tridentate non-innocent ligands. Though the various dinuclear complexes of such ligand systems have been demonstrated in literature^[54-57], complexes containing electron deficient bridging donor had not yet been investigated.

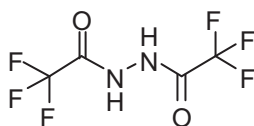


Figure 1.9. Molecular formula of the 1,2-bis(trifluoroacetyl)-hydrazine (H_2adcCF_3) ligand.

The oligonuclear ruthenium and copper-iron complexes containing the strong π -acceptor TCNQF₄ (Figure 1.8) or the weak π -acceptor TCNB (Figure 1.8) or the H_2adcCF_3 ligand (Figure 1.9) have been studied in this thesis. The metal-metal interactions and the light absorption properties were investigated by spectroscopic methods such as EPR in electrochemically generated forms, UV-Vis-NIR-IR spectroelectrochemistry, and by single crystal X-ray diffraction measurements.

Chapter 5 deals with the NIR and IR absorbing properties of radical, non-radical and mixed-valent intermediate species of the complex cation $\{[Ru(NH_3)_5]_4(\mu_4-TCNQF_4)\}^{n+}$ containing π -electron deficient bridging ligand. The complex was made to study the reversibly obtained oxidized and reduced species in solution, resulting in long-wavelength absorbing intermediates. The non-innocent behaviour of the TCNQF₄ ligand has been studied by EPR spectroscopy. The nitrile stretching vibrations and UV-Vis-NIR absorptions of the electrochemically generated species were detected by spectroelectrochemistry.

Chapter 6 deals with the exploration of various coordination modes in oligonuclear $Cu^I Fe^{II}$ -TCNB complexes. Discrete and polymeric complexes containing the organometallic fragments either $[Cu(dppf)]^+$ or $[Cu(dchpf)]^+$ were investigated for TCNB binding mode determination by single crystals X-ray structure analysis. The nitrile vibrations were studied

by IR-spectroelectrochemistry. The study also includes UV-Vis spectroelectrochemistry and EPR spectroscopy.

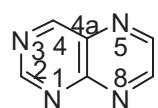
Chapter 7 describes the spectroscopic characterization of redox-intermediates from the complex cation $[(\mu\text{-adc-CF}_3)\{\text{Ru}(\text{bpy})_2\}_2]^{2+}$ including the native $\text{Ru}^{\text{II}}\text{Ru}^{\text{II}}$ species. The involved techniques were cyclic voltammetry, UV-Vis-NIR spectroelectrochemistry, EPR spectroscopy and the single crystal X-ray structure determination. Inter-valence charge transfer processes via $\mu\text{-adc-CF}_3$ bridge have been studied.

Chapter 2

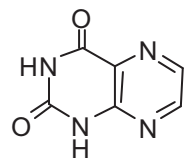
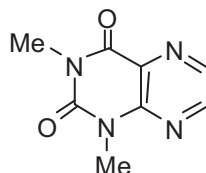
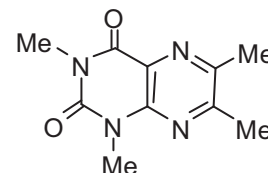
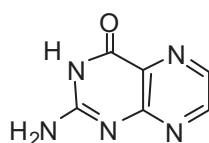
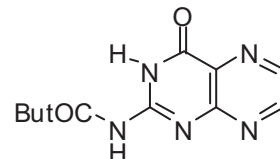
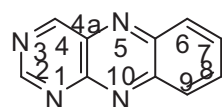
Structural, electrochemical and spectroscopic investigations of organometallic copper(I) complexes with lumazine, alloxazine and pterin ligands

2. 1. Introduction

Pteridine, bearing fused pyrimidine and pyrazine rings, forms a group of biorelevant heterocyclic compounds containing a variety of substitutions on this structure. Lumazine (2,4-dioxo-(1*H*,3*H*)pteridine), alloxazine (2,4-dioxo-(1*H*,3*H*)benzopteridine), flavin (7,8-dimethylisalloxazine) and pterin (2-amino-4-oxo-(3*H*)pteridine) are such substituted forms of pteridine. The presence of lumazine in natural products was reported in 1985^[58]. The alloxazine heterocycle related to flavin coenzymes in electron transfer proteins are famous for the redox switching behavior *in vivo*^[59,60]. Flavin cofactors, when incorporated in a protein framework, can act as a redox mediator between electron donor and acceptor molecules, can take part in various catalytic reactions, and can function as molecular switches in cell signaling processes^[61-63]. Alloxazine, having a low lying π^* molecular orbital, can undergo reversible reduction via a stabilized radical form^[64-66]. In a metal complex, alloxazine can prefer two different redox states, depending on the type of metal fragments. With low-valent (soft) metal fragments, the complexes may be stabilized in the non-reduced state, but with high valent, hard metal fragments the radical form can be isolated^[24,67]. Pterins are found in oxomolybdoenzymes as an active organic redox unit^[1,68]. Pterins and their partially reduced forms (hydropterins) are essential organic redox components in oxo-transfer enzymes (molybdopterin, tungstopterin) for amino acid biosynthesis (phenylalanine, tyrosyl hydroxylase) or NO metabolism (NO synthase)^[5,6,16-18,19]. Another pterin derivative is folic acid (vitamin B9), known as an essential nutrient. The modifications of the pteridine heterocycle carried out here were for the better solubility in aprotic solvents. The modified pteridine and benzopteridine ligands are listed in Figure 2.1.1.



pteridine

2,4-dioxo-(1*H*,3*H*)pteridine
(Lumazine)1,3-dimethyllumazine
(DML) (**A**)1,3,6,7-tetramethylalumazine
(TML)2-amino-4-oxo (3*H*)pteridine
(Pterin)2-pivaloylpterin
(PP) (**B**)

benzopteridine

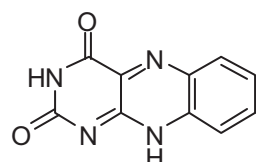
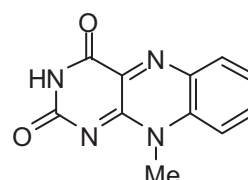
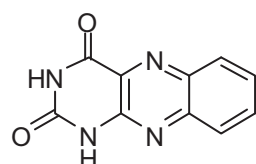
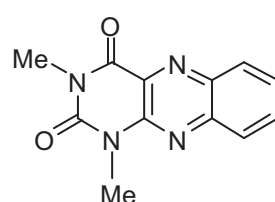
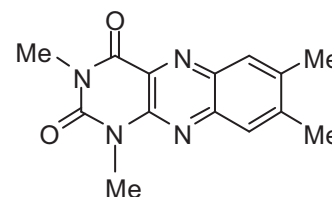
2,4-dioxo-(1*H*,10*H*)benzopteridine
(isoalloxazine)2,4-dioxo-(1*H*,10*Me*)benzopteridine
(10-methylisoalloxazine)2,4-dioxo-(1*H*,3*H*)benzopteridine
(alloxazine)1,3-dimethylalloxazine
(DMA) (**C**)1,3,7,8-tetramethylalloxazine
(TMA) (**D**)

Figure 2.1.1. (benzo)pteridine and its derivatives (**A**, **B**, **C** and **D** ligands have been used in this work).

Metal coordination to the biochemically relevant substituted pteridine heterocycles is of importance in understanding the *in vivo* functions of electron transfer enzymes. Most commonly, an O⁴,N⁵ chelation to transition metals is found in almost all biomolecules containing the α -iminoketo function^[24]. Soft metal centers are found to be strongly N⁵ bonded and comparatively weakly O⁴ bonded in five-membered chelate function, whereas hard metal centers bind strongly to O⁴ and weaker to N⁵ ^[24]. Although various binding modes of pterins are found in the literature, all possible binding modes of pterins are not found in a single complex^[24,69-74]. In this work, I have characterized an oligomeric Cu^IFe^{II}-pterin complex showing all possible binding modes through the heterocyclic donor atoms of pterin *and* the oxygen donor atom from the substituted pivaloyl group. The structural features of the complex are being discussed in detail. Though reports on the crystal structures of Cu^I-lumazine complexes are found in the literature, the electrochemical and spectroelectrochemical studies have not been discussed in detail so far^[69,71,75-78]. The lumazines are known to be biochemically less important due to their irreversible electron transfer process, however, the reversible two-step electrochemical reduction process of lumazine complexes is discussed in this work^[24]. IR-spectroelectrochemistry was measured to investigate the carbonyl stretching frequencies in the reduced and unreduced state. The reversible electron uptake property of the alloxazine complexes was utilized to study the UV-Vis and IR spectroelectrochemical behaviour in the native and the reduced forms.

As the weak π -donor organometallic fragment [Cu(dppf)]⁺ was found to stabilize complexes with very strong π -acceptors in the un-reduced state, I have probed various soft copper(I) complex fragments scaffolded by alkyl- and aryl-ferrocenyldiphosphine ligands for the stabilization of these biomolecule complexes in the un-reduced state. The metal precursors, which have been used in this work, are shown in Figure 2.1.2.

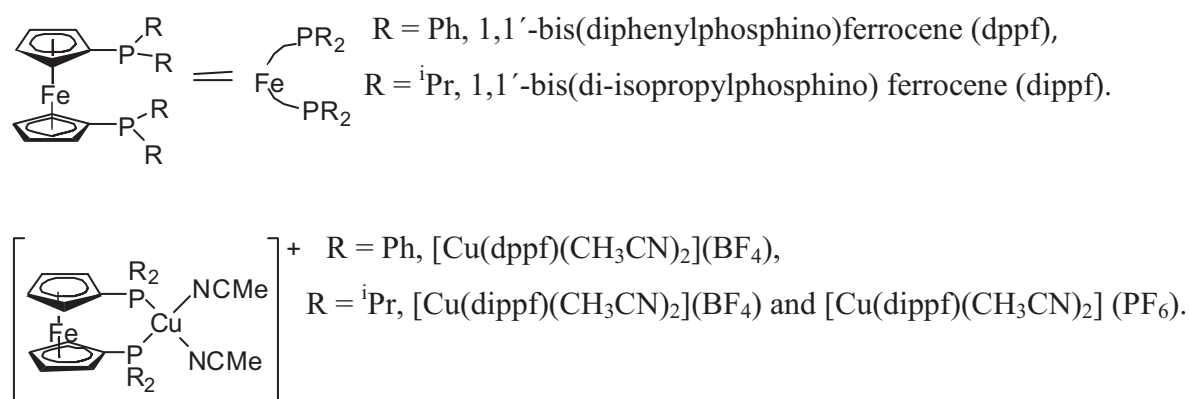


Figure 2.1.2. Co-ligands (top) and copper(I) precursor complexes bottom).

2.2. Synthesis and characterization of $\text{Cu}^{\text{I}}\text{Fe}^{\text{II}}$ complexes

The organic solvent-soluble pteridine ligands 1,3-dimethyllumazine (DML)^[79], 1,3-dimethylalloxazine (DMA)^[80], 1,3,7,8-tetramethylalloxazine (TMA)^[80] and 2-pivaloylpterin (PP)^[81] were synthesized according to the reported literature procedures. The solid precursor complex $[\text{Cu}(\text{dppf})(\text{CH}_3\text{CN})_2](\text{BF}_4)$ was already reported in the literature^[82] and the $[\text{Cu}(\text{dippf})(\text{CH}_3\text{CN})_2](\text{BF}_4)$ precursor complex was newly synthesized to introduce a different coligand. The precursor complex containing PF_6^- as a counter anion was also synthesized to obtain the solid form. Red lumazine complexes $[\text{Cu}(\text{DML})(\text{dppf})](\text{BF}_4)$ and $[\text{Cu}(\text{DML})(\text{dippf})](\text{BF}_4)$ were obtained by stirring a dichloromethane solution of an equimolar mixture of DML and the metal precursors at room temperature under argon atmosphere. The yellow colour of the precursor complex and the ligand turned to a deep red upon the immediate addition of dichloromethane to the reaction mixture.

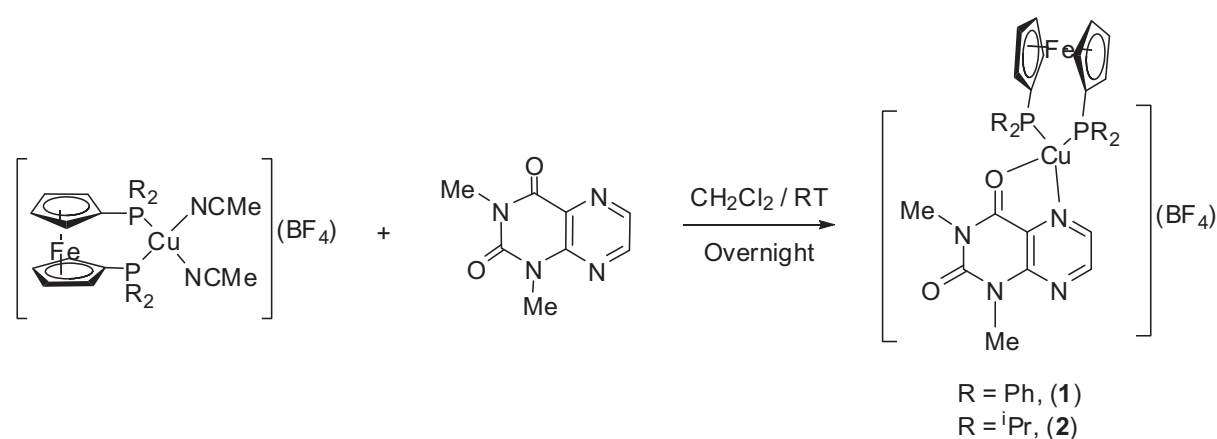


Figure 2.2.1. Synthesis of $\text{Cu}^{\text{I}}\text{Fe}^{\text{II}}$ -DML complexes.

The metal chelation by the lumazine ring is indicated by downfield shifts of the lumazine ring proton NMR signals. The signals at 3.42 (s, 3H, N-CH₃), 3.71 (s, 3H, N-Me), 8.82 (s, br, 1H, DML), and 9.09 (s, br, 1H, DML) ppm are found corresponding to the lumazine ring and the signals at 4.34 (s, 4H, Cp), 4.42 (s, 4H, Cp) and 7.36 (m, br, 20H, Ph) ppm are found for the $[\text{Cu}(\text{dppf})]^+$ moiety present in the complex $[\text{Cu}(\text{DML})(\text{dppf})](\text{BF}_4)$. A signal at -9.88 ppm is found in the ³¹P NMR spectrum. A molecular ion peak centered at $m/z = 809.10$ is also found in the mass spectrum corresponding to $[\text{Cu}(\text{dppf})(\text{DML})]^+$. Satisfactory elemental analysis also supports the formulation of these complexes. The detailed characterization of both lumazine complexes is provided in the Experimental Section.

Alloxazine complexes $[\text{Cu}(\text{DMA})(\text{dppf})](\text{BF}_4)$, $[\text{Cu}(\text{DMA})(\text{dippf})](\text{BF}_4)$ and $[\text{Cu}(\text{TMA})(\text{dppf})](\text{BF}_4)$ were synthesized following a similar method as for the lumazine

complexes. Similarly, the metal binding by the alloxazine ring is indicated by the appearance of a red-brown colour during the reaction. All complexes show the expected NMR signals, satisfactory elemental analyses and molecular ion peaks in their mass spectra. After needful manipulations all new complexes were investigated by FTIR spectroscopy.

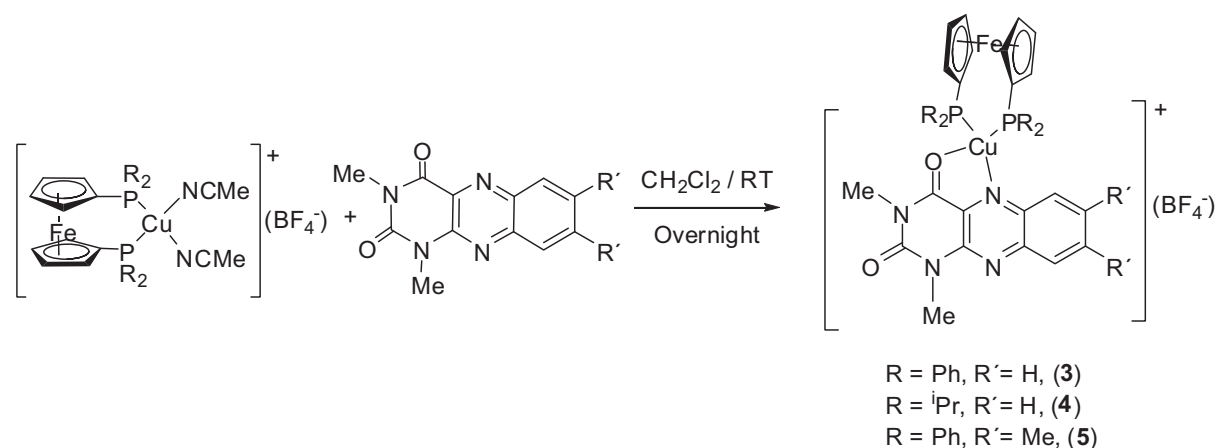


Figure 2.2.2. Synthesis of $\text{Cu}^{\text{I}}\text{Fe}^{\text{II}}$ -DMA and $\text{Cu}^{\text{I}}\text{Fe}^{\text{II}}$ -TMA complexes.

The N^5, O^4 chelated brown pterin complexes $[\text{Cu}(\text{dppf})(\text{PP})](\text{BF}_4)$ (6) and $[\text{Cu}(\text{dippf})(\text{PP})](\text{BF}_4)$ (7) were obtained from 1:1 reactions of PP with the metal precursors in dichloromethane. Both complexes gave molecular ion peaks at $m/z = 864.14$ and $m/z = 728.20$ in the mass spectra for the complex cations $[\text{Cu}(\text{dppf})(\text{PP})]^+$ and $[\text{Cu}(\text{dippf})(\text{PP})]^+$, respectively. These two complexes were also characterized by their NMR spectra, elemental analyses etc. On crystallization of $[\text{Cu}(\text{dppf})(\text{PP})](\text{BF}_4)$ from a hexane dichloromethane (1:1) mixture, the complex dissociated to a new compound having the molecular formula $[\{\text{Cu}(\text{dppf})\}_2(\text{PP})](\text{BF}_4)_2$ (8), as indicated from the partially solved single crystal X-ray structure. From this indication, I gave an effort to make the material fresh by reacting two equivalents of metal precursor with one equivalent of pterin under identical reaction conditions as for the $[\text{Cu}(\text{dppf})(\text{PP})](\text{BF}_4)$. The heterotetranuclear complex, bonded through N^5, O^4 and $\text{N}^1, \text{O}(\text{pivaloyl})$ chelation, was characterized by its molecular ion peak at 1480.16 in the mass spectrum. The characterization of all complexes is provided in the Experimental Section. The tendency to use the maximum of possible coordination sites was again observed when the complex $[\{\text{Cu}(\text{dppf})\}_2(\text{PP})](\text{BF}_4)_2$ was dissociated in hexane/dichloromethane solution (during crystallization) to yield the stable oligomeric complex $[\text{Cu}_3(\text{dppf})(\mu_2\text{-dppf})(\text{PP})(\text{PP}^-)]_2(\text{BF}_4)_4$ (9) containing partly deprotonated pterin ligands (PP^-). The coordination pattern of this oligomeric complex could be identified from the crystal structure

analysis. The solution equilibria of the pterin complexes have been represented in Figure 2.2.3.

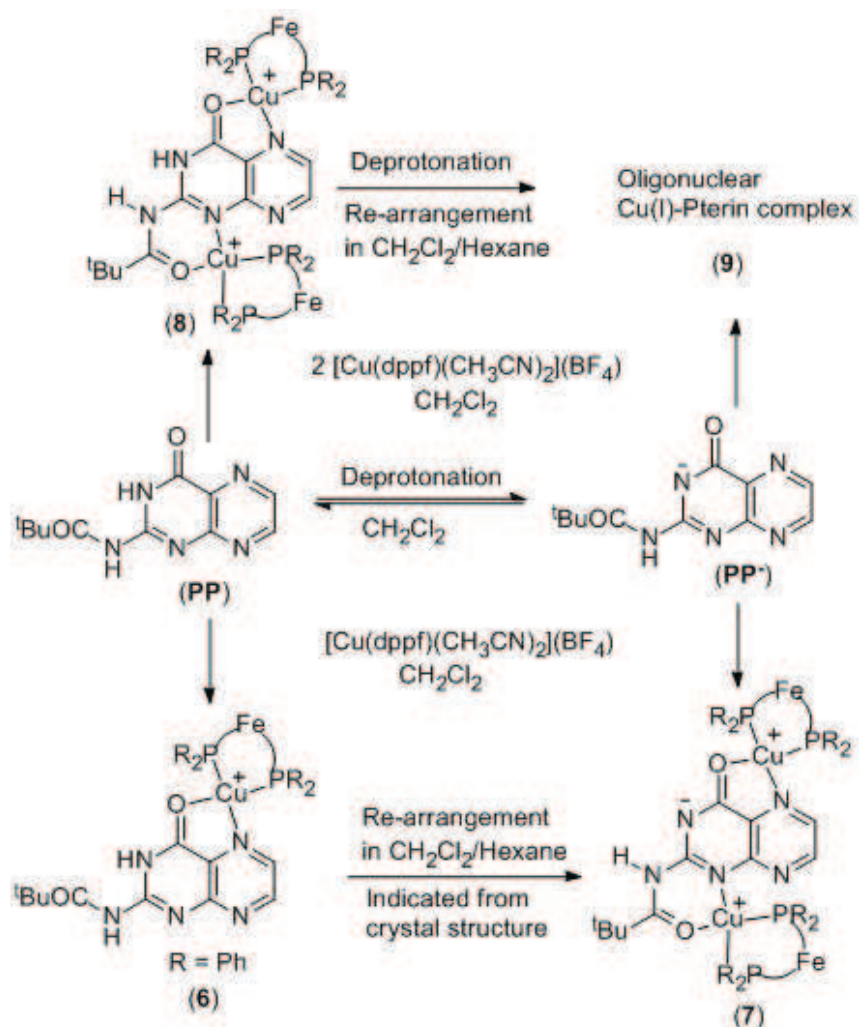


Figure 2.2.3. Dissociation of pterin complex.

2.3. Crystal structures

2.3.1. Crystal structures of the Cu^IFe^{II}-DML complexes [Cu(dppf)(DML)](BF₄) (**1**) and [Cu(dippf)(DML)](BF₄) (**2**).

Red single crystals of complexes **1** and **2** were obtained by slow crystallization of saturated dichloromethane solutions of the complexes at low temperature. Complex **1** was crystallized in $P\bar{1}$ and complex **2** was crystallized in $P2_1/n$ space group. The crystal structure analyses of **1** and **2** revealed the expected^[24] O⁴,N⁵ chelation of DML to the Cu^I centre, forming a 5-membered planar ring system (Figure 2.3.1.1 and Figure 2.3.1.2). The soft metal fragments [Cu(dopf)]⁺ are bonded strongly to the N⁵ (2.027(4) and 2.041(2) Å) and weakly to O⁴ (2.236(3) and 2.261 (2) Å). The negative Δ value ($d_{\text{Cu-N}}-d_{\text{Cu-O}}$), calculated at -0.209 Å and -0.220 Å for the structures of **1** and **2**, respectively, illustrate the stronger N⁵ binding^[24]. The higher negative value for complex **2** was observed as the [Cu(dippf)]⁺ fragment binds to N⁵ more strongly as compared to [Cu(dppf)]⁺. One small chelating angle at the lumazine ring (O1-Cu1-N1 = 78.77(14)° and 78.44(8)°) and another large chelating angle at the dopf unit (P1-Cu-P2 = 114.79(6)° and 117.61(3)°) show the distorted tetrahedral geometry around the Cu^I center.

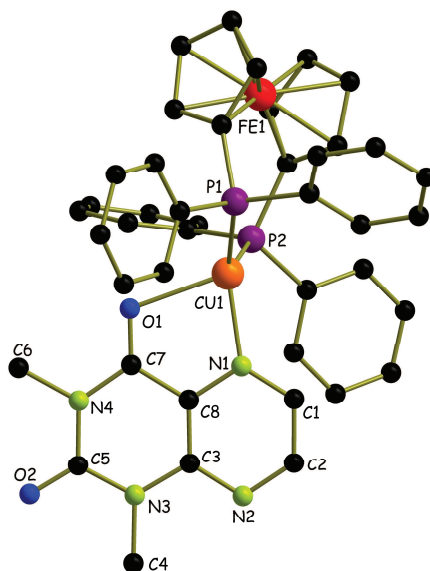


Figure 2.3.1.1. Single crystal X-ray molecular structure of the complex monocation [**1**]⁺ in the crystal of [Cu(dppf)(DML)](BF₄). The BF₄⁻ counter anion is omitted for clarity.

The carbonyl bond lengths, 1.226(6) and 1.211(6) Å in complex **1** and 1.228(3) and 1.214(3) Å in complex **2**, confirm the presence of un-reduced carbonyl groups in the complexes. The differences in carbonyl bond lengths (C⁴-O⁴ and C²-O²) are 0.015 and 0.014 Å for complexes **1** and **2**, respectively. A small change of the carbonyl bond lengths was observed for the weak

metal binding to the O⁴ donor site. The important bond lengths and angles of two crystal structures are given in Table 2.3.2.1 for comparison.

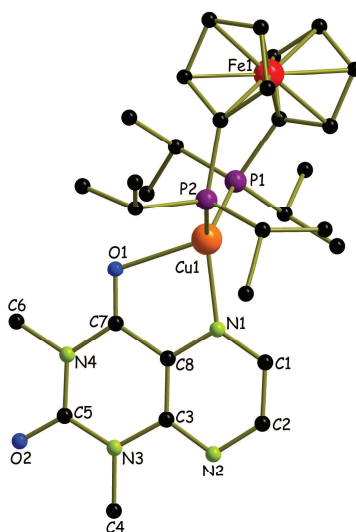


Figure 2.3.1.2. Single crystal X-ray molecular structure of the complex monocation $[2]^+$ in the crystal of $[\text{Cu}(\text{dppf})(\text{DML})](\text{BF}_4) \times \text{CH}_2\text{Cl}_2$. The BF_4^- counter anion and the CH_2Cl_2 molecule (solvent of crystallization) were omitted for clarity.

2.3.2. Crystal structure of the alloxazine complex $[\text{Cu}(\text{dppf})(\text{TMA})](\text{BF}_4)$

Single crystals of complexes **3** and **4** could not be grown even after using various solvent combinations and following different methods. Complex **5** crystallized very easily from hexane / dichloromethane mixture (3:1) at -4°C .

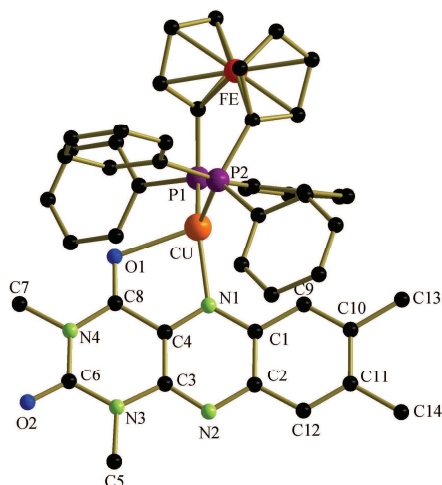


Figure 2.3.2.1. Single crystal X-ray molecular structure of the complex monocation $[5]^+$ in the crystal of $[\text{Cu}(\text{dppf})(\text{TMA})](\text{BF}_4) \times \text{CH}_2\text{Cl}_2$. The BF_4^- counter anion and the CH_2Cl_2 molecule (solvent of crystallization) were omitted for clarity.

Table 2.3.2.1. Selected bond distances (Å) and angles (°) of [Cu(dppf)(DML)](BF₄), **1**, [Cu(dippf)(DML)](BF₄), **2** and [Cu(dppf)(TMA)](BF₄), **5**.

Bonds	1	2	5
Cu-N	2.027(4)	2.041(2)	2.032(2)
Cu-O	2.236(3)	2.261(2)	2.243(2)
C ⁴ -O	C7-O1 1.226(6)	C7-O1 1.228(3)	C8-O1 1.228(3)
C ² -O	C5-O2 1.211(6)	C5-O2 1.214(3)	C6-O2 1.210(3)
Cu-P	2.220(2) 2.250(2)	2.243(1) 2.247(1)	2.234(1) 2.258(1)
O-Cu-N	78.77(14)	78.44(8)	77.94(7)
P-Cu-P	114.79(6)	117.61(3)	113.71(2)
Cu-N-C	Cu1-N1-C1 130.0(3) Cu1-N1-C8 113.1(3)	Cu1-N1-C1 129.9(2) Cu1-N1-C8 113.9(2)	Cu1-N1-C1 127.72(16) Cu-N1-C4 116.7(2)
C-N-C	C1-N1-C8 116.0(4)	C1-N1-C8 116.2(2)	C1-N1-C4 116.7(2)
N-C-C	N1-C8-C7 116.7(4)	N1-C8-C7 117.1(2)	N1-C4-C8 116.3(2)
O-C-C	O1-C7-C8 122.2 (4)	O1-C7-C8 122.2(2)	O1-C8-C4 121.5(2)

The red single crystals of complex **5** were analyzed in space group *P* $\bar{1}$. The α -iminoketo function of the alloxazine unit was involved in a 5-membered chelation to the copper(I) centre (Figure 2.3.2.1). The Cu-N and Cu-O distances were found at 2.032(2) and 2.243(2) Å. The Δ value (-0.211 Å) was found to be in between that of the two lumazine complexes **1** and **2**. The binding of the [Cu(dppf)]⁺ unit to the alloxazine ring is very similar as with the lumazine ring.

The metal coordination on the alloxazine ring did not affect the planarity of the heterocyclic ring system. The carbonyl bond distances C8-O1 = 1.228(3) and C6-O2 = 1.210(3) Å proved the existence of the non-reduced carbonyl groups, as is confirmed by the spectroscopic measurements (innocent behaviour of TMA despite the less negative reduction potential). The two chelate angles at the distorted tetrahedral CuP₂NO coordination are P1-Cu-P2 = 113.71(2)° and O1-Cu-N1 = 77.94(7)°. All other structural features are very much comparable to that of the lumazine complexes **1** and **2** discussed before.

2.3.3. Crystal structure of the pterin complex [Cu₃(dppf)(μ₂-dppf)(PP)(PP⁻)₂(BF₄)₄]

In the crystal structure of a Cu^I-pterin aggregate ([Cu₃(dppf)(μ₂-dppf)(PP)(PP⁻)₂(BF₄)₄, **9**), formed in the solution equilibrium (Figure 2.2.3), the expected O⁴,N⁵ chelation to the [Cu(dppf)]⁺ fragment is found in addition to metal binding through N¹, N³ and N⁸ donor sites. Also, the pivaloyl O atom is bonded to Cu^I to form 6-membered O,N chelate. A threefold metal coordination through N¹, N³, N⁵, N⁸, O⁴ and O² is found for the deprotonated pterin PP⁻ and a twofold metal coordination through N⁵ and N⁸ is observed for the neutral pterin ligand PP (Figure 2.3.3.1). The anionic PP⁻ ligand is formed due to mono-deprotonation in solution during the crystallization process, possibly involving another pterin as base (Figure 2.2.3). The deprotonated pterin is involved in intermolecular hydrogen bonding (O3-H101 = 2.256 Å, O3-N5 = 2.982 Å) to a neutral pterin. Also in the neutral pterin, strong intramolecular hydrogen bonding through 6-membered ring formation is found (O4-H103 = 2.008 Å, O4-N9 = 2.589 Å) between the pivaloyl O4 and the ring N-H proton. This structure is a first example where all pterin-heteroatoms are involved in metal-coordination to stabilize a dimeric structure. The structure contains 2 PP / 2 PP⁻ / 6 Cu^I / 2 dppf / 2 μ₂-dppf. Binding of Cu^I to the non-reduced pterin is confirmed by the carbonyl bond lengths. The O⁴ (O1) atom bridges two Cu^I centers with very different Cu-O distances of Cu3-O1 = 2.667(1) Å and Cu1-O1 = 2.182(2) Å. The angle across this bridge is Cu3-O1-Cu1 = 167.394(2)°, indicating an almost linear type of bridging. The five-coordinated Cu^I centre Cu3 adopts a square pyramidal (C_{4v}) type geometry with weak bonding interaction to O⁴ (O1). Three different coordination spheres, CuPN₂O for Cu1, CuPN₂O₂ for Cu3 and CuP₂NO for Cu2 (Figure 2.3.3.1) are found in the crystal structure. The structure contains both chelating (P3, P4) and bridging dppf units (P1, P2). Torsional conformations of the Cp rings are also different for these two types of dppf. The chelating dppf is found to be in a synclinal staggered conformation and the bridging μ₂-dppf is observed in the anticlinal staggered conformation. The μ₂-dppf is involved in stabilizing the Cu3-O1-Cu1 bridge and the chelating dppf unit is involved in the formation of

stable five-membered chelates. The bridging mode is illustrated in the simplified Figure 2.3.3.2.

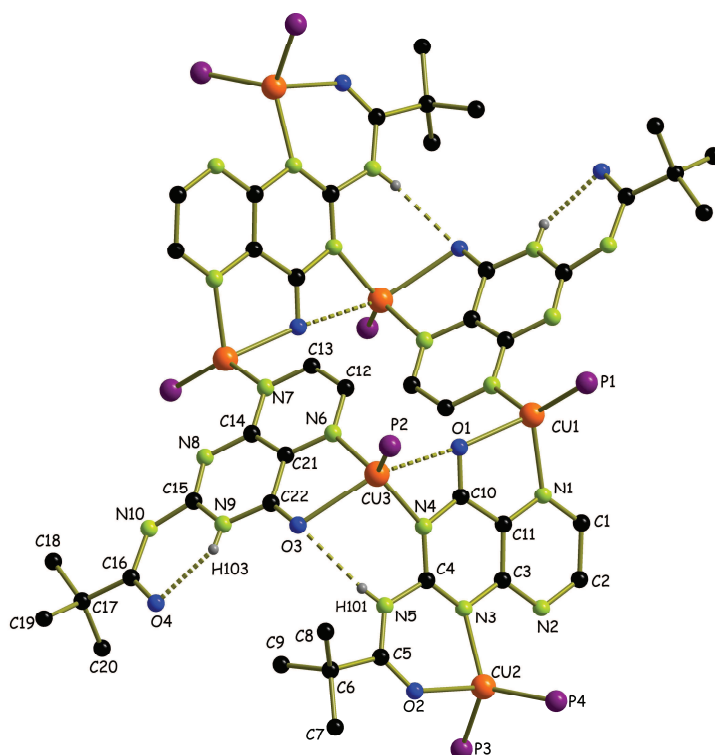


Figure 2.3.3.1. Single crystal X-ray molecular structure of the complex $[\text{Cu}_3(\text{dppf})(\mu_2\text{-dppf})(\text{PP})(\text{PP}')]_2(\text{BF}_4)_4 \times 5 \text{CH}_2\text{Cl}_2$, **9**. The BF_4^- counter anions, dppf and one CH_2Cl_2 molecules were omitted for clarity.

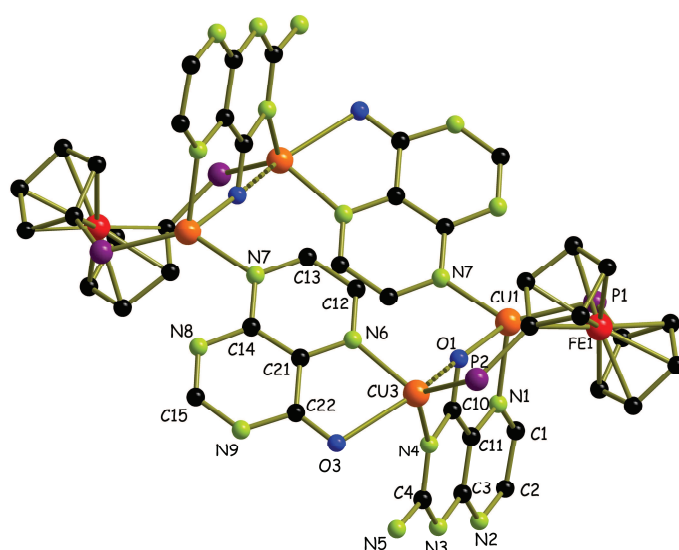


Figure 2.3.3.2. Bridging of dppf unit (P1, P2) to two Cu centers (Cu1, Cu2) forming a Cu-O-Cu bridge (simplified view after omitting certain atoms).

Table 2.3.3.1. Selected bond lengths (Å) and angles (°) of the complex $[\text{Cu}_3(\text{dppf})(\mu_2\text{-dppf})(\text{PP})(\text{PP}^-)]_2(\text{BF}_4)_4$, **9**.

Cu-N	C-O	Cu-O	Cu-P	O-Cu-N	P-Cu-P
Cu1-N1 2.083(3)	C10-O1 1.252(4)	Cu1-O1 2.182(2)	Cu1-P1 2.178(1)	80.57(10)	116.67(4)
Cu1-N7 2.033(3)	C22-O3 1.232(4)	Cu2-O2 2.152(3)	Cu2-P3 2.224(1)	85.23(11)	
Cu2-N3 2.040(3)	C5-O2 1.219(4)	Cu3-O3 2.370(2)	Cu2-P4 2.232(1)	77.62(10)	
Cu3-N6 2.010(3)	C16-O4 1.235(5)	Cu3-O1 2.667(1)	Cu3-P2 2.161(1)	55.76 (1)	
Cu3-N4 2.022(3)					

2.4. Infrared spectroscopy

Infrared spectroscopic measurements for solids were carried out to identify the carbonyl stretching bands in the free ligands and the metal complexes. Two sharp characteristic bands in the carbonyl region were found for DML, DMA, TMA and PP in the range of 1612-1718 cm^{-1} . The band at lower energy was assigned to the $\text{C}^4\text{-O}$ carbonyl group of the α -iminiketo function while the band at higher energy was assigned to $\text{C}^2\text{-O}$ stretching. In the metal complexes, $\nu(\text{C}^4\text{-O})$ was found in the range 1612-1652 cm^{-1} and $\nu(\text{C}^2\text{-O})$ was found in the range of 1660-1718 cm^{-1} . On metal coordination through O^4, N^5 chelation, a comparatively large shift ($< -60 \text{ cm}^{-1}$) was found for the $\text{C}^4\text{-O}$ carbonyl functions whereas shifts for $\text{C}^2\text{-O}$ was smaller ($< -11 \text{ cm}^{-1}$). The stretching frequency of both carbonyls is shifted to lower energy on metal coordination. The stretching frequencies of free ligands, metal complexes and the corresponding shifts are given in Table 2.4.1 for comparison. However, as the soft Cu^1 metal fragment binds to O^4 rather weakly, a large shift of carbonyl stretching is not expected in either case. In the metal complexes of DML, DMA and TMA, it was observed that the $\Delta\nu(\text{C}^4\text{-O})$ is in the range of -11 to -30 cm^{-1} and $\Delta\nu(\text{C}^2\text{-O})$ is in the range of 0 to -5 cm^{-1} . Larger shifts of $\nu(\text{C}^4\text{-O})$ was found for the pterin complexes (-57 and -59 cm^{-1}), indicating a stronger

binding to O of the metal centre compared to the lumazine and alloxazine complexes. The analyses and assignments of the carbonyl bands are given in Table 2.4.1.

Table 2.4.1 IR stretching frequency data^a of ligands and their metal complexes

Compounds	$\nu_{\text{C=O}}$ (in cm^{-1})		$\Delta\nu_{\text{C=O}}$ on metalation (cm^{-1}) ^b	
	(C ² -O)	(C ⁴ -O)	$\Delta\nu$ (C ² -O)	$\Delta\nu$ (C ⁴ -O)
DML	1712(s)	1658(vs)	n.a.	n.a.
DMA	1718(s)	1667(vs)	n.a.	n.a.
TMA	1717(s)	1671(vs)	n.a.	n.a.
PP	1675(vs)	1671(vs)	n.a.	n.a.
[Cu(dppf)(DML)](BF ₄) 1	1712(s)	1643(vs)	0	-15
[Cu(dippf)(DML)](BF ₄) 2	1707(s)	1647(vs)	-5	-11
[Cu(dppf)(DMA)](BF ₄) 3	1715(s)	1644(vs)	-3	-23
[Cu(dippf)(DMA)](BF ₄) 4	1718(s)	1652(vs)	0	-15
[Cu(dppf)(TMA)](BF ₄) 5	1713(s)	1641(vs)	-4	-30
[Cu(dppf)(PP)](BF ₄) 6	1660(w) ^c	1614(s)	-1 ^{5c}	-57
[Cu(dippf)(PP)](BF ₄) 7	1664(s) ^c	1612(s)	-11 ^c	-59

^aIR data from measurements in the solid state. ^b $\Delta\nu_{\text{C=O}}$ on metalation (cm^{-1}) is the difference of the carbonyl stretching frequency between the free ligand and the corresponding metal complex. Negative sign indicates the decrease of stretching frequency on metalation. ^c(C²-O) is the carbonyl group in the pivaloyl substituent.

2.5. Electrochemistry

2.5.1. Cyclic voltammetry

To study electrochemical processes, cyclic voltammograms of all complexes were measured in CH_2Cl_2 / 0.1 M Bu_4NPF_6 with 100 mV/sec scan rate in argon atmosphere. The obtained electrochemical data along with the potentials of free ligands and reported metal complexes are provided in Table 2.5.1.1. The cyclic voltammograms of the complexes versus ferrocene/ferrocenium in dichloromethane can be found in Figure 2.5.1.1. Metal complexes of lumazine are known to undergo one-electron irreversible reduction process^[78]. For the free DML ligand only one irreversible reduction process is found at -1.98 V vs. ferrocenium/ferrocene^[78]. Besides the expected ferrocene-based one-electron oxidation, a seemingly reversible two-step reduction was observed for the lumazine complexes **1** and **2**. The first reduction leads to the formation of a pyrazine-based radical complex which was later confirmed by an isotropic *g* value for the EPR signal (Section 2.8). A quasi reversible second reduction at more negative potential with smaller cathodic and anodic peak currents was noticed in these complexes. This second reduction can not be considered as the formation of a dianionic lumazine heterocycle since the peak currents for the first and second reduction differ by a large amount. As the origin of second reduction wave was unclear from the measured cyclic voltammogram, a variety of electrochemical experiments such as cyclic voltammogram under various conditions, polarography, bulk electrolysis, phase sensitive A.C. cyclic voltammetry with complex $[\text{Cu}(\text{dippf})(\text{DML})](\text{PF}_6)$ (**2**) was performed in collaboration with Dr. Jan Fiedler at the J. Heyrovský Institute of Physical Chemistry, v.v.i., Academy of Sciences of the Czech Republic, Prague, Czech Republic. The obtained results are discussed separately later in section 2.5.2-2.5.6. The behaviour of complex **1** was very similar to **2** in the electrochemical experiments. Both reduction waves were found at somewhat less negative potentials, -1.45 and -1.92 V. The easier reduction of the Ph analogue can be explained by taking into consideration the electronic effect of dppf vs. dippf (Ph acceptor vs. ⁱPr donor). Cyclic voltammograms measured at 100 mV/s scan rate, showed a very small (almost negligible) second reduction wave for **1** which is attributed to the higher stability of the complex as compared to the dippf derivative **2**.

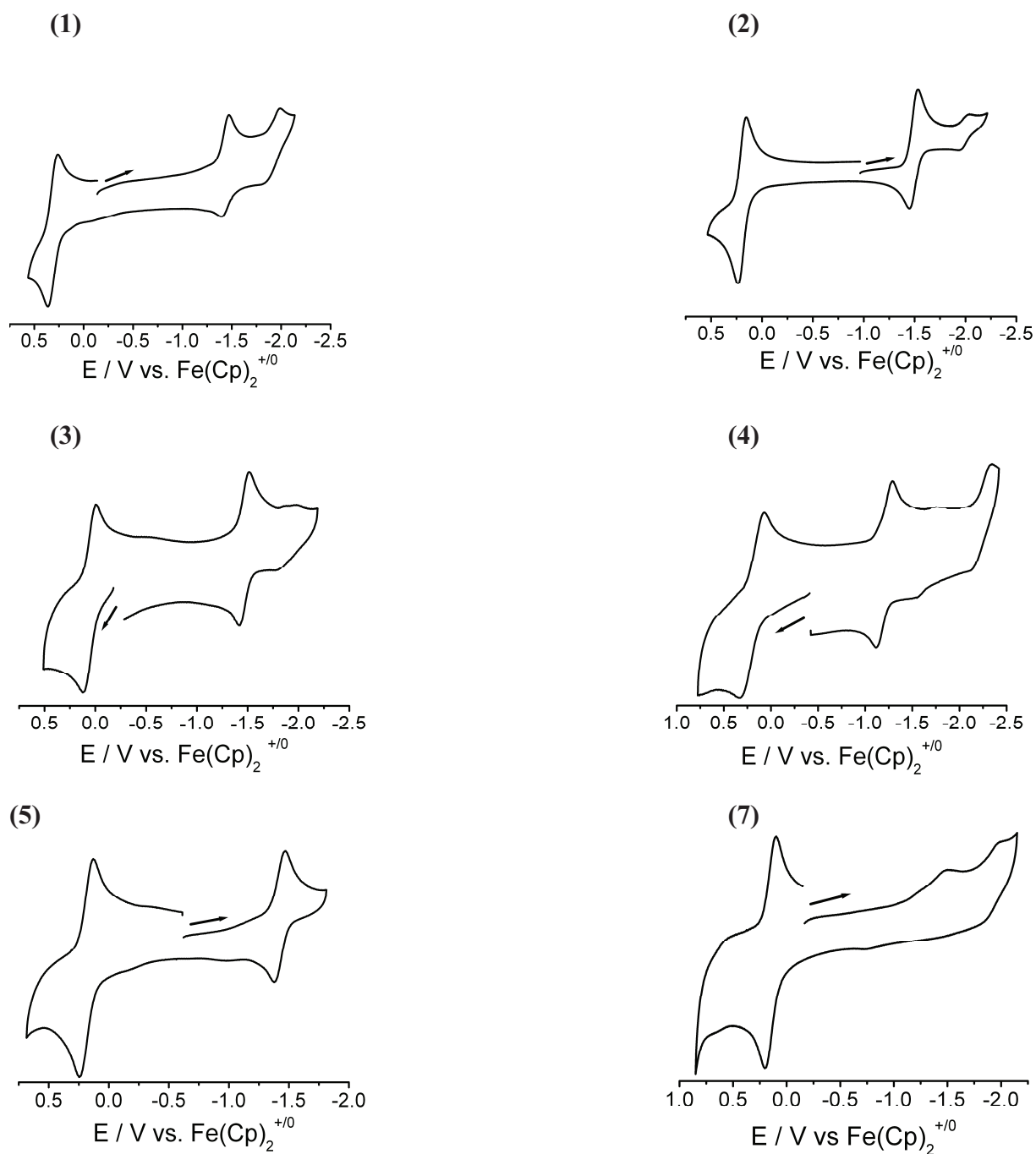


Figure 2.5.1.1. Cyclic voltammograms of $[\text{Cu}(\text{dppf})(\text{DML})](\text{BF}_4)$ (top left), $[\text{Cu}(\text{dippf})(\text{DML})](\text{BF}_4)$ (top right), $[\text{Cu}(\text{dppf})(\text{DMA})](\text{BF}_4)$ (middle left), $[\text{Cu}(\text{idppf})(\text{DMA})](\text{BF}_4)$ (middle right), $[\text{Cu}(\text{dppf})(\text{TMA})](\text{BF}_4)$ (bottom left), $[\text{Cu}(\text{dippf})(\text{PP})](\text{BF}_4)$ (bottom right) in $\text{CH}_2\text{Cl}_2 / \text{Bu}_4\text{NPF}_6$ on glassy carbon electrode, scan rate 100 mV/s, calibrated with respect to ferrocene/ferrocenium.

Table 2.5.1.1. Redox potentials^{a)} from cyclic voltammetry.

Compound	E _{1/2} (ox)/V (ΔE / mV)	E _{1/2} (red 1)/V (ΔE / mV)	E _{1/2} (red 2)/V (ΔE / mV)	Solvent	Reference
DML	n.d.	-1.98 (ir) ^b	n.o.	THF	78
DMA	n.d.	-1.68	-2.33 (ir) ^b	THF	78
PP	n.d.	-1.83 (ir) ^b	n.o.	THF	70
[Cu(PPh ₃) ₂ (DML)](BF ₄)	-	-1.43(ir) ^b	-	DCE	83
[Cu(dppf)(DML)](BF ₄) 1	0.31(100)	-1.45(60)	-1.92(150)	CH ₂ Cl ₂	This work
[Cu(dippf)(DML)](BF ₄) 2	0.19(80)	-1.49(90)	-2.00(70)	CH ₂ Cl ₂	This work
[Cu(PPh ₃) ₂ (DMA)](BF ₄)		-1.00	-1.87 ^b	THF	84
[Cu(dppf)(DMA)](BF ₄) 3	0.06(130)	-1.45 (90)	-1.86(130)	CH ₂ Cl ₂	This work
[Cu(dippf)(DMA)](BF ₄) 4	0.21(270)	-1.21(170)	-2.23(200)	CH ₂ Cl ₂	This work
[Cu(dppf)(TMA)](BF ₄) 5	0.19(120)	-1.42(80)	n.d.	CH ₂ Cl ₂	This work
[Cu(PPh ₃) ₂ (PP)](BF ₄)	0.81 (ir) ^b	-1.23 (ir) ^b	n.d.	THF	85
[Cu(dppf)(PP)](BF ₄) 6	0.18(110)	-1.31(ir) ^b	-2.02(ir) ^b	CH ₂ Cl ₂	This work
[Cu(dippf)(PP)](BF ₄) 7	0.15(100)	-1.48(ir) ^b	-1.98(ir) ^b	CH ₂ Cl ₂	This work
[{Cu(dppf)(PP)} ₂](BF ₄) ₂ 8	0.16(140) ^c	-1.25(ir) ^b	-2.07(ir) ^b	CH ₂ Cl ₂	This work

^{a)}Potentials (V) vs. ferrocenium/ferrocene. Half-wave potentials, unless noted otherwise: (qr):quasi-reversible, (i): irreversible (peak potential given). ^{b)}Peak potentials for the corresponding process. ^{c)}Two-electron broad wave for Fe oxidation.

In the alloxazine complexes **3**, **4** and **5**, the expected one-electron reversible reductions were found at less negative potentials compared to the free DMA or TMA ligand. The second irreversible reductions were found in complexes **3** and **4** (Figure 2.5.1.1). The cyclic voltammogram of complex **5** was only measured up to the first one-electron reversible reduction.

Pterin and its derivatives undergo only irreversible reduction processes accompanying proton transfer reactions during the electrochemical process. The pterin complexes **6**, **7** and **8** showed expected irreversible reductions at a less negative potential than the free PP ligand as well as one ferrocene based reversible oxidation.

2.5.2. Cyclic voltammetry of [Cu(dippf)(DML)](PF₆) (2)

The cyclic voltammogram (Figure 2.5.2.1) was obtained when measured with carefully dried electrolyte and solvent applying a scan rate of 200 mV/s. It was observed that the second cathodic peak current is dependent on the electrode and on the delay time in solution. The peak current ratio $i_{pa}/i_{pc} < 1$ for the first reduction step indicated a reaction following the charge transfer or/and an inhibition by an adsorbed (decomposition) product on the electrode surface. When the cyclic voltammogram was further measured with a higher scan rate of 25 V/sec (Figure 2.5.2.3), $i_{pa}/i_{pc} = 1$ for the first reduction step but the second small peak still appeared. It therefore seems to belong to a second species in solution, not formed on the electrode. The small peak does not show adsorption character. There is also a possibility of two contradictory effects: increase of peak with scan rate due to adsorption and decrease due to limited reversibility or rate of formation.

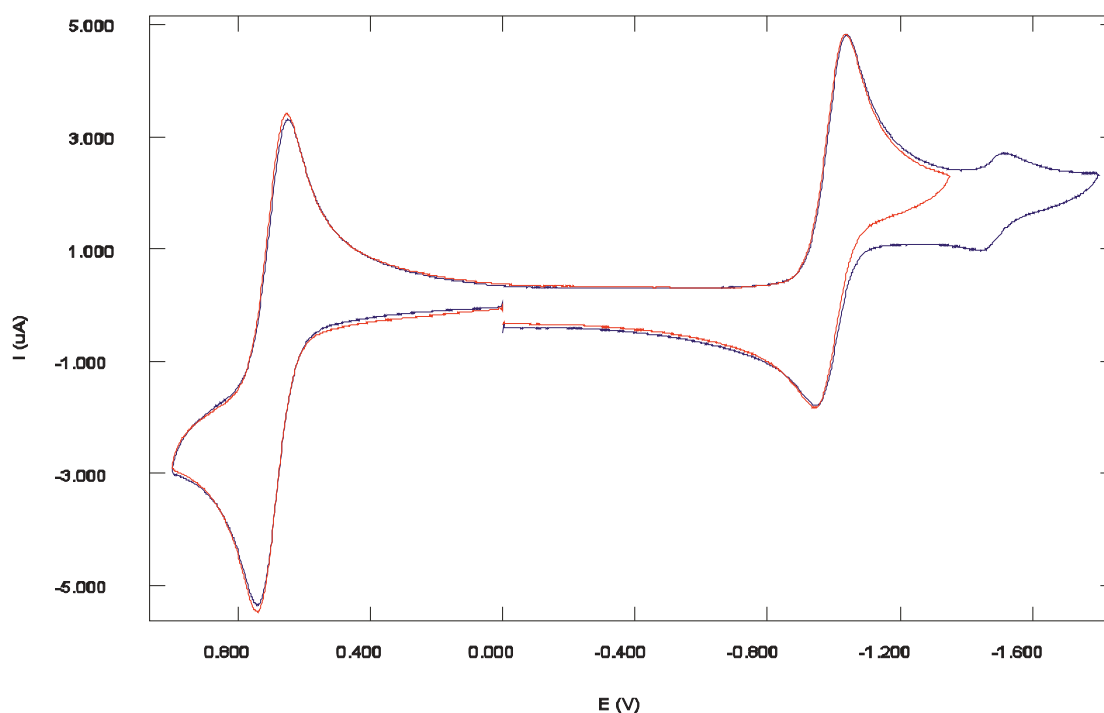


Figure 2.5.2.1. Cyclic voltammogram of [Cu(dippf)(DML)](PF₆) (2) in CH₂Cl₂ / Bu₄NPF₆ at a glassy carbon electrode, scan rate 200 mV/s.

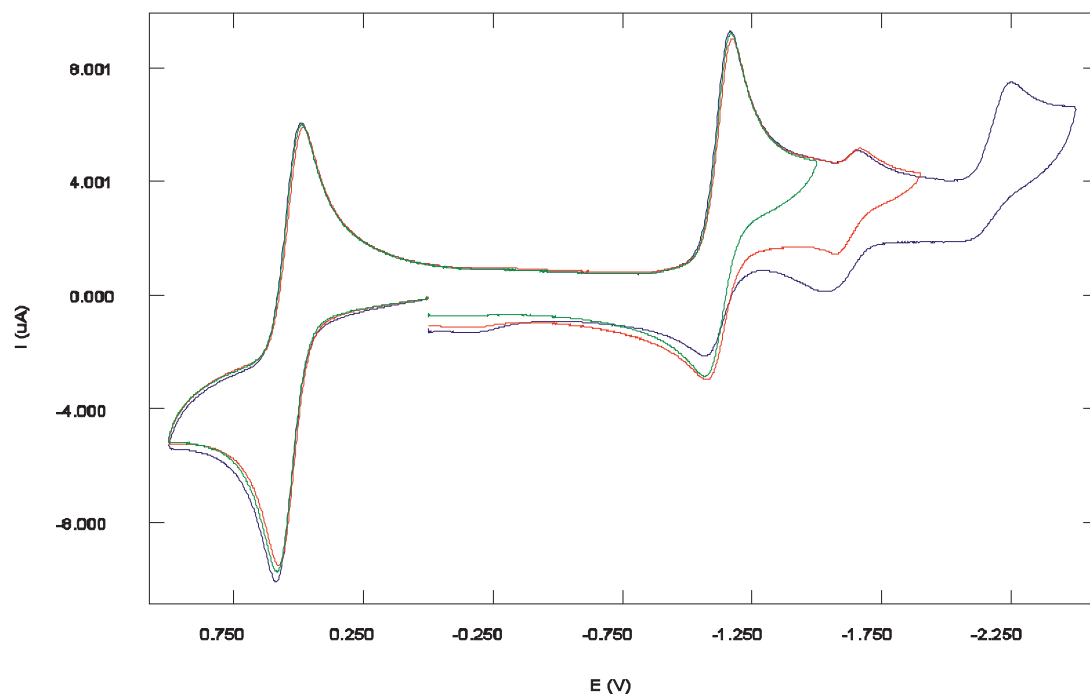


Figure 2.5.2.2. Cyclic voltammogram of $[\text{Cu}(\text{dipf})(\text{DML})](\text{PF}_6)$ (**2**) in acetone / Bu_4NPF_6 at a glassy carbon electrode, scan rate 200 mV/s.

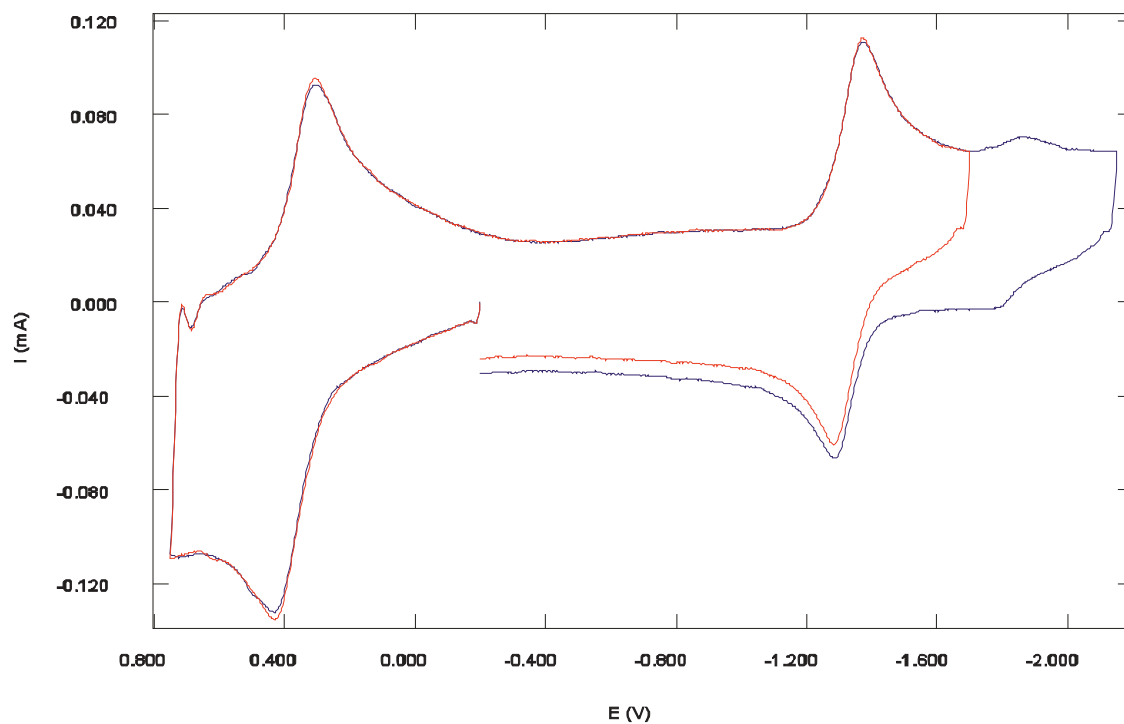


Figure 2.5.2.3. Cyclic voltammogram of $[\text{Cu}(\text{dipf})(\text{DML})](\text{PF}_6)$ (**2**) in CH_2Cl_2 / Bu_4NPF_6 at a glassy carbon electrode, scan rate 25 V/s.

2.5.3. Polarography of [Cu(dippf)(DML)](PF₆) (2)

Polarography was measured with a Hanging Mercury Drop Electrode (HMDE), both in dichloromethane and acetone solutions of the complex, using Bu₄NPF₆ as an electrolyte. A polarographic maximum (caused by increased mass transport due to convection around the growing mercury drop) was observed at the second small wave which indicates a change on the electrode surface (double-layer) and a change of surface tension due to forming a layer on the electrode. The polarogram measured in dichloromethane is represented in Figure 2.5.3.1 and polarogram in acetone is in Figure 2.5.3.2. The polarographic maximum at the second small wave was found to be larger in acetone than in dichloromethane.

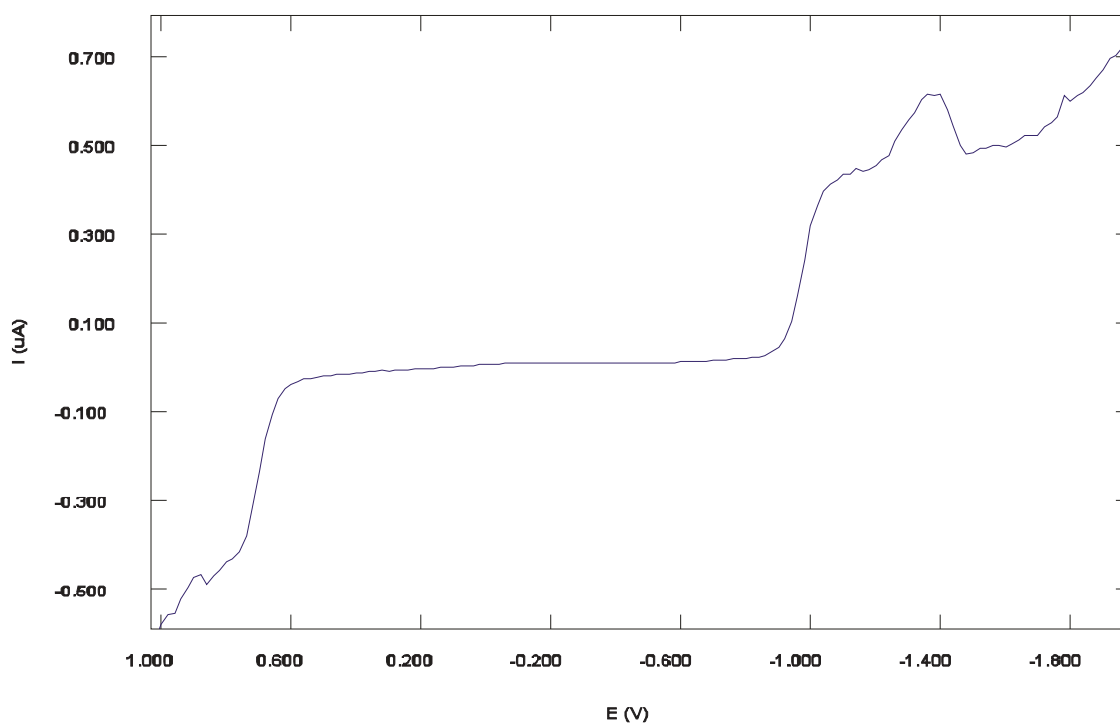


Figure 2.5.3.1. Polarography of [Cu(dippf)(DML)](PF₆) (2) in CH₂Cl₂ / Bu₄NPF₆.

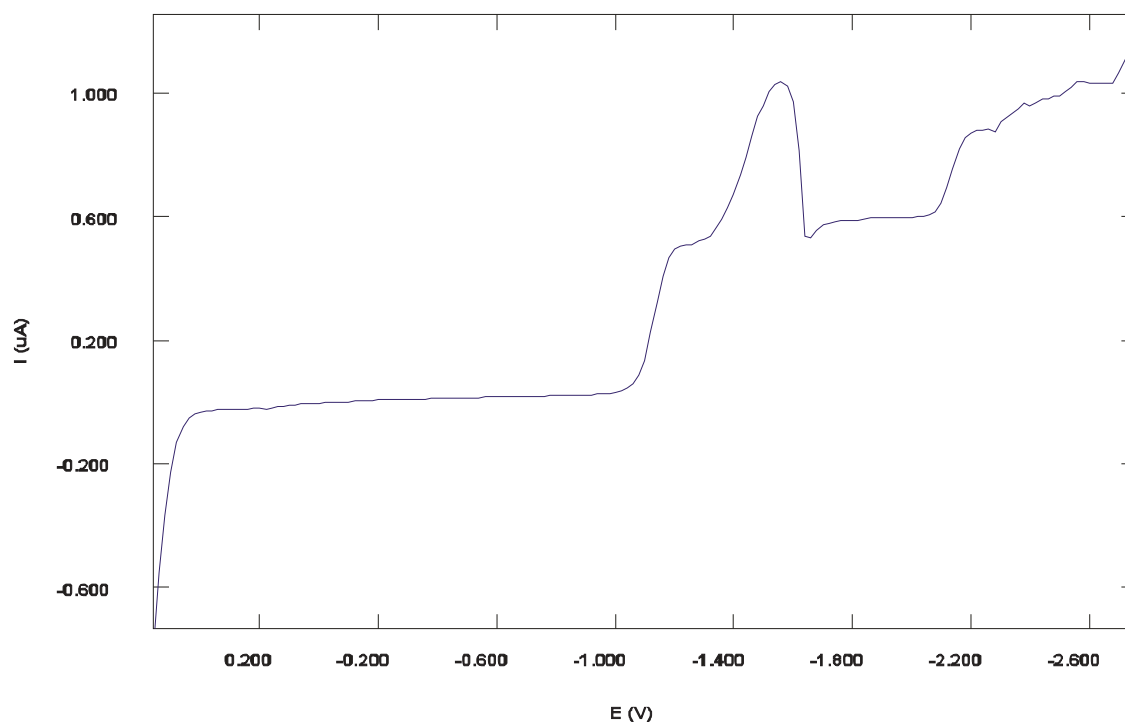


Figure 2.5.3.2. Polarography of [Cu(dippf)(DML)](PF₆) (2) in acetone / Bu₄NPF₆ .

2.5.4. Effect of electrolyte on the cyclic voltammogram of [Cu(dippf)(DML)](PF₆) (2)

Cyclic voltammograms, using various combinations of electrolytes and solvents, were measured to demonstrate the effect of electrolytes and solvents on the reduction process. Only in the case of lithium perchlorate in propylenecarbonate the second smaller reduction peak was suppressed (Figure 2.5.4.1 - 2.5.4.4). At the same time, however, the reversibility of the first step was also diminished. From this observation, it is assumed that a layer of the Li salt forms on the electrode which inhibits the electron transfer reaction (one hypothesis was low soluble LiF, if fluoride present in the sample).

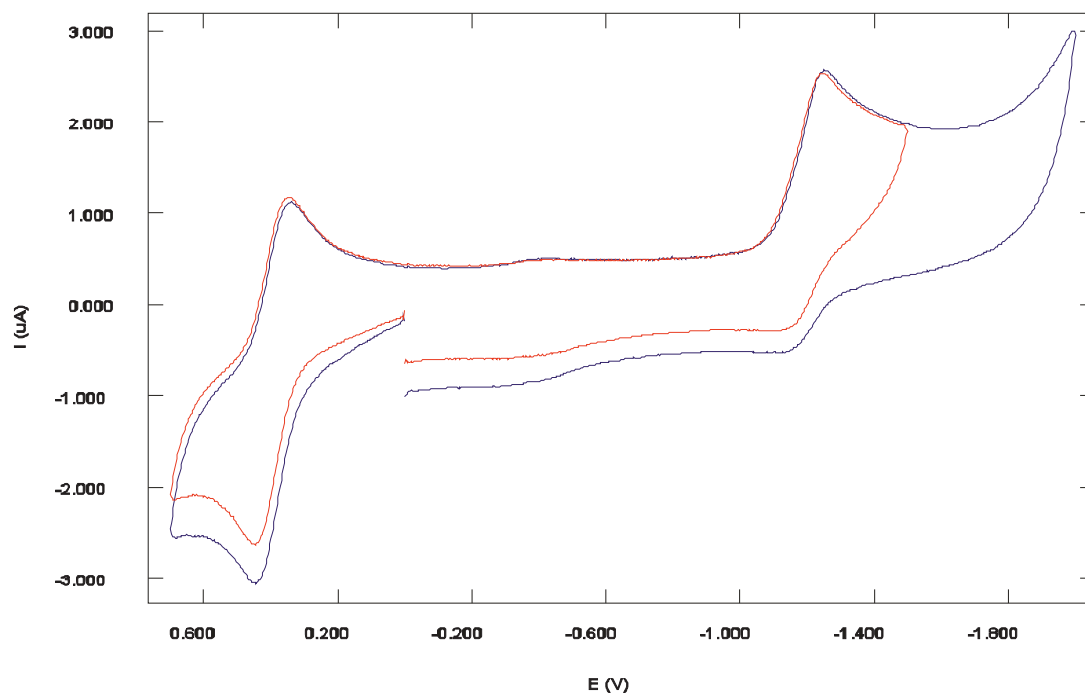


Figure 2.5.4.1. Cyclic voltammogram of $[\text{Cu}(\text{dippf})(\text{DML})](\text{PF}_6)$ (**2**) in propylenecarbonate / LiClO_4 at a glassy carbon electrode, scan rate 200 mV/s.

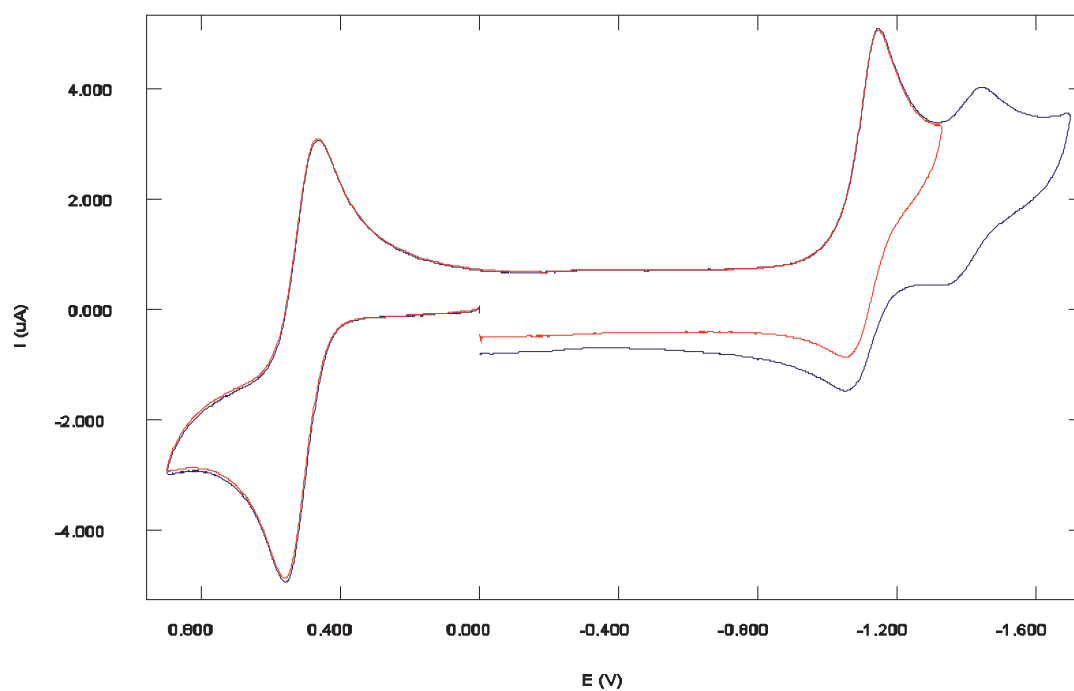


Figure 2.5.4.2. Cyclic voltammogram of $[\text{Cu}(\text{dippf})(\text{DML})](\text{PF}_6)$ (**2**) in propylenecarbonate / KPF_6 on glassy carbon electrode, scan rate 200 mV/s.

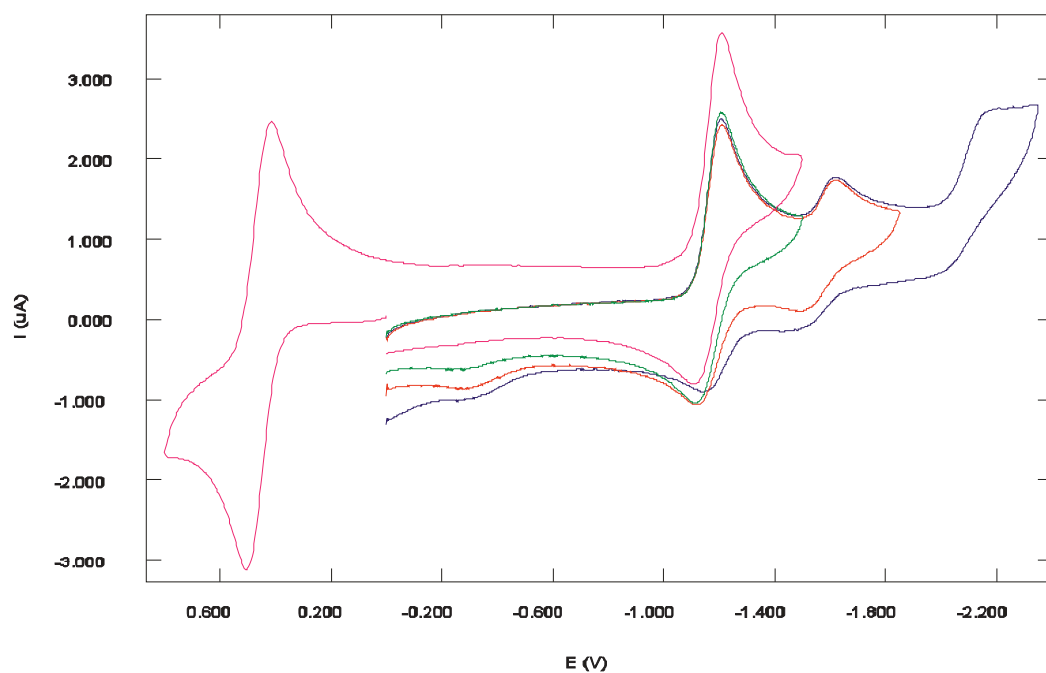


Figure 2.5.4.3. Cyclic voltammogram of $[\text{Cu}(\text{dippf})(\text{DML})](\text{PF}_6)$ (**2**) in propylenecarbonate / Bu_4NClO_4 on glassy carbon electrode, scan rate 200 mV/s.

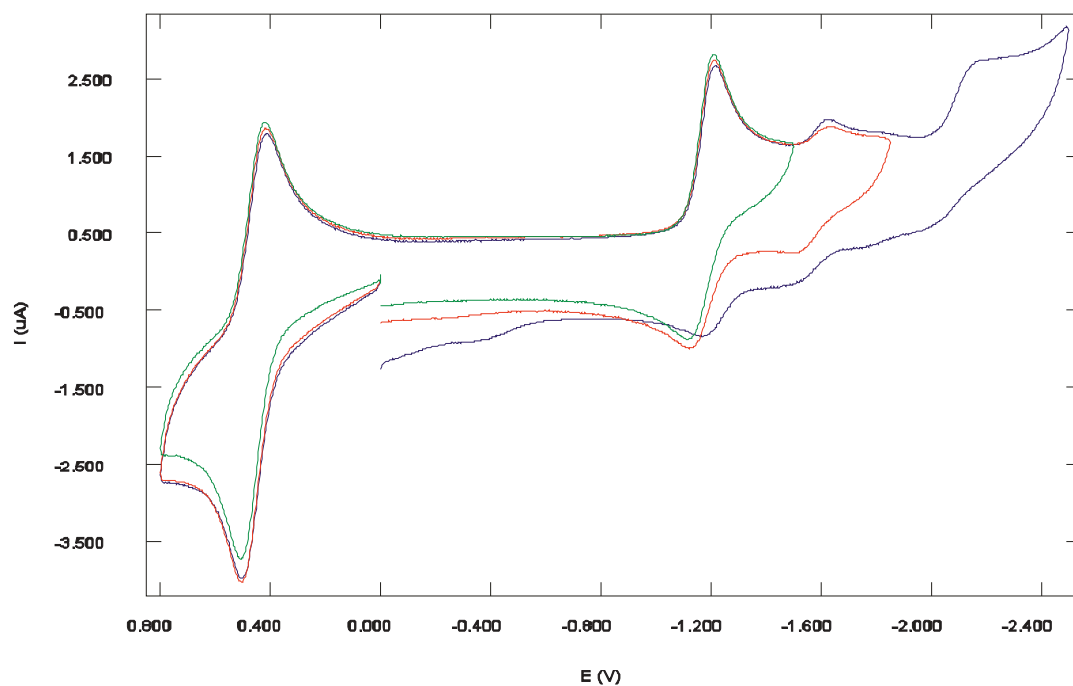


Figure 2.5.4.4. Cyclic voltammogram of $[\text{Cu}(\text{dippf})(\text{DML})](\text{PF}_6)$ (**2**) in propylenecarbonate / Bu_4NPF_6 on glassy carbon electrode, scan rate 200 mV/s.

2.5.5. Bulk electrolysis / coulometry of [Cu(dippf)(DML)](PF₆) (2)

From the above results, it is assumed to have a combination of more than one effects leading to the second reduction wave. The complexes were found not to be very stable in solution during the electrochemical experiments, and after longer delay time, the second reduction wave became larger. It is possible that even in the fresh solution a decomposition product is formed at the electrode by an electro-catalytic reaction. The primary one-electron reduction product was moderately stable and the decomposition rate was slower. This was seen from both bulk electrolysis (Figure 2.5.5.1) and spectroelectrochemistry (Section 2.6).

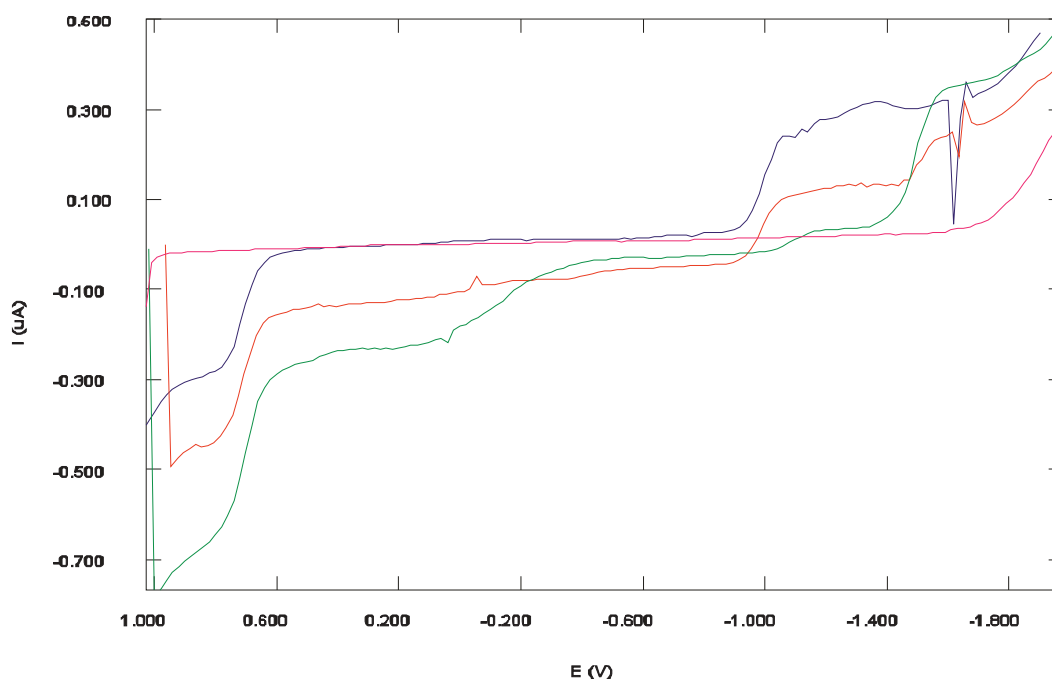


Figure 2.5.5.1. Polarography of 0.99 mM [Cu(dippf)(DML)](PF₆) (2) in CH₂Cl₂ / Bu₄NPF₆ and after reduction by 0.5 F/mol, and 0.9 F/mol (Not corrected for partial CH₂Cl₂ evaporation.).

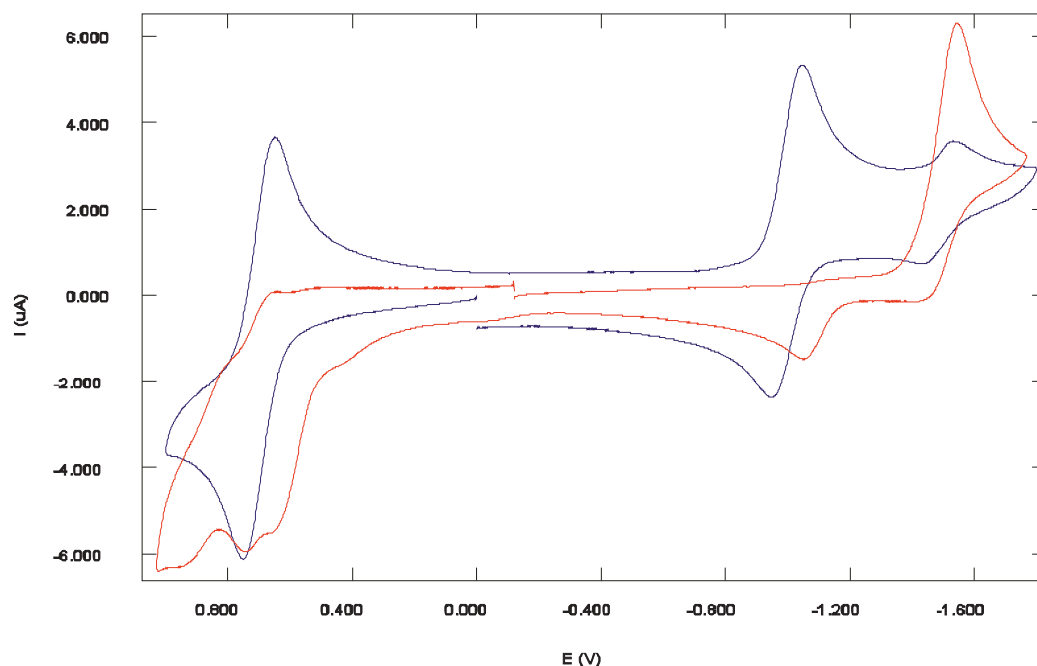


Figure 2.5.5.2. Cyclic voltammogram of 0.99 mM $[\text{Cu}(\text{dippf})(\text{DML})](\text{PF}_6)$ (**2**) in CH_2Cl_2 / Bu_4NPF_6 on glassy carbon electrode, scan rate 200 mV/s (top) and cyclic voltammogram after reduction by 1.1 F/mol (bottom). (Corrected for CH_2Cl_2 evaporation.).

2.5.6. Phase-sensitive alternating current (A.C.) cyclic voltammetry of $[\text{Cu}(\text{dippf})(\text{DML})](\text{PF}_6)$ (**2**)

A 1:1 ratio of in-phase and quadrature (capacitive) component of the electrode admittance showed Nernstian behaviour (sufficiently large rate constant of charge transfer, low rate of a coupled reaction, if any). The decrease of both components in the reversal scan can be due to the coupled reaction (resulting in decreased d.c. concentrations of electroactive species during the scan to negative region), however, such a strong decrease (in comparison to only little smaller anodic counter-peak in normal cyclic voltammetry) may indicate some inhibition, deactivation of the electrode surface by a (decomposition) product. Second, small peak: similarly as in normal cyclic voltammetry, no indication of adsorption (which would result in a strong change of electrode (double-layer) capacity).

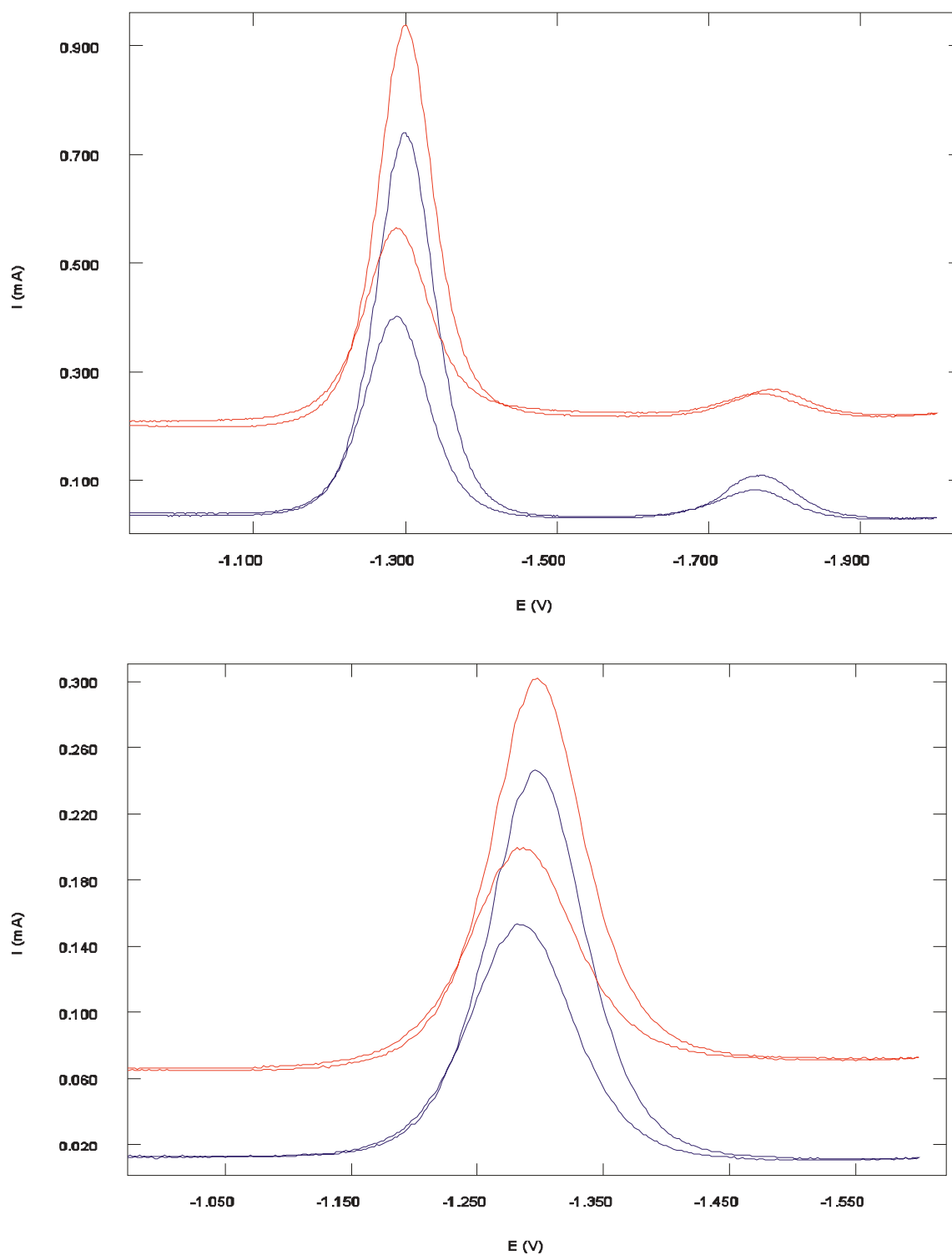


Figure 2.5.6.1. Phase-sensitive alternating current (a.c.) cyclic voltammetry of $[\text{Cu}(\text{dippf})(\text{DML})](\text{PF}_6)$ (**2**) in $\text{CH}_2\text{Cl}_2 / \text{Bu}_4\text{NPF}_6$ on glassy carbon electrode, scan rate 100 mV/s, frequency 80 Hz.

A partial decomposition of the one-electron reduced product can occur on the cyclic voltammetry time scale, causing the second reduction peak to exhibit a decrease of the anodic peak. Decrease of the anodic peak current can also be caused by inhibition due to an adsorption of the decomposition product. At high scan rate the decomposition of the one-

electron reduced product is suppressed and the ratio of i_{pc}/i_{pa} is almost 1. The small second peak still remains perhaps because of partial adsorption. Cyclic voltammetry scan rate dependence was not indicative because of opposite effects: increase of adsorption peak with scan rate vs. decrease of second reduction peak due to avoiding of the follow-up reaction on a shorter time scale. Similarly, low temperature measurements stop the reduction but increase adsorption. However, good indication of adsorption comes from polarography, an unstable mercury drop and formation of a polarographic maximum at the limiting current due to a change of the mercury drop surface.

2.6. Infrared spectroelectrochemistry

IR carbonyl stretching frequency in non-reduced native, reversibly oxidized and in reversibly reduced state were measured performing IR spectroelectrochemical experiments in CH_2Cl_2 / Bu_4NPF_6 in OTTLE cell at room temperature. These studies provide information on the location of electron transfer site and the effect on carbonyl stretching frequency during reversible electrochemical processes. Infrared spectroelectrochemistry of Cu-lumazine complexes have been studied here for the first time. IR spectroelectrochemistry of the two-electron reduced forms was not studied. In the native, unreduced states of the lumazine and alloxazine complexes, two carbonyl bands ($\nu(\text{C}^4\text{-O})$ and $\nu(\text{C}^2\text{-O})$) appear. The band corresponding to $\nu(\text{C}^4\text{-O})$ is seen in the region $1715\text{-}1730\text{ cm}^{-1}$ and the other, comparatively stronger band corresponding to $\nu(\text{C}^2\text{-O})$ is observed in the region of $1645\text{-}1660\text{ cm}^{-1}$. The obtained data are summarized in Table 2.6.1. On oxidation, the carbonyl stretching frequency, $\nu(\text{C}^2\text{-O})$, shifts to higher energy only by 1 to 5 cm^{-1} whereas $\nu(\text{C}^4\text{-O})$ shifts to lower energy by 4 to 7 cm^{-1} in all cases (Table 2.6.1). The minute change is expected because the oxidation is occurring on Fe centres of the dopf unit which has very little influence on the electronic environment of the heterocycles.

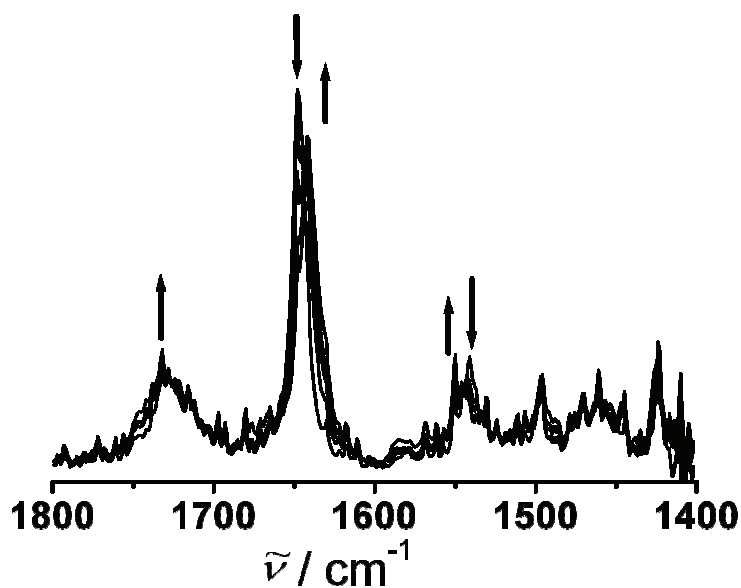


Figure 2.6.1. IR spectroelectrochemical change of carbonyl bands for the oxidation of $[\text{Cu}(\text{dppf})(\text{DML})]^+$ to $[\text{Cu}(\text{dppf})(\text{DML})]^{2+}$ in $\text{CH}_2\text{Cl}_2 / \text{Bu}_4\text{NPF}_6$.

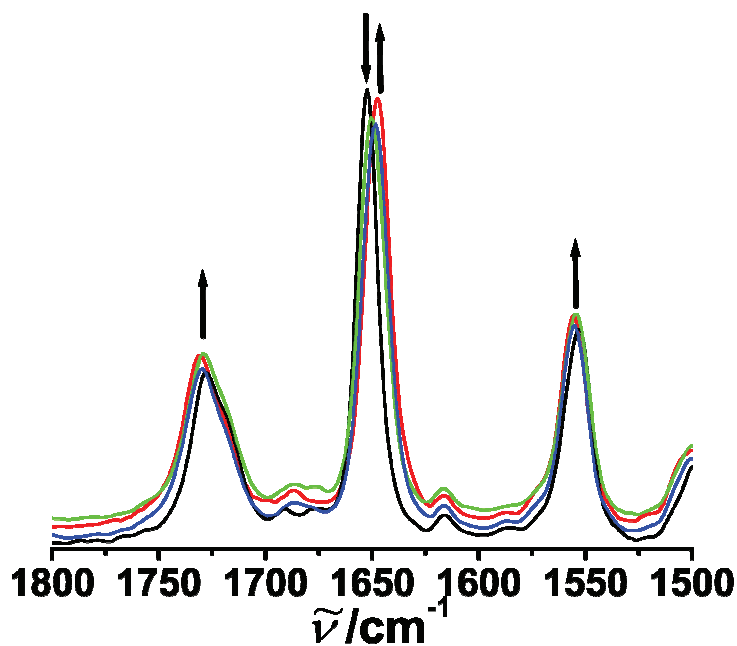


Figure 2.6.2. IR spectroelectrochemical change of the carbonyl bands for oxidation of $[\text{Cu}(\text{dppf})(\text{DMA})]^+$ to $[\text{Cu}(\text{dppf})(\text{DMA})]^{2+}$ in $\text{CH}_2\text{Cl}_2 / \text{Bu}_4\text{NPF}_6$.

On one-electron reversible reduction, the radical anion form of the heterocycle is produced leading to large low-energy shifts of both $\nu(\text{C}^4\text{-O})$ and $\nu(\text{C}^2\text{-O})$ in all five complexes (Table 2.6.1). The intensity for $\nu(\text{C}^4\text{-O})$ was increasing whereas for $\nu(\text{C}^2\text{-O})$ was decreasing on

reduction. The $\nu(\text{C}^4\text{-O})$ band is shifted by 68 cm^{-1} and the $\nu(\text{C}^2\text{-O})$ band is shifted by 78 cm^{-1} to the lower energy region in reduced species of the complexes.

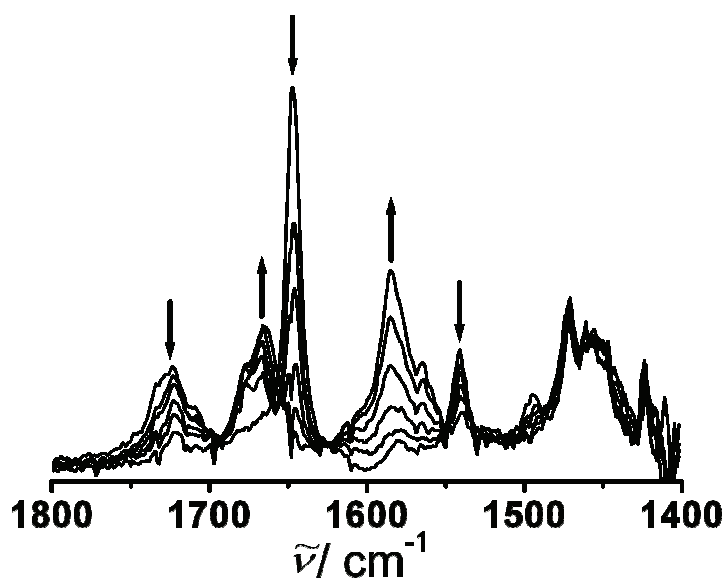


Figure 2.6.3. IR spectroelectrochemical change of the carbonyl bands for the reduction of $[\text{Cu}(\text{dppf})(\text{DML})]^+$ to $[\text{Cu}(\text{dppf})(\text{DML}^-)]$ in $\text{CH}_2\text{Cl}_2 / \text{Bu}_4\text{NPF}_6$.

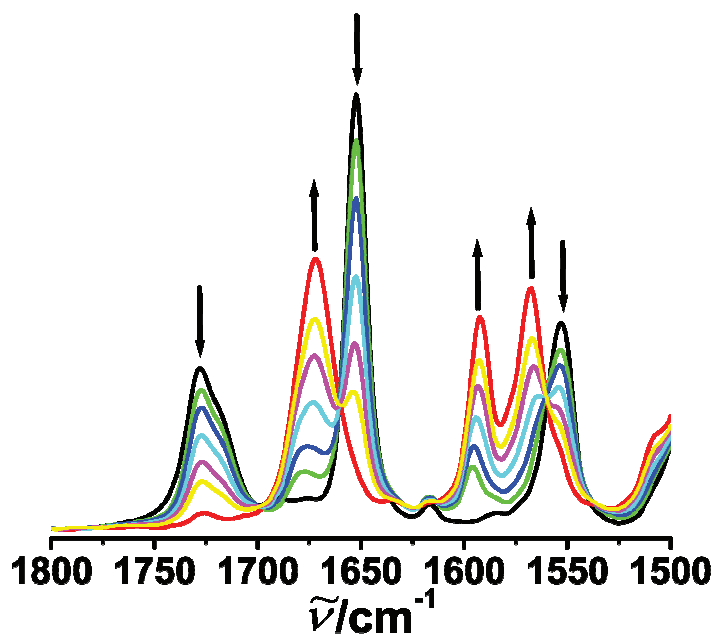


Figure 2.6.4. IR spectroelectrochemical change of the carbonyl bands for the reduction of $[\text{Cu}(\text{dppf})(\text{DMA})]^+$ to $[\text{Cu}(\text{dppf})(\text{DMA}^-)]$ in $\text{CH}_2\text{Cl}_2 / \text{Bu}_4\text{NPF}_6$.

The IR spectroelectrochemical data of the reported^[84] complex $[\text{Cu}(\text{PPh}_3)_2(\text{DMA})]^+$ was compared with the newly synthesized complexes **3**, **4** and **5** in Table 2.6.1. It was observed that carbonyl shifts of **3** and **4** were similar both in the native and in the one-electron reduced state as observed in the reported complex. Complex **5** showed a larger shift for $\nu(\text{C}^4\text{-O})$ because of the presence of two extra methyl groups on TMA, increasing the unpaired electron density on C^4 position.

Table 2.6.1. Data from IR spectroelectrochemistry^a

Complex ion	$\nu(\text{C}^2\text{-O})$	$\nu(\text{C}^4\text{-O})$	$\Delta\nu(\text{C}^2\text{-O})$	$\Delta\nu(\text{C}^4\text{-O})$	Reference / solvent
1 ²⁺	1732 (s)	1641 (vs)	+4	-7	This work
1 ⁺	1728 (s)	1648 (vs)	n.a.	n.a.	
1	1666 (s)	1585 (s)	-62	-63	
2 ²⁺	1727 (s)	1645 (vs)	+1	-4	This work
2 ⁺	1726 (s)	1649 (vs)	n.a.	n.a.	
2	1658 (s)	1588(vs)	-68	-61	
$[\text{Cu}(\text{PPh}_3)_2(\text{DMA})]^+$	1727(s)	1653(vs)	n.a.	n.a.	84
$[\text{Cu}(\text{PPh}_3)_2(\text{DMA}^\cdot)]$	1679(s)	1590(w)	-48	-63	
3 ²⁺	1732(s)	1647(vs)	+4	-5	This work
3 ⁺	1728(s)	1652(vs)	n.a.	n.a.	
3	1672(vs)	1593(s)	-56	-59	
4 ²⁺	1731(s)	1652(vs)	+3	-5	This work
4 ⁺	1728(s)	1657(vs)	n.a.	n.a.	
4	1672(vs)	1593(vs)	-58	-64	
5 ²⁺	1724(s)	1642(vs)	+5	-5	This work
5 ⁺	1719(s)	1647(vs)	n.a.	n.a.	
5	1668(s)	1569(s)	-51	-78	

^a From spectroelectrochemistry in an OTTLE cell in CH_2Cl_2 / 0.1 M Bu_4NPF_6 at 298 K.

2.7. UV-Vis spectroelectrochemistry

In free DML, absorption bands are found between 320 and 345 nm for intra-ligand transitions^[70]. In the metal complexes **1** and **2**, new bands were found at 465 nm ($\epsilon = 3170 \text{ M}^{-1} \text{ cm}^{-1}$) and 470 nm ($\epsilon = 2460 \text{ M}^{-1} \text{ cm}^{-1}$), respectively, for the MLCT transition from $d^{10}\pi(\text{Cu})$ to π^* (DML). In addition, the π to π^* transition of DML was found in the complexes at 347 nm. On reversible one-electron oxidation, characteristic bands were arising at 845 nm (in complex **1**) and 828 nm (in complex **2**) for the ferrocenium (Figure 2.7.1). A blue shift of the MLCT transition was observed on oxidation (427 nm for $\mathbf{1}^{2+}$ and 431 nm for $\mathbf{2}^{2+}$).

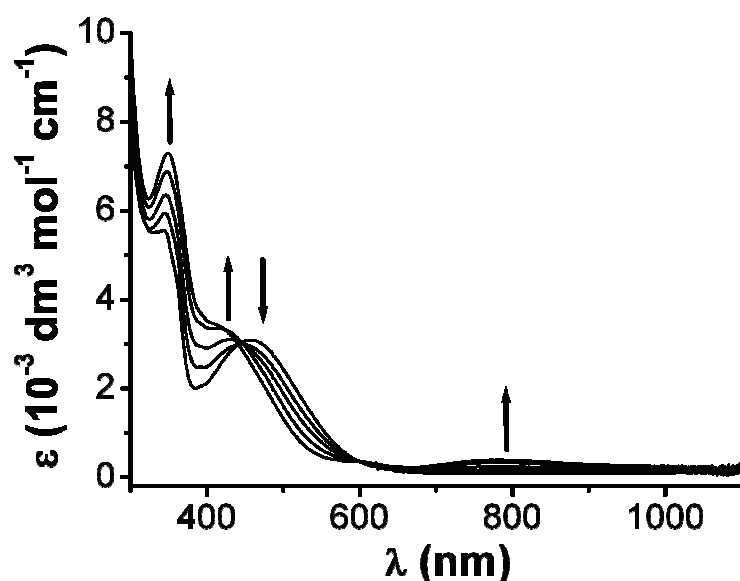


Figure 2.7.1. UV-Vis spectroelectrochemical change during the oxidation of $[\text{Cu}(\text{dppf})(\text{DML})]^+$ to $[\text{Cu}(\text{dppf})(\text{DML})]^{2+}$ in $\text{CH}_2\text{Cl}_2 / \text{Bu}_4\text{NPF}_6$.

On reduction, the MLCT band diminished completely for the occupation of the added unpaired electron in the lumazine ring, inhibiting the charge transfer process. In the one-electron reduced species only a shoulder was found for the intraligand transition in the near ultra-violet region (Figure 2.7.2).

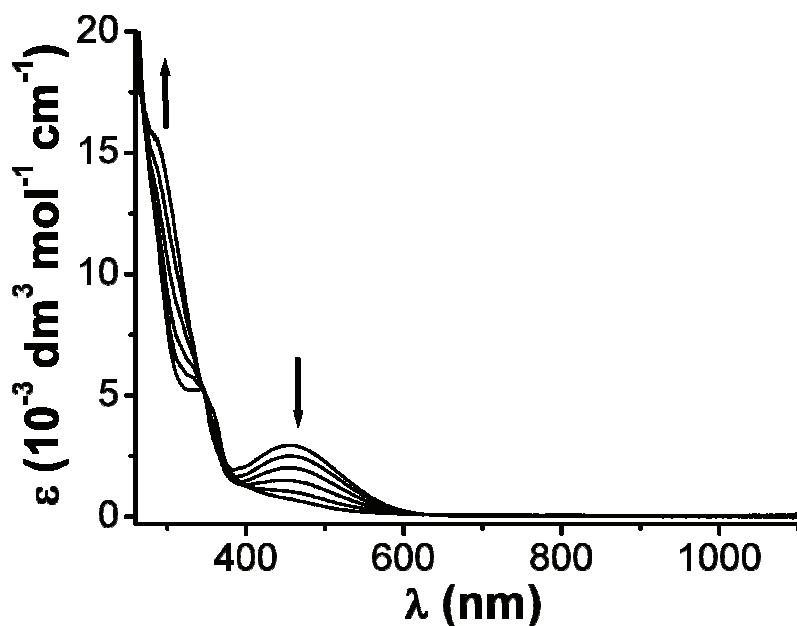


Figure 2.7.2. UV-Vis spectroelectrochemical change during the reduction of $[\text{Cu}(\text{dppf})(\text{DML})]^+$ to $[\text{Cu}(\text{dppf})(\text{DML}^-)]$ in $\text{CH}_2\text{Cl}_2 / \text{Bu}_4\text{NPF}_6$.

In the free DMA ligand, the intraligand transitions are observed between 319 and 393 nm^[84]. When the UV-Vis spectrum was measured for $[\text{Cu}(\text{dppf})(\text{DMA})]^+$ in an electrochemical cell, a band at 527 nm ($\epsilon = 5270 \text{ M}^{-1}\text{cm}^{-1}$), corresponding to an MLCT, was observed. In the reported complex $[\text{Cu}(\text{PPh}_3)_2(\text{DMA})]^+$, the band was found at a lower wavelength at 470 nm. The change of the co-ligand has shifted the MLCT transition by 57 nm. On oxidation (Figure 2.7.3), the band corresponding to ferrocenium was observed at 778 nm and blue shifted MLCT band at 462 nm. More bands were found at 419 and 355 nm which were assigned as intraligand bands. In the reversibly one-electron reduced species, a shoulder at 505 nm was found, possibly for the shifted MLCT transition. Bands at 478 and 379 nm were also found for the intraligand transitions. UV-Vis spectroelectrochemical data of the complexes are summarized and compared with available literature data in Table 2.7.1.

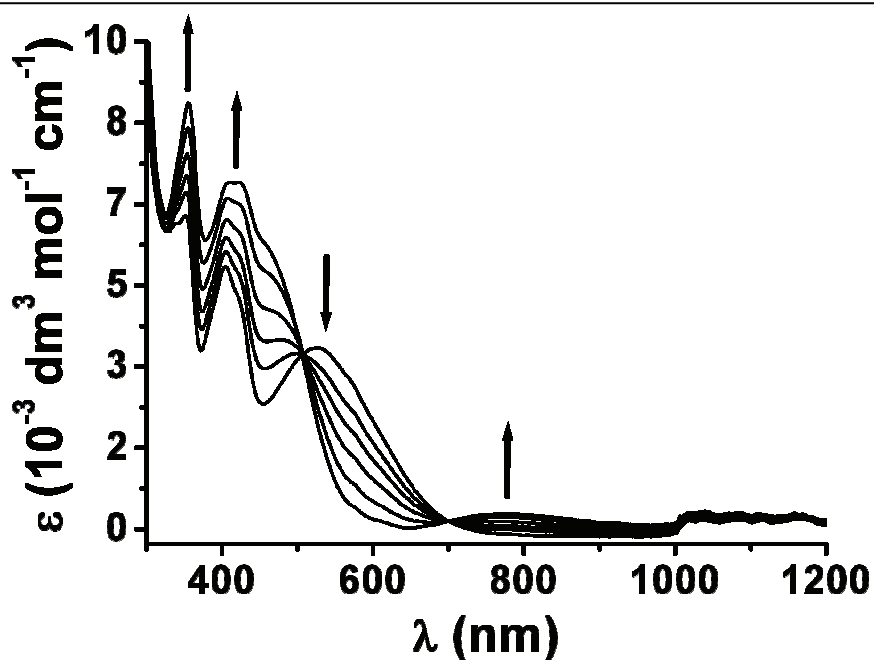


Figure 2.7.3. UV-Vis spectroelectrochemical change during the oxidation of $[\text{Cu}(\text{dppf})(\text{DMA})]^+$ to $[\text{Cu}(\text{dppf})(\text{DMA})]^{2+}$ in $\text{CH}_2\text{Cl}_2 / \text{Bu}_4\text{NPF}_6$.

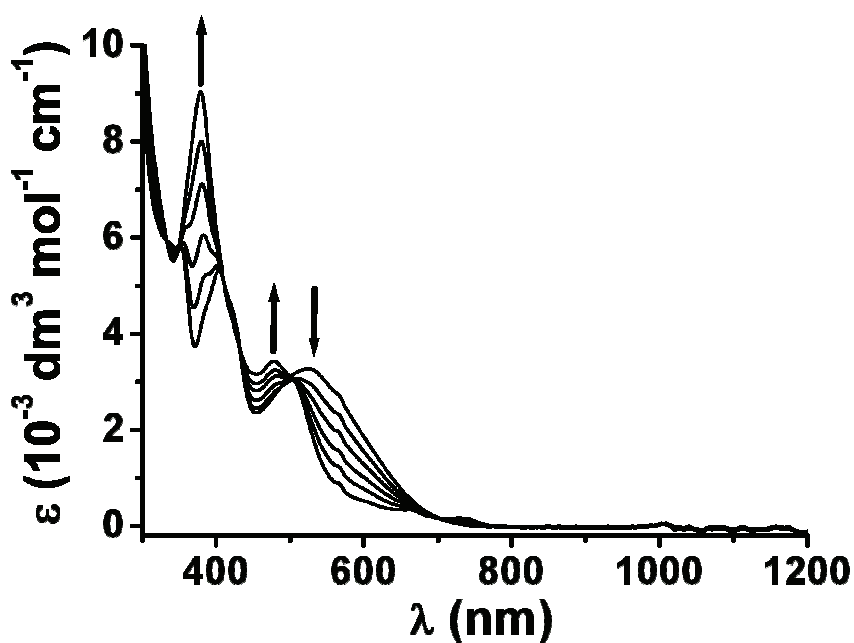


Figure 2.7.4. UV-Vis spectroelectrochemical change during the reduction of $[\text{Cu}(\text{dppf})(\text{DMA})]^+$ to $[\text{Cu}(\text{dppf})(\text{DMA})]^-$ in $\text{CH}_2\text{Cl}_2 / \text{Bu}_4\text{NPF}_6$.

Table 2.7.1. Data from UV-Vis spectroelectrochemistry^a

Complex ion	λ_{\max} / nm (ϵ / 10^{-3} M ⁻¹ cm ⁻¹)	Reference/ solvent
DML	344(sh), 330(4.02), 320(sh)	[70], CH ₂ Cl ₂
DMA	393(sh), 378(4.03), 364(sh), 319(3.96)	[70], THF
1 ²⁺	845 (sh), 427 (sh), 349 (7.37)	This work CH ₂ Cl ₂
1 ⁺	465 (3.17), 347 (5.66),	
1	287 (sh)	
2 ²⁺	828 (sh), 431 (sh), 346 (4.37), 284 (7.34)	This work CH ₂ Cl ₂
2 ⁺	470 (2.46), 347 (3.11)	
2	291 (sh)	
[Cu(PPh ₃) ₂ (DMA)] ⁺	470(3.62), 420(sh), 404(3.92), 352(4.00)	[84], CH ₂ Cl ₂
[Cu(PPh ₃) ₂ (DMA ⁻)]	665(2.56), 470(3.44), 380(4.17), 323(4.03)	
3 ²⁺	778(sh), 462(sh), 419(7.15), 355(8.71)	This work CH ₂ Cl ₂
3 ⁺	527(3.74), 404(5.36), 352(6.44)	
3	505(sh), 478(3.43), 379(9.05)	
4 ²⁺	803(sh), 480(sh), 412(4.45), 351(5.27)	This work CH ₂ Cl ₂
4 ⁺	525(3.41), 402(5.26), 347(5.28), 331(5.37)	
4	497(sh), 478(3.29), 378(6.85)	
5 ²⁺	782(sh), 466(sh), 434(sh), 408(sh), 369(11.21)	This work CH ₂ Cl ₂
5 ⁺	511(3.76), 433(sh), 408(5.36), 367(8.43)	
5	509(sh), 482(3.28), 386(9.78)	

^a From spectroelectrochemistry in an OTTLE cell in CH₂Cl₂ / 0.1 M Bu₄NPF₆ at 298 K.

2.8. EPR spectroscopy

All the complexes are diamagnetic in the native state. As the lumazine and alloxazine complexes undergo reversible one-electron reduction, the EPR active radical species could be generated by electrolysis. EPR spectra were measured to locate the unpaired electron in one-electron reduced species of all five complexes. The reduced paramagnetic species were generated in situ by electrolysis in dichloromethane using Bu_4NPF_6 as an electrolyte. All measured spectra for electrogenerated $[\text{Cu}(\text{dppf})(\text{DML})]^-$ (top left), $[\text{Cu}(\text{dippf})(\text{DML})]^-$ (top right), $[\text{Cu}(\text{dppf})(\text{DMA})]^-$ (middle left), $[\text{Cu}(\text{dippf})(\text{DMA})]^-$ (middle right) and $[\text{Cu}(\text{dppf})(\text{TMA})]^-$ (bottom left) in solution are given in Figure 2.8.1. The g values determined for the reduced species were very close to that of free organic radical, indicating a ligand centred spin. It is clear that the first reduction of the complexes is accompanied by the addition of an electron to the π^* molecular orbital of the pteridine heterocycle. The spectra showed hyperfine structure with coupling contribution from EPR active nuclei present in the complexes. The g values of the measured and reported complexes are presented in Table 2.8.1.

Table 2.8.1. EPR data of reduced species^a

Compounds	g	Solvent	Reference
DMA^-	2.0035	THF	84
$[\text{Cu}(\text{PPh}_3)_2(\text{DMA})]^-$	2.0038	THF	84
$[\text{Cu}(\text{dppf})(\text{DML})]^-$ 1 ⁻	2.0049	CH_2Cl_2	This work
$[\text{Cu}(\text{dippf})(\text{DML})]^-$ 2 ⁻	2.0042	CH_2Cl_2	This work
$[\text{Cu}(\text{dppf})(\text{DMA})]^-$ 3 ⁻	2.0044	CH_2Cl_2	This work
$[\text{Cu}(\text{dippf})(\text{DMA})]^-$ 4 ⁻	2.0056	CH_2Cl_2	This work
$[\text{Cu}(\text{dppf})(\text{TMA})]^-$ 5 ⁻	2.0043	CH_2Cl_2	This work

^aFrom in situ electrolysis in 0.1 M Bu_4NPF_6 solutions. Electrolysis and EPR measurements at 298 K.

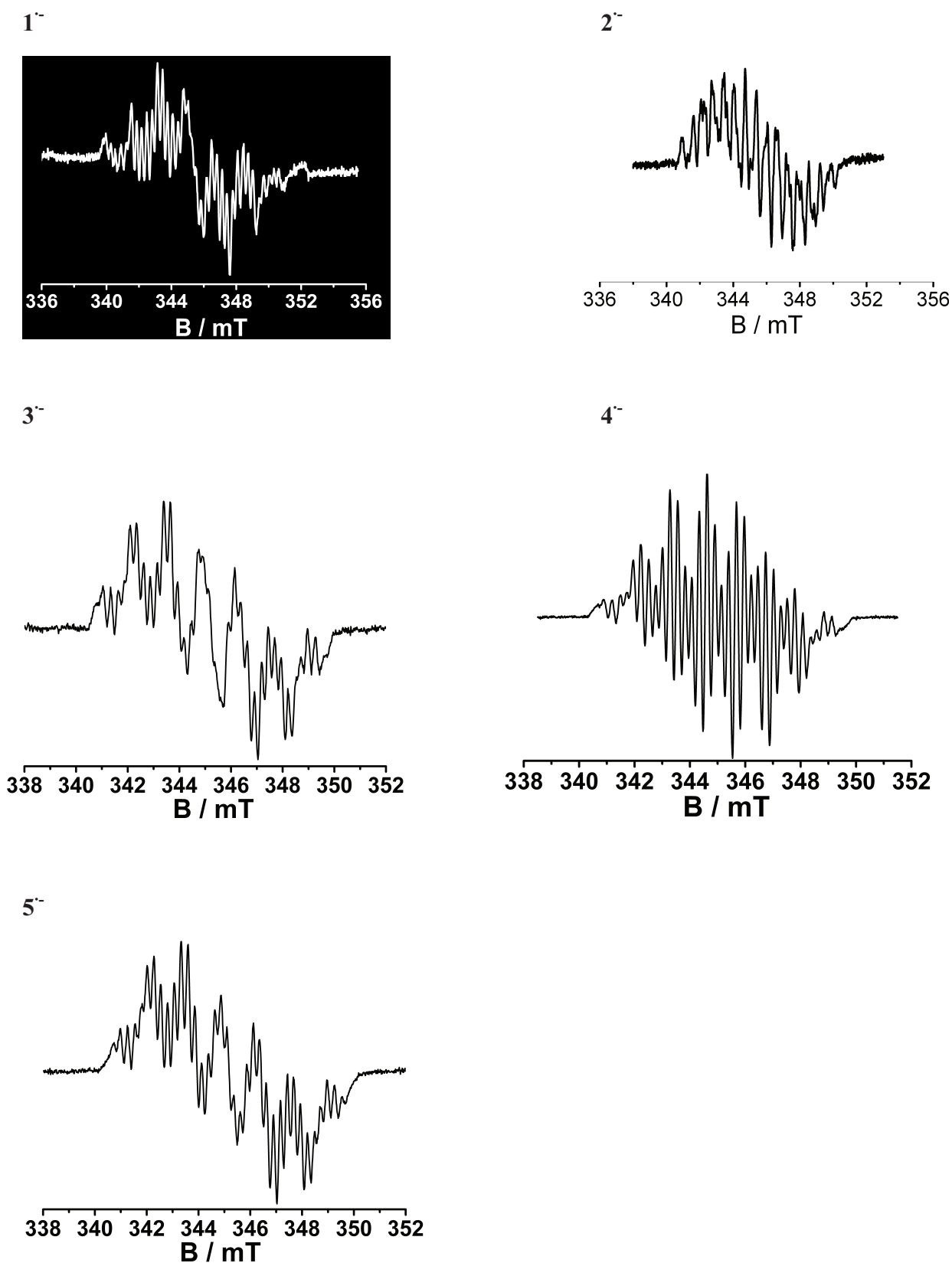


Figure 2.8.1. X-band EPR spectra of electro-generated $[\text{Cu}(\text{dppf})(\text{DML})]^-$ (top left), $[\text{Cu}(\text{dippf})(\text{DML})]^-$ (top right), $[\text{Cu}(\text{dppf})(\text{DMA})]^-$ (middle left), $[\text{Cu}(\text{dippf})(\text{DMA})]^-$ (middle right) and $[\text{Cu}(\text{dppf})(\text{TMA})]^-$ (bottom left) at 298 K in $\text{CH}_2\text{Cl}_2/0.1 \text{ M Bu}_4\text{NPF}_6$ solution.

2.9. Conclusion

A detail structural and spectroscopic analyses of copper-pteridine interactions have been demonstrated in this chapter. The stable organometallic fragment, $[\text{Cu}(\text{dopf})]^+$, was probed for studying copper(I)-pteridine interaction. The unique O^4, N^5 unsymmetrical planar chelation to d^{10} $[\text{Cu}(\text{dopf})]^+$ metal fragments was established by single crystal X-ray structure determination. In addition to the expected O^4, N^5 chelation, the various possible coordination modes of pterin ring have been discussed for the first time in the crystal structure of an oligomeric $\text{Cu}^{\text{I}}\text{Fe}^{\text{II}}$ -pterin complex. The reversible electrochemistry and spectroelectrochemistry of lumazine complexes was investigated to understand the redox property of these complexes. The carbonyl bands in *in situ* generated oxidized and reduced species were studied with the aid of IR-spectroelectrochemistry. EPR spectra were measured to ensure the ligand centered spin in one-electron reduced species of the pteridine complexes.

Chapter 3

Variable metal binding of the unsymmetrical α -iminoketo chelate function in biomolecules: Structures of complexes between heterodinuclear (Cu, Fe) organometallics and purine bases.

3.1. Introduction

The systematic study of metal-nucleobase interactions is a very important field in bioinorganic chemistry. Metal ions are present in the cellular environment to neutralize the existing negative charge of nucleic acids by binding either to the anionic phosphodiester linkage or to the heterocyclic nucleobases^[86,87]. Thus, the understanding of metal-nucleobase interactions has become a very important area in bioinorganic chemistry. The transition metal-nucleobase interaction has become important after the discovery of cisplatin *cis*-[Pt(NH₃)₂Cl₂], showing the effect of inhibition of cancer cell division by cross linking polynucleotide chains^[25]. The inhibition process may also take place in presence of metal ions without cross linking. The first X-ray crystal structure of a metal-nucleobase complex was found in a dinuclear Cu^{II} complex containing four bridging negatively charged adenine ligands (through N³ and N⁹) and two water molecules at the axial position^[88]. Guanine, one of the five classical nucleobases, has received recent interest due to its formation of tetramers (G4) which are involved in telomerase activity (2009 Nobel Prize in Medicine). The imine-N⁷ atom both in the nucleic acid and the isolated nucleobase is known as the preferential binding site for metal complex fragments, most famously for the platinum(II) metabolites formed from cytostatic platinum drugs^[26]. Apart from Pt, other transition metal complexes of Ru, Re, Mo, Rh etc. show similar binding to the N⁷ hetero atom, exhibiting antitumour activity in protic media^[89-93]. The exclusive N⁷ binding, in the absence of excess metal ions, is favoured by a number of factors. The easy accessibility in the DNA major groove, its non-involvement in base pairing, the higher basicity of N⁷ and favourable electrostatic interactions direct metal fragments to bind with the N⁷ atom^[94-96].

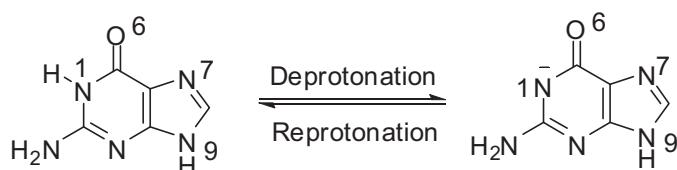


Figure 3.1.1. Deprotonation of guanine to a monoanionic species.

At physiological pH the N⁷ metalated guanine residue is neutral and in the deprotonated form, the negative charge on N atom is also delocalized to the O⁶ donor site. The increased electron density on N¹ and O⁶ helps to understand various binding pattern other than the N⁷ mode. In this work with a lipophilic guanine derivative (P-9MG) (Figure 3.1.2), the binding through N⁷ was found in a single crystal X-ray structure of a heterodinuclear Cu^IFe^{II} complex. Xanthine (3,7-dihydro-purine-2,6-dione) is also a modified purine base found in most human body tissues and fluids and in other organisms as one of the constituents in RNA. It is also found as an intermediate in the purine degradation pathway to uric acid, catalyzed by a Mo and Fe containing enzyme, xanthine oxidase^[97]. Several studies on the metal complexes of xanthine have appeared in the literature for the understanding of metal-xanthine binding^[98-107].

I have considered guanine and xanthine as bio-inspired ligand systems and synthesized complexes with [Cu(dopf)]⁺ (Figure 3.1.2), dopf = 1,1'-bis(diorganophosphino)ferrocene, an organometallic fragment, to study the structural features. Copper(I) is important to study with biomolecules as it has π donor properties and does not allow the biomolecule to get oxidized. Cu^I gets stabilized even with exclusive sigma donor ligand systems because of the d- π mixing allowing some extent of π back-bonding to the sigma donor ligand^[108]. These studies thus help to investigate the metal-purine interaction maintaining the basic structure and electronic properties of the native purine bases. The dopf unit was used to stabilize the Cu^I state and to make the system more hydrophobic considering the effect on penetration through cell membranes. The intermolecular H-bonding effect was eliminated by performing the reactions and crystallization techniques in organic medium

1,3,9-Trimethylxanthine (Figure 3.1.2) is known for its commercial availability and low toxicity. Variable behaviour of metal binding was observed from the crystal structure analysis. Electronic and steric factors of the coligands have been modulated in order to study the structural variation of these complexes. To study the metal-xanthine interaction we have considered commercially available and organic solvent soluble trimethylxanthine (TMX) as a potential ligand for metalation reaction. Three different metal fragments [Cu(dppf)]⁺, [Cu(dippf)]⁺ and [Cu(dchpf)]⁺ were utilized for the metalation purpose. The imine and keto groups are the only possible coordination sites in TMX. The α -iminoketo function of the purine base has also the possibility to act as a chelating ligand^[110]. The purine bases, their lipophilic derivatives and the metal precursor complexes have been shown below.

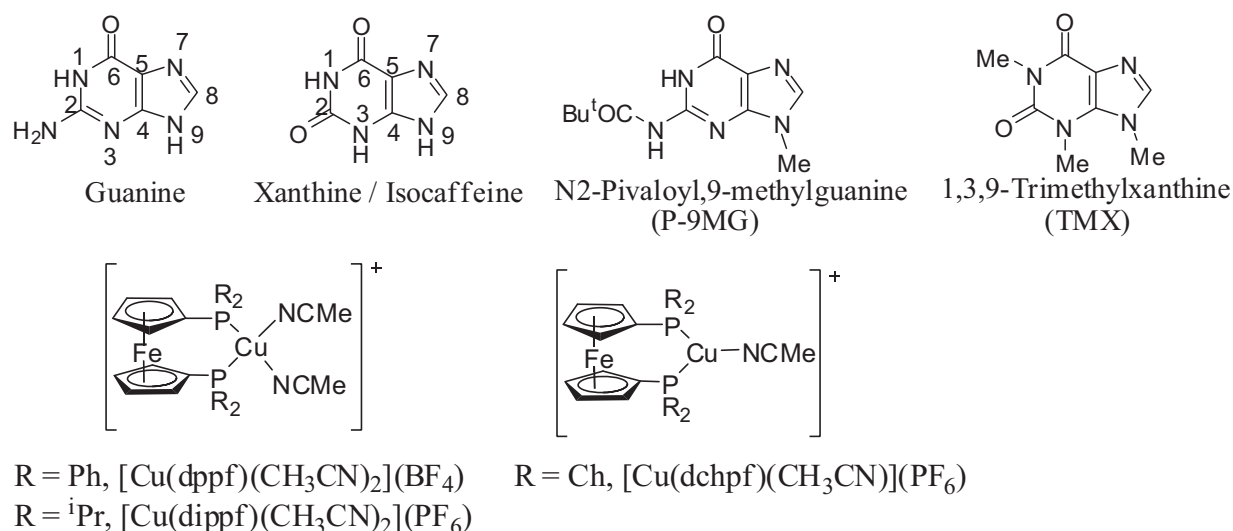


Figure 3.1.2. Guanine, xanthine and their derivatives (top). Metal precursors (bottom), dppf = 1,1'-bis(diphenylphosphino)ferrocene, dippf = 1,1'-bis(di-isopropylphosphino)ferrocene, dchpf = 1,1'-bis(dicyclohexylphosphino)ferrocene.

3.2. Synthesis and characterization

3.2.1. Synthesis and characterization of the Cu^IFe^{II}-guanine complexes

Guanine, 2-amino-1*H*-purin-6(9*H*)-one, having 4 heterocyclic purine N atoms, one amino group at the C² position and one keto function at C⁶, is highly polar and only soluble in protic solvents. In this work, I have chosen commercially available 9-methylguanine (9MG) (Figure 3.2.1.1) as a starting material to have a biologically more relevant system, as the N⁹ position is also substituted in nucleotides^[26]. Moreover, the blocked N⁹ position increases the possibility of coordination through the N⁷ donor atom. As low-valent copper fragments have a tendency to get oxidized to Cu^{II}, it was necessary to perform the metalation reactions in an organic solvent. That is why few organic synthetic routes were followed to lipophilize 9MG for better solubility in aprotic media. The attempted substitution of the ring NH function by a suitable alkyl group ended with unreacted materials and decomposed products. The N²-H function was then substituted with a pivaloyl substituent. The reaction was carried out following a reported literature procedure for the lipophilization of pterin^[81].

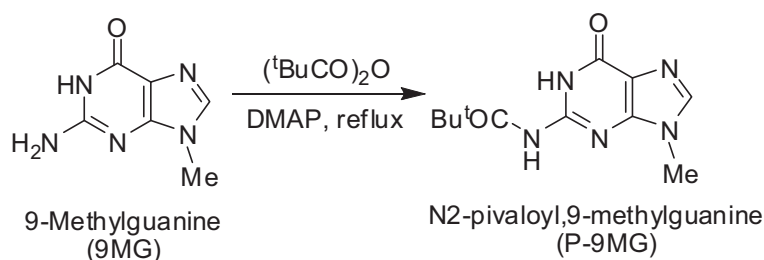


Figure 3.2.1.1. Lipophilization of 9-methylguanine (9MG).

Reaction of 9MG with trimethylacetic anhydride in the presence of a Lewis base (N,N-dimethylaminopyridine, DMAP) followed by chromatographic separation yielded 73% of colourless desired product N2-pivaloyl,9-methylguanine (P-9MG). P9MG was found to be well soluble in organic solvents such as dichloromethane, chloroform etc. Though P-9MG contains the same α -iminoketo function for metal chelation, the hydrogen bond donor property of the 2-amino group was reversed as the N2-pivaloyl group can now act as H-bond acceptor. The H atom on N¹ was still accessible for intra- and intermolecular H-bonding. Characterization of P-9MG was done by ¹H NMR spectrum. Identity of the purine ring was confirmed from NMR signals at 3.67 (s, 3H, CH₃), 7.64 (bs, 1H, -NH, P-9MG), 8.01 (s, 1H, -CH, P-9MG) and 11.94 (bs, 1H, -NH, P-9MG) ppm. Presence of pivaloyl group was confirmed from a signal at 1.33 (m, 9H, ^tBu) ppm. Integration ratios of the ¹H NMR signals clearly suggested the formation of desired product. The FTIR signals measured in solid state at 1740(w), 1662(s) and 1596(s) cm⁻¹ indicated the presence of two non-reduced carbonyl groups, one on the purine ring and another on the pivaloyl substituent. This ligand also exhibited satisfactory elemental analysis.

The yellow Cu^I-precursor complex [Cu(dppf)(CH₃CN)₂](BF₄) was reacted with P-9MG in 1:1 molar ratio in dry and de-oxygenated dichloromethane at room temperature for 12 h. Colour change was not observed even after the completion of reaction. The downfield shifted N-H and ring C-H proton NMR signals indicated metal-guanine binding. Signal intensity ratio of Cp protons to the protons of P-9MG [4.37 (s, 4H, Cp), 4.45 (s, 4H, Cp), 8.11 (s, 1H, -N-H), 8.53 (s, 1H, -C-H), 12.17 (s, 1H, -N-H)] also suggested the formation of 1:1 metal complex. Change in carbonyl vibration on complexation was also observed in their stretching frequency from 1740(w), 1662(s) and 1596(s) to 1701(w), 1673(s), 1662(s), 1606(s) cm⁻¹. Finally, the molecular ion peak in the mass spectrum centered at m/z = 866.15 was observed corresponding to [Cu(dppf)(P-9MG)]⁺.

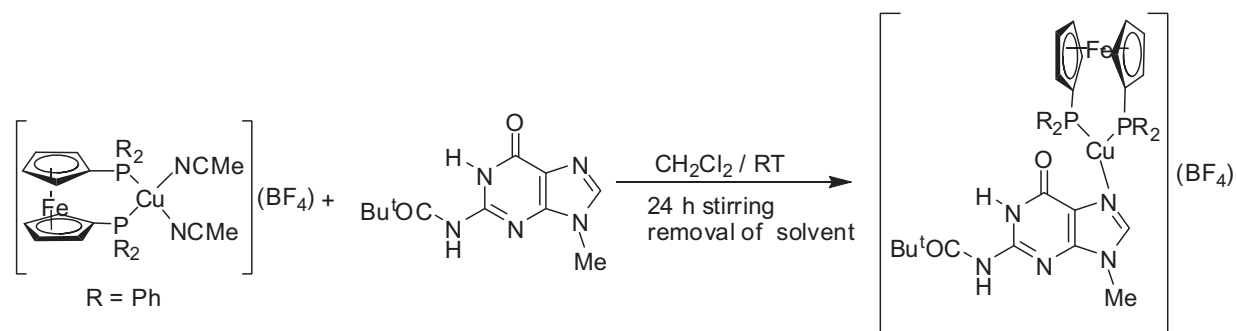


Figure 3.2.1.2. Synthesis of a discrete $\text{Cu}^{\text{I}}\text{Fe}^{\text{II}}$ -guanine complex.

To explore further binding modes of P-9MG, I repeated the same reaction but with two equivalents of the metal precursor and one equivalent of P-9MG. ^1H and ^{31}P NMR signal analyses indicated the formation of a new complex with 2:1 metal-ligand ratio. ^1H NMR signal (CD_2Cl_2) at 1.36 (s, 9H, tBu), 3.85 (s, 3H, Me), 8.16 (s, 1H, CH, P-9MG), 8.66 (s, 1H, NH), 12.21 (s, br, 1H, NH) ppm indicate the presence of P-9MG ligand and signals at 4.29 (s, 8H, Cp), 4.45 (s, 8H, Cp), 7.45 (m, 40H, Ph) prove the presence of two $[\text{Cu}(\text{dppf})]^+$ (possibly binding through N^7 , N^3 and pivaloyl O atoms). A signal at -13.31 ppm in ^{31}P NMR spectrum also indicates the formation of a new complex. The complex shows IR (solid) signals at 1738 (w), 1704 (vw), 1668 (s) and 1605 (s) cm^{-1} , indicating the presence of un-reduced carbonyls. On crystallization of the complex, a new complex aggregate, $[\text{Cu}_3(\text{P-9MG})_2(\text{dppf})_2](\text{BF}_4)_2$, was formed in solution which has been investigated by single crystal X-ray structure analysis (Section 3.3.2).

3.2.2. Synthesis and characterization of the $\text{Cu}^{\text{I}}\text{Fe}^{\text{II}}$ -xanthine complexes

The reaction of TMX with metal precursor complexes (Figure 3.1.2) was performed by following similar procedures as for P-9MG complexes. Three organometallic precursor complexes $[\text{Cu}(\text{dppf})(\text{CH}_3\text{CN})_2](\text{BF}_4)$, $[\text{Cu}(\text{dppf})(\text{CH}_3\text{CN})_2](\text{PF}_6)$ and $[\text{Cu}(\text{dchpf})(\text{CH}_3\text{CN})](\text{PF}_6)$ were reacted separately with TMX in 1:1 ratio in dichloromethane to form the discrete complexes. Repeated recrystallization from hexane / dichloromethane solution at -4°C yielded the pure products. The complexes were characterized by downfield shifted singlet ^1H NMR signals of ring and Me protons in TMX. The ^1H and ^{31}P NMR signals for all complexes have been interpreted and are presented in the Experimental Section. Satisfactory elemental analyses were obtained after including appropriate amounts of solvent molecules. The identity of the complex $[\text{Cu}(\text{dppf})(\text{TMX})](\text{PF}_6)$ was also found from a molecular ion peak in the mass spectrum centered at $m/z = 675.17$ for the cation

$[\text{Cu}(\text{dippf})(\text{TMX})]^+$. The molecular formulae of the three complexes are given in Figure 3.2.2.1.

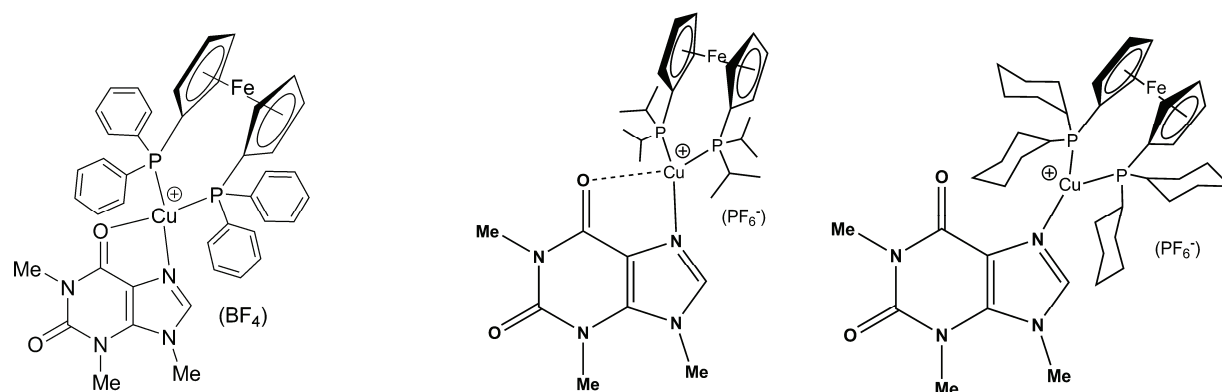


Figure 3.2.2.1. Molecular formulae of $\text{Cu}^{\text{I}}\text{Fe}^{\text{II}}\text{-TMX}$ complexes.

Infrared spectroscopy in the carbonyl stretching region is a very useful tool to distinguish between a free ligand and its metal complexes. Careful analysis of stretching bands helps to recognize metal coordination sites in a complex containing carbonyl functions. Carbonyl stretchings are also indicative for completion of a reaction from the comparison with free ligand. Solid state IR signals were measured both for the TMX ligand and its metal complexes. Obtained results are summarized in Table 3.2.2.1. It was observed that the carbonyl functions remain non-reduced even after metalation. High energy shift of $\nu_{\text{C}^4\text{-O}}$ and low energy shift of $\nu_{\text{C}^2\text{-O}}$ was found in all TMX complexes. As the $[\text{Cu}(\text{dopf})]^+$ fragments interact very weakly with carbonyl functions, $\Delta\nu_{\text{C}=\text{O}}$ values on metalation (cm^{-1}) were found to be very small (in the range of +5 to +10 cm^{-1}).

Table 3.2.2.1. IR (solid) carbonyl stretching frequencies of $\text{Cu}^{\text{I}}\text{Fe}^{\text{II}}\text{-TMX}$ complexes

Ligand and its metal complexes	$\nu_{\text{C}=\text{O}}$ (in cm^{-1})		$\Delta\nu_{\text{C}=\text{O}}$ on metallation (cm^{-1})	
	$\text{C}^2\text{-O}$	$\text{C}^4\text{-O}$	$\Delta\nu \text{C}^2\text{-O}$	$\Delta\nu \text{C}^4\text{-O}$
TMX	1716(w)	1652(s)	n.a	n.a
$[\text{Cu}(\text{dppf})(\text{TMX})](\text{BF}_4)$	1704(s)	1657(vs)	-12	+5
$[\text{Cu}(\text{dippf})(\text{TMX})](\text{PF}_6)$	1706(s)	1660(vs)	-10	+8
$[\text{Cu}(\text{dchpf})(\text{TMX})](\text{PF}_6)$	1707(s)	1662(vs)	-9	+10

3.3. Crystal structures

3.3.1 Crystal structure of [Cu(dppf)(P-9MG)](BF₄)

The block-yellow single crystals of the complex [Cu(dppf)(P-9MG)](BF₄) were grown by layered-liquid phase diffusion of hexane into a dichloromethane solution of the complex inside thin glass tubes. The complex was crystallized in the monoclinic space group *C2/c* with ½ molecule of dichloromethane in each unit cell. Structural analysis showed N⁷-monodentate binding to the copper centre of the organometallic [Cu(dppf)]⁺ fragment. (The crystallographic numbering of atoms in Figure 3.3.1.1 was done in a different way from the numbering according to the IUPAC nomenclature for heterocycles). The structure involves strong intramolecular H-bonding in a six-membered ring formed between the H bond donor at the N¹ position of guanine (N4-H4--O2) and the acceptor on the pivaloyl group. It was found that strong intramolecular H-bonding between ring H4 and pivaloyl O2 at a distance of 2.06(5) Å (heteroatom distance N4-O2 = 2.65Å) has a contributing effect in stabilizing the structure. The [Cu(dppf)]⁺ fragment is bonded to P-9MG in a non-chelating fashion through N1 (N⁷) atom; O1 (O⁶) remains non-coordinated at a distance of 3.870(1) Å to copper. The C10-O1 (CO group at C⁶) and C5-O2 (carbonyl in pivaloyl group at N²) bond lengths of 1.219(6) and 1.223(6) Å proved the presence of non-reduced carbonyl groups in the molecule. The short Cu-N1 (N⁷) distance at 1.989(4) Å in relation to α -iminoketo-chelating Cu complexes, indicate a strong N⁷ binding (Table 3.3.3.2 and Figure 3.3.3.5). The Cu⁺ ion adopts a tri-coordinated, partially T shaped planar geometry (Figure 3.3.1.1) with non-interacting O1 atom in the axial position of the PNPcopper plane. The distance of the Cu atom from the PNP plane was found to be only 0.202 Å. Selected bond lengths and angles of the structure are given in Table 3.4.1.1.

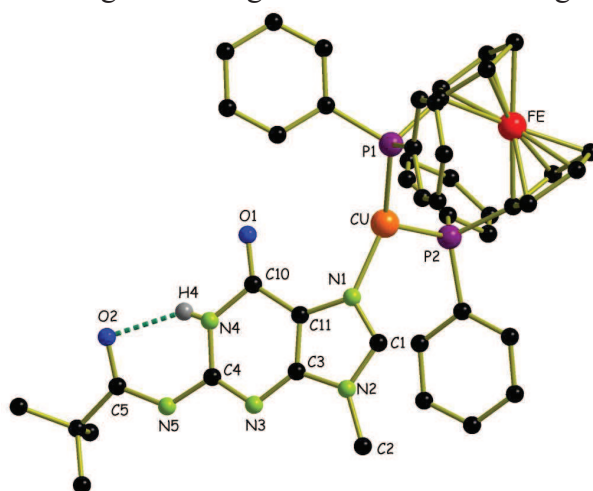


Figure 3.3.1.1. Molecular structure of the complex monocation in the crystal of [Cu(dppf)(P-9MG)](BF₄) × 0.5 CH₂Cl₂. The counter anion, BF₄, and the solvent molecule, CH₂Cl₂, are omitted for clarity.

Table 3.3.1.1. Selected bond lengths (Å) and angles (°) for [Cu(dppf)(P-9MG)](BF₄). 0.5 CH₂Cl₂

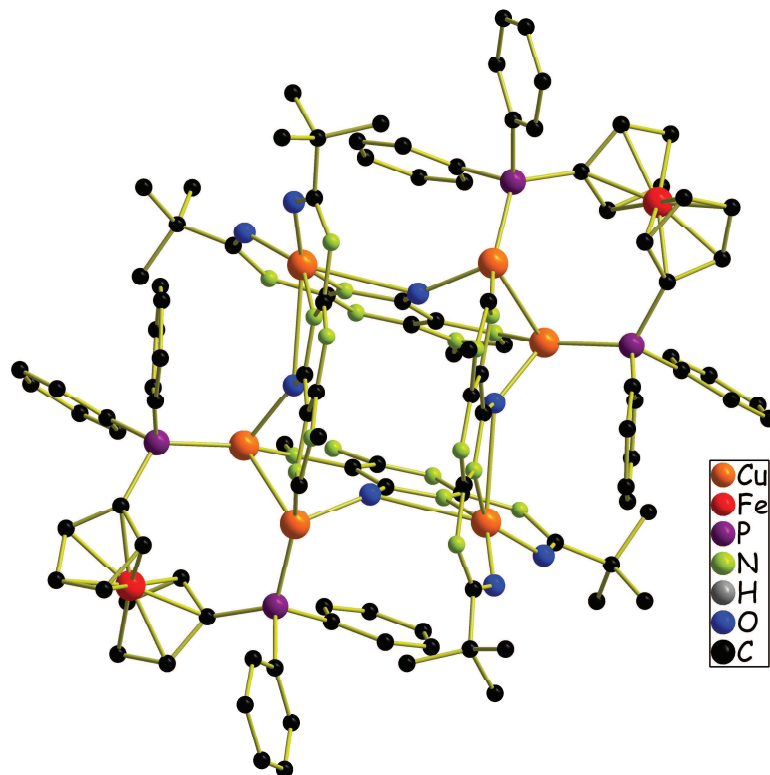
Bonds	Lengths	Bonds	Lengths
Cu-N1	1.989(4)	C1-N2	1.361(6)
Cu-O1	3.387(3)	N2-C3	1.365(6)
Cu-P1	2.229(1)	C4-N5	1.383(6)
Cu-P2	2.307(1)	Bonds	Angles(°)
C10-O1	1.219(6)	O1-Cu-N1	64.41(12)
C5-O2	1.223(6)	P1-Cu-P2	116.09(5)
O2-H4	2.056(48)	N1-Cu-P2	106.00(11)
C10-C11	1.428(6)	P1-Cu-N1	135.18(11)
C11-C3	1.376(6)	Cu-N1-C1	127.1(3)
C3-N3	1.350(6)	Cu-N1-C11	126.1(3)
N3-C4	1.302(6)	N1-C11-C10	130.5(4)
C4-N4	1.366(6)	C11-C10-O1	129.2(5)
N4-C10	1.405(6)	N4-H4-O2	144.1(51)
C11-N1	1.384(5)	C1-N1-C11	104.3(4)
N1-C1	1.315(6)	O1-C10-C11	129.2(5)

The pyrimidine ring C-C bond lengths are in the range of 1.350(6) - 1.405(6) Å and the C-N double bond distance is 1.302(6) Å. Imidazole ring C-N single bond lengths C11-N1 = 1.384(5) Å, C1-N2 = 1.361(6) Å, N2-C3 = 1.365(6) Å and C-N double bond length N1-C1 = 1.315(6) Å indicate little conjugation of π electrons in the imidazole ring. The shorter C-N bond length for C1-N2 compared to C11-N1 indicates that the N⁹ lone pair electron is conjugated to the imidazole double bond and as a consequence electron density on N⁹ was increased favouring metal binding at the position. The C-C double bond length of P-9MG is 1.376(6) Å and C-C single bond length is 1.428(6) Å. This account for the non-conjugation of the double bond in the ring π -system.

3.3.2 Crystal structure of the cluster complex [Cu₃(P-9MG⁻)₂(dppf)]₂(BF₄)₂

Coarse shaped red single crystals of the complex were grown during the crystallization of [$\{Cu(dppf)\}_2(P-9MG)](BF_4)_2$ from a hexane-dichloromethane solution. The structural analysis revealed that the cluster complex contains 6 Cu^I ions, 2 μ_2 -dppf unit and 4 deprotonated guanine residues (P-9MG⁻) (Figure 3.3.2.1). Two BF₄⁻ counter anions are present to balance the dipositive charge of the complex ion. Deprotonation of P-9MG in organic solvent was favoured due to the presence of excess metal species in the solution. As deprotonation increases the basicity of the heterocycle, anionic P-9MG has more potential coordination sites and patterns for metal binding than the corresponding neutral form^[26]. Considering various possible binding modes, the self aggregation process was favoured to re-

organize for a stable geometry around the metal ions. Cu and ligand O atoms form a 10 membered-puckered ring structure (Figure 3.3.2.2). Chelating dppf units change their binding mode from chelating to bridging in such a way that a single dppf molecule can bridge to two tetracoordinated Cu^{I} centers resulting in a weak d^{10} - d^{10} metal-metal interaction (Figure 3.3.2.3).



3.3.2.1. Structure of the cluster compound $[\text{Cu}_3(\text{P-9MG})_2(\text{dppf})]_2(\text{BF}_4)_2$ represented in capped sticks style. The counter anions are omitted for clarity.

Coordination to N^1 [110] or O^6 [111]; twofold metal binding either through N^1 and N^7 simultaneously [112] or through N^1 and O^6 [113]; threefold metal binding through N^1 , N^7 , N^3 [114]; threefold metal binding through N^1 , N^7 , O^6 [115] are all documented in the literature. The example of threefold metal coordination to a dianionic guanine nucleobase has also been reported in the literature [116]. From the structural analysis of the cluster complex it was found that threefold coordination through N^7 , N^1 and O^6 is present to three different Cu^{I} centres (Figure 3.3.2.2). Only N^2 and N^3 remains non-coordinated as the N^9 position was already blocked by a methyl group. N^7 and O^6 are bonded to two copper centers through a stable bridge formation by a dppf unit. The Cu2-Cu1 distance was found at 2.763(1) Å, sufficiently shorter than the sum of the van-der-Walls radii (2.8 Å), accounting for d^{10} - d^{10} metal-metal interaction [117,118]. A similar type of bridge formation was found between identical or different metal ions in guanine complexes previously [119].

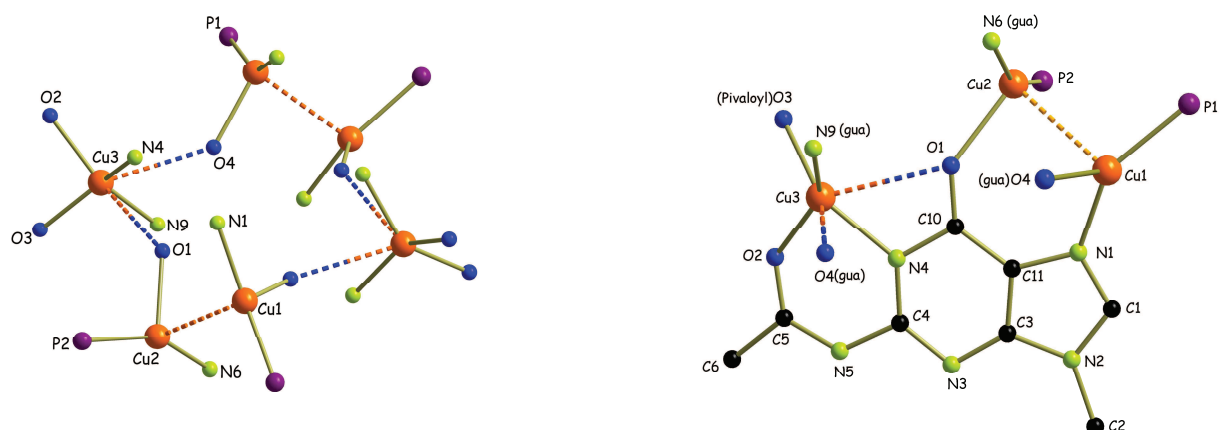


Figure 3.3.2.2. 10 membered 6Cu-4O cluster ring in $[\text{Cu}_3(\text{P-9MG}^-)_2(\text{dppf})]_2(\text{BF}_4)_2$ (left). Binding mode of deprotonated N2-pivaloyl,9-methylguanine (P-9MG^-) (right).

O^6 binding has an importance in maintaining the guanine quadruplex structure for the activity of telomeres^[120]. Metal binding to O^6 has previously been reported in a rhodium complex containing triphenylphosphine and CO as coligands^[121]. Simultaneous N^7 and O^6 binding in a chelating fashion was found in a cyclic, hexanuclear theophyllinato complex of a platinum complex fragment^[122]. In this copper cluster complex, the neutral O^6 atom is bonded simultaneously to two copper centers (Cu2 and Cu3) through an unsymmetrical bridge without the support of a bridging dppf unit (Figure 3.3.2.2). One of the Cu-O distances is shorter (Cu2-O1 = 2.072(4) Å) and the other one is longer (Cu3-O1 = 2.759(4) Å). The distance between Cu2 and Cu3 is 4.484(1) Å. In the crystal structure three distinctly different type Cu geometries are found. Two tri-coordinated, approximately T-shaped planar CuNPO moieties and one six-coordinated CuN_2O_4 center are present. Two tricoordinated Cu^{I} units involve the coordination of N^7 , O^6 of P-9MG^- and the P atoms. The CuNPO tri-coordinated systems are further linked by a weak Cu-Cu interaction at a distance of 2.763(1) Å. The bond angles around Cu1 are $\text{N1-Cu1-P1} = 146.93(16)^\circ$, $\text{N1-Cu1O4} = 95.24(19)^\circ$, $\text{P1-Cu1-O4} = 111.04(14)^\circ$ and the Cu1 atom is deviated from the PNO plane by only 0.281Å. The angles around Cu2 are $\text{N6-Cu2-O1} = 96.53(19)^\circ$, $\text{P2-Cu2-O1} = 106.33(13)^\circ$, $\text{P2-Cu2-N6} = 152.76(16)^\circ$ and the Cu2 atom is deviated from this PNO plane by 0.217Å. The geometry around the Cu^{I} ions is highly distorted. Hexacoordinated copper (CuN_2O_4) is formed by strong coordination of P-9MG^- N^1 donor (in deprotonated form), the weak coordination by O^6 of P-9MG^- (weak coordination due to unsymmetrical bridging), and strong coordination by pivaloyl O donors. The bond angles around Cu3, $\text{O3-Cu3-O2} = 91.94(19)^\circ$, $\text{O3-Cu3-N4} = 143.3(2)^\circ$, $\text{O2-Cu3-N4} = 87.9(2)^\circ$, $\text{O3-Cu3-N9} = 88.6(2)^\circ$, $\text{O2-Cu3-N9} = 144.3(2)^\circ$ and $\text{N4-Cu3-N9} = 112.1(2)^\circ$ indicate a highly distorted geometry. The cluster complex is packed in the unit cell through intermolecular π - π

interactions between phenyl rings. That interaction is illustrated in the Figure 3.3.2.4. The strong interaction is inferred from the short average distances of 2.392 Å between phenyl rings (involved in π - π interaction) and their parallel arrangement (angle between the average planes of phenyl rings is 0.09°). Selected bond lengths and angles are given in Table 3.3.2.1.

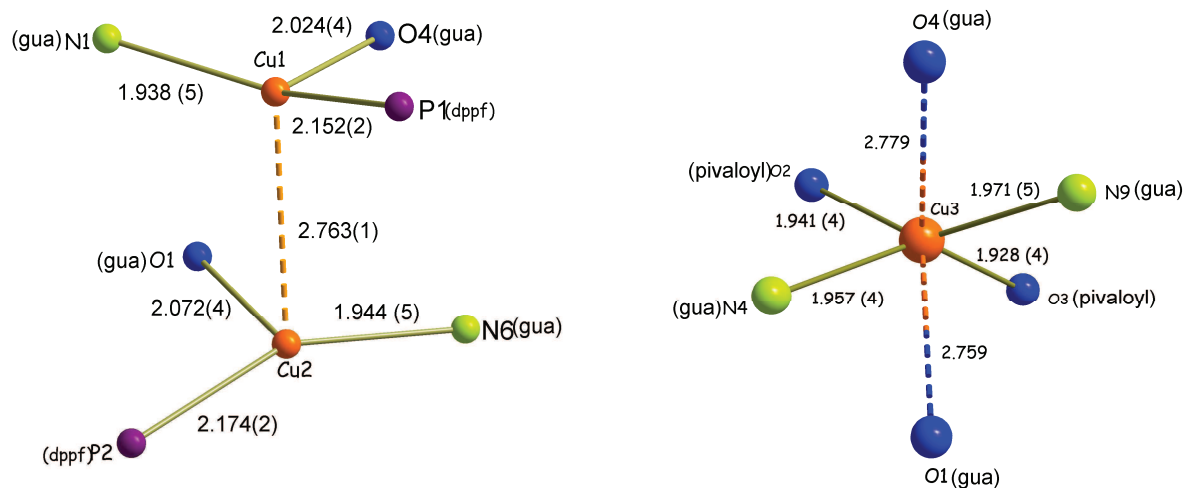


Figure 3.3.2.3. Representation of the metal-metal interaction between tri-coordinated Cu^I units (left), and the hexa-coordinated Cu^I center in the cluster (right).

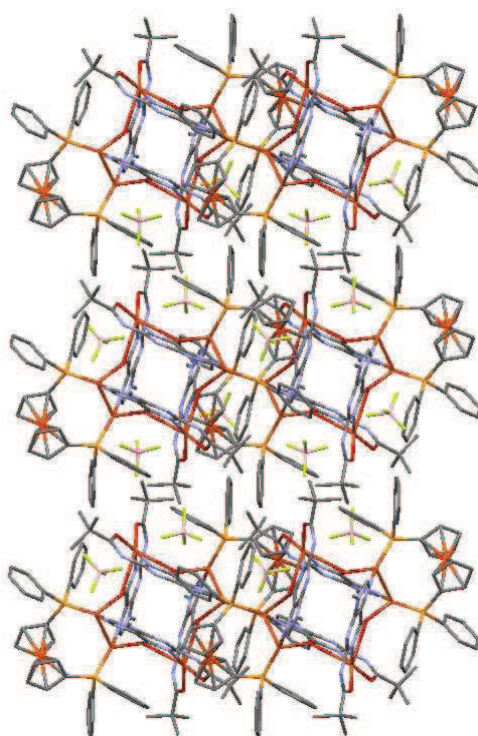


Figure 3.3.2.4. Packing diagram showing intermolecular π - π stacking arrangement between phenyl rings.

Table 3.3.2.1. Selected bond lengths (Å) and angles (°) for cluster complex $[\text{Cu}_3(\text{P-9MG})_2(\text{dppf})]_2(\text{BF}_4)_2$.

Bonds	Lengths	Bonds	Lengths
Cu1-N1	1.938(5)	N3-C4	1.318(8)
Cu2-N6	1.944(5)	N3-C3	1.348(8)
Cu3-N4	1.957(5)	Bonds	Angles(°)
Cu3-N9	1.971(5)	N1-Cu1-O4	95.24(19)
Cu1-O4	2.024(4)	N1-Cu1-P1	146.93(16)
Cu2-O1	2.072(4)	O4-Cu1-P1	111.04(14)
Cu3-O3	1.928(4)	N1-Cu1-Cu2	99.03(16)
Cu3-O2	1.941(4)	O4-Cu1-Cu2	86.81(13)
Cu1-P1	2.152(2)	P1-Cu1-Cu2	102.03(5)
Cu2-P2	2.174(2)	N6-Cu2-O1	96.53(19)
Cu1-Cu2	2.763(1)	N6-Cu2-P2	152.76(16)
O1-C10	1.254(7)	O1-Cu2-P2	106.33(13)
O2-C5	1.242(7)	N6-Cu2-Cu1	94.94(16)
O3-C16	1.259(8)	O1-Cu2-Cu1	82.60(12)
O4-C21	1.261(7)	P2-Cu2-Cu1	102.41(5)
N1-C1	1.330(8)	O3-Cu3-O2	91.94(19)
N2-C1	1.350(8)	O3-Cu3-N4	143.3(2)
N2-C3	1.385(8)	O2-Cu3-N4	87.9(2)
C3-C11	1.369(8)	O3-Cu3-N9	88.6(2)
C10-C11	1.411(8)	O2-Cu3-N9	144.3(2)
N4-C10	1.394(8)	N4-Cu3-N9	112.1(2)
N4 C4	1.354(8)		

3.3.3 Crystal structure of $\text{Cu}^{\text{I}}\text{Fe}^{\text{II}}$ -TMX complexes

The labile-coordination of trimethylxanthine (TMX) to $[\text{Cu}(\text{dppf})]^+$ moieties was studied by single crystal X-ray structure analysis. Orange single crystals of complexes $[\text{Cu}(\text{dppf})(\text{TMX})](\text{BF}_4)$, $[\text{Cu}(\text{dippf})(\text{TMX})](\text{PF}_6)$ and $[\text{Cu}(\text{dchpf})(\text{TMX})](\text{PF}_6)$ were grown by the diffusion method using hexane and dichloromethane as solvents. The complexes $[\text{Cu}(\text{dppf})(\text{TMX})](\text{BF}_4)$, and $[\text{Cu}(\text{dchpf})(\text{TMX})](\text{PF}_6)$ were crystallized in the triclinic space $P\bar{1}$ group and the complex $[\text{Cu}(\text{dippf})(\text{TMX})](\text{PF}_6)$ was crystallized in the monoclinic space $P2_1/c$ group. Solvent of crystallization (CH_2Cl_2) were incorporated in the crystal structures of the $[\text{Cu}(\text{dppf})(\text{TMX})](\text{BF}_4) \times 2\text{CH}_2\text{Cl}_2$ and $[\text{Cu}(\text{dchpf})(\text{TMX})](\text{PF}_6) \times \text{CH}_2\text{Cl}_2$. The molecular structures of the complexes are presented in Figure 3.3.3.1-3.3.3.3 and selected structural parameters are provided in Table 3.3.3.1

The coordination of TMX through the imidazole nitrogen is much stronger compared to the oxygen donor of pyrimidine ring. The variable feature of all the crystal structures is the Cu-O

distance. The distance is very dependent on the electronic and steric environment around the Cu centre. In the complexes Cu^{I} ions adopt nearly a trigonal planar geometry ($\text{P1-Cu-P2} = 115.72(4)\text{-}118.65(2)^\circ$, $\text{P2-Cu-N1} = 118.47(8)\text{-}127.25(10)^\circ$, $\text{P1-Cu-N1} = 117.02(10)\text{-}121.03(8)^\circ$ and $d_{\text{Cu-PPN plane}} = 0.010\text{-}0.211 \text{ \AA}$), accompanied by a weakly interacting O atom at the axial position of the trigonal plane (Figure 3.3.3.4).

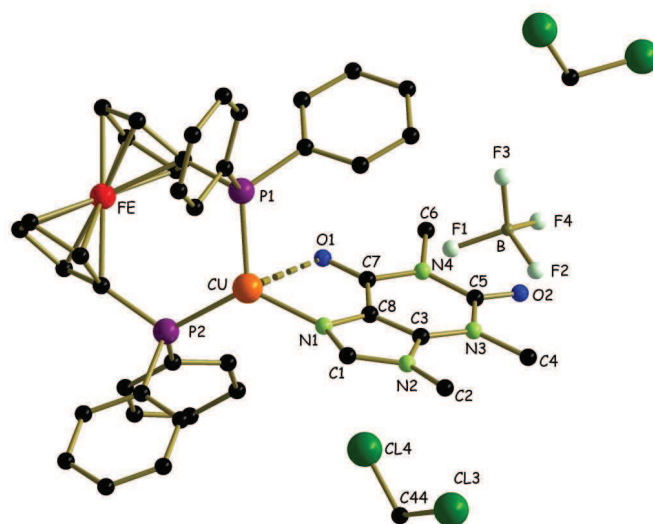


Figure 3.3.3.1. Crystal structure of $[\text{Cu}(\text{dppf})(\text{TMX})](\text{BF}_4) \times 2\text{CH}_2\text{Cl}_2$

The coordination of O can be fine-tuned by changing the chelating ferrocenyldiphosphine ligands (dppf, dippf, dchpf). In the case of dchpf, it was found that the Cu-O distances of 3.062(2) and 3.070(2) Å [$> \sum \text{vdw}(\text{Cu} \ \& \ \text{O}, 2.92\text{Å})$]^[118] are larger than the sum of their van-der-Waals radii. When the phosphine was changed to dppf and dippf, the distance decreased to 2.799(3) Å and 2.772(2) Å, respectively. Thus the electronic (and probably steric effects) of the coligands also govern the metal binding property in such biomolecules. The cofacial C-O bond lengths are in the range of 1.223(5)-1.227(4) Å whereas the free C-O bond lengths are in the range of 1.213(5)-1.221(4) Å. This clearly indicates that the cofacial O atom very weakly interacts with the Cu centre. The Cu-N distances were found in a range of 1.972 (3)-2.006(2) Å and the Cu-P distances in the range of 2.227(1)-2.260(1) Å. The O-Cu-N chelate angles are 68.80 (8) to 74.22 (11)°. The bite angles are 115.72(4), 118.65(2) and 118.23(3)-118.30(3)° in dppf, dippf and dchpf, respectively.

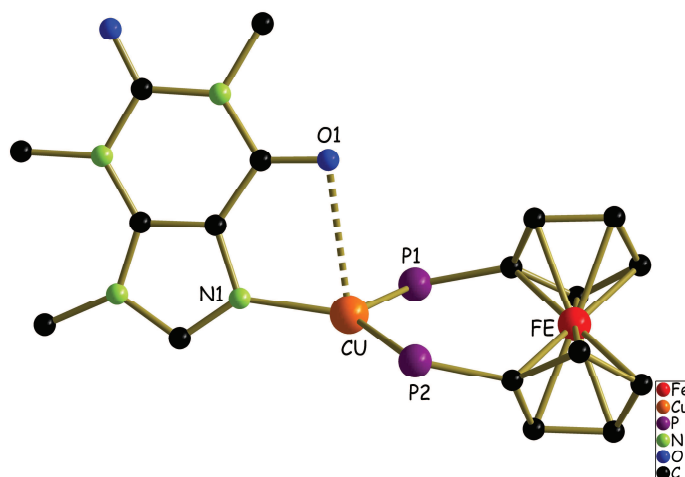


Figure 3.3.3.4. The representation of average geometry around Cu ion in the $\text{Cu}^{\text{I}}\text{Fe}^{\text{II}}\text{-TMX}$ complexes.

The plot of Cu-O and Cu-N distances vs. $[\text{Cu}(\text{dopf})]^+$ -biomolecule complexes in Figure 3.3.3.5 shows that the change of Cu-N bond distances is less dependent on phosphines or on the ring systems of the biomolecules. The N-coordination is much stronger than O-coordination. The Cu-O distance changes from a strong bond situation ($\text{Cu-O} \approx 2.24 \text{ \AA}$) in lumazine or alloxazine complexes to a completely non-bonding situation ($3.387(3) \text{ \AA}$) in the P-9MG complex (Table 3.3.3.2). Lumazine and alloxazine complexes have Cu-O distance $2.236(3) - 2.261(2) \text{ \AA}$ which changes to $2.799(3) \text{ \AA}$ when the pyrazine ring is replaced by an imidazole ring. It is seen that the ring size has a very important role towards the binding nature of biomolecules. The Cu-O distances in xanthine complexes changes from $2.772(2) \text{ \AA}$ [$< \sum\text{vdw}(\text{Cu} \ \& \ \text{O}, 2.92\text{\AA})$]^[118] to $3.070(2) \text{ \AA}$ [$> \sum\text{vdw}(\text{Cu} \ \& \ \text{O}, 2.92\text{\AA})$]^[118] only by altering the ferrocenyldiphosphines (dippf to dppf to dchpf). Finally, it is seen that the metal binding depends on the heterocyclic ring of biomolecule and the coligand on the metal fragment.

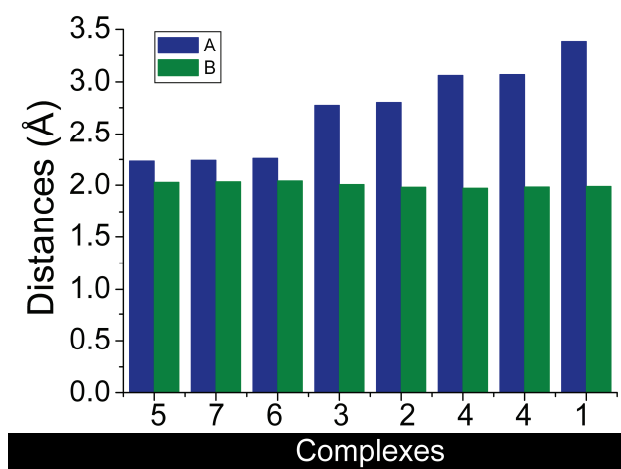


Figure 3.3.3.5. Graphical representation of Cu-O and Cu-N distances in Cu-biomolecule complexes (numbering from Table 3.3.3.2).

Table 3.3.3.2. Comparison of bond lengths and angles among Cu^I-biomolecule complexes.

Complexes	Cu-O (Å)	Cu-N(Å)	$\Delta 1$ (Å) ^a	C-O (Å)	C-O (Å)	$\Delta 2$ (Å) ^b
				cofacial	free	
[Cu(dppf)(P9MG)](BF ₄) 1	3.387(3)	1.989(4)	-1.398	1.225(4)	1.221(4)	0.004
[Cu(dppf)(TMX)](BF ₄) 2	2.799(3)	1.982(3)	-0.817	1.223(5)	1.213(5)	0.010
[Cu(dippf)(TMX)](PF ₆) 3	2.772(2)	2.006(2)	-0.766	1.225(2)	1.213(3)	0.012
[Cu(dchpf)(TMX)](PF ₆) 4	3.062(2)	1.972(3)	-1.090	1.227(4)	1.216(4)	0.011
	3.070(2)	1.984(3)	-1.086	1.225(4)	1.221(4)	0.004
[Cu(dppf)(DML)](BF ₄) ^c 5	2.236(3)	2.027(4)	-0.209	1.226(6)	1.211(6)	0.015
[Cu(dippf)(DML)](BF ₄) ^c 6	2.261(2)	2.041(2)	-0.220	1.228(3)	1.214(3)	0.014
[Cu(dppf)(TMA)](BF ₄) ^c 7	2.243(2)	2.032(2)	-0.211	1.228(3)	1.210(3)	0.018

^a $\Delta 1 = (d_{\text{Cu-N}} - d_{\text{Cu-O}})$, ^b $\Delta 2 = (d_{\text{C-O}}(\text{cofacial}) - d_{\text{C-O}}(\text{free}))$. ^cComplexes from chapter 2

3.4. Cyclic Voltammetry

The cyclic voltammograms of the complexes **1**, **3**, **4** and **5** were measured in CH₂Cl₂ / 0.1 M Bu₄NPF₆ at room temperature with 100 mV/s scan rate using a three-electrode configuration (glassy carbon working electrode, Pt counter electrode, Ag reference electrode) and a PAR 273 potentiostat and function generator. The ferrocene/ferrocenium (Fc/Fc⁺⁰) couple served as internal reference (+0.46 V vs. SCE). The oxidation of Cu^I in the complexes was not accessible either due to oxidation at a high positive potential (beyond the solvent window) or due to the instability of the oxidized species in the electrochemical cell. The ferrocene unit, present in the organometallic fragment of the complexes undergoes a quasi-reversible (large difference between peak potentials) one-electron oxidation. Cathodic peaks were not observed in the negative potential region. The electrochemical data for the ferrocene based oxidations are given in Table 3.4.1.

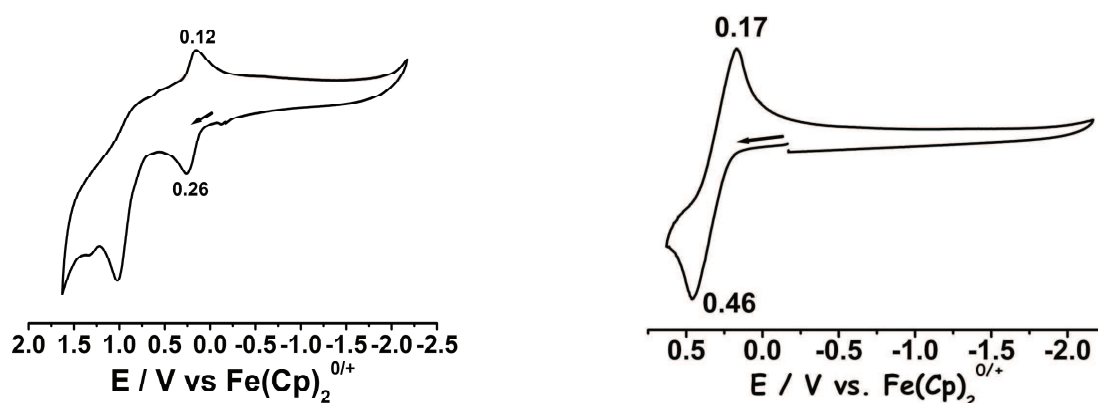


Figure 3.4.1. Cyclic voltammograms of $[\text{Cu}(\text{dppf})(\text{P-9MG})](\text{BF}_4)$ (**1**) (left) and $[\text{Cu}(\text{dppf})(\text{TMX})](\text{BF}_4)$ (**2**) (right) in CH_2Cl_2 / 0.1 M Bu_4NPF_6 at room temperature with 100 mV/sec scan rate.

Table 3.4.1. Half wave oxidation potentials from cyclic voltammetry in CH_2Cl_2 / 0.1 M Bu_4NPF_6 at RT with 100 mV/sec scan rate.

Complexes	$E_{1/2}$ / V (ΔE / mV)
$[\text{Cu}(\text{dppf})(\text{P-9MG})](\text{BF}_4)$ 1	0.19 (140)
$[\text{Cu}(\text{dppf})(\text{TMX})](\text{BF}_4)$ 2	0.32 (290)
$[\text{Cu}(\text{dippf})(\text{TMX})](\text{PF}_6)$ 3	0.41 (253)
$[\text{Cu}(\text{dchpf})(\text{TMX})](\text{PF}_6)$ 4	0.24 (170)

$E_{1/2}$ potentials for ferrocene-based oxidations are dependent on the substitution in the ferrocenyldiphosphine. They are also dependent on the type of metal coordination to the purine bases. In the case of stronger metal binding to axial O, oxidation occurred at comparatively higher positive potential, and in the case of weaker binding, the oxidation occurred at less positive potential. The interaction between the metal fragment and the purine base depends on steric and electronic factors of the coligand. As the binding of the metal fragment containing the isopropyl group was found to be strongest (from crystal structure analysis), the complex was oxidized at a high potential of +0.41 V, whereas the fragment containing dppf was oxidized at a lower potential of 0.32 V and $[\text{Cu}(\text{TMX})(\text{dchpf})](\text{PF}_6)$ was oxidized at an even lower potential of 0.24 V (Table 3.4.1). From the crystal structure studies of the TMX complexes it is seen that the bond lengths are in the order of $\text{Cu-O}(\text{dippf}) < \text{Cu-O}(\text{dppf}) < \text{Cu-O}(\text{dchpf})$. In the complex $[\text{Cu}(\text{P-9MG})(\text{dppf})](\text{BF}_4)$, the metal fragment has almost no

interaction (as found from crystal structure analysis) with the co-facial O atom, and, as a result, the Fe centre was oxidized at lowest potential of +0.19 V. Thus, the metal purine interaction has an influence on the oxidation potential of the ferrocene unit.

3.5. UV-Vis spectroscopy

The UV-Vis spectra of the complexes **1**, **3**, **4** and **5** in CH₂Cl₂ show a very weak absorption at around 440 nm which could be attributed to the MLCT transition or to a intraligand transition of a metal coordinated purine base. The UV-Vis spectrum of the complex **1** is shown in Figure 3.5.1. The λ_{max} and ϵ values of all the complexes are given in Table 3.5.1.

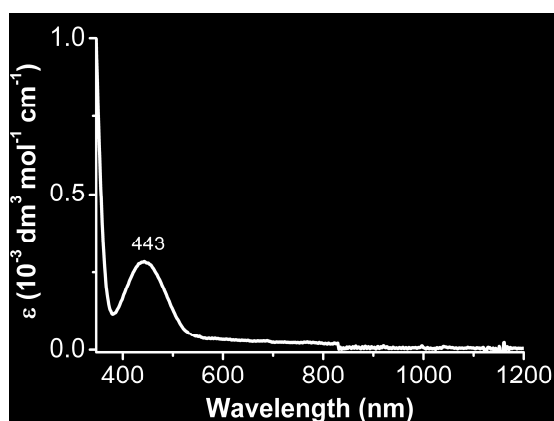


Figure 3.5.1. UV-Vis Spectrum of [Cu(P-9MG)(dppf)](BF₄) **1** in CH₂Cl₂

Table 3.5.1. UV-Vis data from complexes **1**, **3**, **4** and **5**.

Complexes	λ_{max} in nm (ϵ in $10^{-3} \text{ dm}^3 \text{ mol}^{-1} \text{ cm}^{-1}$)
[Cu(P-9MG)(dppf)](BF ₄) 1	443 (0.28)
[Cu(TMX)(dppf)](BF ₄) 3	441 (0.15)
[Cu(TMX)(dippf)](PF ₆) 4	442 (0.16)
[Cu(TMX) (dchpf)](PF ₆) 5	442 (0.14)

3.6. Conclusion

Binding of α -iminoketo containing modified purine bases to the soft d^{10} metal fragment $[\text{Cu}(\text{dopf})]^+$ was studied structurally in discrete and cluster complexes. The N^7 -binding mode of substituted guanine has been established in its native state. The presence of the H atom on N^1 allowed us to study the discrete Cu complex and to establish the role of intramolecular H bonding in stabilizing the structure. The crystallographic study was further extended to explore all other possible coordination modes by attempts at synthesizing Cu-guanine cluster complexes having higher metal contents. In the presence of excess metal, the deprotonation process was favoured even in organic solvents. The crystallization of the complex followed by single crystal X-ray diffraction revealed a cluster complex exhibiting multi-coordination modes of the guanine derivative. The bridging mode of dppf resulted in d^{10} - d^{10} metal-metal interaction at a shorter distance than the sum of van-der-Waals radii. The variable binding modes of trimethylxanthine were also studied in a series of copper complexes containing three different ferrocenyldiphosphine chelating ligands. The various effects on metal binding were explained from the structural parameters. Reversible ferrocene based one-electron oxidation process and the UV-Vis absorption property were investigated. These studies provide useful informations on the metal binding to purine bases and explore the various effects in determining the binding property of these nucleobases.

Chapter 4

Structural comparison and spectroscopy of electrochemically generated radical and non-radical bridged heterotetra-nuclear complexes

4.1. Introduction

Bis-chelating π -electron deficient azo ligands have a special interest in coordination chemistry for studying metal-metal interaction at a shorter distance of about 5 Å via low-lying azo-centered π^* molecular orbitals^[27-31]. The azo ligands are famous for having easy accessible redox states in respective complexes, stabilizing radical intermediates, metal-metal interaction at shorter distance, and metal- to -ligand charge transfer absorption in the UV-Vis-NIR region^[27,30]. The non-reduced azo form has the electronic configuration $\sigma^2\pi^2\pi^*$, in the partially reduced form it is $\sigma^2\pi^2\pi^{*1}$, and in the hydrazido form $\sigma^2\pi^2\pi^{*2}$ ^[123]. MLCT transitions can occur in the near infrared region and are attributed to the charge transfer from electron rich transition metal fragments, $d^m\pi ML_n$, to the vacant π^* of the electronic configuration, either $\sigma^2\pi^2\pi^*$ or $\sigma^2\pi^2\pi^{*1}$ ^[27,28]. The N-N bond length is roughly 1.25 Å when the bond order is 2 but it increases to 1.33 Å when in the azo anion radical (AAR) form, having bond order of 1.5, and further to 1.45 Å in the hydrazido(2-) form. A plot of bond order vs. bond length (Figure 4.1.1) has been reproduced from the literature to depict the variation^[123].

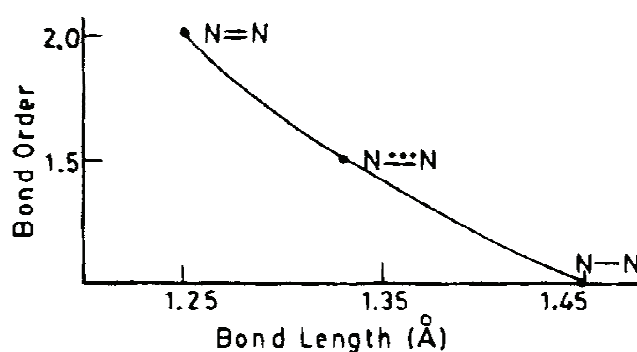


Figure 4.1.1. A plot of bond order versus bond length (Å).

Among various substituted ligands in the azo family, abcp (2,2'-azobis(5-chloropyrimidine)) has certain advantages over the others. The presence of two electron withdrawing chlorine atoms at C5 position and four N atoms in the pyrimidine ring make it a better π -acceptor and

easy reducible at less negative potential. The ligand can be prepared by chlorinating oxidative coupling of 2-aminopyrimidine and was first introduced by Kaim et al^[28].

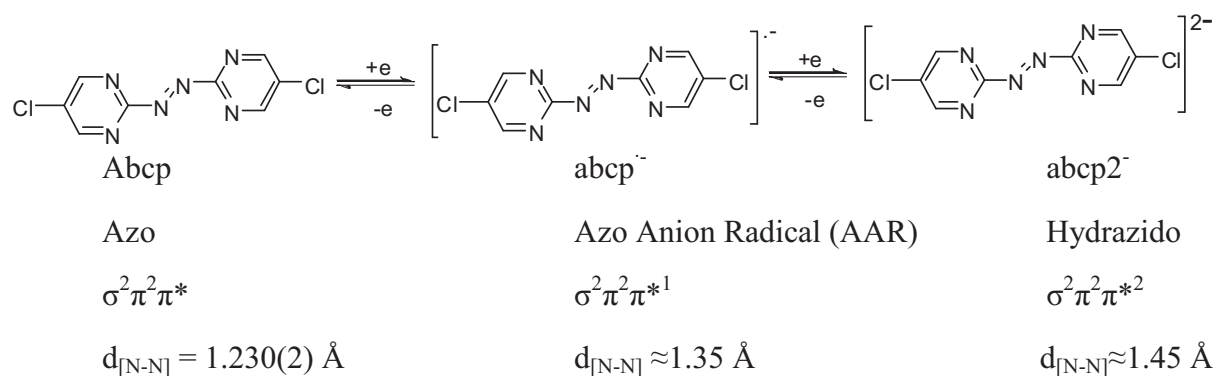


Figure 4.1.2. Two step one-electron reduction processes showing electronic configurations and N-N distances in different redox states.

The azo ligands are capable of undergoing two-step one-electron reduction processes, accompanying the externally added electrons to the π^* molecular orbital (Figure 4.1.2). Metal complexes containing the above forms of the ligand are characterized by their low energy metal- to -ligand charge transfer bands. The effect of metal coordination is also found in the corresponding azo bond lengths. Over various possible binding modes, the following two (Figure 4.1.3) are more favorable for the formation of a five-membered chelate ring in mononuclear complexes and two common edge sharing 5-membered chelates in dinuclear complexes. The dinuclear Cu^{I} complexes with both un-reduced and one-electron reduced abpy ligand are found to be stabilized by chelating diphosphines^[124].

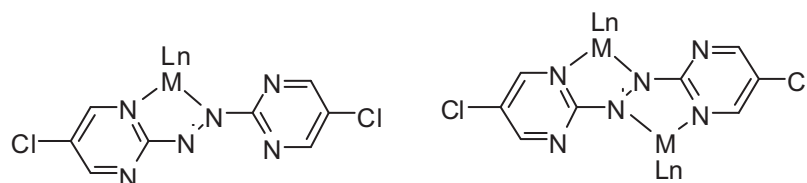


Figure 4.1.3. Favourable binding modes of the abcp ligand to metal fragments

Though literature reports are found for structural and spectroscopic evidence of azo-bridged mono- and dinuclear Cu, Ru and Pt complexes, the structural evidence for both azo and azo anion radical (AAR) forms for a given complex was not yet reported. In this work are provided structural informations for an abcp bridged oligonuclear complex in both redox states. 1,1'-Bis(diphenylphosphino)ferrocene, dppf, was used as a coligand to stabilize the complexes. The first structural information on a dinuclear Cu complex with abcp ligand in the radical form was found in a literature report by Kaim et al^[28]. Though crystallographic studies along with calculations it is possible to compute the azo bond length in its reduced form but

the information on unreduced system was still missing in the literature. Although a report evidenced the isolation of a Cu^{I} -abcp complex in both forms, the structural determination was only possible for the radical species^[125]. Following a general synthetic route for the synthesis of Cu-azo complex, it was possible to characterize a heterotetranuclear Cu complex with abcp as a bridging ligand and dppf as a coligand. The structural determination and other analysis revealed a heterotetranuclear diamagnetic complex, $\text{Fe}^{\text{II}}\text{Cu}^{\text{I}}\text{-abcp-Cu}^{\text{I}}\text{Fe}^{\text{II}}$ with un-reduced abcp. The Significant difference between the first and second reduction potentials of the complex allowed us to isolate the radical form of the complex by bulk electrolysis. The X-ray diffraction study of a single crystal of the radical form provided the structural details in the reduced form as well.

Furthermore, a new abpy-bridged heterodinuclear Cu^{I} complex was synthesized to introduce a different coligand, 1,1'-bis(di-isopropylphosphino)ferrocene (dippf). The idea was to study the effect of coligands on azo systems for the preferential formation of radical or non-radical species. The complex has been analyzed both spectroscopically and structurally for comparing with the reported^[124] dppf analogue.

4.2. Synthesis and characterization

The abcp ligand^[28] and the metal precursor complex $[\text{Cu}(\text{dppf})(\text{CH}_3\text{CN})_2](\text{BF}_4)^{[82]}$ were synthesized according to literature procedures. The diamagnetic heterotetranuclear complex was synthesized from a reaction of abcp and the metal precursor in a 1:2 molar ratio in dichloromethane. The green diamagnetic complex was characterized by ^1H and ^{31}P NMR spectroscopy. Detailed synthetic procedures and characterization are given in Experimental Section The peak at $m/z = 1490.1$ in the mass spectrum was found for the species, $[\mathbf{1-H}]^+$ (calculated $m/z = 1489.94$).

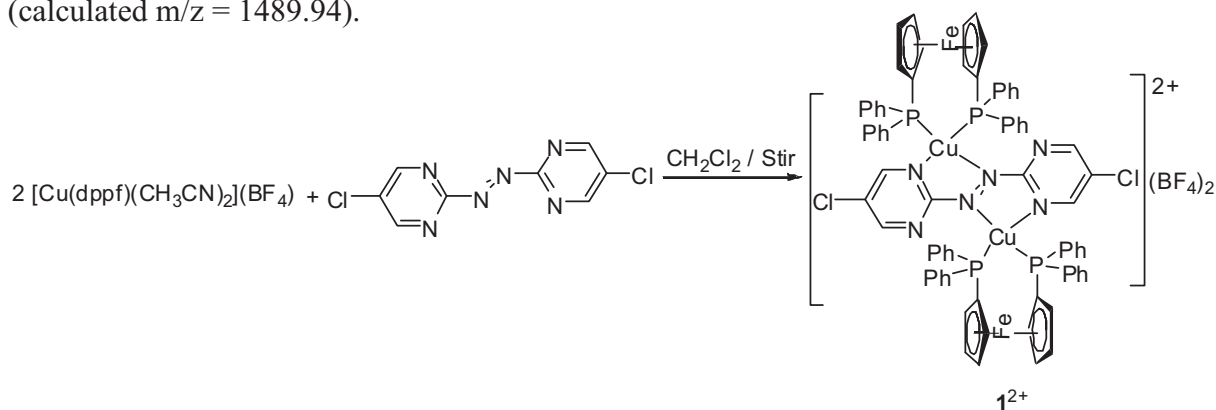


Figure 4.2.1. Synthesis of the heterotetranuclear diamagnetic complex $[(\mu\text{-abcp})\{\text{Cu}(\text{dppf})\}_2](\text{BF}_4)_2$, $[\mathbf{1}](\text{BF}_4)_2$.

A self-assembly process in the presence of the azo-ligand, involving comproportionation of Cu^0 and Cu^{II} , is generally utilized to obtain radical dinuclear complexes^[125]. A similar reaction pathway for the heterotetranuclear radical abcp complex was found to be ineffective due to the formation of a mixture of products and the instability at higher temperature. To isolate the radical complex, we have employed an electrochemical experiment in argon atmosphere. The paramagnetic complex was obtained from bulk electrolysis of the diamagnetic complex at mercury with the appropriate amount of dc current, using an excess of Bu_4NBF_4 as electrolyte in dichloromethane. After complete electrolysis, as indicated by the polarographic maxima (Figure 4.2.3), the solution was taken out from the electrochemical cell, maintaining an inert atmosphere, and then dried under reduced pressure to yield a brown solid of complex $[\mathbf{1}](\text{BF}_4)$. The stability of the formed paramagnetic substance in solution was checked by measuring polarographic waves after certain intervals (Figure 4.2.4). As the complex was found to be considerably stable in solution under argon atmosphere, repeated recrystallization at -4°C was done to remove all excess of electrolyte to have a pure crystalline material.

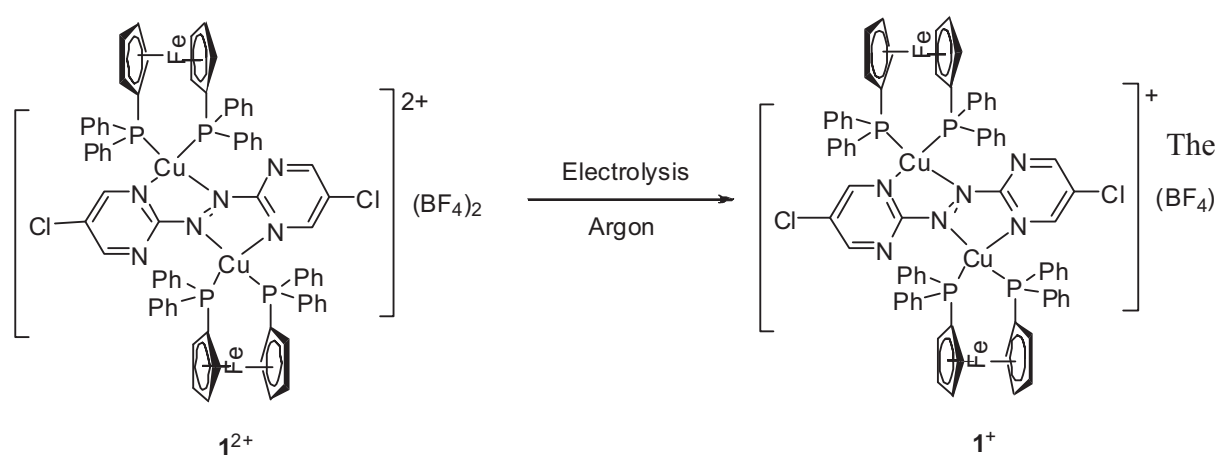


Figure 4.2.2. Electrochemical conversion of $[\mathbf{1}](\text{BF}_4)_2$ to $[\mathbf{1}](\text{BF}_4)$.

The heterotetranuclear paramagnetic complex cation was characterized by a peak at $m/z = 1488.05$ in the mass spectrum, measured by the ESI method with positive ion polarity (calculated $m/z = 1488.05$). The complex was crystallized in inert atmosphere by liquid phase diffusion of dry hexane to a dichloromethane solution of the complex. After few days, brown single crystals had grown inside thin glass tubes. The cell parameters, calculated from X-ray diffraction data, were different from those of the crystals of $[\mathbf{1}](\text{BF}_4)_2$ and was identified as a new crystal of a different molecular formula. A detailed study of the crystal structure is given in Section 4.3.1.

The heterodinuclear complex, $[(\mu\text{-abpy})\{\text{Cu}(\text{dipf})_2\}](\text{BF}_4)_2$, **[2]**(BF_4) was obtained by a similar procedure for **[1]**(BF_4)₂ but with a 1:1 mixture of abpy and the metal precursor complex $[\text{Cu}(\text{dippf})(\text{CH}_3\text{CN})_2](\text{BF}_4)$ in dichloromethane^[125]. The detailed characterization is provided in the Experimental Section.

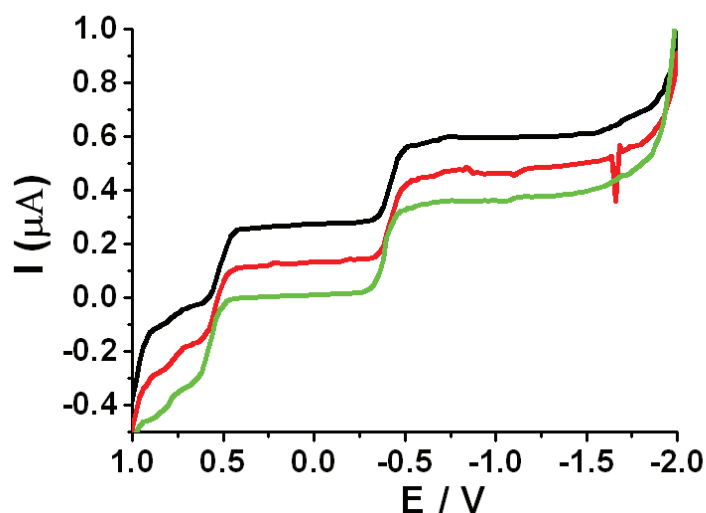


Figure 4.2.3. Polarography of 0.94 mM $[(\mu\text{-abcp})\{\text{Cu}(\text{dppf})_2\}](\text{BF}_4)_2$ **[1]**(BF_4)₂ in CH_2Cl_2 / Bu_4NBF_4 (top), after reduction by 0.5 F/mol (middle) and after reduction by 0.94 F/mol (bottom) (All polarograms were corrected for partial CH_2Cl_2 evaporation during measurements).

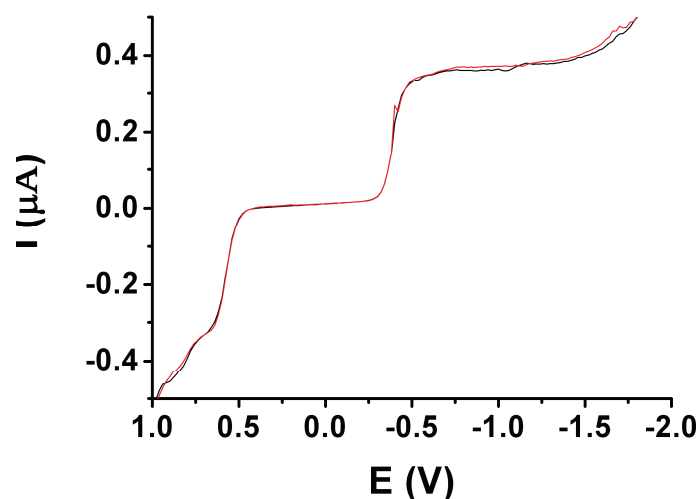


Figure 4.2.4. Polarography of 0.94 mM $[(\mu\text{-abcp})\{\text{Cu}(\text{dppf})_2\}](\text{BF}_4)_2$ **[1]**(BF_4)₂ in CH_2Cl_2 / Bu_4NPF_6 immediate after reduction by 0.94 F/mol and after 15 minutes.

4.3. Crystal structure

4.3.1. Crystal structure of $[1](BF_4)_2$ and $[1](BF_4)$

Green, air-stable single crystals of $1(BF_4)_2$ were grown at $-4^\circ C$ by slow diffusion of hexane into a dichloromethane solution of the complex. The complex crystallized in triclinic space group $P\bar{1}$. Two dichloromethane molecules are incorporated in each unit cell during the crystallization process. The important bond lengths and angles are given in Table 4.3.1.1 in comparison to those of reported structures.

In the X-ray structure of $1(BF_4)_2$, two CuP_2N_2 coordination spheres have similar distorted tetrahedral geometry around the Cu centers. Two CuP_2N_2 five-membered ring chelates share a common edge (Figure 4.3.1.1). The Cu centres are bridged by abcp at a distance of 4.8 Å. Fe centres were found at a distance of 12.5 Å and the Fe-Cu distance was found at 4.06 Å. The bite angles of dppf and abcp around the Cu centers are $109.79(6)^\circ$ and $76.92(18)^\circ$, respectively. Planar five-membered ring chelation with a comparatively smaller bite angle of $76.92(18)^\circ$ is observed by the NCNN S-frame orientation of the abcp ligand.

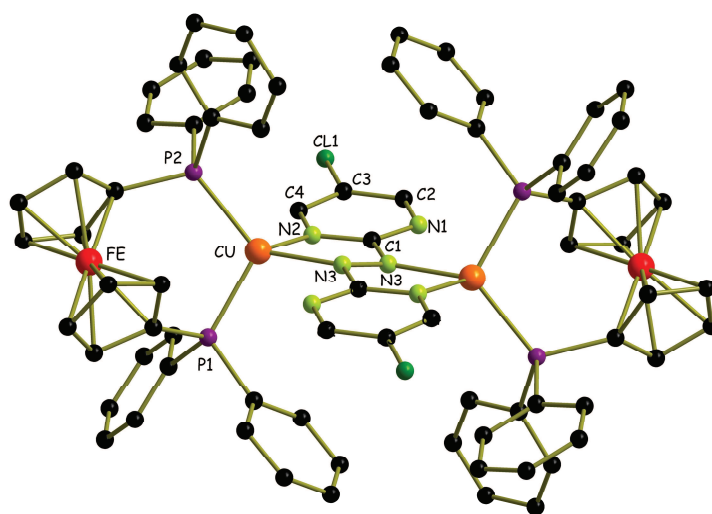


Figure 4.3.1.1. Single crystal X-ray molecular structure of the complex dication $[(\mu\text{-abcp})\{Cu(dppf)\}_2]^{2+}$ in the crystal of $[1](BF_4)_2 \times 2CH_2Cl_2$. Two BF_4^- counter anions and two dichloromethane molecules are omitted for clarity.

Cu- N_{azo} bonds at $2.014(4)$ Å were found to be shorter than the Cu- N_{py} bonds ($2.054(5)$ Å) due to the higher π -acceptor effect of azo N donors vs. pyrimidine N donors. The N-N bond length found at $1.308(9)$ Å, is in the expected range for non-reduced abcp^[28]. The azo bond length is shorter when compared to one-electron reduced azo bond, $1.345(7)$ Å, reported for $[Cu(abcp)(PPh_3)_2](BF_4)$ ^[28]. The azo bond length in the free ligand has increased by 0.078 Å on twofold $[Cu(dppf)]^+$ coordination. The observation can be explained by effective π -back-

donation from $d^{10} \text{Cu}^I$ centres to the empty π^* molecular orbital of abcp ($\sigma^2\pi^2\pi^*$). The metallation effect was also reflected by the C-N bond lengths which have shortened by 0.036 Å. Electron density transfer from the metal to the azo-centered π^* molecular orbital causes the shortening of C-N_{azo} bond lengths. The Cu-P bond lengths are Cu-P1 = 2.246(2) and Cu-P2 = 2.273(2) Å. The small torsional angle (15.0(8)°) in the N3-N3-C1-N2 frame suggested the planar like orientation of the abcp ligand. The dihedral angles are N3-N3-C1-N1 = 164.9(6)° and N3-N3-C1-N2 = 15.0(8)°.

Air-sensitive crystals of $[\mathbf{1}](\text{BF}_4)$ were taken from the capillaries and immediately covered with a layer of paraffin oil. A selected single crystal was mounted in a liquid nitrogen stream for the diffraction measurement. The crystal was analyzed in monoclinic space group $P2_1/c$. In the crystal structure of the radical complex $\mathbf{1}(\text{BF}_4)$, two crystallographically different molecules were found in each unit cell (Figure 4.3.1.2).

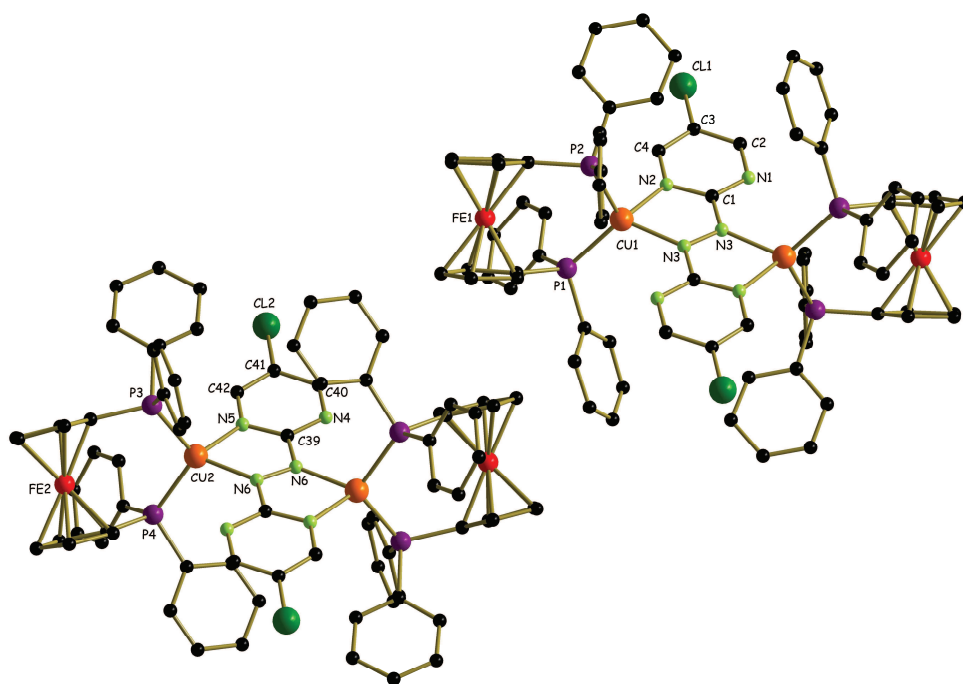


Figure 4.3.1.2. Single crystal X-ray molecular structure of two crystallographically independent radical cations $[(\mu\text{-abcp})\{\text{Cu}(\text{dppf})\}_2]^+$ in the crystal of $[\mathbf{1}](\text{BF}_4) \times \text{CH}_2\text{Cl}_2$. One BF_4^- counter anion and one dichloromethane molecule have been omitted for clarity.

The azo bond lengths in these two complexes were found at 1.348(11) Å and 1.351(12) Å. The azo bond length had increased by 0.043-0.048 Å in this radical form relative to the diamagnetic form. The Cu-N bond lengths have also increased compared to the non-reduced form. The azo bond lengths are comparable to that of the reported crystal structure (1.345(7) Å) for the complex $[(\mu\text{-abcp})\{\text{Cu}(\text{PPh}_3)_2\}_2](\text{PF}_6)$. The C-N(azo) bond lengths have further

decreased to 1.361(9)-1.368(9) Å. Important bond lengths, bond angles and dihedral angles are compared in Table 4.3.1.1.

Table 4.3.1.1 Comparison of structural parameters [distance (Å), angle, torsional angle (°)].

Bonds	[1](BF ₄) ₂ × 2CH ₂ Cl ₂	[1](BF ₄) × CH ₂ Cl ₂		[(μ-abcp) {Cu(PPh ₃) ₂ } ₂](PF ₆) ^[28]
N-N	N3-N3 1.308(9)	N3-N3 1.348(11)	N6-N6 1.351(12)	N2-N2' 1.345(7)
Cu-N	Cu-N2 2.054(5) Cu-N3 2.014(4)	Cu1-N2 2.089(6) Cu1-N3 2.017(6)	Cu2-N5 2.065(6) Cu2-N6 2.003(6)	Cu1-N1 2.098(3) Cu1-N2' 2.045(3)
Cu-P	Cu-P1 2.246(2) Cu-P2 2.273(2)	Cu1-P1 2.245(2) Cu1-P2 2.258(2)	Cu2-P3 2.234(2) Cu2-P4 2.246(2)	Cu1-P1 2.264(1) Cu1-P2 2.246(1)
Cu-Cu	4.8013(3)	4.8223(1)	4.8016(1)	4.8656(7)
Fe-Fe	12.4578(7)	12.8240(3)	12.3462(3)	n.a
C-N	C1-N3 1.403(7) C1-N1 1.330(7)	C1-N3 1.361(9) C1-N1 1.333(9)	C39-N6 1.368(9) C39-N4 1.361(9)	C1-N2 1.363(5) C1-N3 1.344(5)
C-N	C1-N2 1.348(7) C2-N1 1.335(8) C4-N2 1.338(7)	C1-N2 1.368(9) C2-N1 1.342(10) C4-N2 1.328(10)	C39-N5 1.368(9) C40-N4 1.323(11) C42-N5 1.331(10)	C1-N1 1.360(5) C4-N3 1.322(6) C2-N1 1.377(5)
C-C	C2-C3 1.390(9) C3-C4 1.369(8)	C2-C3 1.424(11) C3-C4 1.376(10)	C40-C41 1.397(12) C41-C42 1.374(10)	C4-C3 1.402(6) C2-C3 1.379(6)
N-Cu-N	N2-Cu-N3 76.92(18)	N2-Cu1-N3 77.1(2)	N5-Cu2-N6 77.9(2)	N1-Cu1-N2' 76.58(14)
P-Cu-P	P1-Cu-P2 109.79(6)	P1-Cu1-P2 110.16(7)	P3-Cu2-P4 111.07(8)	P1-Cu1-P2 124.10(5)
C-N-N	C1-N3-N3 111.8(5)	C1-N3-N3 113.5(7)	C39-N6-N6 111.9(8)	C1-N2-N2' 113.6(4)
N-C-N	N2-C1-N3 117.5(5)	N2-C1-N3 118.8(6)	N5-C39-N6 119.8(6)	N1-C1-N2 119.2(4)
Cu-N-N	Cu-N3-N3 119.0(5)	Cu1-N3-N3 118.3(6)	Cu2-N6-N6 118.6(7)	Cu1-N2'-N2 117.8(4)
N-N-C-N	N3-N3-C1-N1 164.9(6) N3-N3-C1-N2 15.0(8)	N3-N3-C1-N1 176.8(7) N3-N3-C1-N2 3.8(11)	N6-N6-C39-N4 174.0(8) N6-N6-C9-N5 6.2(11)	N2-N2-C1-N3 174.6(4) N2-N2-C1-N1 6.5(6)

4.3.2. Crystal structure of [2](BF₄)

Dark-violet single crystals of **2**(BF₄) were grown by gas phase diffusion of hexane into a dichloromethane solution, separated by a thin glass wall inside a sealed tube. After few weeks, single crystals had grown on the glass wall. The solvents were taken out from the tube to separate single crystals from solvent. X-ray single crystal diffraction data showed that the complex **2**(BF₄) crystallized in monoclinic space group P2₁/c. The crystallographic data are given in Table 4.3.2.1. Important bond lengths and angles are given in Table 4.3.2.1.

The [Cu(dippf)]⁺ was found to bind abpy through expected five-membered ring chelation leading to formation of a CuP₂N₂ coordination sphere (4.3.2.1). The geometry around the Cu centre is distorted tetrahedral with one large chelate angle P1-Cu-P2 = 107.54(2)° and another small chelate angle N2-Cu-N4 = 76.44(6)°. The N2-N3 bond length was found at 1.275(2) Å, corresponding to the non-reduced azo form and only elongated by 0.001 Å from that of the reported complex {(μ-abpy)Cu(dppf)}(BF₄)^[125]. The better π-acceptance property of abcp over abpy is reflected in the change of N-N bond length. In the abcp complexes, the N-N bond length has increased by 0.078 Å on bis-chelation in non-reduced form and 0.115-0.121 Å in reduced state. But, in abpy complexes the changes are 0.020 and 0.071 Å respectively. The N-N bond length found in various Cu-azo complexes and their respective changes on complexation are given in Table 4.3.2.2.

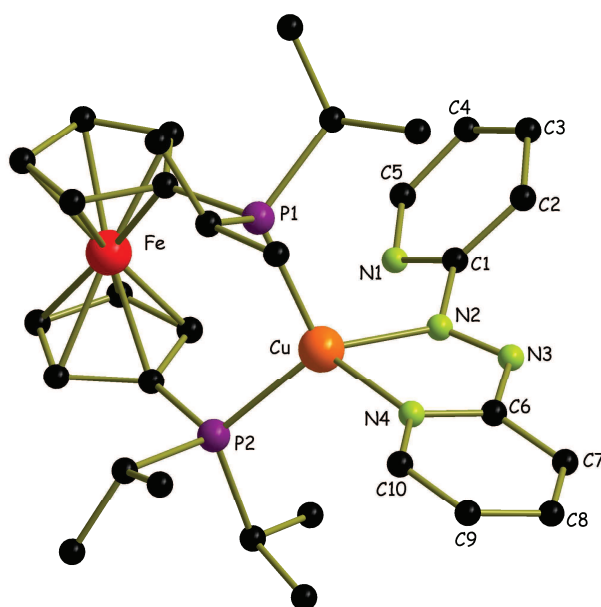


Figure 4.3.2.1. Single crystal X-ray molecular structure of the complex cation, [(μ-abpy)Cu(dippf)]⁺ in the crystal of [2](BF₄). One counter anion, BF₄⁻, is omitted for clarity.

Table 4.3.2.1. Selected bond lengths (Å) and bond angles (°) for $[(\mu\text{-abpy})\text{Cu}(\text{dippf})](\text{BF}_4)$ [2](BF₄)

Bonds	Lengths	Bonds	Lengths
N2-N3	1.275(2)	C7-C8	1.381(3)
Cu-N2	2.009(2)	C8-C9	1.389(3)
Cu-N4	2.107(1)	C9-C10	1.388(2)
N4-C6	1.347(2)	C10-N4	1.349(2)
C6-N3	1.410(2)	Bonds	Angles
N2-C1	1.434(2)	N2-Cu-N4	76.44(6)
C1-N1	1.332(2)	P1-Cu-P2	107.54(2)
P1-Cu	2.264(1)	N2-N3-C6	112.03(14)
P2-Cu	2.256(1)	C1-N2-N3	113.14(14)
C6-C7	1.397(2)	N4-C6-N3	118.57(15)

Table 4.3.2.2. Azo bond lengths in abpy and abcp complexes.

Compound	N-N Distances (Å)	$\Delta(\text{N-N})$ (Å) ^{a)}	Reference
abcp	1.230(2)	n.a.	30
$\{(\mu\text{-abcp})[\text{Cu}(\text{dppf})]_2\}(\text{BF}_4)_2$ [1](BF ₄) ₂	1.308(9)	0.078	This work
$\{(\mu\text{-abcp})[\text{Cu}(\text{dppf})]_2\}(\text{BF}_4)$ [1](BF ₄)	1.348(11)	0.118	This work
	1.351(12)	0.121	
$[(\mu\text{-abcp})\{\text{Cu}(\text{PPh}_3)_2\}_2](\text{PF}_6)$	1.345(7)	0.115	28
abpy	1.246(2)	n.a.	126
$\{(\mu\text{-abpy})\text{Cu}(\text{dppf})\}(\text{BF}_4)$	1.274(3)	0.028	124
$\{(\mu\text{-abpy})\text{Cu}(\text{dippf})\}(\text{BF}_4)$ [2](BF ₄)	1.275(2)	0.029	This work
$\{(\mu\text{-abpy})[\text{Cu}(\text{PPh}_3)_2]_2\}(\text{BF}_4)$	1.248(11)	0.020	127
$\{(\mu\text{-abpy})[\text{Cu}(\text{dppf})]_2\}(\text{BF}_4)$	1.317(5)	0.071	124

^{a)} $\Delta(\text{N-N})$ = Change in azo bond length on complexation.

4.4. Electrochemistry

Cyclic voltammograms were measured for complexes **[1](BF₄)₂** and **[2](BF₄)** in CH₂Cl₂ / 0.1 M Bu₄NPF₆ at room temperature with 100 mV/s scan rate and compared with free ligands and reported complexes in Table 4.4.1. The abcp ligand can be reduced in two one-electron steps at -1.01 and -1.49 (qr) V versus ferrocene/ferrocenium in acetonitrile^[30]. The expected two reductions were also observed for the corresponding heterotetranuclear metal complex **[1](BF₄)₂**, but at less negative potentials of -0.24 V and -1.20 V versus ferrocene/ferrocenium (Figure 4.4.1).

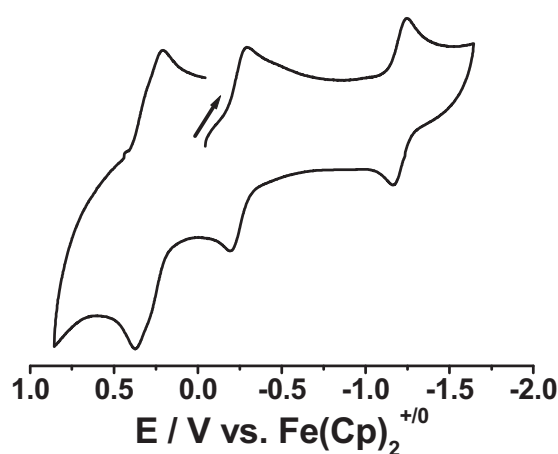


Figure 4.4.1. Cyclic voltammogram of **[1](BF₄)₂** in CH₂Cl₂ / 0.1 M Bu₄NPF₆ at room temperature with 100 mV/s scan rate.

The first reduction potential has decreased by 0.77 V and the second reduction potential by 0.29 V in the complex relative to the free abcp ligand. As a result, twofold increase in the difference between the first and the second reduction potentials $[(\Delta E = E_{1/2}(\text{red1-red2}) \text{ in complex} - E_{1/2}(\text{red1-red2}) \text{ in abcp}]$ observed on bis-chelation of **[Cu(dppf)]⁺** complex fragments. The unusual stability of the one-electron reduced product, **1⁺**, is also supported by $K_c > 10^{16}$ for the azo-aromatic anion radical species.

The ferrocene based two-electron oxidation wave, corresponding to two dppf units, was found at +0.3 V. The broad nature of the oxidation wave was further investigated by a differential pulse voltammetric experiment in CH₂Cl₂ / 0.1 M Bu₄NPF₆ at room temperature with 70 mV/sec scan rate. The differential pulse voltammogram (Figure 4.4.2.) showed two one-electron oxidations at slightly different potential of +0.496 and +0.424 V (not calibrated with respect to Fc⁺⁰) instead of one as found in the cyclic voltammogram. The complex **[1](BF₄)₂** is an

unusual example showing ferrocene oxidations at different potentials, having a K_c value of 16.6 for the $\text{Fe}^{\text{II}}/\text{Fe}^{\text{III}}$ mixed valent intermediate.

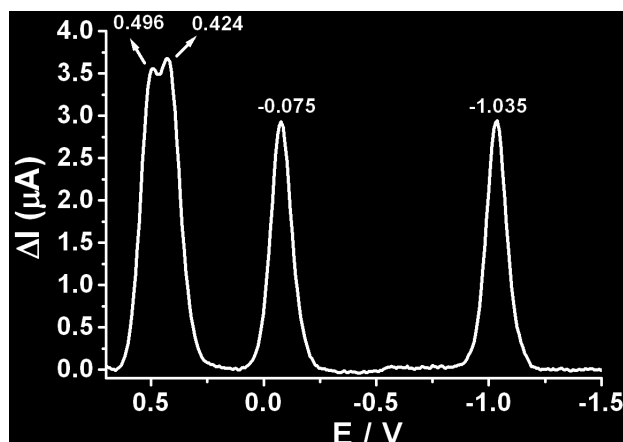


Figure 4.4.2. Differential pulse voltammogram of $[1](\text{BF}_4)_2$ in $\text{CH}_2\text{Cl}_2 / 0.1 \text{ M Bu}_4\text{NPF}_6$ at room temperature with 70 mV/sec scan rate (potentials are not calibrated).

The cyclic voltammogram of complex $2(\text{BF}_4)$ is very similar to that of the reported dppf analogue, $[(\mu\text{-abpy})\text{Cu}(\text{dppf})](\text{BF}_4)^{[124]}$. The expected one-electron reduction occurred at a 0.2 V positively shifted potential. This is due to the less π back donation from $d^{10}\text{Cu}$ to the azo centre of abpy. The one-electron ferrocene based oxidation was also found at $+0.41 \text{ V}$, corresponding to $\text{Fe}^{\text{II}}/\text{Fe}^{\text{III}}$ couple in dppf. Anodic peak potential for irreversible second one-electron reduction has also anodically shifted to -2.18 V . The redox potentials are given in Table 4.3.1.

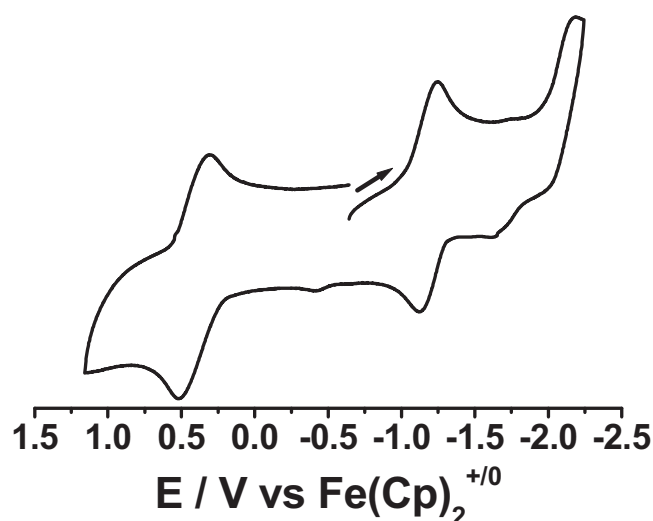


Figure 4.4.3. Cyclic voltammogram of $[(\mu\text{-abpy})\text{Cu}(\text{dippf})](\text{BF}_4)$ $[2](\text{BF}_4)$ in $\text{CH}_2\text{Cl}_2 / 0.1 \text{ M Bu}_4\text{NPF}_6$ at room temperature with 100 mV/s scan rate.

Table 4.4.1. Comparison of the redox potentials^{a)} obtained from cyclic voltammetry.

Compound	E _{ox}	E _{red 1}	E _{red 2}	Solvent	Reference
abcp	n.d.	-1.01	-1.49(qr)	CH ₃ CN	30
[(μ-abcp){Cu(PPh ₃) ₂ } ₂](PF ₆) ₂	+1.42(i)	+0.06	-0.75	CH ₃ CN	30
[(μ-abcp){Cu(dppf)} ₂](BF ₄) ₂ [1](BF ₄) ₂	+0.30 ^{b)}	-0.24	-1.20	CH ₂ Cl ₂	This work
abpy	n.d.	-1.46	-2.04	CH ₂ Cl ₂	125
[(μ-abpy)Cu(dppf)](BF ₄)	+0.43	-0.98	-1.76(i)	CH ₂ Cl ₂	125
[(μ-abpy)Cu(dippf)](BF ₄) [2](BF ₄)	+0.41	-1.18	-2.18 (i)	CH ₂ Cl ₂	This work

^{a)}Potentials (V) vs. ferrocenium/ferrocene. Half-wave potentials, unless noted otherwise: (qr):quasi-reversible, (i): irreversible (peak potential given). ^{b)} Two-electron broad wave for Fe oxidation, for splitting see Figure 4.3.2.

4.5. UV-Vis-NIR spectroelectrochemistry

UV-Vis-NIR spectroelectrochemical measurements of [1](BF₄)₂ and [2](BF₄) were carried out in CH₂Cl₂ / Bu₄NPF₆ using an optically transparent thin layer electrode for all reversible oxidation and reduction processes. The complex [1](BF₄)₂ exhibited an MLCT band of the type d¹⁰πCu to π*(abcp) at 948 nm with ε = 8270 M⁻¹ cm⁻¹. Two shoulders found at 451 and 357 nm were assigned for the intraligand π to π* transition of the non reduced, metal coordinated abcp.

On first reversible one-electron reduction, the original MLCT band at 948 nm hypsochromically shifts to 800 nm and the ε value is diminished to 3830 M⁻¹ cm⁻¹. The shift of the MLCT band and its lower intensity is due to the lower wavelength and less favored transition for d¹⁰πCu to singly occupied π* molecular orbital of -N=N-. In addition, a band arises at 566 nm (ε = 5170 M⁻¹ cm⁻¹) which could also be attributed to a metal- to -ligand charge transfer transition. The intra-ligand charge transfer band is hypsochromically shifted to 411 nm (ε = 11300 M⁻¹ cm⁻¹).

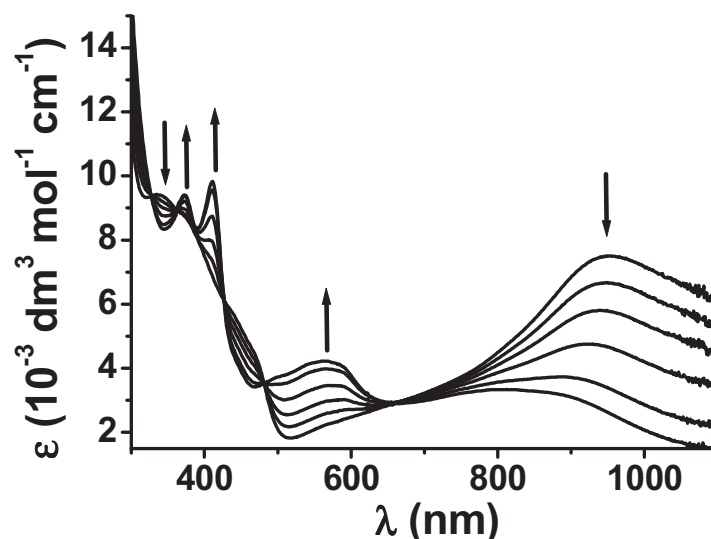


Figure 4.5.1. UV-Vis-NIR spectroelectrochemistry for the reduction $\{(\mu\text{-abcp})[\text{Cu}(\text{dppf})_2]_2\}^{2+}$ to $\{(\mu\text{-abcp})[\text{Cu}(\text{dppf})_2]_2\}^+$ in $\text{CH}_2\text{Cl}_2 / \text{Bu}_4\text{NPF}_6$ in OTTLE cell.

On further reduction to the neutral species at a potential of -1.20 V versus ferrocene/ferrocenium, the MLCT band diminished completely due to full occupancy in π^* molecular orbital of the azo-center. Also the intraligand charge transfer transition disappeared.

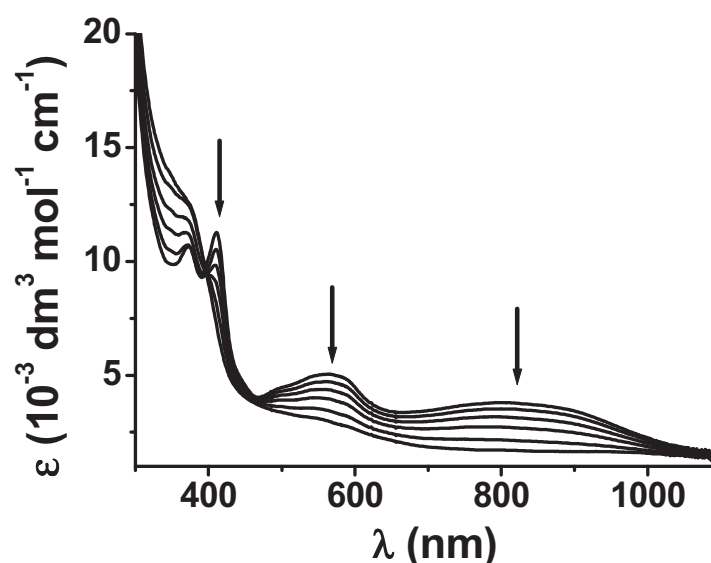


Figure 4.5.2. UV-Vis-NIR spectroelectrochemistry for the reduction $\{(\mu\text{-abcp})[\text{Cu}(\text{dppf})_2]_2\}^+$ to $\{(\mu\text{-abcp})[\text{Cu}(\text{dppf})_2]_2\}$ in $\text{CH}_2\text{Cl}_2 / \text{Bu}_4\text{NPF}_6$.

Though the ferrocene-based oxidations were observed at different potentials in differential pulse voltammetry, it was not possible to monitor them separately in spectroelectrochemical cell. I have observed two different trends in the spectra measured over the whole range of oxidation processes. They were considered as the first and second oxidation occurring during

the measurements. On first oxidation, the long wavelength MLCT band slightly shifts to 910 nm ($\epsilon = 11338 \text{ M}^{-1} \text{ cm}^{-1}$) and shorter wave length charge transfer shoulder to 445 nm. The intraligand transitions bathochromically shifts to 367 nm ($\epsilon = 8090 \text{ M}^{-1} \text{ cm}^{-1}$).

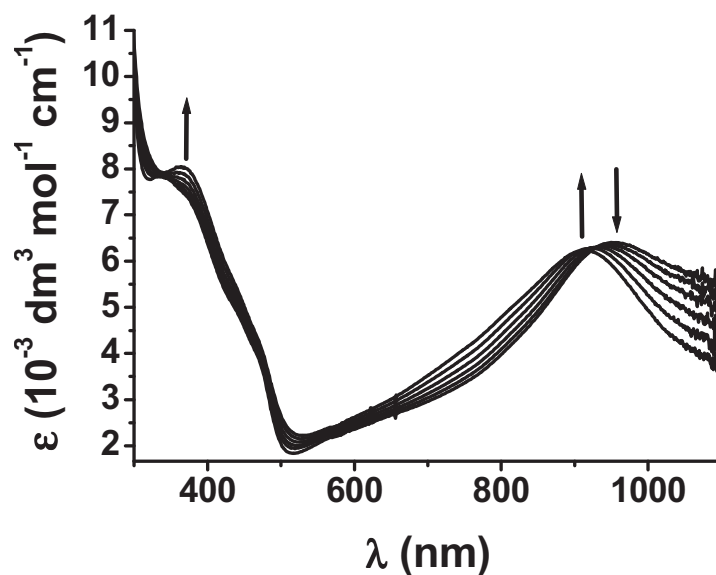


Figure 4.5.3. UV-Vis-NIR spectroelectrochemical oxidation of $\{(\mu\text{-abcp})[\text{Cu}(\text{dppf})_2]_2\}^{2+}$ to $\{(\mu\text{-abcp})[\text{Cu}(\text{dppf})_2]_2\}^{3+}$ in $\text{CH}_2\text{Cl}_2 / \text{Bu}_4\text{NPF}_6$.

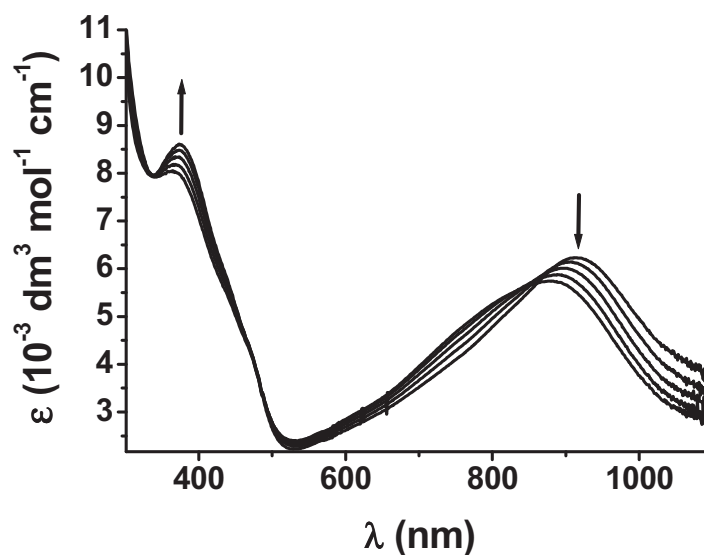


Figure 4.5.4. UV-Vis-NIR spectroelectrochemical oxidation of $\{(\mu\text{-abcp})[\text{Cu}(\text{dppf})_2]_2\}^{3+}$ to $\{(\mu\text{-abcp})[\text{Cu}(\text{dppf})_2]_2\}^{4+}$ in $\text{CH}_2\text{Cl}_2 / \text{Bu}_4\text{NPF}_6$.

On second oxidation, the MLCT band further shifts hypsochromically to 880 nm ($\epsilon = 5750 \text{ M}^{-1} \text{ cm}^{-1}$) and 435 nm (sh). Shift is also observed for the intraligand transition band to 375 nm (ϵ

= 8640 M⁻¹ cm⁻¹). All spectroelectrochemical data along with that of reported compounds are given in Table 4.5.1.

UV-Vis spectroelectrochemical data of abpy, 2²⁺, 2⁺, 2, and related reported complexes have been compared in Table 4.4.1. Complex ion 2⁺ shows Cu to π* (abpy) transition band at 563 nm and intra ligand charge transfer band at 337 nm. For the reported complex [(abpy)Cu(dppf)]⁺, MLCT bands are found at 630 nm and 530 nm^[125]. The sharp band at 350 nm was assigned to a typical abpy-based intra-ligand transition.

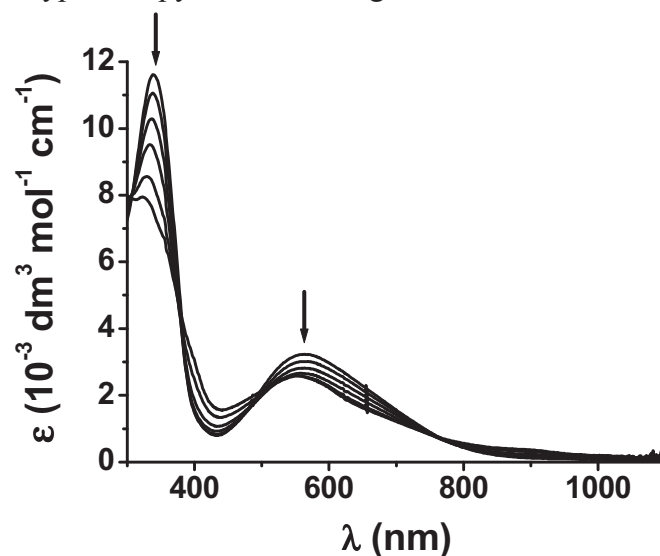


Figure 4.5.5. UV-Vis-NIR spectroelectrochemistry for the reduction [(abpy)Cu(dippf)]⁺ to [(abpy)Cu(dippf)] in CH₂Cl₂ / Bu₄NPF₆.

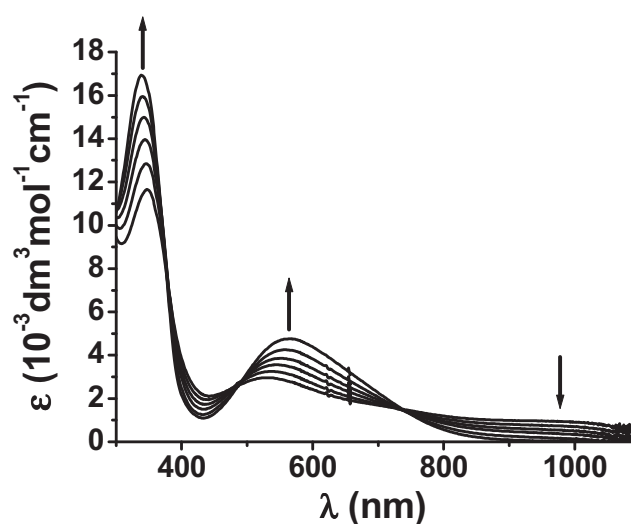


Figure 4.5.6. UV-Vis-NIR spectroelectrochemistry for the oxidation of [(abpy)Cu(dippf)]⁺ to [(abpy)Cu(dippf)]²⁺ in CH₂Cl₂ / Bu₄NPF₆ in OTTLE cell.

The red shift of MLCT transition on changing coligand from dippf to dppf is possibly due to the higher electron donating capability of alkylphosphine over arylphosphine. On oxidation,

only the intraligand charge transfer band shifts to higher wavelength and the Cu to π^* (abpy) transition band remains unchanged, indicating a very less influence of ferrocene based oxidation on MLCT. In the reduced species **2**, a blue shift by 12 nm is observed for the Cu to $\pi^*(abpy^-)$ transition.

Table 4.5.1. Data from UV-Vis spectroelectrochemistry^a of [1](BF₄)₂ and [2](BF₄).

	λ_{\max} / nm (ϵ / 10^{-3} M ⁻¹ cm ⁻¹)	Reference
abcp	455(0.37), 286(26.0)	30
abcp ⁻	555(sh), 477(sh), 404(44), 350(sh)	30
abcp ²⁻	457(sh), 352(45)	30
{(μ-abcp)[Cu(PPh ₃) ₂] ₂ } ²⁺	93 (1.1), 870(0.8), 365(1.54)	30
{(μ-abcp)[Cu(PPh ₃) ₂] ₂ } ⁺	700(0.63), 560(0.9), 403(2.6), 373 (2.6)	30
{(μ-abcp)[Cu(PPh ₃) ₂] ₂ }	515(sh), 363(2.8)	This work
{(μ-abcp)[Cu(dppf) ₂] ₂ } ⁴⁺	880(5.75), 435(sh), 375(8.64)	This work
{(μ-abcp)[Cu(dppf) ₂] ₂ } ³⁺	910(6.22), 445(sh), 367(8.09)	This work
{(μ-abcp)[Cu(dppf) ₂] ₂ } ²⁺	948(8.27), 451(sh), 347(sh), 260(sh)	This work
{(μ-abcp)[Cu(dppf) ₂] ₂ } ⁺	800(3.83), 566(5.17), 411(11.33), 372(10.78)	This work
{(μ-abcp)[Cu(dppf) ₂] ₂ }	500(sh), 372(sh), 270(sh)	This work
abpy	312(8.7), 470(0.9)	128
abpy ⁻	286(sh), 360(sh), 408(26.5), 548(2.6)	128
[(abpy)Cu(dppf)] ²⁺	862(sh), 479(2.9)	124
[(abpy)Cu(dppf)] ⁺	630(sh), 530(2.6), 350(8.8)	124
[(abpy ⁻)Cu(dppf)]	530(3.3), 389(6.9)	124
[(abpy)Cu(dippf)] ²⁺	564(4.81), 338(7.06)	This work
[(abpy)Cu(dippf)] ⁺	563(3.27), 337(11.66)	This work
[(abpy)Cu(dippf)]	551(2.65), 323(8.03)	This work

^a From spectroelectrochemistry in CH₂Cl₂ / 0.1 M Bu₄NPF₆.

4.6. EPR spectroscopy

EPR spectrum was measured for electrochemically produced one electron reduced paramagnetic heterotetranuclear complex $\{(\mu\text{-abcp})[\text{Cu}(\text{dppf})_2]_2\}^{\cdot+}$, using Bu_4NPF_6 as electrolyte in dichloromethane at 298 K. The isotropic g value measured at 2.0091 indicated a predominantly ligand centred EPR signal. A very little shift in g value is observed in comparison to the reduced free abcp ligand (abcp \cdot^- , $g = 2.0041$, from reduction with K in THF solution at 298 K) and the reported paramagnetic complex, $\{(\mu\text{-abcp})[\text{Cu}(\text{PPh}_3)_2]_2\}^{\cdot+}$ ($g = 2.0071$). This proves that the first one electron reduction corresponds to the addition of an electron in π^* molecular orbital of the azo-centre. Insufficient hyperfine resolution restricted computer simulation to obtain individual coupling constants from EPR active nuclei.

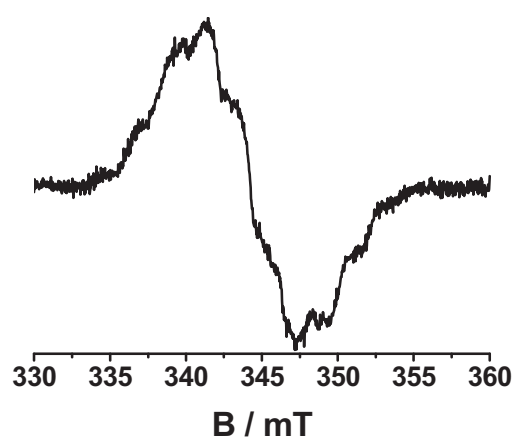


Figure 4.6.1. EPR spectrum of $\{(\mu\text{-abcp})[\text{Cu}(\text{dppf})_2]_2\}^{\cdot+}$ in $\text{CH}_2\text{Cl}_2 / 0.1 \text{ M Bu}_4\text{NPF}_6$.

4.7. Conclusion

First structural characterization of both the radical and non-radical states of a azo-bridged oligonuclear complex have been reported in this chapter. An electrochemical method has enabled the synthesis of azo anion radical intermediate from the diamagnetic species. The heterotetranuclear diamagnetic complex is an unusual example showing ferrocene oxidations at different potentials, having a K_c value of 16.6 for the $\text{Fe}^{\text{II}}\text{Fe}^{\text{III}}$ mixed valent intermediate. These two separate oxidations indicate that the metal-metal interactions at a longer distance ($>12 \text{ \AA}$) stabilizes $\text{Fe}^{\text{II}}\text{Fe}^{\text{III}}$ mixed valent species during the electrochemical process. Charge transfer transitions in the NIR region have been studied with the aid of spectroelectrochemical experiments. The effect of coligand on azo-metal binding is found to be very less as seen from the studied crystal structure, electrochemistry and spectroelectrochemistry.

Chapter 5

Facilitated reduction *and* oxidation of $\{[\text{Ru}(\text{NH}_3)_5]_4(\mu_4\text{-TCNX})\}^{8+}$ by changing from TCNX = TCNQ to TCNQF₄

5.1. Introduction

7,7,8,8,-Tetracyano-*p*-benzoquinodimethane, TCNQ, and its derivatives continue to be applied in the construction of new materials with special optical, electrical and magnetic properties^[34-37, 129-132]. In addition to layered systems and coordination polymers^[129-138], there have also been reports of discrete complexes with different nuclearity which were subjected to physical characterization^[34]. Coordinative saturation in tetranuclear complexes $[(\mu_4\text{-TCNQ})(\text{ML}_n)_4]$ was described in a dichotomous fashion, involving either little^[36,140] or extensive^[141-144] intramolecular electron transfer, corresponding to innocent or non-innocent behaviour^[145] of the TCNQ bridging ligand towards different kinds of metal complex fragments, ML_n . In order to probe such effects in more detail from the ligand side, I have now prepared and analyzed in a comparative way the TCNQF₄ analogue $\{[(\mu_4\text{-TCNQF}_4)\text{-Ru}(\text{NH}_3)_5]_4\}(\text{PF}_6)_8$ (**[1]**(PF₆)₈) of the well investigated^[34,36] $\{(\mu_4\text{-TCNQ})[\text{Ru}(\text{NH}_3)_5]_4\}(\text{PF}_6)_8$ (**[2]**(PF₆)₈). The inductive effects of four fluorine substituents make TCNQF₄ an even stronger π acceptor than TCNQ, the potentials for the first reduction of the free ligands are 0.13 and -0.25 V vs. ferrocenium/ferrocene. For comparison with the TCNQ parent the new $\{(\mu_4\text{-TCNQF}_4)[\text{Ru}(\text{NH}_3)_5]_4\}(\text{PF}_6)_8$ is characterized by cyclic voltammetry, IR, UV-VIS-NIR and EPR spectroelectrochemistry.

5.2. Synthesis and characterization

The green discrete tetranuclear diamagnetic complex, $\{(\mu_4\text{-TCNQF}_4)[\text{Ru}(\text{NH}_3)_5]_4\}(\text{PF}_6)_8$, was formed from a reaction of four equivalents freshly prepared $[\text{Ru}^{\text{II}}(\text{NH}_3)_5(\text{H}_2\text{O})]\text{Cl}_2$ and one equivalent TCNQF₄ in deoxygenated H₂O /Acetone mixture under exclusive argon atmosphere (Figure 5.2.1). All the spectroscopic measurements of the highly air-sensitive tetranuclear complex was carried out in absence of oxygen. The diamagnetic complex was identified from its ¹H- and ¹⁹F-NMR spectra. Two singlet lines

were found at 2.79 and 3.19 ppm in the $^1\text{H-NMR}$ spectrum for the axial and equatorial NH_3 protons. The broad ^{19}F signal from four fluorine atoms of the 2,3,5,6-tetrafluoro-7,7,8,8-tetracyano-*p*-quinodimethane (TCNQF_4) unit was observed at -147.80 ppm and a doublet signal with 710 Hz coupling constant ($^1J_{\text{P-F}}$) for the counter anions, PF_6^- , was found at -71.11 ppm.

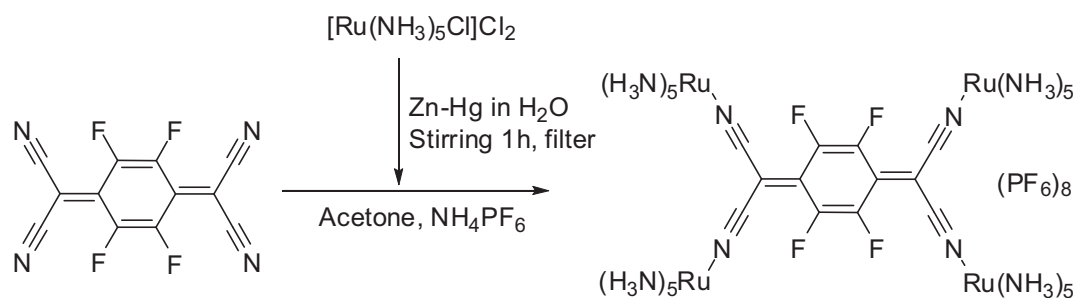


Figure 5.2.1. Synthesis of the tetranuclear complex

In the IR spectrum, two vibrational bands are expected for the tetranuclear complex from the different modes of cyano stretching. The measured IR spectrum in CH_3CN showed the expected bands at 2149 and 2099 cm^{-1} with higher intensity for the lower energy band. A long wavelength, broad band at 1022 nm was observed in the UV-Vis-NIR spectrum (measured in degassed CH_3CN), for the diamagnetic tetranuclear complex. The number of counter anions was confirmed not only from the satisfactory elemental analysis (including three acetone molecule in the formula) but also from its spectroscopic data.

5.3. Cyclic voltammetry

The cyclic voltammogram measured in $\text{CH}_3\text{CN} / 0.1 \text{ M Bu}_4\text{NPF}_6$ revealed expected two reductions (-0.45 and -0.66 V) at lower potentials compared to the non-fluorinated analogue (-0.59, -0.84 V). Instead of having two oxidation waves in the previously reported non-fluorinated derivative, it showed only one two-electron reversible oxidation wave with relatively lower positive potential (Figure 5.3.1). The one step two-electron oxidation leads to the formation of a (10+) species at +0.07 V. Both the oxidation and reductions at a comparatively lower potential clearly indicate for an appreciable amount of charge transfer from the four Ru^{II} centers to the electron-deficient π -conjugated TCNQF_4 moiety. The substitution of TCNQ by four strong electron withdrawing fluorine atoms, has decreased the difference between the oxidation and first reduction potentials by 0.26 V, leading to a smaller comproportionation constant ($K_c = 6.5 \times 10^8$) for the isolated (8+) form. The effect of the substitution was found to be more promising on the oxidation and first reduction processes

but comparatively less on the second reduction. The second reduction was positively shifted by 0.18 V and the difference between first and second reduction potential by 0.21 V. As a result, the comproportionation constant for the electrogenerated (7+) form was found less than the non-fluorinated analogue. All the electrochemical data of the obtained tetranuclear complex have been given in comparison to the non-fluorinated species in Table 5.5.1.

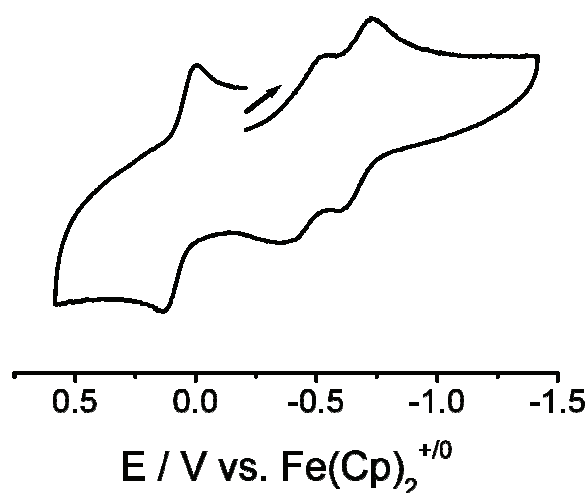


Figure 5.3.1. Cyclic voltammogram of $\{[\text{Ru}(\text{NH}_3)_5]_4(\mu_4\text{-TCNQF}_4)\}(\text{PF}_6)_8$ measured in $\text{CH}_3\text{CN} / 0.1 \text{ M Bu}_4\text{NPF}_6$ at room temperature with 100 mV/s scan.

5.4. IR spectroelectrochemistry

The complex ion (8+) exhibits in the infrared spectrum expected two C-N stretching bands (Vibrational modes B_{1u} , B_{2u} in D_{2h} symmetry)^[146,147] at 2162 (m) and 2092 (s) cm^{-1} (Figure 5.4.1). Similar spectrum (bands maxima 2155, 2099 cm^{-1}) was found for the fluoride-unsubstituted analogue^[36]. One-electron reduction of the complex leads to a slight shift of the bands maxima to lower wave numbers, 2147 and 2083 cm^{-1} (Figure 5.4.1). Noticeable is that the intensities of the bands are inverted on reduction. The large intensity of the band at 2147 cm^{-1} indicates a higher dipole moment change in the z-axis (mode B_{1u}) and a partial changed geometry in the reduced state. A more intense higher-frequency band was observed either in the electrochemically generated anion TCNQ^- or in a solution of LiTCNQ ^[146] too.

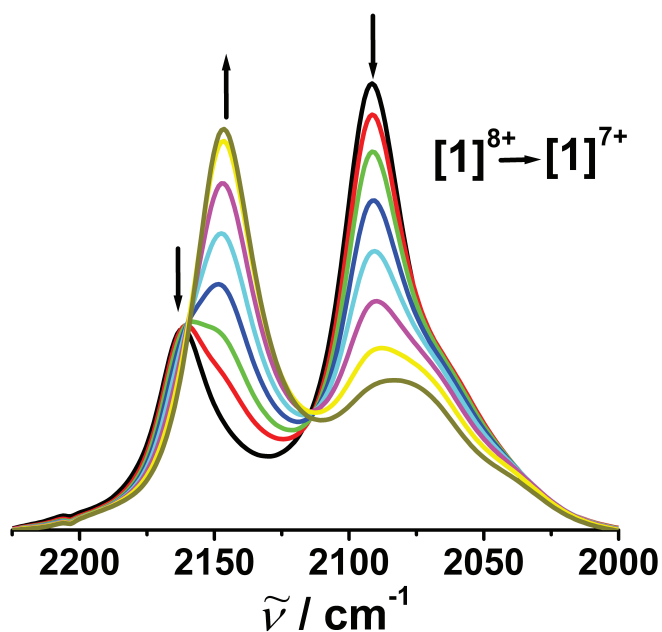


Figure 5.4.1. IR spectroelectrochemistry for the first reduction process in CH_3CN / 0.1 M Bu_4NPF_6 at 298 K

The second reduction (to 6+ state, Figure 5.4.2) results in a strong decrease of the bands intensities and in a shift to higher frequencies, 2186 and 2153 cm^{-1} . The obvious strengthening of the C-N bonds can be explained by a decreased or absent delocalization among metals and ligands in the double-reduced state^[36].

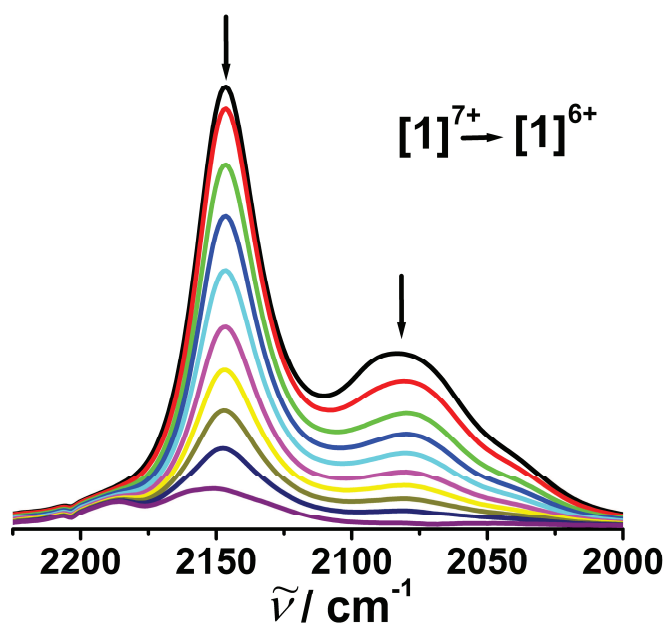


Figure 5.4.2. IR spectroelectrochemical second reduction in CH_3CN / 0.1 M Bu_4NPF_6 at 298 K.

The infrared spectrum (Figure 5.4.3) obtained on a two electron oxidation of the complex shows a bad response consisting from vibrational bands and an increased absorption over the whole infrared range, which can be ascribed to a weak electronic transition band of the highly delocalized system. Merging of the electron-transfer bands and vibrational bands make the exact determination of the bands maxima difficult. Apparently overlapping bands occur in the C-N stretching region around 2100 cm^{-1} ; in comparison, a weak band 2066 cm^{-1} and a shoulder 2142 cm^{-1} was detected for the two electron oxidized TCNQ analogue. The IR spectroelectrochemical data of the complex is given in Table 5.5.2 in comparison to the fluorine unsubstituted analogue.

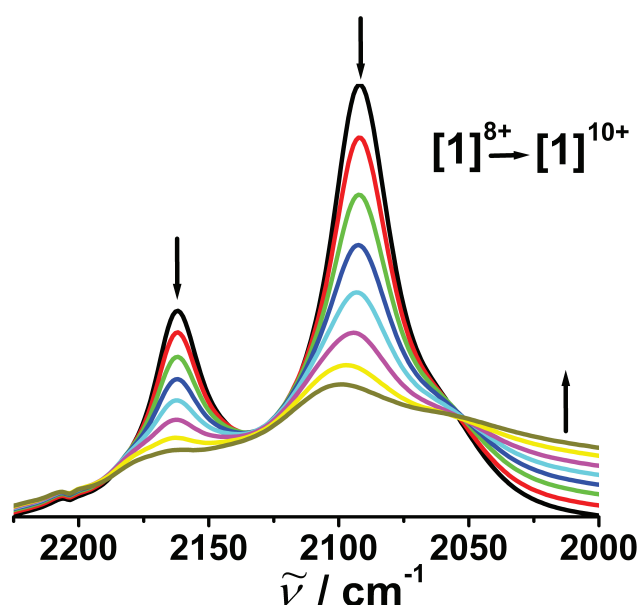


Figure 5.4.3. IR spectroelectrochemical two-electron oxidation in $\text{CH}_3\text{CN} / 0.1\text{ M Bu}_4\text{NPF}_6$ at 298 K.

5.5. UV-Vis-NIR spectroelectrochemistry

UV-Vis-NIR spectroelectrochemistry was performed for the tetranuclear complex in $\text{CH}_3\text{CN} / 0.1\text{ M Bu}_4\text{NPF}_6$ at room temperature. The complex in (8+) form showed one broad, very intense band (Figure 5.5.1) in the NIR region at 1103 nm ($\epsilon = 44400\text{ dm}^3\text{ mol}^{-1}\text{ cm}^{-1}$). In the analogous $\{[\text{Ru}(\text{NH}_3)_5]_4(\mu_4\text{-TCNQ})\}(\text{PF}_6)_8$ complex^[36], the corresponding NIR band was found at 935 nm. The bathochromic shift of the NIR band by 168 nm has occurred due to the presence of electron deficient TCNQF₄. The one-electron reduction to (7+) species was characterized by a new NIR band at 1822 nm (Figure 5.5.1). The intensity of the band at 1103 nm in the (8+) form was decreased and splitted to two shoulders at 1462 and 1191 nm.

Most likely, these two shoulders appeared due to the vibrational splitting of the parent band. The spectrum of the one electron reduced species (7+) (Figure 5.5.1) showed the decrease in intensity and the shift of the long-wavelength charge transfer bands towards the higher wavelength.

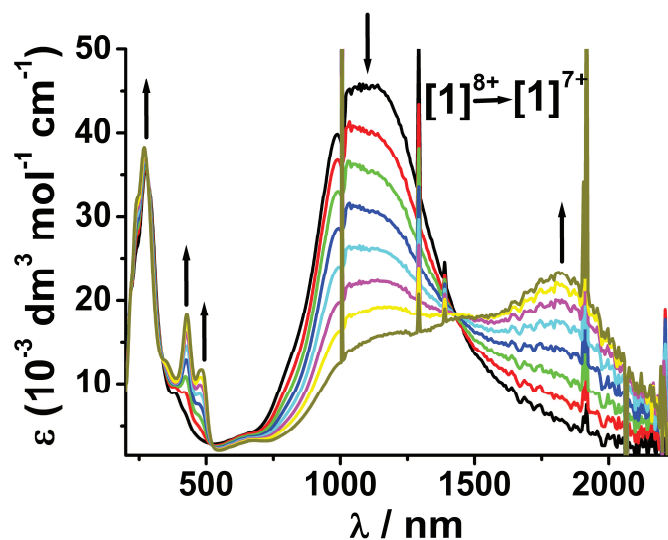


Figure 5.5.1. UV-Vis-NIR spectroelectrochemistry for the first reduction in CH_3CN / 0.1 M Bu_4NPF_6 .

On second reduction to (6+) form, the long wavelength charge transfer bands disappeared completely (Figure 5.5.2). The similar observation was also found for the non-fluorinated analogues.

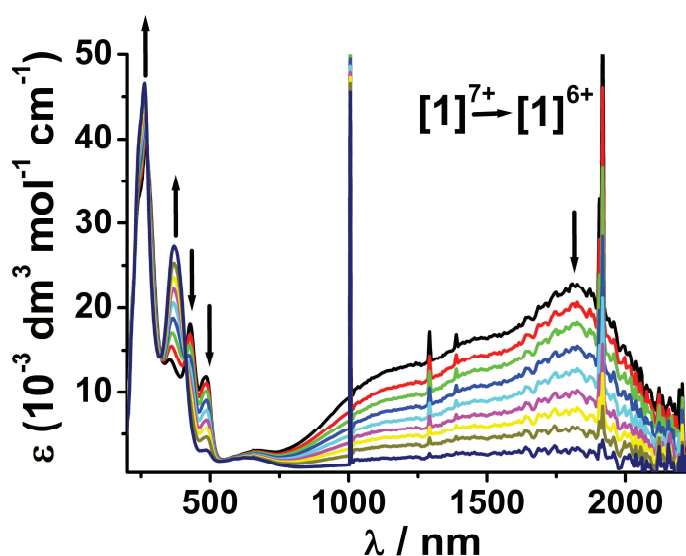


Figure 5.5.2. UV-Vis-NIR spectroelectrochemistry for the second reduction in CH_3CN / 0.1 M Bu_4NPF_6 .

On two-electron oxidation to the (10+) species, the charge transfer band is shifted hypsochromically to 880 nm and the intensity of the charge transfer transition is also lowered (Figure 5.5.3). The oxidation of the non-fluorinated complex causes the intensity decrease of the parent band at 935 nm and a new band arises at 1170 nm. All spectroscopic data of the native diamagnetic species and also of the electrogenerated oxidized and reduced species have been provided (Table 5.5.1) for the comparison with the fluorine-unsubstituted species.

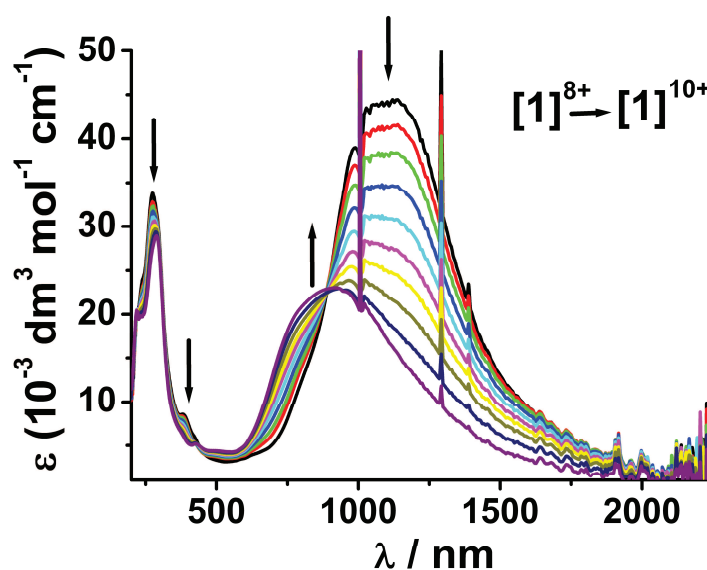


Figure 5.5.3. UV-Vis-NIR spectroelectrochemistry for the two electron oxidation process in $\text{CH}_3\text{CN} / 0.1 \text{ M Bu}_4\text{NPF}_6$.

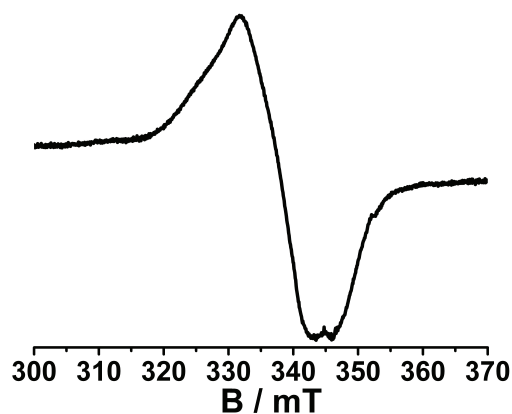
Table 5.5.1. Comparison of electrochemical and spectroscopic data.

	[1](PF ₆) ₈	[2](PF ₆) ₈ ^[36]
E _{1/2} (ox 1) /V (ΔE / mv) ^a	+0.07 (128)	+0.19 (60)
E _{1/2} (ox 2) /V (ΔE / mv) ^a	n.o.	+0.64 (110)
E _{1/2} (red 1) /V (ΔE / mv) ^a	-0.45 (166)	-0.59 (105)
E _{1/2} (red 2) /V (ΔE / mv) ^a	-0.66 (118)	-0.84 (80)
$\nu_{\text{CN}} / \text{cm}^{-1}$ ^b		
Ru ₄ TCNX ¹⁰⁺	2162 (w), 2099 (w)	2142 (sh), 2066
Ru ₄ TCNX ⁸⁺	2162 (m), 2092 (s)	2155 (s), 2099 (vs)
Ru ₄ TCNX ⁷⁺	2147 (vs), 2083 (s)	2154 (m), 2099 (w)
Ru ₄ TCNX ⁶⁺	2153 (w), 2186(vw)	2174 (w), 2132 (w)
λ / nm ^b (ϵ in 10 ⁻³ dm ³ mol ⁻¹ cm ⁻¹)		
Ru ₄ TCNX ¹⁰⁺	880 (23.08), 286 (29.00)	1170 (28.84), 935 (22.39), 454 (5.62), 277 (22.39)
Ru ₄ TCNX ⁸⁺	1103 (44.40; $\Delta\nu_{1/2}$ 4030 cm ⁻¹ ^c), 383 (8.78), 273 (33.98)	935 (50.12; $\Delta\nu_{1/2}$ 3260 cm ⁻¹ ^c), 360 (10.96), 267 (35.48)
Ru ₄ TCNX ⁷⁺	1822 (23.48), 1462 (sh), 1191 (sh), 483 (11.80),	1561 (21.88), 1315 (13.18), 918 (16.98), 460 (10.47), 420
Ru ₄ TCNX ⁶⁺	641 (sh; 2.34), 490 (3.33), 369 (27.60), 261 (46.66)	610 (6.92), 350 (15.14), 258 (37.15)
K _c (7+), K _c (8+)	3.6 × 10 ³ , 6.5 × 10 ⁸	2 × 10 ⁴ , 1.7 × 10 ¹³
g (7+)	2.047 ^d	g = 2.019 ^e

^aFrom cyclic voltammetry in 0.1 M Bu₄NPF₆ solution at 100 mV /s. ^bFrom spectroelectrochemistry in acetonitrile /0.1 M Bu₄NPF₆. ^c $\Delta\nu_{1/2}$: Band width at half height. ^dEPR data for [$\{\text{Ru}(\text{NH}_3)_5\}_4(\mu_4\text{-TCNQF}_4)]^{7+}$ in acetonitrile /0.1 M Bu₄NPF₆ solution at 110 K. ^eEPR data for [$\{\text{Ru}(\text{NH}_3)_5\}_4(\mu_4\text{-TCNQ})]^{7+}$ in acetonitrile solution between 3 and 4 K.

5.6. EPR spectroscopy

EPR signal was not detected for (8+) species in CH₃CN solution at 110 K due to its diamagnetic nature. The EPR spectrum was measured for the *insitu* generated one-electron reduced species. The (7+) species gave a broad EPR signal with 2.05 mT peak- to -peak line width. Larger extent mixing of the Ru^{II} centred HOMO to the LUMO (TCNQF₄) has not only been reflected in their redox potentials but also in the g value determined for the electrochemically generated (7+) species. The EPR signal measured in CH₃CN / 0.1 M Bu₄NPF₆ at 110K showed the g value at 2.047 whereas it was found at 2.019 for the previously reported TCNQ analogue^[36]. So it is clear that the fluorinated derivative has more metal contribution to the singly occupied MO (SOMO) compared to the non-fluorinated species.



Figur 5.6.1. X-band EPR spectra of $[\{\text{Ru}(\text{NH}_3)_5\}_4(\mu_4\text{-TCNQF}_4)]^{7+}$ in CH₃CN / 0.1 M Bu₄NPF₆ at 110 K.

5.7. Conclusion

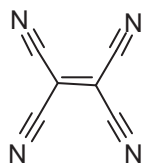
The tetraruthenium complex $\{[\text{Ru}(\text{NH}_3)_5]_4(\mu_4\text{-TCNQF}_4)\}(\text{PF}_6)_8$, TCNQF₄ = 2,3,5,6-tetrafluoro-7,7,8,8-tetracyano-*p*-benzoquinodimethane, was obtained and studied by cyclic voltammetry, IR, UV-VIS-NIR and EPR spectroelectrochemistry. Expectedly, the better π acceptor qualities of TCNQF₄ in comparison to TCNQ cause more accessible reduction to produce $\{[\text{Ru}(\text{NH}_3)_5]_4(\mu_4\text{-TCNQF}_4)\}^{7+}$ with enhanced metal contribution to the singly occupied MO and low-energy shifted IR vibrational and NIR electronic absorptions. However, the two-electron oxidation to the (10+) ion is also facilitated. The reason is seen in a more metal centered oxidation for the TCNQF₄ complex while the previously studied TCNQ analogue is assumed to undergo a higher degree of oxidation at the bridging ligand. As a result, the title species has a redox potential range of only 0.51 V, indicating a significantly diminished HOMO-LUMO difference.

Chapter 6

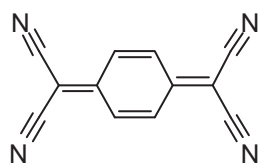
Exploring various coordination modes of redox-innocent TCNB in discrete and polymeric copper(I) complexes: A structural, electrochemical and spectroscopic study

6.1. Introduction

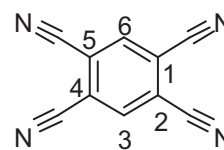
The π -conjugated tetracyano systems TCNX (TCNE = tetracyanoethene, TCNQ = 7,7,8,8-tetracyanoquinodimethane, TCNB = 1,2,4,5-tetracyanobenzene) are very useful and versatile ligands in coordination chemistry for σ/π - type coordination, for their tendency to form polymeric networks utilizing various coordination modes, and for interesting electronic and magnetic properties^[34,44,46,139,141,145,148,149]. Rich electronic and magnetic properties of TCNX complexes arise due to facile reduction of TCNX system to radical (TCNX \cdot^-) or dianionic (TCNX $^{2-}$) forms. Each single TCNX molecule can bridge up to four metal fragments through σ -donor cyano-nitrogens or π electron density (μ_1 , μ_2 , μ_3 , μ_4 and η^2). Transition metal chemistry with TCNE and TCNQ is being most important due to the strong σ -polarization effect and the π -back donation property of d-electron rich transition metal centers and the facile electron uptake by TCNE and TCNQ in their low lying π^* molecular orbital. Often, electron-rich metal fragments involve electron transfer process when bound to TCNX system, resulting in interesting magnetic and electronic behaviour. Aromatic and weaker π accepting TCNB serves as a potential candidate for the stabilization of metal complexes having non-reduced (“innocent”) TCNB, allowing the studies of metal-TCNB interactions in the desired redox state^[150]. TCNB is also widely used as a pseudo-square-planar building block for the construction of self-assembled network structures^[47,48]. Only a few reports on structural investigations of transition metal-TCNB complexes are found in the literature^[47,48,151].



Tetracyanoethene
(TCNE)



7,7,8,8-tetracyano-*p*-quinodimethane
(TCNQ)



1,2,4,5-tetracyanobenzene
(TCNB)

TCNB can have various σ -bridging modes (μ_{1-4}) to metal centers. To the best of our knowledge there are no reports on a π -bonded metal complex. Among the binding modes, μ_1 , μ_3 , μ_4 and η^6 can have only one type of coordination to the metal centers whereas μ_2 can have three different coordination μ_2 (1,2), μ_2 (1,3), μ_2 (1,4), depending on the metal positions of coordinating σ -donor atoms.

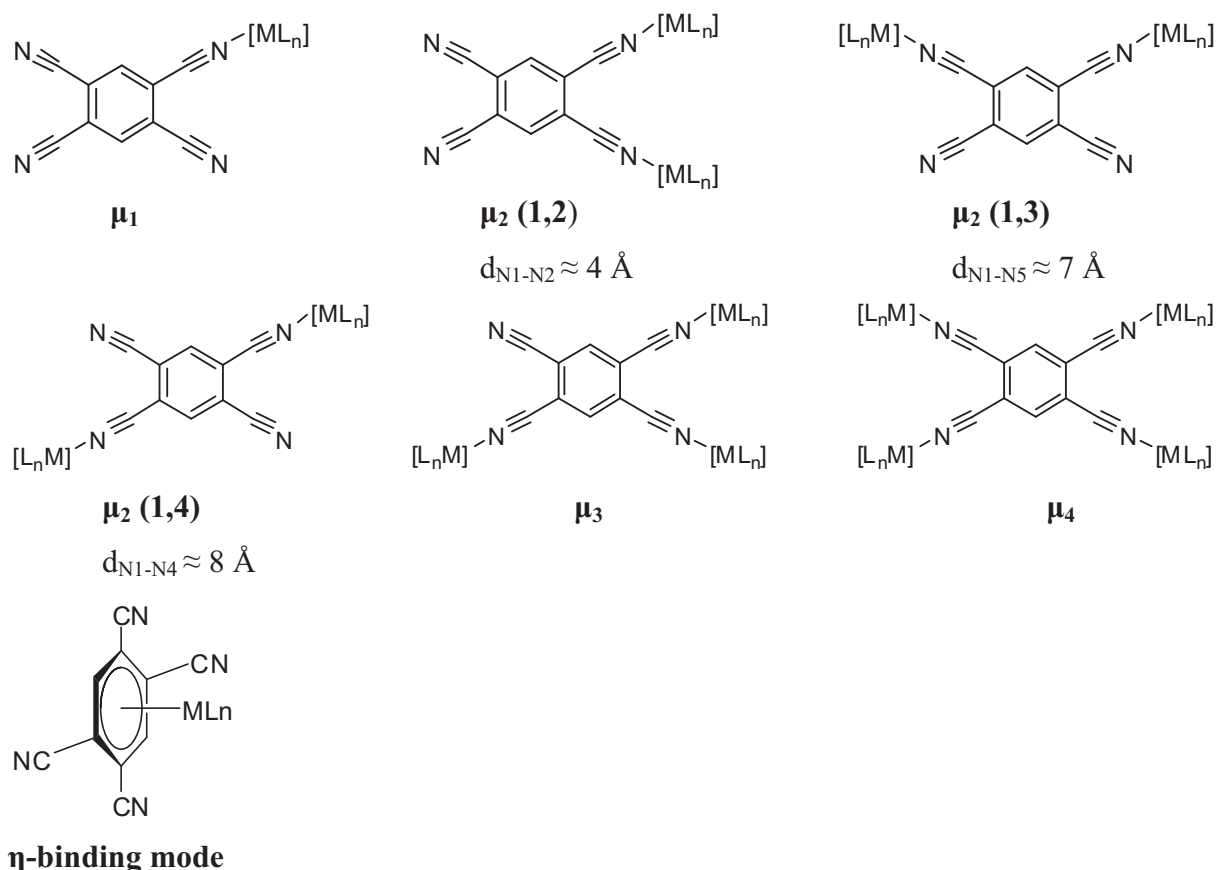


Figure 6.1.1. Possible binding modes and distances between σ -donor atoms of TCNB

Distances between coordinating cyano-nitrogen atoms govern the characteristics of the assembled structures. These three types of μ_2 binding in combination to μ_1 , μ_3 , μ_4 and η^6 may lead to the formation of various self-assembled network materials. Reports are found for μ_2 (1,2)^[47], μ_2 (1,3)^[47], μ_3 and μ_4 binding in polymeric materials^[48] and μ_2 (1,4) has recently been reported in a dimeric Yb^{III} complex^[151].

The stable organometallic fragment $[\text{Cu}(\text{dppf})]^+$, dppf = 1,1'-bis(diphenylphosphino)-ferrocene, is found to stabilize complexes with unreduced strong acceptors such as α -azoimines or o -quinones^[152-155]. This knowledge prompted us to explore the coordination of $[(\text{dppf})\text{Cu}]^+$ with TCNB. In addition to $[\text{Cu}(\text{dppf})]^+$, we have synthesized a new copper(I)

fragment, $[\text{Cu}(\text{dchpf})]^+$, $\text{dchpf} = 1,1'$ -bis(dicyclohexylphosphino)ferrocene for the formation of Cu-TCNB materials. The precursor complex $[\text{Cu}(\text{dppf})(\text{CH}_3\text{CN})_2]^+$ containing two labile acetonitriles, was reacted to produce a cyclic dinuclear product, $\{[\text{Cu}(\text{dppf})(\mu_2\text{-TCNB})](\text{BF}_4)\}_2$ **1**, whereas $[\text{Cu}(\text{dchpf})(\text{CH}_3\text{CN})]^+$ was reacted to isolate a hetero-octanuclear complex of the formula $[\{\text{Cu}(\text{dchpf})\}_4(\mu_4\text{-TCNB})](\text{BF}_4)_4$, **2**.

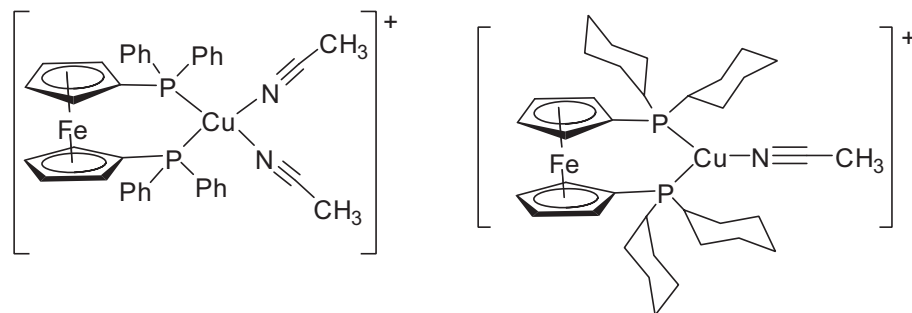


Figure 6.1.2. Cu^{I} - precursor complexes with chelating di-phosphine ligands.

The organometallic fragments have been considered here on the basis of their reactivity and steric factors to enable the isolation and characterization of Cu^{I} -TCNB complexes in both discrete and polymeric forms. The 1,3 (μ_2 -) coordination to $[\text{Cu}(\text{dppf})]^+$ resulted in the formation of a cyclic dimer **1** (Figure 6.2.1) whereas μ_4 -coordination to $[\text{Cu}(\text{dchpf})]^+$ led to the formation of a coordinatively saturated hetero-octanuclear Cu^{I} complex, **2** (Figure 6.2.3). In addition to the detailed structural studies of the above materials, investigations were also made on their electrochemical and spectroscopic properties

6.2 Synthesis and characterization

The precursor complexes $[\text{Cu}(\text{dppf})(\text{CH}_3\text{CN})_2](\text{BF}_4)$ ^[82] and $[\text{Cu}(\text{dchpf})(\text{CH}_3\text{CN})](\text{BF}_4)$ were prepared from a 1:1 reaction of $[\text{Cu}(\text{CH}_3\text{CN})_4]^+$ with dppf or dchpf in acetonitrile at room temperature. The number of acetonitriles present in the precursor complex was confirmed by ^1H NMR spectroscopy and elemental analysis. The precursor complex $[\text{Cu}(\text{dppf})(\text{CH}_3\text{CN})_2](\text{BF}_4)$ contains two labile acetonitriles whereas the complex $[\text{Cu}(\text{dchpf})(\text{CH}_3\text{CN})](\text{BF}_4)$ contains only one acetonitrile. The reaction of an equimolar mixture of $[\text{Cu}(\text{dppf})(\text{CH}_3\text{CN})_2](\text{BF}_4)$ and TCNB in dichloromethane resulted a doubly TCNB bridged cyclic dimeric complex, **1** as shown in Figure 6.2.1. One sharp signal at -11.49 ppm in ^{31}P NMR spectrum indicated the formation of a new product and the absence of the signal at -13.8 ppm, corresponding to the precursor complex, indicated completion of the reaction. The 1:1 NMR integration ratio of $[\text{Cu}(\text{dppf})]$ unit to the TCNB proton [8.20 (s, 4H, TCNB), 4.24 (s, 8H, Cp), 4.45 (s, 8H, Cp)] and the absence of the NMR signal for coordinated

acetonitriles in the complex indicated the formation of the product. The identity was further confirmed by its reproducible elemental analysis. The mass spectrum of the compound could not provide any useful information but indicated the formation of a high molecular weight species.

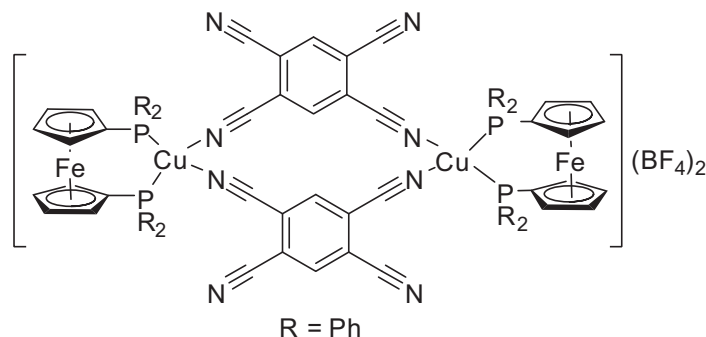


Figure 6.2.1. Cyclic, dimeric Cu^{I} -TCNB complex **1** with 16-membered ring.

The precursor $[\text{Cu}(\text{dchpf})(\text{CH}_3\text{CN})_2](\text{BF}_4)$, having one acetonitrile, was reacted in 4:1 ratio in dichloromethane to obtain a brown, coordinatively saturated μ_4 -bridged TCNB complex (Figure 6.2.3). The measured ^{31}P NMR signal at -2.46 ppm (-3.16 ppm for the precursor complex) indicated the formation of a new product. The formulation was done on the basis of the integral ratio of the ^1H NMR signal at 8.59 (s, 2H, TCNB) and 4.28 (s, 16H, Cp), 4.52 (s, 16H, Cp) ppm (see Figure 6.2.2). The formation of a hetero-octanuclear complex **2** $[\{\text{Cu}(\text{dchpf})\}_4(\mu_4\text{-TCNB})](\text{BF}_4)_4$ was further supported by elemental analysis.

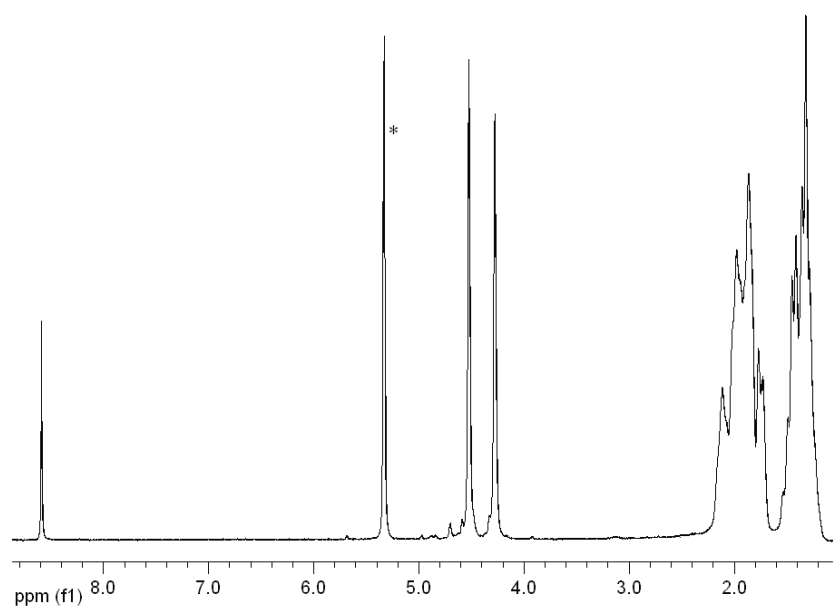


Figure 6.2.2. ^1H NMR spectrum of $[\{\text{Cu}(\text{dchpf})\}_4(\mu_4\text{-TCNB})](\text{BF}_4)_4$ in CD_2Cl_2 at 250 MHz (* represents signal from the solvent).

The cyclic voltammogram of the complex also shows a ferrocene-based four-electron oxidation wave and a one-electron reduction wave on the TCNB ring, supporting the above formulation. On crystallization attempts, the 4:1 complex **2** re-assembled to dark block type single crystals **3** which were later identified by X-ray diffraction as belonging to a 1:1 coordination polymer with 1,4-bridging TCNB.

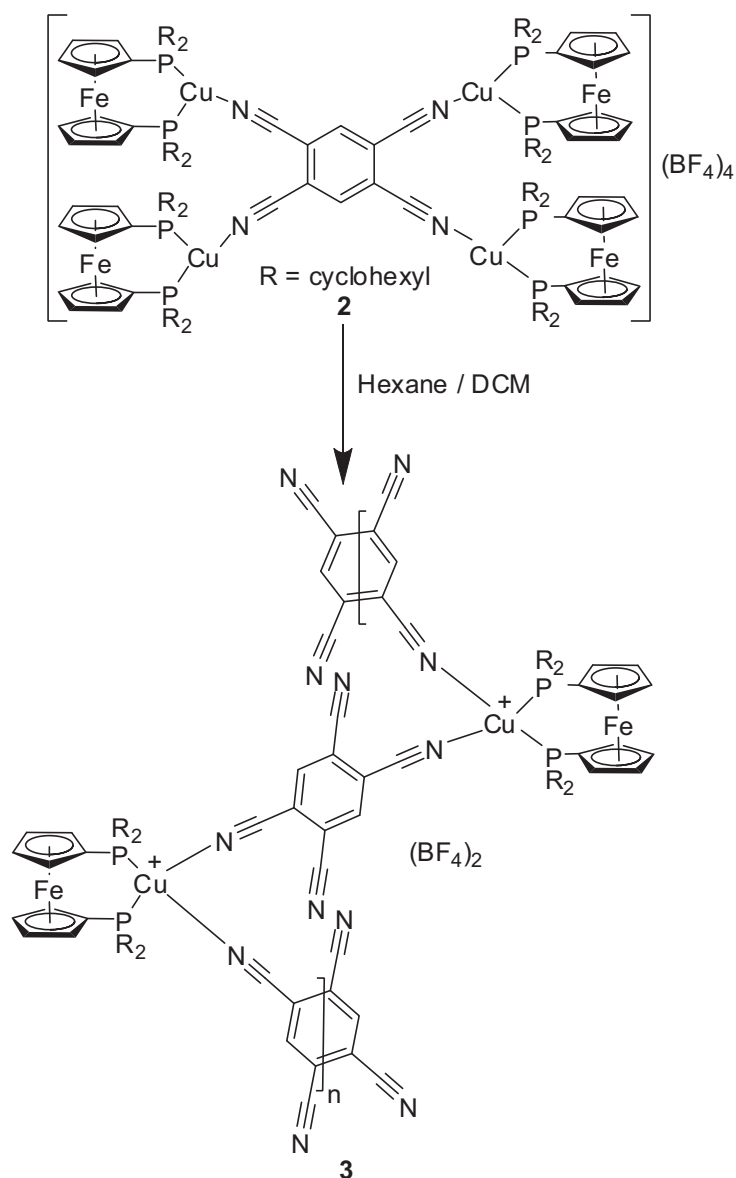


Figure 6.2.3. Formation of polymeric 1:1 complex **3** from 4:1 compound **2**.

6.3. Crystal structure

6.3.1. Molecular structure of $\{[\text{Cu}(\text{dppf})(\mu_2\text{-TCNB})](\text{BF}_4)\}_2 \mathbf{1}$

The orange block-shaped crystals of $\{[\text{Cu}(\text{dppf})(\mu_2\text{-TCNB})](\text{BF}_4)\}_2 \cdot 3\text{CH}_2\text{Cl}_2 \cdot 3\text{H}_2\text{O}$ were grown by slow diffusion of hexane into a dichloromethane solution of the complex at 4°C in an argon sealed-tube. The complex crystallized in monoclinic $P2_1/n$ space group. X-ray

crystal structural analysis reveals details about the coordination pattern of TCNB and geometry of the Cu^{I} centers. There exist only two $\mu_2(1,3)$ type bridging of the cyano nitrogen atoms of each TCNB, while the other two CN groups remain non-coordinated. Two $\mu_2(1,3)$ TCNB bridge to two $[\text{Cu}(\text{dppf})]^+$ units to construct a dimeric structure with a 16-membered planar ring. The interesting feature of the structure is that two TCNB rings are in planar orientation satisfying the geometrical restriction for this particular type of geometry. When compared to the similar structure reported^[151] for the complex $[\text{Cp}^* \text{Yb}\{(\mu\text{-CN})_2(\text{C}_6\text{H}_4)(\text{CN})_2\}]_2$, we observe that $\mu_2(1,4)$ TCNB is bridged to Yb^{III} centres resulting in a parallel, nearly eclipsed orientation of the TCNB rings^{17,18}. The pseudo-tetrahedral geometry around the Cu^{I} centres in **1** is formed by the two P donor atoms from chelated dppf and two N atoms from each of the $\mu_2(1,3)$ -bonded TCNB.

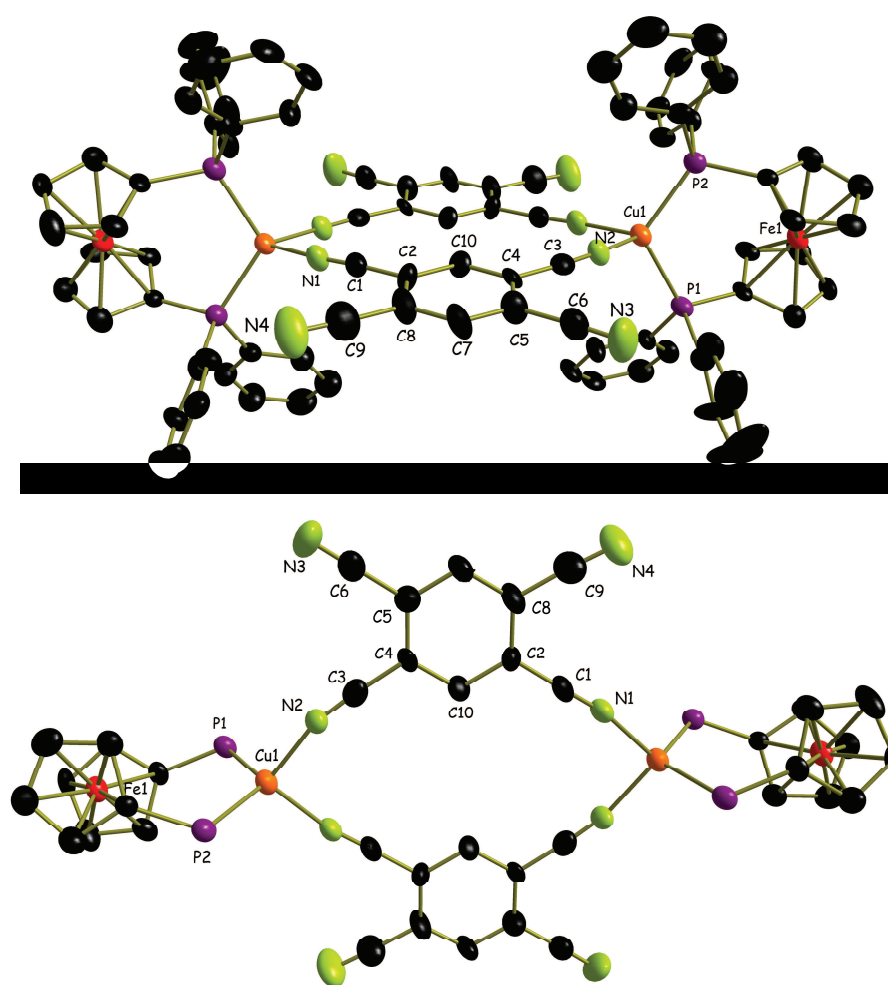


Figure 6.3.1. X-ray structure of the dication in the crystal of **1** · 3 CH_2Cl_2 · 3 H_2O . Solvent molecules (solvent of crystallization) and two counter anions, BF_4 , are omitted for clarity (top). A different perspective after omitting certain atoms, solvent molecules and counter anions (bottom).

Bond lengths of coordinated C-N are C1-N1 = 1.135(10) Å and C3-N2 = 1.133(9) Å whereas non-coordinated C-N bond lengths are C6-N3 = 1.123(11) Å and C9-N4 = 1.146(11) Å. Thus the π -donor property of Cu^I centres is not reflected in the coordinated and non-coordinated C-N bond lengths due to the very weak π -accepting property of TCNB. The Cu-N bond lengths Cu1-N1 = 2.019(8) Å and Cu1-N2 = 2.034(8) Å are comparatively longer than the previously reported^[47,48] Cu^I-TCNB polymeric network with the similar coordination mode, indicating a weaker coordination of Cu^I to the cyano-nitrogen atoms of μ_2 (1,3)-TCNB. The C-C bond lengths of the ring are in the range of 1.370(11)-1.409(11) Å, being greater than a C-C double bond but reasonably shorter than single bonds. This proves that the ring is non-reduced. The complex **1** is the first example of structurally characterized discrete transition metal-TCNB complex. Important bond lengths and angles of **1** are given in Table 6.3.1.

Table 6.3.1 Selected bond lengths (Å) and bond angles (°) of **1** · 3CH₂Cl₂ · 3H₂O.

Bonds	Lengths	Bonds	Lengths
Cu1-N1	2.019(8)	C8-C7	1.383(12)
Cu1-N2	2.034(8)	C7-C5	1.380(11)
Cu1-P1	2.250(2)	C5-C4	1.409(12)
Cu1-P2	2.252(3)	C4-C10	1.370(11)
C1-N1	1.135(10)	Bonds	Angles
C3-N2	1.133(9)	N1-Cu1-N2	95.1(3)
C9-N4	1.146(11)	P1-Cu1-P2	113.90(9)
C6-N3	1.123(11)	C1-N1-Cu1	168.3(7)
C1-C2	1.439(12)	C3-N2-Cu1	162.9(7)
C3-C4	1.435(11)	C2-C1-N1	177.1(10)
C5-C6	1.450(13)	C4-C3-N2	176.1(10)
C8-C9	1.445(13)	C5-C6-N3	177.7(12)
C2-C8	1.407(12)	C8-C9-N4	177.4(12)
C10-C2	1.389(10)		

6.3.2. Structure of $\{[(\mu_2\text{-TCNB})\text{Cu}(\text{dppf})]_2(\text{BF}_4)_2\}_n \cdot 3 \cdot \text{CH}_2\text{Cl}_2$.

Block-shaped black single crystals of the polymeric material with the composition **3** · CH₂Cl₂ were found during the crystallization process of compound **2** by slow diffusion of hexane onto a dichloromethane solution of the complex. The chemical change during the process is

attributed to the instability of the hetero-octanuclear complex with the bulkier cyclohexyl groups on the $[\text{Cu}(\text{dchpf})]^+$ fragment. During the process, TCNB changes the binding mode from μ_4 to $\mu_2(1,4)$ to reduce the steric bulk on the complex. The same observation was made when the crystallization process was repeated, thus indicating the reproducibility. We measured the single crystal X-ray diffraction to identify the material. The X-ray crystal structure analysis reveals only one type of $\mu_2(1,4)$ -coordination in the network. In the complex **1**, $\mu_2(1,3)$ -coordination led to the formation of a cyclic dimer whereas in this case $\mu_2(1,4)$ -coordination gives a 2D polymeric network. In the asymmetric unit (Figure 6.3.2.2), two $[\text{Cu}(\text{dchpf})]^+$ fragments and two TCNB molecule are present according to a metal- to -TCNB ratio of 1:1. The asymmetric unit contains two $[\text{Cu}(\text{dchpf})]^+$ fragments, one TCNB ring, and $2 \times \frac{1}{2}$ of another TCNB ring. The complete TCNB ring bridges two Cu centers through its 1,4 bridging mode. Selected bond lengths and angles are given in Table 6.3.2.1.

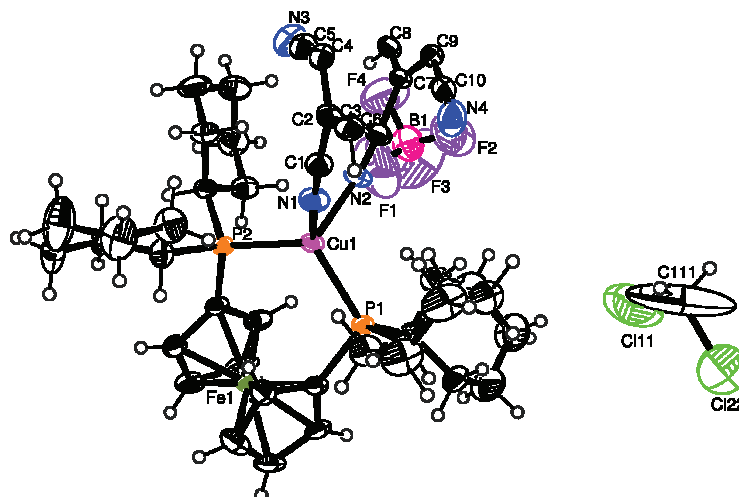


Figure 6.3.2.1. Half molecule in asymmetric unit of $3 \cdot \text{CH}_2\text{Cl}_2$, $[(2 \times \frac{1}{2} \mu_2(1,4)\text{-TCNB})\text{Cu}(\text{dchpf})](\text{BF}_4) \times \text{CH}_2\text{Cl}_2$. The counter anion BF_4 is omitted for clarity.

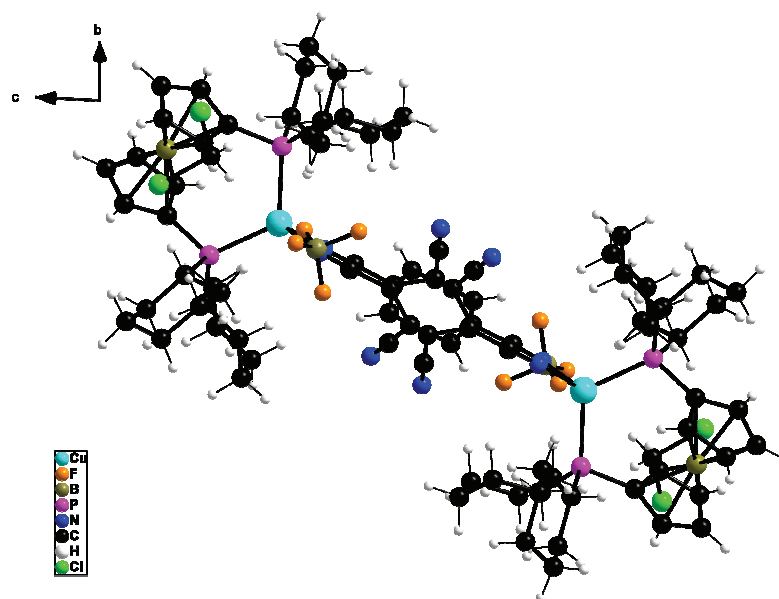


Figure 6.3.2.2. The asymmetric unit of **3**, $[(\mu_2(1,4)\text{TCNB})(2 \times \frac{1}{2} \mu_2(1,4)\text{TCNB}) - \{\text{Cu}(\text{dchpf})_2\} (\text{BF}_4)_2 \times 2\text{CH}_2\text{Cl}_2$. Counter anions BF_4 and solvent molecules CH_2Cl_2 are omitted for simplification of the figure.

Table 6.3.2.1. Selected bond lengths (Å) and bond angles ($^\circ$) of **3** in the crystal of $\mathbf{3} \cdot \text{CH}_2\text{Cl}_2$.

Bonds	Lengths	Bonds	Lengths
Cu1-N1	2.109(3)	C3-C4	1.388(5)
Cu1-N2	2.051(4)	C7-C9	1.395(6)
Cu1-P1	2.279(1)	C8-C9	1.387(6)
Cu1-P2	2.274(1)	C7-C8	1.387(6)
C1-N1	1.139(5)	Bonds	Angles
C6-N2	1.129(5)	N1-Cu1-N2	86.70(15)
C5-N3	1.127(5)	P1-Cu1-P2	116.66(4)
C10-N4	1.137(6)	Cu1-N1-C1	164.4(4)
C4-C5	1.452(6)	Cu1-N2-C6	161.5(4)
C9-C10	1.436(6)	C2-C1-N1	174.9(5)
C6-C7	1.431(6)	C7-C6-N2	174.2(5)
C2-C4	1.390(6)	C4-C5-N3	178.0(5)
C2-C3	1.376(6)	C9-C10-N4	177.5(5)
C1-C2	1.436(6)		

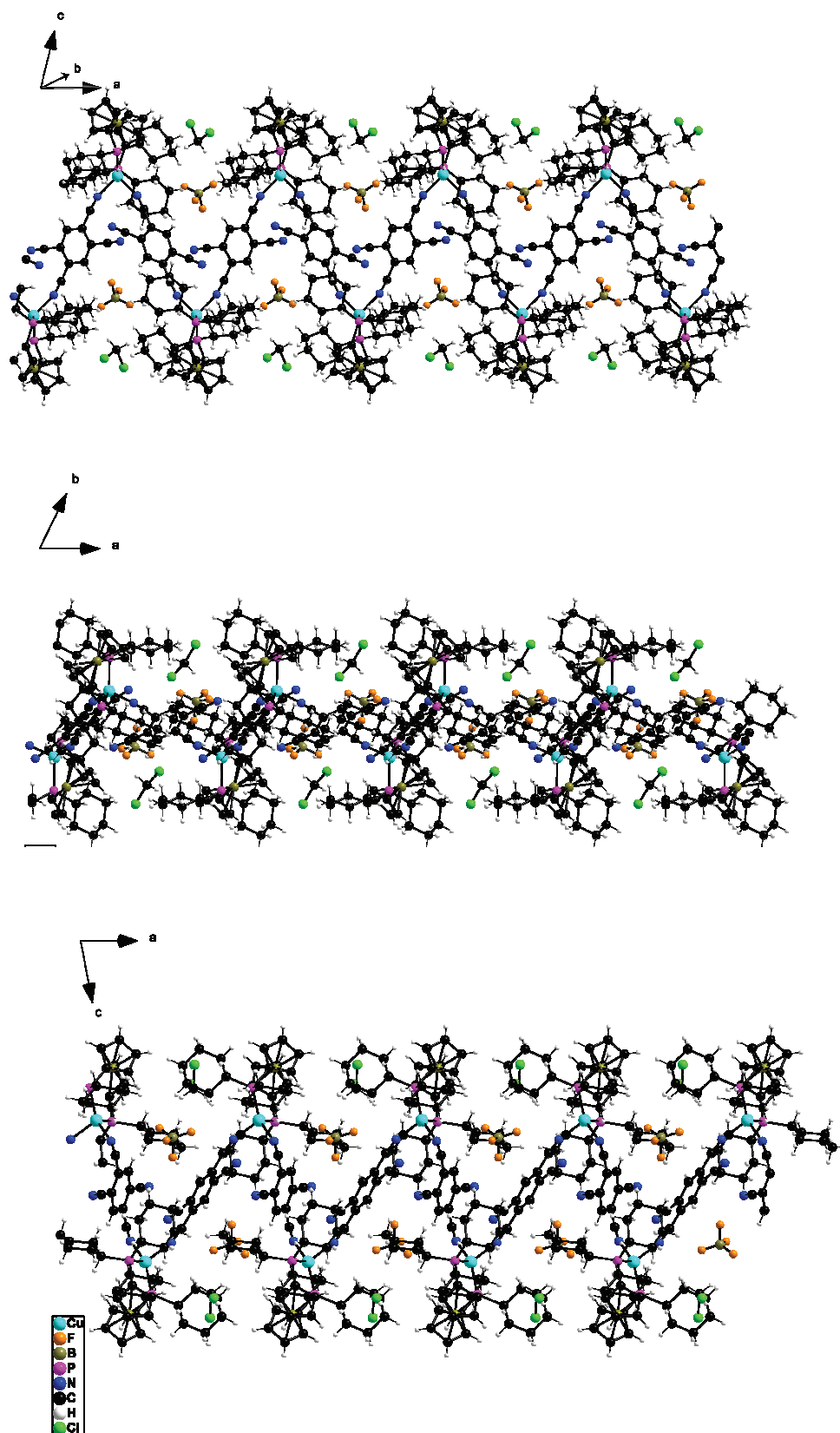


Figure 6.3.2.3. View along different axes of the 2D polymeric network structure of **3** in the crystal of $3 \cdot \text{CH}_2\text{Cl}_2$.

6.4. Cyclic voltammetry

The cyclic voltammogram of **1** (Figure 6.4.1) shows one quasi-reversible two-electron oxidation wave at 0.11 V, corresponding to the oxidation of the ferrocene moieties. The first and second reductions are not fully reversible and are assigned to the addition of electrons to the π^* molecular orbital of the bridging TCNB ligand. The octanuclear complex **2** shows one four-electron ferrocene-based oxidation wave and a one-electron reduction process (Figure 6.4.1). The expected second reduction has possibly shifted to more negative potential and that is why it was not observed in the solvent window. The redox potential of both the complexes are given in Table 6.4.1.

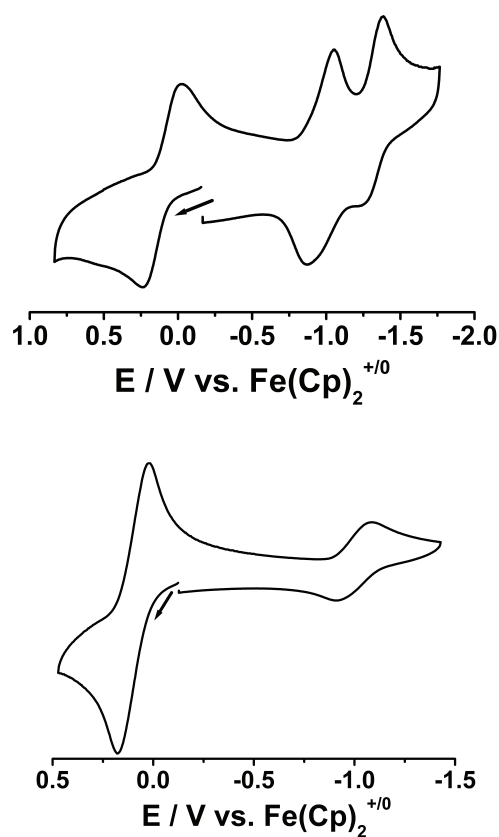


Figure 6.4.1. Cyclic voltammograms of **1** (top) & **2** (bottom) in CH_2Cl_2 / 0.1 M Bu_4NPF_6 at 298 K with 100 mv /sec scan rate.

Table 6.4.1. Electrochemical data^{a)} for **1** & **2**.

	1	2
$E_{1/2}(\text{ox } 1) / \text{V} (\Delta E / \text{mV})$	0.11 (260)	0.10 (160)
$E_{1/2}(\text{red } 1) / \text{V} (\Delta E / \text{mV})$	-0.96 (166)	-0.99 (170)
$E_{1/2}(\text{red } 2) / \text{V} (\Delta E / \text{mV})$	-1.31 (123)	n.o

^{a)}Measurements in CH_2Cl_2 / 0.1 M Bu_4NPF_6 .

Potentials in V vs. $\text{Fc}^{+/0}$, Scan rate 100 mV/s.

6.5. IR and UV-Vis spectroelectrochemistry

Although infrared absorption corresponding to the CN vibration is a useful tool to study the metal-TCNX interaction in ground state, the technique was not much useful in this case. The IR band in the CN stretching region was not detectable for complex **1** when measured in the solid state or in dichloromethane solution. As the 1st reduction is only quasi-reversible in nature, the IR-spectroelectrochemical experiment was not performed for further study. A similar behaviour was also observed for complex **2**. A very weak broad band at $\nu_{\text{CN}} = 2244 \text{ cm}^{-1}$ was observed when measured in a KBr pellete. The infrared spectroelectrochemical experiment in dichloromethane / 0.1 M Bu_4NPF_6 was carried out to observe the shift of the band after one-electron reduction. The band at 2244 cm^{-1} in the native state is shifted to 2168 and 2160 cm^{-1} , confirming the reduction on the TCNB aromatic ring^[36].

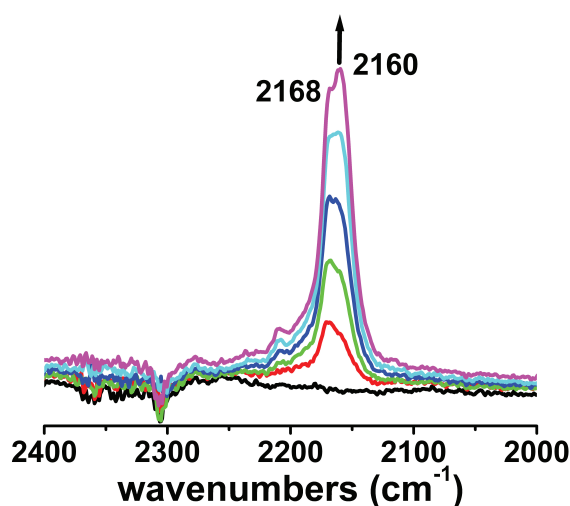


Figure 6.5.1. IR-spectroelectrochemical reduction of **2** measured at 298 K in CH_2Cl_2 / 0.1 M Bu_4NPF_6 solution.

On UV-Vis spectroelectrochemical four-electron oxidation of complex **2**, a low energy broad band at 790 nm appears (Figure 6.5.2) which is assigned to the typical ferrocenium transition in the oxidized form of the dppf unit. In addition, the MLCT band for the Cu^{I} -TCNB is shifted from 447 nm to 413 nm during the oxidation process. On reduction, the new maxima at 490 and 392 nm appear (Figure 6.5.2). A weaker absorption band occurs for the tetracopper complex^[46], $\{(\mu_4\text{-TCNB})[\text{Cu}(\text{Me}_3\text{TACN})]_4\}(\text{BF}_4)_4$ at 372 nm. The UV-Vis spectroelectrochemical data are given in Table 6.5.1.

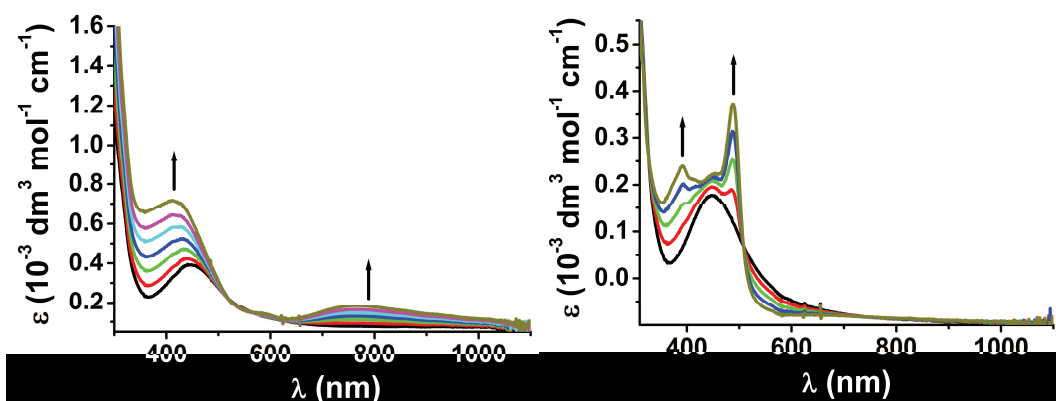


Figure 6.5.2. UV-Vis spectroelectrochemical oxidation (left) and reduction (right) of complex **2** measured at 298 K in $\text{CH}_2\text{Cl}_2/0.1 \text{ M Bu}_4\text{NPF}_6$ solution.

Table 6.5.1. UV-Vis spectroelectrochemical data for **2**

Complex ion	λ / nm (ϵ in $10^{-3} \text{ dm}^3 \text{ mol}^{-1} \text{ cm}^{-1}$)
2^{8+}	413 (0.72), 790 (0.18)
2^{4+}	447 (0.40)
2^{3+}	392 (0.22), 490 (0.34)

6.6. EPR spectroscopy

The EPR spectra were measured by Dr. Brigitte Schwederski for the *in situ* generated one-electron reduced species of complexes **1** and **2**. Electrolysis in de-oxygenated dichloromethane was carried out inside the EPR tube using Bu_4NPF_6 as electrolyte. Electrolysis was continued over a period of time until considerable signal- to -noise ratio was achieved. The g values determined at 2.0036 for 1^- & 2.0033 for 2^- , respectively are close to that of the free unpaired electron value, $g_e = 2.0023$. This implies that the ratio of the unpaired electron's spin magnetic moment to its angular momentum does not differ much from the free electron value. Thus the very minute changes in the magnitude of g values indicate that the π^* molecular orbital of TCNB contains the unpaired electron.



Figure 6.6.3. EPR spectra of electro-generated one-electron reduced species of $1^{\cdot-}$ (left) & $2^{\cdot-}$ (right) at 298 K in $\text{CH}_2\text{Cl}_2 / 0.1 \text{ M Bu}_4\text{NPF}_6$ solution.

The one-electron reductions produce predominant ligand centred radicals by adding an electron to the TCNB ring. The free ligand radical anion $\text{TCNB}^{\cdot-}$ has $g = 2.0028$. These data, viz., the marginal shifts of g and the relatively small copper isotope coupling (Table 6.6.1) indicate a predominately ligand-based singly occupied molecular orbital. The EPR data of the free ligand and metal complexes are given in Table 6.6.1.

Table 6.6.1. EPR data^{a)} of free ligand, $1^{\cdot-}$ and $2^{\cdot-}$.

	$\text{TCNB}^{\cdot-}$ ^[46]	$1^{\cdot-}$	$2^{\cdot-}$
g	2.0028	2.0036	2.0033
A	$a(^{14}\text{N}) = 1.13 \text{ G}$ $a(^{63, 65}\text{Cu}) = 4.2 \text{ G}$	un-resolved peak- to -peak distance = 9 G spectral width = 35 G	partially resolved peak- to -peak distance = 8 G spectral width = 24 G $a(^{63, 55}\text{Cu}) = 1.47 \text{ G (4Cu)}$ $a(^{31}\text{P}) = 0.85 \text{ G (8P)}$

a) From measurements in $\text{CH}_2\text{Cl}_2 / 0.1 \text{ M Bu}_4\text{NPF}_6$ at 298 K

6.7. Conclusion and outlook

Various possible binding modes of TCNB have been discussed in detail along with interesting aspects of structural features in discrete and polymeric forms. Steric factor and binding angle has prominent effect to direct either the formation of discrete molecule or

polymeric network structure. Investigated structural and electrochemical properties of such complexes give insight to design desired chemical form of matter. In addition to σ -polarization of the metal centres, π -polarization could also enhance the electron uptake capability of TCNB, resulting in interesting electronic properties. Although there are no reports on complexes exhibiting significant σ together with π type interaction with weakly electron accepting TCNB but it could be rationally designed with half-sandwich low-valent transition metal complexes. Well designed reaction pathways can facilitate the isolation of π -bonded metal fragments, $[(\eta^6\text{-TCNB})\text{M}(\text{CH}_3\text{CN})_m]^{n+}$, which on further reaction can utilize four free cyano-nitrogen atom on TCNB as source of σ donors to bind additional metal centres. This would not only make TCNB a better acceptor but also could increase metal contents in discrete or polymeric materials having more electrochemical processes.

Chapter 7

Structure, electrochemistry and spectroscopy of a new diacylhydrazido-bridged diruthenium complex with a strongly near-infrared absorbing Ru^{III}Ru^{II} intermediate

7.1 Introduction

Compounds which absorb and perform other functions in the near-infrared region of the electromagnetic spectrum have become of interest for information technology^[156]. The efficient transmission of information by glass fiber optics was promoted by Kao's discovery which was recently honoured by the Nobel Prize 2009 in Physics^[157]. Among the optimum wavelengths with minimal loss are the 1310 nm and 1550 nm regions^[158], therefore, robust systems operating in that spectral regions are of interest^[159,160]. Earlier studies by Wang and coworkers^[160] on substances $[(\mu\text{-adc-R})\{\text{Ru}(\text{bpy})_2\}_2]^{3+}$ developed in our group^[55] have shown the principal applicability of such coupled systems which are stable intermediates of two-step redox series^[27,55]. The identity of the intermediates as diruthenium(II) radical complexes or as Ru^{III}Ru^{II} mixed-valent forms has been probed, it depends on the donor/acceptor characteristics of the substituents R.^[55]

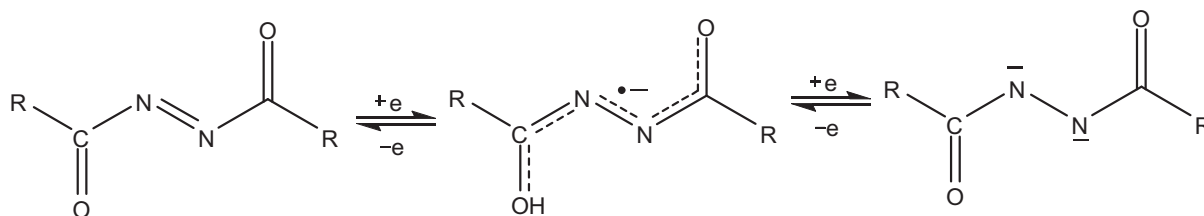


Figure 7.1.1. Two step one electron reductions of the azodicarboxylic ligands

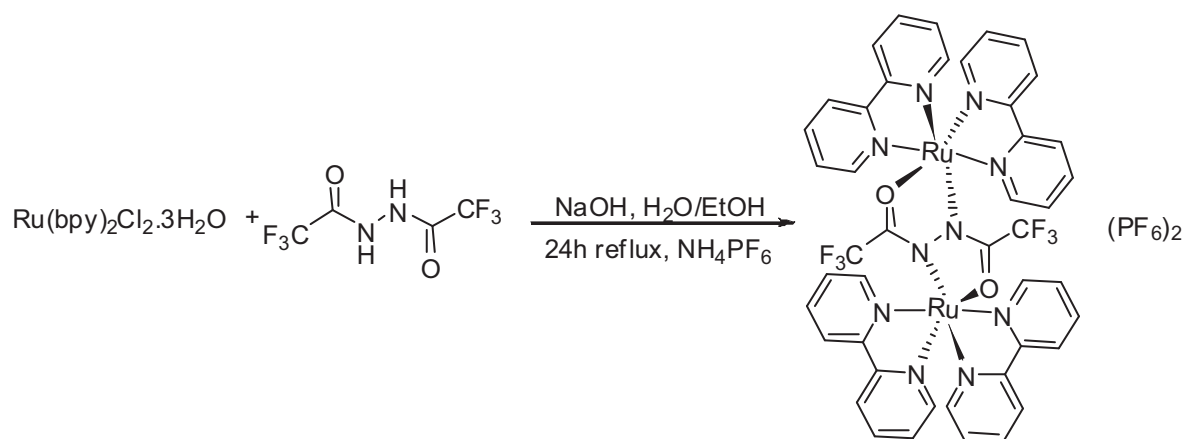
Azodicarboxylic esters and their anions and dianions as well as related molecular ions such as di μ -R, diiminohydrazido(2-)^[161], constitute easily available yet rather special ligands because they exhibit quinone type two-step redox behavior, a π conjugated bis-chelate function^[27,162], a small 6 π center system of which 4 centers are coordinating, a radical intermediate stable against disproportionation^[163], resonance stabilization of the dianionic form (cf. the aromatic catecholates), an „S frame“ conformation *s-cis*/*E*/*s-cis* which allows for a rather short M--M distance ($\gg 5$ Å) despite molecule bridging^[162], a tuning potential through the substituents R at the non-coordinating carbon π centers (e.g. donor or acceptor substitution)^[55], and the

possibility to introduce additionally coordinating groups R, leading to bis-tridentate non-innocent ligands^[164].

While earlier work has dealt mostly with donor-substituted derivatives^[55], I have synthesized an example involving a classical acceptor substituent, viz., trifluoromethyl $\text{CF}_3 = \text{R}$, and I am able for the first time to provide structural information on the $\text{Ru}^{\text{II}}\text{Ru}^{\text{II}}$ precursor. The diacylhydrazido bridged dinuclear complexes can be expected to exhibit relatively small metal-metal distances around 5 Å in spite of the molecular bridge.

7.2. Synthesis and characterization

The reaction of two equivalents of $\text{Ru}(\text{bpy})_2\text{Cl}_2 \cdot 2\text{H}_2\text{O}$ with 1,2-bis(trifluoroacetyl)-hydrazine^[165] under basic conditions yields the dinuclear $[(\mu\text{-adc-CF}_3)\{\text{Ru}(\text{bpy})_2\}_2]^{2+}$ ion which was isolated as the bis(hexafluorophosphate).



The presence of two chiral metal centers in such compounds leads to the alternatives of *meso* and *rac* isomers^[166], both of which were observed, leading to two ^{19}F -NMR resonance signals at -66.89 and -67.12 ppm for CF_3 groups in a 60:40 intensity ratio. The peak at $m/z = 1195.03$ was observed in the mass spectrum for the (2+) form.

7.3 Crystal Structure

The dinuclear $[(\mu\text{-adc-CF}_3)\{\text{Ru}(\text{bpy})_2\}_2]^{2+}$ ion was isolated and crystallized for structure determination in the *meso* form as the bis(hexafluorophosphate). The structure analysis, although marred by anion disorder and ill-defined solvent electron density, provided not only information on the identity of the isolated diastereoisomer (the *meso* form, Figure 7.3.1) but also additional essential parameters (Table 7.3.1).

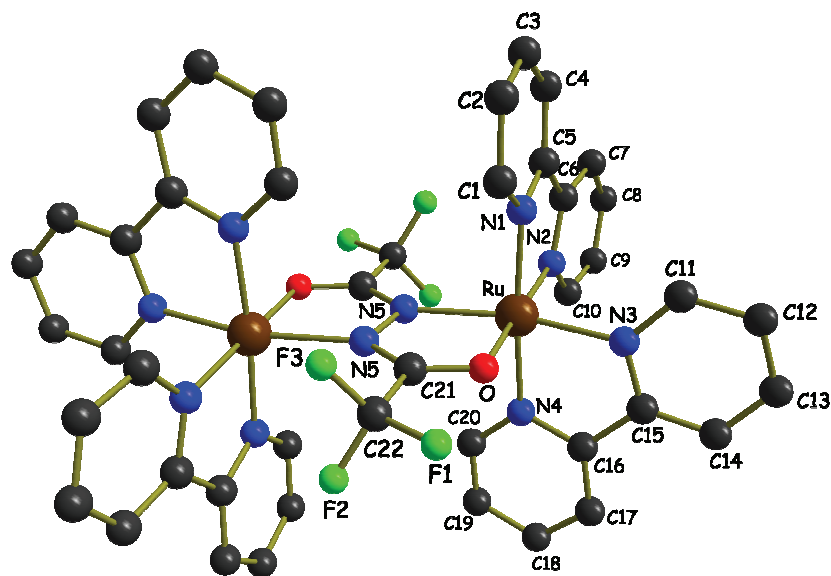


Figure 7.3.1. Molecular structure of the complex dication in the crystal of $[(\mu\text{-adc-CF}_3)\{\text{Ru}(\text{bpy})_2\}_2](\text{PF}_6)_2 \cdot 2 (\text{CH}_3)_2\text{CO}$. Counter anions and solvent molecules (solvent of crystallization) are omitted for clarity.

The Ru \cdots Ru distance was determined at 5.029(1) Å, a relatively short distance for a molecule bridged dinuclear species. The N-N bond length at 1.463(5) Å reveals a single bond and thus the hydrazido(2-) form of the bridge. The remaining structural data reveal an amide type resonance within the OCNCO framework, i.e. forming two N-connected carbamoyl functions. Two five-membered chelate rings thus share a common N-N edge in a largely planar arrangement, the angles are unspectacular with a small bite angle O-Ru-N of about 77° and a large amide angle O-C-N of 127.5(5)°.

Table 7.3.1. Selected bond lengths (Å) and angles (°) for $[(\mu\text{-adc-CF}_3)\{\text{Ru}(\text{bpy})_2\}_2](\text{PF}_6)_2 \cdot 2(\text{CH}_3)_2\text{CO}$.

Bonds	Lengths	Bonds	Angles(°)
C21-O	1.269(6)	C21-N5-N5	110.9(4)
C21-N5	1.311(6)	C21-O-Ru	112.4(3)
N5-N5	1.463(5)	N5-C21-O	128.1(4)
Ru-O	2.093(3)	N5-Ru-O	77.97(13)
N5-Ru	2.151(4)	Ru-N5-N5	111.7(2)
Ru-N4	2.073(5)	N4-Ru-N3	79.38(19)
Ru-N3	2.050(4)	N2-Ru-N1	79.16(19)
Ru-N2	2.085(4)	C22-C21-O	114.0(4)
Ru-N1	2.059(5)		
C21-C22	1.538(7)		

7.4 Cyclic voltammetry

Besides the expected^[55], rather invariant bpy-based reductions (2 two-electron waves at -1.89 and -2.19 V vs $\text{Fc}^{+/0}$), the electrochemical analysis by cyclic voltammetry in $\text{CH}_3\text{CN}/0.1 \text{ M Bu}_4\text{NPF}_6$ revealed two one-electron oxidation waves at +0.48 and +1.00 V vs $\text{Fc}^{+/0}$ with a (3+) intermediate (Figure 7.4.1). The comproportionation constant of $K_c = 10^{8.8}$ for that intermediate is not much different from those of the differently substituted analogues^[55], however, the potentials of the oxidation lie rather positive, in agreement with the acceptor character of the CF_3 substituents.

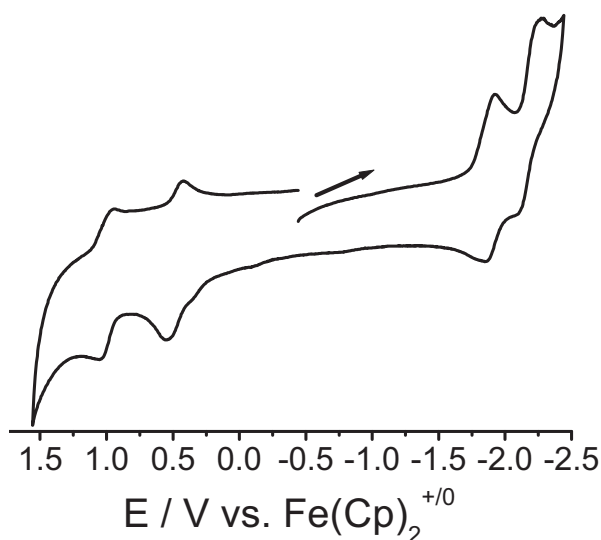


Figure 7.4.1. Cyclic voltammogram in $\text{CH}_3\text{CN} / 0.1 \text{ M Bu}_4\text{NPF}_6$ at room temperature, Scan rate 100mV/s.

7.5 UV-Vis-NIR spectroelectrochemistry

Two-step UV-Vis-NIR spectroelectrochemistry in $\text{CH}_2\text{Cl}_2/0.1 \text{ M Bu}_4\text{NPF}_6$ shows a typical^[55] absorption (Figure 7.5.1) for the intermediate at 1680 nm ($\epsilon = 9900 \text{ M}^{-1} \text{ cm}^{-1}$) which could be attributed to the intervalence charge transfer (IVCT) transition of a mixed-valent species or to a $\pi\text{-}\pi^*$ transition of a metal coordinated organic radical bridge^[55]. Neither the wavelength nor the intensity provide a straightforward criterion for differentiating between these two alternatives.

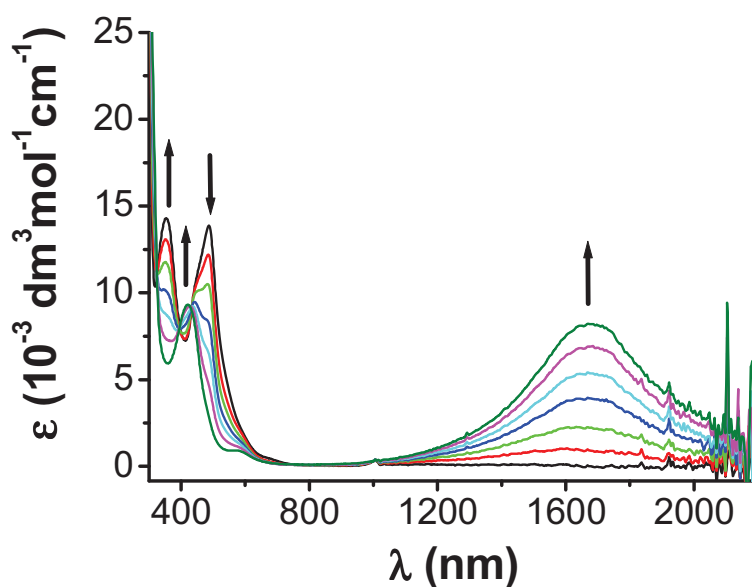


Figure 7.5.1. UV-vis-NIR spectroelectrochemical oxidation of $[(\mu\text{-adc-CF}_3)\{\text{Ru}(\text{bpy})_2\}_2]^{2+}$ in $\text{CH}_2\text{Cl}_2/0.1 \text{ M Bu}_4\text{NPF}_6$.

The absorption band for the $\text{Ru}^{\text{II}}\text{Ru}^{\text{III}}$ intermediate diminishes on further one-electron reduction to the $\text{Ru}^{\text{III}}\text{Ru}^{\text{III}}$ form (Figure 7.5.2). The spectroelectrochemical data of all the electrochemically generated species are presented in Table 7.5.1.

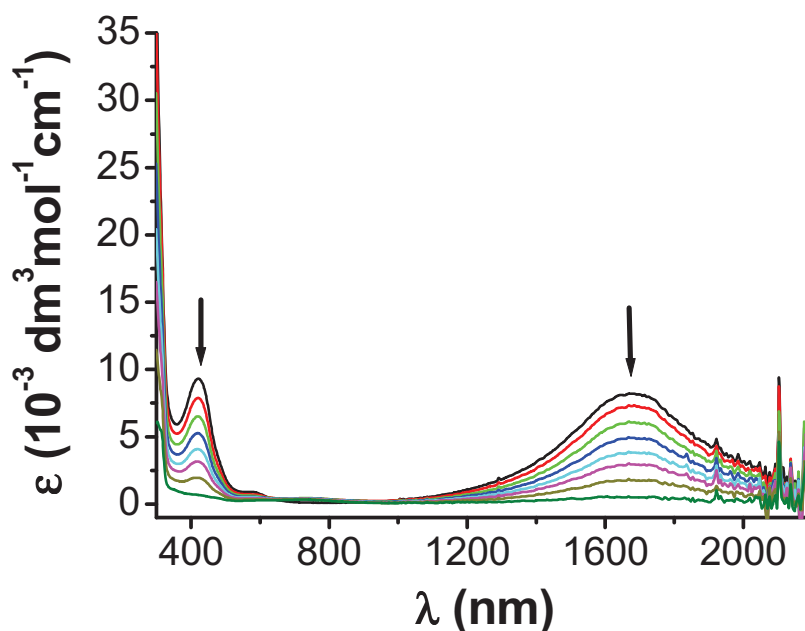


Figure 7.5.2. UV-Vis-NIR spectroelectrochemical second oxidation of $[(\mu\text{-adc-CF}_3)\{\text{Ru}(\text{bpy})_2\}_2]^{3+}$ in $\text{CH}_2\text{Cl}_2/0.1 \text{ M Bu}_4\text{NPF}_6$. (electrode adsorption).

Table 7.5.1. Data from UV-vis-NIR spectroelectrochemistry^{a)}

Compound	$\lambda_{\text{max}} / \text{nm} (\epsilon / 10^{-3} \text{ M}^{-1} \text{ cm}^{-1})$
$\mathbf{1}^{4+}$	304 (sh), 248 (7.40)
$\mathbf{1}^{3+}$	1680 (9.89), 486 (16.75), 410 (10.97), 290 (58.50)
$\mathbf{1}^{2+}$	486 (16.75), 356 (17.07), 290 (75.80)
$\mathbf{1}$	495 (sh), 367 (24.54), 290 (80.93)

^{a)}From spectroelectrochemistry in an OTTLE cell in $\text{CH}_3\text{CN} / 0.1 \text{ M Bu}_4\text{NPF}_6$ at 298 K. $\lambda_{\text{IVCT}} / \text{nm} (\epsilon / 10^{-3} \text{ M}^{-1} \text{ cm}^{-1}) = 1680$ (9.89), $\Delta\nu_{1/2}^a / \text{cm}^{-1} = 1724$.

7.6 EPR spectroscopy

As the literature reports evidenced^[55,27,164,167], EPR spectroscopy is a superb method for probing spin distribution and hence for the determination of charge and oxidation states. A radical complex should exhibit small g anisotropy due to the small contributions from the metals with their large spin orbit coupling constants whereas genuine mixed-valent complexes typically show large such g deviations from the free electron value at 2.0023^[167]. In addition, mixed-valent compounds with metal-based spin are frequently affected by short relaxation times which causes EPR silence at higher temperatures^[55]. Intermediate $[(\mu\text{-adc-CF}_3)\{\text{Ru}(\text{bpy})_2\}_2]^{3+}$ as generated by *intra muros* electrolysis (Figure 7.6.1) exhibits EPR parameters at $g_1 = 2.239$, $g_2 = 2.065$ and $g_3 = 1.891$ ($g_{\text{av}} = 2.101$, $\Delta g = g_1 - g_3 = 0.348$) which are values signifying considerable metal participation at the singly occupied MO (SOMO).

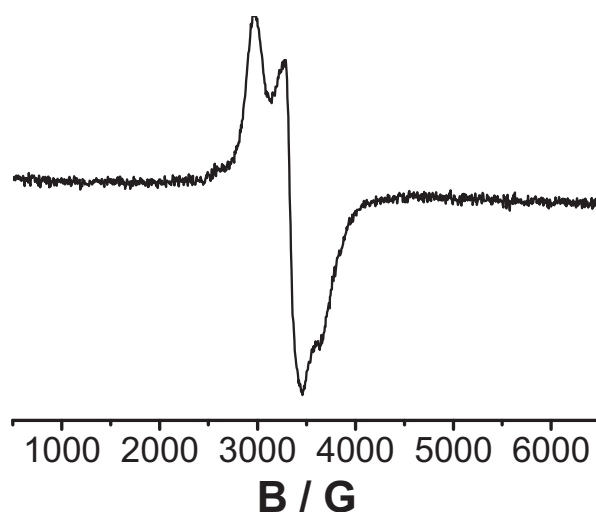


Figure 7.6.1. EPR spectrum of electrogenerated $[(\mu\text{-adc-CF}_3)\{\text{Ru}(\text{bpy})_2\}_2]^{3+}$ at 4 K in glassy frozen $\text{CH}_3\text{CN}/0.1 \text{ M Bu}_4\text{NPF}_6$ solution.

7.7 Conclusion

I have identified the $[(\mu\text{-adc-CF}_3)\{\text{Ru}(\text{bpy})_2\}_2]^{3+}$ intermediate as a $\text{Ru}^{\text{III}}\text{Ru}^{\text{II}}$ mixed-valent species involving an electron donating hydrazido(2-) bridging ligand. This understanding implies a hole transfer mechanism^[57] for the valence exchange in the excited state and an assignment of the strong near infrared absorption as the result of an predominant intervalence charge transfer (IVCT) transition. With a bandwidth of about 1700 cm^{-1} at half height this absorption is much narrower than the 4800 cm^{-1} that is calculated from the Hush equation $\Delta\nu(1/2) = (2310 \times \epsilon_{\text{max}})^{1/2}$ for localized mixed-valent systems, suggesting a valence-averaged situation in agreement with the high K_c value.

Chapter 8

Experimental Section

8.1. Instrumentation

^1H , ^{31}P and ^{19}F -NMR experiments at 250 MHz and 400 MHz were carried out by Ms. K. Török on Bruker AC-250 spectrometer and Bruker AM 400 MHz spectrometer. Tetramethylsilane (TMS) was used as an external chemical shift standard. Elemental analyses were carried out with a Perkin-Elmer 240C elemental analyser by Ms. B. Förtsch. Electrospray ionization mass spectra with positive ion polarity were recorded on Bruker Daltonics-microTOF-Q by Mr. J. Trinker and Ms. K. Wohlbold. Cyclic and Differential Pulse voltammetry measurements were performed on an EG&G PAR 273 potentiostat. The measurements were carried out under argon atmosphere in 0.1 M tetrabutylammonium hexafluorophosphate solutions using a three electrode configuration (glassy carbon as working electrode, platinum as counter electrode and silver as pseudoreference electrode). The ferrocene/ferrocenium ($\text{Fc}/\text{Fc}^{+/0}$) couple served as internal reference (+0.46 V vs. SCE). Polarography, bulk electrolysis and phase-sensitive alternating-current cyclic voltammetry was performed using a PAR 263A instrument. X-band EPR spectra at 9.5 GHz were obtained from Bruker system ESP 300 equipped with a Hewlett-Packard Frequency counter 5350B, a Bruker ER035M gaussmeter for g value determination. For 110K measurements, the same instrumental configurations were used with a liquid nitrogen cryostat. A two-electrode capillary^[168] served to electrogenerate intermediates for X-band EPR. The EPR measurements were carried out by Dr. Biprajit Sarkar and Dr. Brigitte Schwederski at Institut für Anorganische Chemie, Universität Stuttgart IR spectra were obtained using Perkin-Elmer FTIR 684 and 283 instruments or a Nicolet 6700 FT-IR spectrometer. The solid state IR measurements were performed with an ATR unit (smart orbit with diamond crystal) on a Nicolet 6700 FTIR instrument. UV–Vis absorption spectra were recorded on J& M TIDAS and Agilent 8453 diode array spectrophotometers. The measurements were done in solution using quartz cuvettes of 1 cm path length. Spectroelectrochemistry was performed under argon atmosphere using an optically transparent thin-layer electrode (OTTLE) cell developed by Dr. Krejčík^[169]. The windows of the cell consist of CaF_2 plates. Between the plates there is a spacer into which the working (platinum mesh), auxiliary (platinum mesh) and reference electrodes (silver wire as pseudo reference) are melt-sealed. The (spectro)electrochemical measurements were carried out by Dr. Jan Fiedler at the Institut für Anorganische Chemie,

Universität Stuttgart and at the J. Heyrovský Institute of Physical Chemistry, v.v.i., Academy of Sciences of the Czech Republic, Prague, Czech Republic

8.2. Solvents and working conditions

Solvents were dried by refluxing under argon atmosphere over calcium hydride (dichloromethane, acetonitrile, methanol ethanol and hexane), calcium chloride (acetone), sodium (toluene) or lithium aluminium hydride (diethyl ether). They were degassed by freeze-pumped-thaw method using argon as inert gas. All the air and moisture sensitive syntheses were performed under argon atmosphere using a standard Schlenk-line technique.

8.3. Syntheses

The following substances were commercially available

1,3,9-Trimethylxanthine (TMX) from Aldrich. Pentaaminechlororuthenium(III) dichloride from Alfa-aesar. 1, 1'-Bis(diphenylphosphino)ferrocene from Acros Organics. 2,3,5,6-tetrafluoro-7,7,8,8-tetracyano-*p*-quinodimethane (TCNQF₄) from TCI Europe. 9-Methylguanine (9MG) and 1,2,4,5-tetracyanobenzene from Fluka. 1, 1'-Bis(diisopropylphosphino)ferrocene and Ru(bpy)₂Cl₂ from ABCR. 1,1'-Bis(dicyclohexylphosphino)ferrocene (dchpf), alloxazine and 7,8-dimethylalloxazine from Sigma.

The following ligands were synthesized according to literature procedures

2-pivaloyl pterin^[81]. 2,2'-azobispyridine^[170]. 1,3-dimethylumazine^[79]. 1, 3 dimethyl-alloxazine^[80]. 1,3,7,8-tetramethylalloxazine^[80]. 2,2'-azobis(5-chloropyrimidine)^[28]. 1,2-bis(trifluoroacetyl)hydrazine^[165]

8.3.1. Synthesis of N2-pivaloyl-, 9-methylguanine (P-9MG)

A mixture of 133 mg (0.81 mmol) 9-methylguanine, 2 mg (0.02 mmol) 4-N,N dimethylaminopyridine (DMPA) and 5 ml trimethylacetic anhydride was stirred under reflux condition for 4 h. The obtained black reaction mixture was then slowly cooled to room temperature. Diethyl ether (50 mL) was added to the solution which was kept in the refrigerator for several hours. The brown precipitate formed was filtered and dissolved in dichloromethane. The solution was then dried completely and the obtained solid was chromatographed on a silica gel column (silical gel, mesh 60) using a MeOH / CH₂Cl₂ mixture (5:95). Further, the solid was crystallized from a saturated solution in dichloromethane and then dried under vacuum. Yield: 147 mg (73%). Anal. Calcd. for C₁₁H₁₅N₅O₂ (fw = 249.28) C, 53.00; H, 6.07; N, 28.10. Found: C, 53.03; H, 6.07; N, 27.99. ¹H NMR [250 MHz, CDCl₃, δ (ppm)]: 1.326 (m, 9H, ^tBu), 3.672 (s, 3H, CH₃), 7.64 (bs, 1H, -NH, P-9MG), 8.01 (s, 1H, -CH, P-9MG), 11.94 (bs, 1H, -NH, P-9MG). FT-IR/cm⁻¹ (solid): 1662(s), 1740(w) (ν_{C=O}).

8.3.2. Synthesis of copper(I) precursors

Synthesis of [Cu(dppf)(CH₃CN)₂](BF₄)

Synthesis and characterization of the precursor complexes [Cu(dppf)(CH₃CN)₂](BF₄) is reported in the literature^[82]. [Cu(CH₃CN)₄]BF₄ (300 mg, 0.95 mmol) and 1,1'-diphenylphosphinoferrocene (dppf) (500 mg, 0.95 mmol) were stirred at room temperature in dry acetonitrile for 8 h. Acetonitrile was removed from the yellow solution under reduced pressure to get the yellow solid. Yield: 500 mg (75 %). Anal. Calcd. for C₃₈H₃₄N₂B₁F₄P₂CuFe (fw = 768.8) C, 58.01; H, 4.36; N, 3.56. Found: C, 57.57; H, 4.55; N, 2.98. ¹H NMR [250 MHz, CD₂Cl₂, δ (ppm)]: 12.18 (s, 6H, CH₃CN), 4.09 (s, 4H, Cp), 4.27 (s, 4H, Cp), 7.28-7.62 (m, 20H, Ph);. ³¹P {¹H} NMR [CD₂Cl₂, δ (ppm)]: -13.8.

Synthesis of [Cu(dippf)(CH₃CN)₂](BF₄), [Cu(dippf)(CH₃CN)₂](PF₆) and [Cu(dchpf)(CH₃CN)](PF₆)

The precursor complexes [Cu(dippf)(CH₃CN)₂](BF₄), [Cu(dippf)(CH₃CN)₂](PF₆) and [Cu(dchpf)(CH₃CN)](PF₆) were synthesized following similar procedures for [Cu(dppf)(CH₃CN)₂](BF₄)^[82]. Room temperature overnight stirring of acetonitrile solution containing 1:1 mixtures of [Cu(CH₃CN)₄](BF₄) or [Cu(CH₃CN)₄](PF₆) and dippf or dchpf under argon, resulted the formation of the complexes. The detailed characterizations are given below.

[Cu(dippf)(CH₃CN)₂](BF₄): Yield: 80 %. ¹H NMR [250 MHz, CDCl₃, δ (ppm)]: 1.12-1.18 (m, 24H, P-CH-CH₃), 2.07 (s, 6H, CH₃CN), 3.61 (s, 3H, N-Me), 2.13 (m, 4H, P-CH-CH₃), 4.16 (s, br, 4H, Cp), 4.37 (t, br, 4H, Cp). ³¹P{¹H} NMR [CDCl₃, δ (ppm)]: 2.595. MS (ESI, Micromass Q-ToF): molecular ion peak centered at m/z = 481.09, corresponds to [Cu(dippf)]⁺.

[Cu(dippf)(CH₃CN)₂](PF₆): Yield: 96 %. Anal. Calcd. for C₂₆H₄₂N₂P₃F₆FeCu (fw = 708.95) C, 44.05; H, 5.97; N, 3.95. Found: C, 43.89; H, 6.02; N, 3.85. ¹H NMR [250 MHz, CD₂Cl₂, δ (ppm)]: 1.27 (m, 24H, P-CH-CH₃), 2.31 (m, br, 4H, P-CH-CH₃), 2.26 (s, 6H, CH₃CN), 4.31 (s, br, 4H, Cp), 4.54 (t, br, 4H, Cp). ³¹P{¹H} NMR [CD₂Cl₂, δ (ppm)]: 5.33 (s, dippf), -144.47 (sept, ¹J_{P-F} = 710.24 Hz, -PF₆).

[Cu(dchpf)(CH₃CN)₂](PF₆): Yield: 85 %. Anal. Calcd. for C₃₆H₅₅NP₃F₆FeCu (fw = 828.15) C, 52.21; H, 6.69; N, 1.69. Found: C, 52.42; H, 6.95; N, 1.62. ¹H NMR [250 MHz, CD₂Cl₂, δ (ppm)] 1.36 (m, 20H, dchpf), 1.90 (m, 24H, dchpf), 2.41 (s, 3H, CH₃CN), 4.24 (s, 4H, Cp), 4.52 (t, br, 4H, Cp). ³¹P{¹H} NMR [CD₂Cl₂, δ (ppm)]: -3.06 (s, dchpf), -144.48 (sept, ¹J_{P-F} = 710.31 Hz, PF₆). MS (ESI, Micromass Q-ToF): molecular ion peak centered at m/z = 642.2219, corresponds to [Cu(dchpf)]⁺.

8.3.3. Synthesis of copper(I)-lumazine complexes

A 1:1 mixture of 1,3-dimethylalumazine (DML) and the Cu^I precursor complex was taken in a Schlenk flask. Then 30 mL of dry and deoxygenated dichloromethane was added under argon atmosphere. The solution turned deep red immediately, and the mixture was stirred at RT overnight. The solvent was removed under reduced pressure and the obtained solid was washed several times with dry hexane. The red solid was crystallized from a dry dichloromethane/hexane (2:1) mixture at 4° C.

[Cu(dppf)(DML)](BF₄): Yield: 92%. Anal. Calcd. for C₄₂H₃₆BCuF₄FeN₄O₂P₂ (fw = 896.89) C, 56.24; H, 4.05; N, 6.25. Found: C, 55.15; H, 4.02; N, 6.09. ¹H NMR [250 MHz, CDCl₃, δ (ppm)]: 3.42 (s, 3H, N-CH₃), 3.71 (s, 3H, N-CH₃), 4.34 (s, 4H, Cp), 4.42 (s, 4H, Cp), 7.36 (m, br, 20H, Ph), 8.82 (s, br, 1H, DML), 9.09 (s, br, 1H, DML). ³¹P{¹H} NMR [CDCl₃, δ (ppm)]: -9.88 (s, dppf). FT-IR/cm⁻¹ (solid): 1712, 1643 (ν_{C=O}). MS (ESI, Micromass Q-ToF): molecular ion peak centered at m/z = 809.10, corresponds to [Cu(dppf)(DML)]⁺.

[Cu(dippf)(DML)](BF₄): Yield: 95 %. Anal. Calcd. for C₃₀H₄₄BCuF₄FeN₄O₂P₂ × CH₂Cl₂ (fw = 845.76) C, 44.02; H, 5.48; N, 6.62. Found: C, 44.18; H, 5.44; N, 6.58. ¹H NMR [250 MHz, CDCl₃, δ (ppm)]: 1.07 (dd, ³J_{H-H} = 7.1 Hz, ³J_{P-H} = 15.5, 12H, P-CH-CH₃), 1.22 (dd, ³J_{H-H} = 7.1 Hz, ³J_{P-H} = 15.3, 12H, P-CH-CH₃), 2.15 (m, 4H, P-CH-CH₃), 3.61 (s, 3H, N-Me), 3.78 (s, 3H, N-Me), 4.37 (s, br, 4H, Cp), 4.47 (t, br, 4H, Cp), 8.85 (d, ²J_{H-H} = 2.5 Hz, 1H, DML), 9.12 (s, br, 1H, DML). ³¹P{¹H} NMR [CDCl₃, δ (ppm)]: 4.41 (s, dippf). FT-IR/cm⁻¹ (solid): 1707, 1647 (ν_{C=O}).

8.3.4. Synthesis of copper(I)-alloxazine complexes

A mixture of the alloxazine (DMA or TMA) and the Cu^I precursor complex was prepared in 1:1 ratio in a Schlenk flask. Then 30 mL of dry and deoxygenated dichloromethane were added under argon atmosphere. The solution turned deep red immediately and the mixture was stirred at room temperature overnight. The solvent was removed under reduced pressure and the obtained solid was washed several times with dry hexane. The red solid was crystallized from dry dichloromethane/hexane (2:1) mixture at 4° C.

[Cu(dppf)(DMA)](BF₄): Yield: 88 %; Anal. Calcd. for C₄₆H₃₈BCuF₄FeN₄O₂P₂ × CH₂Cl₂ (fw = 1031.91) C, 54.71; H, 3.91; N, 5.43. Found: C, 54.68; H, 3.89; N, 5.42. ¹H NMR[CD₂Cl₂, 250 MHz, δ(ppm)]: 3.39 (s, 3H, N-CH₃), 3.87 (s, 3H, N-CH₃), 4.94 (s, 4H, Cp), 4.57 (s, 4H, Cp), 7.34-7.44 (m, br, 20H, -Ph), 7.68 (t, br, 1H, DMA), 8.05 (t, br, 2H, DMA), 8.20 (d, br, 1H, DMA). ³¹P NMR[CD₂Cl₂, 250 MHz, δ(ppm)]: -7.22. FT-IR/cm⁻¹ (solid): 1715, 1644 (ν_{C=O}). MS (ESI, Micromass Q-ToF): molecular ion peak centered at m/z = 860.10, corresponds to [Cu(dppf)(DMA)]⁺.

[Cu(dppf)(TMA)](BF₄): Yield: 92%. Anal. Calcd. for C₄₈H₄₂BCuF₄FeN₄O₂P₂ × CH₂Cl₂ (fw = 1059.92) C, 55.52; H, 4.18; N, 5.29. Found: C, 55.48; H, 4.15; N, 5.28. ¹H NMR [250 MHz, CD₂Cl₂, δ(ppm)]: 2.25 (s, 3H, Me), 2.57 (s, 3H, Me), 3.37 (s, 3H, N-CH₃), 3.83 (s, 3H, N-CH₃), 4.44 (s, br, 4H, Cp), 4.55 (s, 4H, Cp), 7.39 (m, br, 20H, Ph), 7.80 (s, 1H, TMA), 7.94 (s, 1H, TMA). ³¹P {¹H} NMR [CD₂Cl₂, δ (ppm)]: -7.50 (s, dppf). FT-IR/cm⁻¹ (solid): 1713, 1640 (ν_{C=O}). MS (ESI, Micromass Q-ToF): molecular ion peak centered at m/z = 888.15, corresponds to [Cu(dppf)(TMA)]⁺.

[Cu(dippf)(DMA)](BF₄): Yield: 82 %; Anal. Calcd. for C₃₄H₄₆BCuF₄FeN₄O₂P₂ (fw = 810.92) C, 50.36; H, 5.72; N, 6.91. Found: C, 49.98; H, 5.68; N, 6.84. ¹H NMR[CD₂Cl₂, 250 MHz, δ(ppm)]: 1.06 (m, 12H, P-CH-CH₃), 1.23 (dd, , ³J_{H-H} = 7.2 Hz, ³J_{P-H} = 15.5 Hz, 12H, P-CH-CH₃), 2.22 (m, 4H, P-CH-CH₃), 3.72 (s, 3H, N-Me), 3.92 (s, 3H, N-Me), 4.50 (s, br, 4H, Cp), 4.58 (t, br, 4H, Cp), 8.02 (m, 1H, DMA), 8.15 (m, 1H, DMA), 8.28 (m, 1H, DMA), 8.64 (m, 1H, DMA). ³¹P {¹H} NMR[CD₂Cl₂, δ(ppm)]: 4.61. FT-IR/cm⁻¹ (solid): 1718(s), 1652(vs) (ν_{C=O}).

8.3.5. Synthesis of copper(I)-pterin complexes

Synthesis of [Cu(dppf)(PP)](BF₄) and [Cu(dippf)(PP)](BF₄)

The pterin complexes were synthesized by a reaction of a 1:1 mixture of PP and the metal precursor in degassed dichloromethane under argon atmosphere. Immediately after the addition of dichloromethane, a red colour developed. The solution was stirred overnight and then the solvent removed under reduced pressure. The obtained solid complex was repeatedly washed with a mixture of hexane and dichloromethane (4:1) to remove the impurities. The pure product was obtained after several recrystallizations from hexane-dichloromethane mixture (1:1) at 4°C.

[Cu(dppf)(PP)](BF₄): Yield: 85 %. Anal. Calcd. for C₄₅H₄₁BCuF₄FeN₅O₂P₂ × 2CH₂Cl₂ (fw = 1036.93) C, 53.28; H, 4.18; N, 6.75. Found: C, 53.26; H, 4.15; N, 6.74. ¹H NMR [250 MHz, CDCl₃, δ (ppm)]: 1.29 (s, 9H, ^tBu), 4.34(s, 4H, Cp), 4.41(s, 4H, Cp), 7.35 (m, br, 20H, -Ph), 8.86 (s, br, 1H, PP), 8.99 (s, br, 1H, PP), ³¹P{¹H} NMR [CD₂Cl₂, δ (ppm)]: -10.22 (s, dppf). FT-IR/cm⁻¹ (solid): 1660(w), 1614(s) (ν_{C=O}). MS (ESI, Micromass Q-ToF): molecular ion peak centered at m/z = 864.14, corresponds to [Cu(dppf)(PP)]⁺.

[Cu(dippf)(PP)](BF₄): Yield: 82 %. Anal. Calcd. for C₃₃H₄₉BCuF₄FeN₅O₂P₄ × CH₂Cl₂ (fw = 974.82) C, 43.12; H, 5.27; N, 7.18. Found: C, 43.05; H, 5.21; N, 7.13. ¹H NMR [250 MHz, CD₂Cl₂, δ (ppm)]: 1.06 (dd, ³J_{H-H} = 7.2 Hz, ³J_{P-H} = 15.2 Hz, 12H, P-CH-CH₃), 1.24 (m, 12H, P-CH-CH₃), 1.38 (s, 9H, ^tBu), 2.15 (m, 4H, P-CH-CH₃), 4.39 (s, 4H, Cp), 4.46 (s, 4H, Cp), 9.01 (s, br, 2H, PP), 9.40(s, br, 1H, NH, PP), 12.38 (s, br, 1H, NH, PP). ³¹P{¹H} NMR [CD₂Cl₂, δ (ppm)]: 4.66 (s, dppf). FT-IR/cm⁻¹ (solid): 1665(s), 1612(s) (ν_{C=O}). MS (ESI, Micromass Q-ToF): molecular ion peak centered at m/z = 728.80, corresponds to [Cu(dippf)(PP)]⁺.

Synthesis of $[\{\text{Cu}(\text{dppf})\}_2(\text{PP})](\text{BF}_4)_2$ and $[\text{Cu}_3(\text{dppf})(\mu_2\text{-dppf})(\text{PP})(\text{PP}^-)]_2(\text{BF}_4)_4$

An amount of 100 mg (0.13 mmol) of $[\text{Cu}(\text{dppf})(\text{CH}_3\text{CN})_2](\text{BF}_4)$ and 63 mg (0.25 mg) of pivaloylpterin (PP) were taken in a Schlenk flask flushed with argon several times. Then 30 mL of dry dichloromethane was added into the flask. The solution immediately turned deep red, and the stirring was continued overnight. All solvents were evaporated under reduced pressure and the obtained solid was washed several times with a hexane/dichloromethane mixture (2/1). Crystallization of the material was carried out from dichloromethane solution at 4°C. The solid mass was characterized as a pure form of $[\{\text{Cu}(\text{dppf})\}_2(\text{PP})](\text{BF}_4)_2$, which through converted to identified (by X-ray crystallography) $[\text{Cu}_3(\text{dppf})(\mu_2\text{-dppf})(\text{PP})(\text{PP}^-)]_2(\text{BF}_4)_4$.

$[\{\text{Cu}(\text{dppf})\}_2(\text{PP})](\text{BF}_4)_2$: Yield: 90 %. Anal. Calcd. for $\text{C}_{79}\text{H}_{69}\text{B}_2\text{Cu}_2\text{F}_8\text{Fe}_2\text{N}_5\text{O}_2\text{P}_4 \times 3 \text{CH}_2\text{Cl}_2$ (fw = 1911.54) C, 51.52; H, 3.95; N, 3.66. Found: C, 51.13; H, 3.75; N, 3.52. ^1H NMR $[\text{CD}_2\text{Cl}_2, 250 \text{ MHz}, \delta \text{ (ppm)}]$: 0.10 (s, 9H, ^tBu), 4.39 (s, 8H, Cp), 4.50 (s, 8H, Cp), 7.35-7.44 (m, br, 40H, -Ph), 8.80 (s, br, 1H, PP), 8.92 (s, br, 1H, PP), 9.42 (s, br, 1H, NH, PP), 12.49 (s, br, 1H, NH, PP). $^{31}\text{P}\{^1\text{H}\}$ NMR $[\text{CD}_2\text{Cl}_2, \delta \text{ (ppm)}]$: -10.66 (s, dppf). FT-IR/ cm^{-1} (solid): 1736, 1692, 1613 ($\nu_{\text{C=O}}$). MS (ESI, Micromass Q-ToF): molecular ion peak centered at $m/z = 1481.16$, corresponds to $[\{\text{Cu}(\text{dppf})\}_2(\text{PP})]^+$.

8.3.6. Synthesis of copper-purine complexes

A 1:1 mixture of ligand and metal-precursor complex was taken in 25 mL dry and deoxygenated dichloromethane. The mixture was then stirred at room temperature under argon atmosphere for overnight. The solvent was removed under reduced pressure and the obtained solid was washed several times with dry hexane. The solid was crystallized from dry dichloromethane/hexane (2:1) mixture at 4°C.

$[\text{Cu}(\text{dppf})(\text{P-9MG})](\text{BF}_4)$: Yield: 91%. Anal. Calcd. for $\text{C}_{45}\text{H}_{43}\text{BCuF}_4\text{FeN}_5\text{O}_2\text{P}_2 \times \text{CH}_2\text{Cl}_2$ (fw = 1038.95) C, 53.18; H, 4.37; N, 6.74. Found: C, 53.44; H, 4.46; N, 6.71. ^1H NMR $[\text{CD}_2\text{Cl}_2, 250 \text{ MHz}, \delta \text{ (ppm)}]$: 1.28 (s, 3H, CH_3), 1.36 (s, 9H, ^tBu), 4.37 (s, 4H, Cp), 4.45 (s, 4H, Cp), 7.35-7.54 (m, 20H, Ph), 8.11 (s, 1H, N-H), 8.53 (s, 1H, CH, TMX), 12.17 (s, 1H, NH). $^{31}\text{P}\{^1\text{H}\}$ NMR $[\text{CD}_2\text{Cl}_2, \delta \text{ (ppm)}]$: -13.76 (s, dppf). FT-IR/ cm^{-1} (solid): 1701(w), 1673(s), 1662(s), 1606(s) ($\nu_{\text{C=O}}$). MS (ESI, Micromass Q-ToF): molecular ion peak centered at $m/z = 866.15$, corresponds to $[\text{Cu}(\text{dppf})(\text{P-9MG})]^+$.

[Cu(dppf)(TMX)](BF₄): Yield: 95 %. Anal. Calcd. for C₄₂H₃₈BCuF₄FeN₄O₂P₂ × 2CH₂Cl₂ (fw = 1068.76) C, 49.45; H, 3.96; N, 5.24. Found: C, 49.41; H 3.85; N, 5.21. ¹H NMR [CD₂Cl₂, 250 MHz, δ(ppm)]: 3.20 (s, 3H, N-CH₃), 3.78 (s, 3H, N-CH₃), 4.11 (s, 3H, N-CH₃), 4.37 (s, 4H, Cp), 4.46 (t, br, 4H, Cp), 7.36-7.53 (m, 20H, Ph), 7.80 (s, 1H, CH, TMX). ³¹P{¹H} NMR [CD₂Cl₂, δ(ppm)]: -13.50. FT-IR/cm⁻¹ (solid): 1704, 1657 (νC=O).

[Cu(dippf)(TMX)](PF₆): Yield: 91%. Anal. Calcd. for C₃₀H₄₆CuF₆FeN₄O₂P₃ (fw = 821.01) C, 43.89; H, 5.65; N, 6.82. Found: C, 43.79; H, 3.72; N, 6.85. ¹H NMR [CD₂Cl₂, 250 MHz, δ (ppm)]: 1.13 (dd, ³J_{H-H} = 7.1Hz, ³J_{P-H} = 14.9, 12H, P-CH-CH₃), 1.26 (dd, ³J_{H-H} = 7.2 Hz, ³J_{P-H} = 15.5, 12H, P-CH-CH₃), 2.21 (m, br, 4H, P-CH-CH₃), 3.43 (s, 3H, N-CH₃), 3.81 (s, 3H, N-CH₃), 4.10 (s, 3H, N-CH₃), 4.40 (s, 4H, Cp), 4.51 (s, 4H, Cp), 7.73 (s, 1H, CH, TMX). ³¹P{¹H} NMR [CD₂Cl₂, δ (ppm)]: 2.11 (s, dippf), -144.45 (sept, ¹J_{P-F} = 710.54 Hz, -PF₆). FT-IR/cm⁻¹ (solid): 1706, 1660 (νC=O). MS (ESI, Micromass Q-ToF): molecular ion peak centered at m/z = 675.17, corresponds to [Cu(dippf)(TMX)]⁺.

[Cu(dchpf)(TMX)](PF₆): Yield: 95 %. Anal. Calcd. for C₄₂H₆₂CuF₆FeN₄O₂P₃ × CH₂Cl₂ (fw = 1066.18) C, 48.44; H, 6.05; N, 5.25. Found: C, 48.34; H, 5.95; N, 5.20. ¹H NMR [CD₂Cl₂, 250 MHz, δ (ppm)]: 1.28 (m, 20H, dchpf), 1.83 (m, 24H, dchpf), 3.45 (s, 3H, N-CH₃), 3.82 (s, 3H, N-CH₃), 4.10 (s, 3H, N-CH₃), 4.34 (s, 4H, Cp), 4.49 (s, 4H, Cp), 7.64 (s, 1H, CH, TMX). ³¹P{¹H} NMR [CD₂Cl₂, δ (ppm)]: -5.75 (s, dchpf), -144.42 (sept, ¹J_{P-F} = 710.83 Hz, -PF₆). IR/cm⁻¹ (solid): 1707, 1662 (νC=O).

8.3.7. Synthesis of abcp- and abpy-bridged heteronuclear complexes

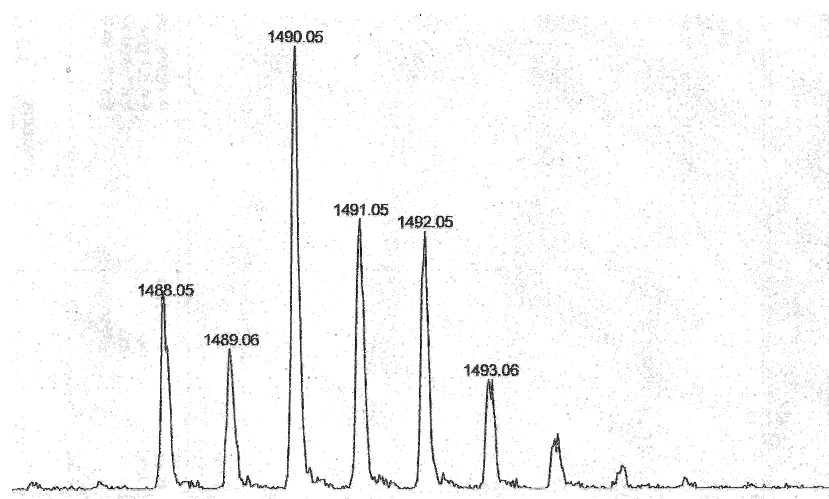
Synthesis of {(μ-abcp)[Cu(dppf)]₂}(BF₄)₂

A mixture of abcp (16.21 mg, 0.064 mmol) and [Cu(dppf)(CH₃CN)₂](BF₄) (100 mg, 0.127 mmol) in 30 ml of dry dichloromethane was stirred overnight under argon to give a green solution. After removal of the solvent, the solid was washed with hexane and crystallized from dichloromethane/hexane (1/6) at 4°C. Yield: 79.3 mg (75%). Anal. Calcd. for C₇₆H₆₀B₂Cl₂Cu₂F₈Fe₂N₆P₄ × 2CH₂Cl₂ (fw = 1834.33) C, 51.07; H, 3.52; N, 4.58. Found: C, 51.03; H, 4.11; N, 5.24. ¹H NMR [CDCl₃, 250 MHz, δ (ppm)]: 4.54 (m, 16H, Cp), 6.97-7.46 (m, br, 40H, Ph), 8.24 (s, br, 2H, abcp), 8.86 (s, br, 2H, abcp). ³¹P NMR [CDCl₃, δ (ppm)]: -14.13. MS (ESI, Micromass Q-ToF): M-1 peak at m/z = 1490.1, corresponds to [(μ-abcp)[Cu(dppf)]₂]-H]⁺ (calculated m/z = 1489.94).

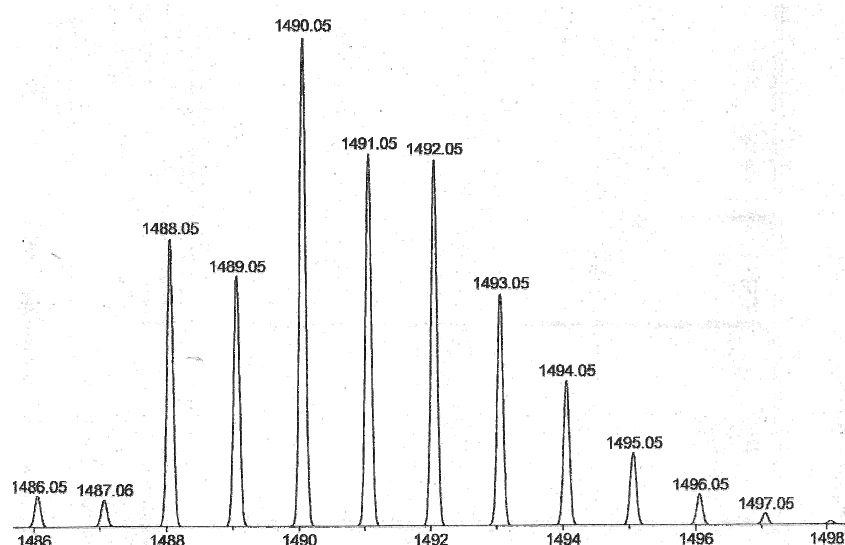
Synthesis of $\{(\mu\text{-abcp})[\text{Cu}(\text{dppf})_2]\}(\text{BF}_4)$

18.3 mg of $\{(\mu\text{-abcp})[\text{Cu}(\text{dppf})_2]\}(\text{BF}_4)_2$ was dissolved in 8 mL $\text{CH}_2\text{Cl}_2 / \text{Bu}_4\text{NBF}_4$ and stepwise electrolyzed at a mercury surface with 0.94 F dc current. After complete electrolysis, indicated by the absence of the polarographic maxima of the first reduction process, the solution was transferred to a Schlenk flask under argon atmosphere. The polarographic experiment indicated no over-reduction or decomposition even after 15 minutes. The solvent was removed under reduced pressure to yield a brown solid which was characterized crystallographically as $\{(\mu\text{-abcp})[\text{Cu}(\text{dppf})_2]\}(\text{BF}_4)$ after crystallization by diffusion of hexane into a dichloromethane solution of the electrolyzed product at 4°C. Yield : 14.2 mg (81.8 %). MS (ESI, Micromass Q-ToF): peak at $m/z = 1488.05$, corresponds to $[\mathbf{1}]^+$ (calculated $m/z = 1488.05$).

Experimental mass spectrum



Simulated mass spectrum



Synthesis of $[(\mu\text{-abpy})\text{Cu}(\text{dippf})](\text{BF}_4)$

$[\text{Cu}(\text{dippf})(\text{CH}_3\text{CN})_2]\text{BF}_4$ (260 mg, 0.4 mmol) and 2,2'-azobispyridine (74 mg, 0.4 mmol) in 20 ml of dry dichloromethane were stirred at room temperature for 8 hours under argon. During this time the solution turned violet. After removal of the solvent the solid was washed with hexane and crystallized from dichloromethane/hexane (1/3). Yield: 230 mg (76.4%). Anal. Calcd. for $\text{C}_{32}\text{H}_{44}\text{BCuF}_4\text{FeN}_4\text{P}_2$ (fw = 752.88) C, 51.05; H, 5.89; N, 7.44. Found: C, 50.79; H, 5.90; N, 7.22. ^1H NMR [CD_2Cl_2 , 250 MHz, δ (ppm)]: 0.91 (dd, $^3J_{\text{H-H}} = 7.2$ Hz, $^3J_{\text{P-H}} = 15.1$, 12H, P-CH-CH₃), 1.05 (dd, $^3J_{\text{H-H}} = 7.1$ Hz, $^3J_{\text{P-H}} = 15.3$, 12H, P-CH-CH₃), 2.16 (m, br, 4H, P-CH-CH₃), 4.43 (s, 4H, Cp), 4.61 (s, 4H, Cp), 7.85 (t, $^3J_{\text{H-H}} = 7.2$ Hz, 2H, abpy), 8.25 (t, $^3J_{\text{H-H}} = 6.5$ Hz, 2H, abpy), 8.43 (d, $^3J_{\text{H-H}} = 6.4$ Hz, 2H, abpy), 9.08 (s, br, 2H, abpy). ^{31}P NMR [CD_2Cl_2 , δ (ppm)]: 4.13. MS (ESI, Micromass Q-ToF): molecular ion peak at $m/z = 665.17$, corresponds to $[(\mu\text{-abpy})\text{Cu}(\text{dippf})]^+$.

8.3.8. Synthesis of $[\{\text{Ru}(\text{NH}_3)_5\}(\mu_4\text{-TCNQF}_4)](\text{PF}_6)_8$

An amount of 150 mg (0.51 mmol) of pentaamminechlororuthenium(III) dichloride was dissolved in hot water, then the cooled solution was reacted with freshly prepared Zn-Hg at room temperature under argon atmosphere for about 1 hour. After reduction was completed, the mixture was filtered over a celite bed in the absence of air. An acetone solution of 27.6 mg (0.1 mmol) tetrafluorotetracyanoquinodimethane was then added slowly to the filtered solution. A green colour developed immediately, and the solution was stirred for 15 h. A saturated ammonium hexafluorophosphate solution in H_2O was then added to the reaction mixture to precipitate the green compound which was washed repeatedly with an acetone/diethylether mixture (6/1). Finally, the solution was dried under reduced pressure and crystallized from acetone/dichloromethane at 4 °C. Yield: 170 mg (76%); Anal. Calcd. for $\text{C}_{12}\text{H}_{60}\text{F}_{52}\text{N}_{24}\text{P}_8\text{Ru}_4 \times 3 \text{CH}_3\text{COCH}_3$ (fw = 2355.06) C, 10.71; H, 3.34; N, 14.27. Found: C, 10.74; H, 3.24; N, 14.74. ^1H NMR [acetone-d₆, 250 MHz, δ (ppm)]: 2.79 (s, br, 12H, NH₃, ax), 3.19 (s, br, 48H, NH₃, eq). ^{19}F NMR [acetone-d₆, 400 MHz, δ (ppm)]: -71.11 (d, $^1J_{\text{P-F}} = 710$ Hz, 48F, PF₆), -147.80 (s, br, 4F, TCNQF₄). FT-IR /cm⁻¹ (CH₃CN): 2149, 2099 ($\nu_{\text{C=N}}$).

8.3.9. Synthesis of copper(I)-TCNB complexes

Synthesis of $[\text{Cu}(\text{dppf})(\text{TCNB})]_2(\text{BF}_4)_2$.

TCNB and the precursor complex $[\text{Cu}(\text{dppf})(\text{CH}_3\text{CN})_2](\text{BF}_4)$ were taken in 1:1 ratio in a Schlenk flask under argon. After addition of 30 mL of dichloromethane, the solution immediately turned red. The reaction mixture was then stirred overnight under argon. Solvents were removed under reduced pressure and the solid washed with hexane-dichloromethane mixture (3:1). Crystallization of the material was performed by slow diffusion of hexane into the dichloromethane solution under argon atmosphere at 4 °C. Yield: 92%; Anal. Calcd. for $\text{C}_{88}\text{H}_{60}\text{B}_2\text{Cu}_2\text{F}_8\text{Fe}_2\text{N}_8\text{P}_4 \times \text{CH}_2\text{Cl}_2$ (fw = 1850.73) C, 57.76; H, 3.38; N, 6.05. Found: C, 56.94; H, 3.82; N, 6.14. ^1H NMR [CD_2Cl_2 , 250 MHz, δ (ppm)]: 4.24 (s, 8H, Cp), 4.45 (s, 8H, Cp), 7.44-7.49 (m, br, 40H, Ph), 8.20 (s, 4H, TCNB). ^{31}P NMR [CD_2Cl_2 , δ (ppm)]: -11.49.

Synthesis of $[\{\text{Cu}(\text{dchpf})\}_4(\text{TCNB})](\text{BF}_4)_4$

The synthesis was carried out by following the above procedure for $[\text{Cu}(\text{dppf})(\text{TCNB})]_2(\text{BF}_4)_2$. Reaction from 1:4 ratio of TCNB and $[\text{Cu}(\text{dchpf})(\text{an})](\text{BF}_4)$ yielded the desired product. Yield: 84%; Anal. Calcd. for $\text{C}_{146}\text{H}_{210}\text{B}_4\text{Cu}_4\text{F}_{16}\text{Fe}_4\text{N}_4\text{P}_8 \times 2\text{CH}_2\text{Cl}_2 \times \text{CH}_3\text{CN}$ (fw = 3304.82) C, 54.52; H, 6.62; N, 2.12. Found: C, 54.49; H, 6.68; N, 2.14. ^1H NMR [CD_2Cl_2 , 250 MHz, δ (ppm)]: 1.32 (m, 80H, cyclohexyl), 1.86 (m, 96H, cyclohexyl), 4.28 (s, 16H, Cp), 4.52 (s, 16H, Cp), 8.59 (s, 2H, TCNB). ^{31}P NMR [CD_2Cl_2 , δ (ppm)]: -2.46. FT-IR/ cm^{-1} (in KBR palette): 2244 (vw).

8.3.10. Synthesis of $[\{(\text{bpy})_2\text{Ru}\}_2(\mu\text{-adc-CF}_3)](\text{PF}_6)_2$

A 100 mg (0.19 mmol) sample of *cis*- $\text{Ru}(\text{bpy})_2\text{Cl}_2 \cdot 2\text{H}_2\text{O}$ and 21 mg (0.095 mmol) of $\text{H}_2\text{adc-CF}_3$ were heated with 20 mg (0.5 mmol) of sodium hydroxide in 60 ml of a water/ethanol mixture (5/1) for 24 h under reflux. After cooling to room temperature and addition of 1 g of ammonium hexafluorophosphate dissolved in 40 ml of water, the precipitated complex was filtered off and dried in vacuum. Dissolution of the material in acetone, re-precipitation with diethyl ether for several times, and drying under vacuum afforded the brown complex. Yield: 65 mg (50%); Anal. Calcd for $\text{C}_{44}\text{H}_{32}\text{F}_{18}\text{N}_{10}\text{O}_2\text{P}_2\text{Ru}_2$ (fw = 1338.89) C, 39.47; H, 2.41; N, 10.46. Found: C, 40.90; H, 2.80; N, 9.73. MS (ESI, Micromass Q-ToF): $m/z = 1195.03$ (M); ^1H NMR [acetone- d_6 , δ (ppm)]: 7.21-7.45 (5H, m, bpy); 7.50-7.63 (2H, m, bpy); 7.73-8.02 (8H, m, bpy); 8.15-8.42 (6H, m, bpy); 8.56-8.69 (5H, m, bpy); 8.79-8.84 (4H, m, bpy); 9.00-

9.10 (2H, m, bpy); ^{19}F NMR [acetone- d_6 , $\delta(\text{ppm})$]: -66.89 (s, $-\text{CF}_3$, 60%); -67.12 (s, $-\text{CF}_3$, 40%); -72.62 (d, $-\text{PF}_6$).

8.4. Crystallography

Crystallographic data collection was carried out in the Institute for Inorganic Chemistry, University of Stuttgart, and the Department of Chemistry, Indian Institute of Technology, Bombay. The crystals were covered with a paraffin oil and sealed in capillaries for the measurements. The selected single crystals were instantly mounted in a liquid nitrogen stream for the diffraction measurement.

Single crystal X-ray diffraction data collection for $[\text{Cu}(\text{dppf})(\text{DML})](\text{BF}_4)$, $\{[\text{Cu}(\text{dppf})(\mu_2\text{-TCNB})](\text{BF}_4)\}_2 \cdot 3\text{CH}_2\text{Cl}_2 \cdot 3\text{H}_2\text{O}$ and $\{[(\mu_2\text{-TCNB})\text{Cu}(\text{dppf})]_2(\text{BF}_4)_2\}_n \cdot \text{CH}_2\text{Cl}_2$ were performed on a CCD Oxford Diffraction XCALIBURS diffractometer equipped with an Oxford Instruments low temperature attachment. Data were collected at 150 K using graphite-monochromated Mo-K α radiation ($\lambda = 0.71073 \text{ \AA}$). The strategy for the data collection was evaluated by using the CrysAlisPro CCD software. The data were collected by the standard phi-omega scan techniques, and were scaled and reduced using the CrysAlisPro RED software.^[171]

Data of $[\text{Cu}(\text{dippf})(\text{DML})](\text{BF}_4) \cdot \text{CH}_2\text{Cl}_2$, $[\text{Cu}(\text{dppf})(\text{TMA})](\text{BF}_4) \cdot \text{CH}_2\text{Cl}_2$, $[\text{Cu}_3(\text{dppf})(\mu_2\text{-dppf})(\text{PP})(\text{PP}^-)]_2(\text{BF}_4)_4 \cdot 5\text{CH}_2\text{Cl}_2$, $[\text{Cu}(\text{dppf})(\text{P-9MG})](\text{BF}_4) \cdot 5\text{CH}_2\text{Cl}_2$, $[\text{Cu}_3(\text{P9MG}^-)_2(\mu\text{-dppf})_2]_2(\text{BF}_4)_2$, $[\text{Cu}(\text{dppf})(\text{TMX})](\text{BF}_4) \cdot 2\text{CH}_2\text{Cl}_2$, $[\text{Cu}(\text{dippf})(\text{TMX})](\text{PF}_6)$, $[\text{Cu}(\text{dchpf})(\text{TMX})](\text{PF}_6) \cdot \text{CH}_2\text{Cl}_2$, $\{(\mu\text{-abcp})[\text{Cu}(\text{dppf})]_2\}(\text{BF}_4)_2 \cdot 2\text{CH}_2\text{Cl}_2$, $\{(\mu\text{-abcp})[\text{Cu}(\text{dppf})]_2\}(\text{BF}_4) \cdot 2\text{CH}_2\text{Cl}_2$, and $\{(\mu\text{-abpy})\text{Cu}(\text{dippf})\}(\text{BF}_4)$ were collected on four circle diffractometer NONIUS Kappa-CCD with a Mo-K α radiation of 0.71073 \AA (graphite-monochromated) at 100 K.

The selected single crystals of $[\{(\text{bpy})_2\text{Ru}\}_2(\mu\text{-adc-CF}_3)](\text{PF}_6)_2$ were measured using MoK α radiation (0.71073 \AA) at 173(2) K with a Siemens P4 diffractometer employing the ω -2 θ scan technique.

The structures were solved via direct methods using the programme SHELXS-97^[172]. Refinement was carried out by the full matrix least squares method employing the programme SHELXL-97.^[174] All non-hydrogen atoms are refined anisotropically, hydrogen atoms were introduced in proper positions with coupled isotropic factors using the riding model.

Absorption corrections were performed numerically using the programme HABITUS^[175]. The programme DIAMOND 2.1^[174] was used for structure drawing.

Crystallographic parameters:

$$R = (\sum | |F_o| - |F_c| |) / \sum |F_o|$$

$$WR = \{ \sum [w(|F_o|^2 - |F_c|^2)^2] / \sum [w(F_o^4)] \}^{1/2}$$

$$GOF = \{ \sum w(|F_o|^2 - |F_c|^2)^2 / (n - m) \}^{1/2} \text{ where } n = \text{number of data and } m = \text{number of variables}$$

Table 8.4.1. Crystallographic data and refinement parameters for [Cu(dppf)(DML)](BF₄)

Empirical formula	C ₄₂ H ₃₆ BCuF ₄ FeN ₄ O ₂ P ₂
Formula mass (g / mol)	896.89
<i>T</i> (K)	150(2)
λ (Å)	0.71073, MoK α
Crystal system	Triclinic
Space group	<i>P</i> $\bar{1}$
<i>a</i> (Å)	12.157(1)
<i>b</i> (Å)	13.536(2)
<i>c</i> (Å)	13.605(2)
α (°)	76.514(10)
β (°)	70.315(10)
γ (°)	70.216(4)
<i>V</i> (Å ³)	1965.6(4)
<i>D</i> _{calcd} (g/cm ³)	1.515
μ (mm ⁻¹)	1.053
Crystal habit, colour	Block, orange
Crystal size (mm)	0.24 × 0.22 × 0.18
Value of <i>Z</i>	2
θ range (°)	3.05-25.00
Index ranges	-14 ≤ <i>h</i> ≤ 14, -13 ≤ <i>k</i> ≤ 16, -16 ≤ <i>l</i> ≤ 16
Refl. collected	17772
Refl. unique	4758
Refl. observed	6902
Goodness of fit on F ²	1.017
<i>R</i> 1(<i>I</i> > 2σ(<i>I</i>))	0.0669
<i>wR</i> 2 (all data)	0.1365
(Δρ) _{max} , (Δρ) _{min}	0.786 / -0.507

Table 8.4.2. Crystallographic data and refinement parameters for [Cu(dippf)(DML)](BF₄)·CH₂Cl₂

Empirical formula	C ₃₀ H ₄₄ BCuF ₄ FeN ₄ O ₂ P ₂ × CH ₂ Cl ₂
Formula mass (g / mol)	845.76
<i>T</i> (K)	100 (2)
λ (Å)	0.71073, MoK α
Crystal system	Monoclinic
Space group	<i>P</i> 2 ₁ / <i>n</i>
<i>a</i> (Å)	15.9608(3)
<i>b</i> (Å)	11.7770(2)
<i>c</i> (Å)	20.7616(4)
β (°)	110.9980(10)
<i>V</i> (Å ³)	3643.41(12)
<i>D</i> _{calcd} (g/cm ³)	1.542
μ (mm ⁻¹)	1.272
Crystal habit, colour	coarse shape, red
Crystal size (mm)	0.6 × 0.4 × 0.2
Value of <i>Z</i>	4
θ range (°)	0.41-28.28
Index ranges	-21 ≤ <i>h</i> ≤ 21, -15 ≤ <i>k</i> ≤ 15, -27 ≤ <i>l</i> ≤ 27
Refl. collected	17116
Refl. unique	6280
Refl. observed	8973
Goodness of fit on F ²	1.009
<i>R</i> 1(<i>I</i> > 2σ(<i>I</i>))	0.0412
<i>wR</i> 2 (all data)	0.0957
(Δρ) _{max} , (Δρ) _{min}	0.696 / -0.477

Table 8.4.3. Crystallographic data and refinement parameters for $[\text{Cu}(\text{dppf})(\text{TMA})](\text{BF}_4)\cdot\text{CH}_2\text{Cl}_2$

Empirical formula	$\text{C}_{48}\text{H}_{42}\text{BCuF}_4\text{FeN}_4\text{O}_2\text{P}_2 \times \text{CH}_2\text{Cl}_2$
Formula mass (g / mol)	1059.92
T (K)	100(2)
λ (Å)	0.71073, MoK α
Crystal system	Triclinic
Space group	$P\bar{1}$
a (Å)	11.9144(4)
b (Å)	13.6523(4)
c (Å)	15.9341(6)
α (°)	90.349(2)
β (°)	79.642(2)
γ (°)	64.304(2)
V (Å ³)	2287.10(13)
D_{calcd} (g/cm ³)	1.539
μ (mm ⁻¹)	1.031
Crystal habit, colour	Block, Orange
Crystal size (mm)	0.25 × 0.22 × 0.2
Value of Z	2
θ range (°)	2.92-27.90
Index ranges	$-15 \leq h \leq 15, -17 \leq k \leq 17, -20 \leq l \leq 20$
Refl. collected	19371
Refl. unique	9039
Refl. observed	10863
Goodness of fit on F^2	1.060
$RI(I > 2\sigma(I))$	0.0399
$wR2$ (all data)	0.0996
$(\Delta\rho)_{\text{max}}, (\Delta\rho)_{\text{min}}$	1.054 / -0.868

Table 8.4.4. Crystallographic data and refinement parameters for $[\text{Cu}_3(\text{dppf})(\mu_2\text{-dppf})(\text{PP})(\text{PP}^-)]_2(\text{BF}_4)_4 \cdot 5\text{CH}_2\text{Cl}_2$

Empirical formula	$\text{C}_{90}\text{H}_{81}\text{B}_2\text{Cu}_3\text{F}_8\text{Fe}_2\text{N}_{10}\text{O}_4\text{P}_4 \times 5\text{CH}_2\text{Cl}_2$
Formula mass (g / mol)	2391.10
T (K)	100(2)
λ (Å)	0.71073, MoK α
Crystal system	Triclinic
Space group	$P\bar{1}$
a (Å)	14.4855(2)
b (Å)	19.4559(3)
c (Å)	20.6255(4)
α (°)	95.4090(10)
β (°)	110.4920(10)
γ (°)	104.3000(10)
V (Å ³)	5170.66(15)
D_{calcd} (g/cm ³)	1.536
μ (mm ⁻¹)	1.270
Crystal habit, colour	Block, orange
Crystal size (mm)	0.2×0.15×0.1
Value of Z	2
θ range (°)	0.41-28.28
Index ranges	$-19 \leq h \leq 19, -25 \leq k \leq 25, -25 \leq l \leq 27$
Refl. collected	44344
Refl. unique	16742
Refl. observed	25218
Goodness of fit on F^2	1.025
$RI(I > 2\sigma(I))$	0.0532
$wR2$ (all data)	0.1228
$(\Delta\rho)_{\text{max}}, (\Delta\rho)_{\text{min}}$	1.455 / -1.292

Table 8.4.5. Crystallographic data and refinement parameters for [Cu(dppf)(P-9MG)](BF₄)·0.5 CH₂Cl₂

Empirical formula	C ₄₅ H ₄₃ BCuF ₄ FeN ₅ O ₂ P ₂ × 0.5 CH ₂ Cl ₂
Formula mass (g / mol)	996.45
<i>T</i> (K)	100(1)
λ (Å)	0.71073, MoK α
Crystal system	Monoclinic
Space group	<i>C2/c</i>
<i>a</i> (Å)	41.9610(11)
<i>b</i> (Å)	12.2831(3)
<i>c</i> (Å)	17.1547(5)
β (°)	97.3110(10)
<i>V</i> (Å ³)	8769.8(4)
<i>D</i> _{calcd} (g/cm ³)	1.509
μ (mm ⁻¹)	1.012
Crystal habit, colour	Block, yellow
Crystal size (mm)	0.25 × 0.22 × 0.18
Value of <i>Z</i>	8
θ range (°)	0.98-26.37
Index ranges	-51 ≤ <i>h</i> ≤ 52, -14 ≤ <i>k</i> ≤ 15, -21 ≤ <i>l</i> ≤ 21
Refl. collected	17066
Refl. unique	5102
Refl. observed	8975
Goodness of fit on <i>F</i> ²	0.990
<i>RI</i> (<i>I</i> > 2σ(<i>I</i>))	0.0600
<i>wR2</i> (all data)	0.1129
($\Delta\rho$) _{max} , ($\Delta\rho$) _{min}	1.000 / -0.597

Table 8.4.6. Crystallographic data and refinement parameters for $[\text{Cu}_3(\text{P}^9\text{MG}^-)_2(\mu\text{-dppf})_2]_2(\text{BF}_4)_2$.

Empirical formula	$\text{C}_{56}\text{H}_{56}\text{B}_2\text{Cu}_3\text{F}_8\text{FeN}_{10}\text{O}_4\text{P}_2$
Formula mass (g / mol)	1415.14
T (K)	100(1)
λ (Å)	0.71073, MoK α
Crystal system	Monoclinic
Space group	$C2/c$
a (Å)	27.3092(9)
b (Å)	22.1245(8)
c (Å)	19.7163(7)
β (°)	90.425(2)
V (Å ³)	11912.3(7)
D_{calcd} (g/cm ³)	1.578
μ (mm ⁻¹)	1.429
Crystal habit, colour	Coarse shaped, red
Crystal size (mm)	0.27×0.24×0.19
Value of Z	8
θ range (°)	0.41-27.88
Index ranges	$-34 \leq h \leq 35, -22 \leq k \leq 29, -25 \leq l \leq 25$
Refl. collected	22514
Refl. unique	8632
Refl. observed	13981
Goodness of fit on F^2	1.103
$R1(I > 2\sigma(I))$	0.0796
$wR2$ (all data)	0.1719
$(\Delta\rho)_{\text{max}}, (\Delta\rho)_{\text{min}}$	0.963 / -1.098

Table 8.4.7. Crystallographic data and refinement parameters for $[\text{Cu}(\text{dppf})(\text{TMX})](\text{BF}_4) \cdot 2\text{CH}_2\text{Cl}_2$

Empirical formula	$\text{C}_{42}\text{H}_{38}\text{BCuF}_4\text{FeN}_4\text{O}_2\text{P}_2 \times 2\text{CH}_2\text{Cl}_2$
Formula mass (g / mol)	1068.76
T (K)	100(2)
λ (Å)	0.71073, MoK α
Crystal system	Triclinic
Space group	$P\bar{1}$
a (Å)	11.3080(3)
b (Å)	13.7827(5)
c (Å)	15.3127(6)
α (°)	105.509(2)
β (°)	92.149(2)
γ (°)	96.616(2)
V (Å ³)	2278.52(14)
D_{calcd} (g/cm ³)	1.558
μ (mm ⁻¹)	1.149
Crystal habit, colour	Block, orange
Crystal size (mm)	0.3 × 0.25 × 0.2
Value of Z	2
θ range (°)	5.95-27.99
Index ranges	$-14 \leq h \leq 14, -16 \leq k \leq 18, -20 \leq l \leq 20$
Refl. collected	19072
Refl. unique	7971
Refl. observed	10722
Goodness of fit on F^2	1.038
$RI(I > 2\sigma(I))$	0.0640
$wR2$ (all data)	0.1488
$(\Delta\rho)_{\text{max}}, (\Delta\rho)_{\text{min}}$	1.200 / -1.419

Table 8.4.8. Crystallographic data and refinement parameters for [Cu(dippf)(TMX)](PF₆)

Empirical formula	C ₃₀ H ₄₆ CuF ₆ FeN ₄ O ₂ P ₃
Formula mass (g / mol)	821.01
<i>T</i> (K)	100(2)
λ (Å)	0.71073, MoK α
Crystal system	Monoclinic
Space group	<i>P2₁/c</i>
<i>a</i> (Å)	16.4313(4)
<i>b</i> (Å)	12.0461(3)
<i>c</i> (Å)	18.7791(4)
β (°)	106.0970(10)
<i>V</i> (Å ³)	3571.27(15)
<i>D</i> _{calcd} (g/cm ³)	1.527
μ (mm ⁻¹)	1.201
Crystal habit, colour	Block, orange
Crystal size (mm)	0.4 × 0.2 × 0.15
Value of <i>Z</i>	4
θ range (°)	2.83-28.22
Index ranges	-21 ≤ <i>h</i> ≤ 21, -12 ≤ <i>k</i> ≤ 16, -24 ≤ <i>l</i> ≤ 24
Refl. collected	13810
Refl. unique	6880
Refl. observed	8690
Goodness of fit on F ²	1.029
<i>R</i> 1(<i>I</i> > 2σ(<i>I</i>))	0.0345
<i>wR</i> 2 (all data)	0.0741
(Δρ) _{max} , (Δρ) _{min}	0.803 / -0.634

Table 8.4.9. Crystallographic data and refinement parameters for [Cu(dchpf)(TMX)](PF₆)·CH₂Cl₂

Empirical formula	C ₄₂ H ₆₂ CuF ₆ FeN ₄ O ₂ P ₃ ×CH ₂ Cl ₂
Formula mass (g / mol)	1066.18
<i>T</i> (K)	100(2)
λ (Å)	0.71073, MoK α
Crystal system	Triclinic
Space group	<i>P</i> $\bar{1}$
<i>a</i> (Å)	15.1977(3)
<i>b</i> (Å)	15.8118(2)
<i>c</i> (Å)	21.3842(3)
α (°)	106.5060(10)
β (°)	104.6470(10)
γ (°)	91.2020(10)
<i>V</i> (Å ³)	4742.88(13)
<i>D</i> _{calcd} (g/cm ³)	1.515
μ (mm ⁻¹)	1.493
Crystal habit, colour	Block, orange
Crystal size (mm)	0.4 × 0.3 × 0.25
Value of <i>Z</i>	4
θ range (°)	1.03-28.23
Index ranges	-20 ≤ <i>h</i> ≤ 19, -20 ≤ <i>k</i> ≤ 20, -28 ≤ <i>l</i> ≤ 28
Refl. collected	39050
Refl. unique	15552
Refl. observed	23034
Goodness of fit on <i>F</i> ²	1.043
<i>RI</i> (<i>I</i> > 2 σ (<i>I</i>))	0.0516
<i>wR2</i> (all data)	0.1171
($\Delta\rho$) _{max} , ($\Delta\rho$) _{min}	1.998 / -1.075

Table 8.4.10. Crystallographic data and refinement parameters for $\{(\mu\text{-abcp})[\text{Cu}(\text{dppf})]_2\}(\text{BF}_4)_2 \cdot 2\text{CH}_2\text{Cl}_2$

Empirical formula	$\text{C}_{76}\text{H}_{60}\text{B}_2\text{Cl}_2\text{Cu}_2\text{F}_8\text{Fe}_2\text{N}_6\text{P}_4 \cdot 2\text{CH}_2\text{Cl}_2$
Formula mass (g / mol)	1834.33
T (K)	100(2)
λ (Å)	0.71073, MoK α
Crystal system	Triclinic
Space group	$P\bar{1}$
a (Å)	12.0203(5)
b (Å)	13.1333(6)
c (Å)	14.5297(6)
α (°)	64.907(3)
β (°)	75.654(3)
γ (°)	64.757(2)
V (Å ³)	1872.62(14)
D_{calcd} (g/cm ³)	1.627
μ (mm ⁻¹)	1.310
Value of Z	1
θ range (°)	7.57-28.26
Index ranges	$-15 \leq h \leq 15, -16 \leq k \leq 17, -19 \leq l \leq 19$
Refl. collected	15180
Refl. unique	5593
Refl. observed	8904
Goodness of fit on F^2	1.141
$R1(I > 2\sigma(I))$	0.0778
$wR2$ (all data)	0.1584
$(\Delta\rho)_{\text{max}}, (\Delta\rho)_{\text{min}}$	0.931 / -0.726

Table 8.4.11. Crystallographic data and refinement parameters for $\{(\mu\text{-abcp})[\text{Cu}(\text{dppf})]_2\}(\text{BF}_4) \cdot 2\text{CH}_2\text{Cl}_2$

Empirical formula	$\text{C}_{76}\text{H}_{60}\text{BF}_4\text{Cl}_2\text{Cu}_2\text{Fe}_2\text{N}_6\text{P}_4 \times \text{CH}_2\text{Cl}_2$
Formula mass (g / mol)	1662.60
T (K)	100(2)
λ (Å)	0.71073, MoK α
Crystal system	Monoclinic
Space group	$P2_1/c$
a (Å)	22.6673(7)
b (Å)	18.0003(7)
c (Å)	18.1507(6)
β (°)	78.52
V (Å ³)	7257.6(4)
D_{calcd} (g/cm ³)	1.522
μ (mm ⁻¹)	1.265
Crystal habit, colour	Block, orange
Crystal size (mm)	0.4 × 0.2 × 0.15
Value of Z	4
θ range (°)	8.18-28.23
Index ranges	$-30 \leq h \leq 30, -23 \leq k \leq 23, -24 \leq l \leq 24$
Refl. collected	26560
Refl. unique	10645
Refl. observed	16490
Goodness of fit on F^2	1.100
$RI(I > 2\sigma(I))$	0.1019
$wR2$ (all data)	0.2311
$(\Delta\rho)_{\text{max}}, (\Delta\rho)_{\text{min}}$	0.864 / -0.184

Table 8.4.12. Crystallographic data and refinement parameters for $\{(\mu\text{-abpy})\text{Cu}(\text{dippf})\}(\text{BF}_4)$

Empirical formula	$\text{C}_{32}\text{H}_{44}\text{BCuF}_4\text{FeN}_4\text{P}_2$
Formula mass (g / mol)	752.85
T (K)	100(2)
λ (Å)	0.71073, MoK α
Crystal system	Monoclinic
Space group	$P2_1/c$
a (Å)	13.1922(2)
b (Å)	14.6586(2)
c (Å)	17.4373(3)
β (°)	104.2410(10)
V (Å ³)	3268.39(9)
D_{calcd} (g/cm ³)	1.530
μ (mm ⁻¹)	1.245
Value of Z	4
θ range (°)	2.62-28.14
Index ranges	$-17 \leq h \leq 17, -19 \leq k \leq 18, -23 \leq l \leq 23$
Refl. collected	14765
Refl. unique	6765
Refl. observed	7876
Goodness of fit on F^2	1.037
$RI(I > 2\sigma(I))$	0.0300
$wR2$ (all data)	0.0766
$(\Delta\rho)_{\text{max}}, (\Delta\rho)_{\text{min}}$	0.513 / -0.678

Table 8.4.13. Crystallographic data and refinement parameters for $\{(\mu\text{-TCNB})[\text{Cu}(\text{dppf})]\}_2(\text{BF}_4)_2 \cdot 3\text{CH}_2\text{Cl}_2 \cdot 3\text{H}_2\text{O}$

Empirical formula	$\text{C}_{88}\text{H}_{60}\text{B}_2\text{Cu}_2\text{F}_8\text{Fe}_2\text{N}_8\text{P}_4 \times 3\text{CH}_2\text{Cl}_2 \times 3\text{H}_2\text{O}$
Formula mass (g / mol)	2359.18
T (K)	150(2)
λ (Å)	0.71073, MoK α
Crystal system	Monoclinic
Space group	$P2_1/n$
a (Å)	13.7221(11)
b (Å)	12.1397(7)
c (Å)	31.1265(17)
β (°)	90.415(6)
V (Å ³)	5185.0(6)
D_{calcd} (g/cm ³)	1.511
μ (mm ⁻¹)	1.119
Crystal habit, colour	Block, orange
Crystal size (mm)	0.28 × 0.23 × 0.18
Value of Z	2
θ range (°)	3.2558-32.7113
Index ranges	$-16 \leq h \leq 15, -14 \leq k \leq 14, -37 \leq l \leq 36$
Refl. collected	38307
Refl. unique	2966
Refl. observed	9117
Goodness of fit on F^2	0.777
$R1(I > 2\sigma(I))$	0.0758
$wR2$ (all data)	0.1931
$(\Delta\rho)_{\text{max}}, (\Delta\rho)_{\text{min}}$	0.899 / -0.652

Table 8.4.14. Crystallographic data and refinement parameters for $\{[(\mu\text{-TCNB})\text{Cu}(\text{dppf})]_n(\text{BF}_4)_2\}_n \cdot \text{CH}_2\text{Cl}_2$

Empirical formula	$\text{C}_{44}\text{H}_{54}\text{BCuF}_4\text{FeN}_4\text{P}_2 \times \text{CH}_2\text{Cl}_2$
Formula mass (g / mol)	991.98
T (K)	150(2)
λ (Å)	0.71073, MoK α
Crystal system	Triclinic
Space group	$P\bar{1}$
a (Å)	11.6575(5)
b (Å)	11.7073(4)
c (Å)	19.9358(7)
α (°)	81.307(3)
β (°)	76.495(3)
γ (°)	62.819(4)
V (Å ³)	2350.30(15)
D_{calcd} (g/cm ³)	1.402
μ (mm ⁻¹)	0.995
Crystal habit, colour	Block, black
Crystal size (mm)	0.28 × 0.23 × 0.18
Value of Z	2
θ range (°)	3.29-25.00
Index ranges	$-13 \leq h \leq 13, -13 \leq k \leq 13, -23 \leq l \leq 23$
Refl. collected	17409
Refl. unique	5721
Refl. observed	8251
Goodness of fit on F^2	0.984
$RI(I > 2\sigma(I))$	0.0535
$wR2$ (all data)	0.1540
$(\Delta\rho)_{\text{max}}, (\Delta\rho)_{\text{min}}$	0.776 / -0.735

Table 8.4.15. Crystallographic data and refinement parameters for $[\{(bpy)_2Ru\}_2(\mu\text{-adc-}CF_3)](PF_6)_2$

Empirical formula	$C_{50}H_{44}F_{18}P_2N_{10}O_4Ru_2$
Formula mass (g / mol)	1455.03
T (K)	173(2)
λ (Å)	0.71073, MoK α
Crystal System	monoclinic
Space group	$P2_1/n$
a (Å)	14.559(2)
b (Å)	15.926(2)
c (Å)	15.796(3)
β (°)	114.026(13)
V (Å ³)	3345.2(9)
D_{calcd} (g/cm ³)	1.445
μ (mm ⁻¹)	0.595
Crystal habit, colour	block, red
Crystal size(mm)	0.5 × 0.45 × 0.4
Value of Z	2
θ range(°)	5.00-12.50
Index ranges	$0 \leq h \leq 17, 0 \leq k \leq 19, -19 \leq l \leq 17$
Refl. Collected	6751
Refl. Unique	4271
Refl. Observed	6498
Goodness of fit on F^2	0.918
$RI(I > 2\sigma(I))$	0.0605
$wR2$ (all data)	0.1604
S (all data)	0.919
$(\Delta\rho)_{\text{max}}, (\Delta\rho)_{\text{min}}$	1.741 / -0.656

Chapter 9

Summary

Copper complexes of biochemically relevant ligands have been studied as a part of this doctoral thesis. The 1,3-dimethylmiazine (DML), 1,3-dimethylalloxazine (DMA), 1,3,7,8-tetramethylalloxazine (TMA), 2-pivaloylpterin (PP) (see Section 2.1.1), N2-pivaloyl-9-methylguanine (P-9MG) and 1,3,9-trimethylxanthine (TMX) (see Section 1.6) ligands were used to obtain metal complexes exhibiting interesting coordination modes, electrochemical behaviour and spectroscopic features. The organometallic fragments $[\text{Cu}(\text{dppf})]^+$, $[\text{Cu}(\text{dippf})]^+$ and $[\text{Cu}(\text{dchpf})]^+$ have been used for metal coordination (dppf = 1,1'-bis(diphenylphosphino)ferrocene; dippf = 1,1'-bis(di-isopropylphosphino)ferrocene; dchpf = 1,1'-bis(dicyclohexylphosphino)ferrocene). Other parts of the thesis contain the study of Ru-Ru, Fe-Fe and Cu-Cu interactions via σ donor and/or π -acceptor bridges. The bridging ligands 2,2'-azobispyridine (abpy), 2,2'-azobis(chloropyrimidine) (abcp) (see Section 1.7), 2,3,5,6-tetrafluoro-7,7,8,8-tetracyano-*p*-benzoquinodimethane (TCNQF₄) (Section 8.2.1), 1,2,4,5-tetracyanobenzene (TCNB) (Section 1.8) and 1,2-bis(trifluoroacetyl)-hydrazine (H₂adcCF₃) (Section 1.9) were used to isolate oligonuclear complexes in radical or non-radical forms.

In Chapter 2, the binding of the organometallic fragments $[\text{Cu}(\text{dppf})]^+$ and $[\text{Cu}(\text{dippf})]^+$ to DML, DMA, TMA and PP was studied in aprotic media. The fragments were found to bind in an un-reduced fashion as evident from the carbonyl bond lengths in the crystal structures (Some biomolecules have a tendency to get reduced on metal coordination). The crystal structure analyses revealed the unsymmetrical O,N chelation in DML and TMA complexes (Figure 9.1). Copper fragments were found to bind strongly to the nitrogen and weakly to the O donor site. The copper centres were found to adopt highly distorted geometry with unequal chelating angles.

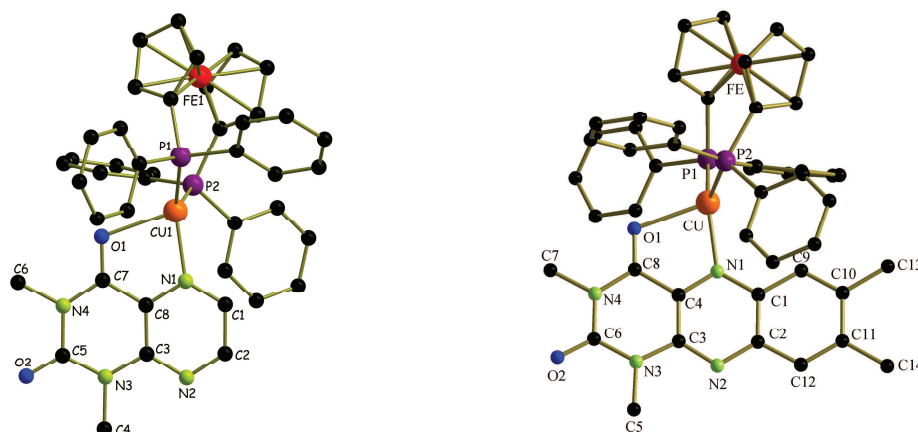


Figure 9.1. Single crystal X-ray molecular structures of the complex monocations $[\text{Cu}(\text{dppf})(\text{DML})]^+$ (left) and $[\text{Cu}(\text{dppf})(\text{TMA})]^+$ (right) in the crystals of $[\text{Cu}(\text{dppf})(\text{DML})](\text{BF}_4)$ and $[\text{Cu}(\text{dppf})(\text{TMA})](\text{BF}_4) \times \text{CH}_2\text{Cl}_2$. Counter anion and CH_2Cl_2 molecule are omitted for clarity.

The obtained metal complexes were studied by infrared spectroscopy. Only small changes of the carbonyl stretching frequencies are observed on metal coordination, indicating a very weak binding of the metal fragment. The reversible electron uptake properties of these complexes were studied by cyclic voltammetric experiments (Figure 9.2). A striking feature was observed in the cyclic voltammograms of the lumazine complexes. In addition to the first reduction process, a second less intense reduction wave at higher negative potential was found, which was further investigated by a variety of electrochemical experiments in collaboration with Dr. Jan Fielder at the *J. Heyrovský Institute of Physical Chemistry, v.v.i., Academy of Sciences of the Czech Republic, Prague*.

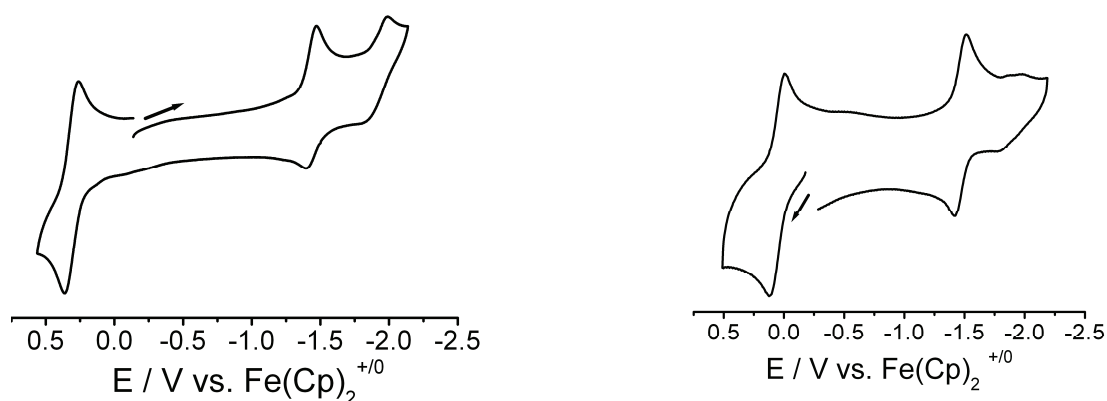


Figure 9.2. Cyclic voltammograms of $[\text{Cu}(\text{dppf})(\text{DML})](\text{BF}_4)$ (left) and $[\text{Cu}(\text{dppf})(\text{DMA})](\text{BF}_4)$ (right) in $\text{CH}_2\text{Cl}_2 / \text{Bu}_4\text{NPF}_6$, Scan rate 100 mV/s.

Infrared spectroelectrochemical experiments were carried out to study the carbonyl stretching frequencies in the oxidized and reduced states of the complexes. Large shifts of carbonyl stretching frequencies indicated ligand centered reduction (Figure 9.3). This observation was confirmed by EPR spectroscopy. A diminished metal- to -ligand charge transfer absorption was also encountered due to the radical nature of the reduced heterocyclic ring.

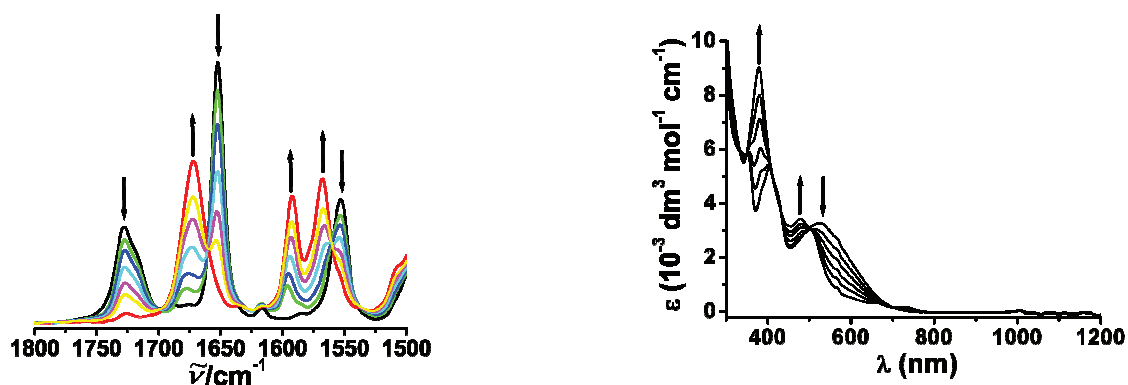


Figure 9.3. IR (left) and UV-Vis (right) spectroelectrochemical change for the reduction $[\text{Cu}(\text{dppf})(\text{DMA})]^+$ to $[\text{Cu}(\text{dppf})(\text{DMA}^{\cdot-})]$ in $\text{CH}_2\text{Cl}_2 / \text{Bu}_4\text{NPF}_6$.

The 2:1 reaction of the copper precursor $[\text{Cu}(\text{dppf})(\text{CH}_3\text{CN})_2](\text{BF}_4)$ to PP resulted in the formation of a pterin bridged heterotetranuclear complex $[\{\text{Cu}(\text{dppf})\}_2(\text{PP})](\text{BF}_4)_2$ which, on crystallization, formed an aggregate containing six copper and four iron centres (Figure 9.4). In the isolated iron-copper-pterin aggregate, the coordination through all heteroatoms except N^2 was observed for pterin ligands. Simultaneous coordination through N^1 , N^3 , N^5 , N^{10} and O^4 resulted in interesting structural features including the bridging mode of a carbonyl O donor, strong intra- and inter-molecular hydrogen bonding, π - π interactions and the bridging and chelating binding mode of dppf unit. Three distinct coordination spheres CuP_2NO , CuPN_2O and CuPN_2O_2 were found in distorted tetrahedral and square pyramidal geometry. The five-coordinated copper centres are involved in a weak coordination from the carbonyl oxygen donor at a shorter distance than the sum of the van-der-Waals radii.

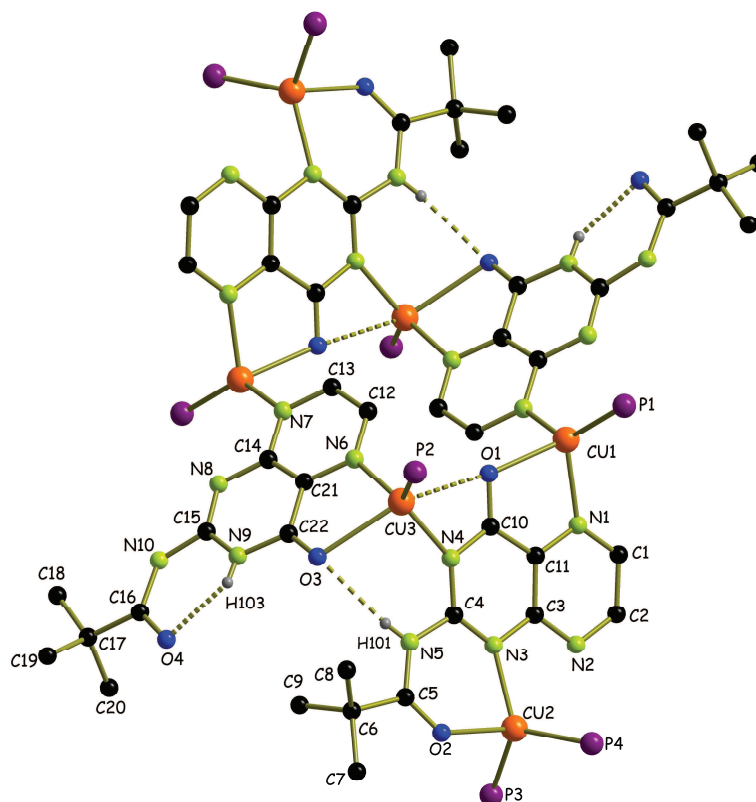


Figure 9.4. Single crystal X-ray molecular structure of the oligomeric $\text{Cu}^{\text{I}}\text{Fe}^{\text{II}}$ -PP complex in the crystal of $[\text{Cu}_3(\text{dppf})(\mu_2\text{-dppf})(\text{PP})(\text{PP}^-)]_2(\text{BF}_4)_4 \times 5\text{CH}_2\text{Cl}_2$. The BF_4^- counter anions and five CH_2Cl_2 molecules are omitted for clarity.

In chapter 3, the variable binding of substituted guanine (P-9MG) and xanthine (TMX) to $[\text{Cu}(\text{dppf})]^+$, $[\text{Cu}(\text{dippf})]^+$ and $[\text{Cu}(\text{dchpf})]^+$ has been investigated by crystal structure determination. The N^7 -monodentate binding of P-9MG was found in a heterodinuclear iron-copper complex $[\text{Cu}(\text{dppf})(\text{P-9MG})](\text{BF}_4)$. Due to the large bite of the α -iminoketo function, the P-9MG binds to the metal centre in a non-chelating fashion. The O^6 donor atom remains un-coordinated at a distance of $3.387(3)$ Å, resulting into a partially T-shaped geometry around the three coordinated copper ion (Figure 9.5).

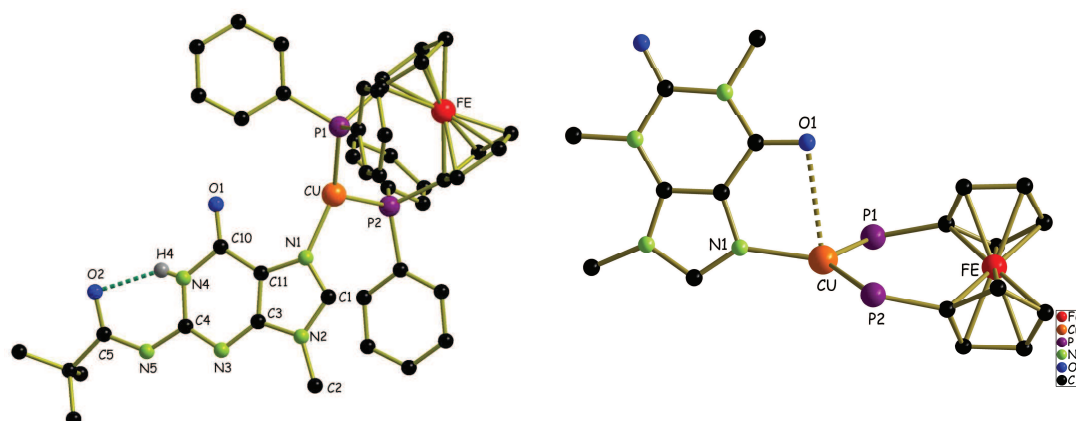


Figure 9.5. Molecular structure of the complex monocation $[Cu(dppf)(P-9MG)]^+$ in the crystals of $[Cu(dppf)(P-9MG)](BF_4) \times 0.5 CH_2Cl_2$. Counter anion, BF_4^- , and solvent molecule, CH_2Cl_2 , are omitted for clarity (left). The representation of average geometry around the Cu^+ ion in copper-TMX complexes (right).

The simultaneous threefold coordination through N^1 , N^7 and O^6 of the P-9MG was found in an iron-copper-P9MG cluster complex $[Cu_3(P-9MG)_2(dppf)]_2(BF_4)_2$. The structural features include a d^{10} - d^{10} interaction at 2.763(1) Å distance, tri- and hexa-coordinated copper ions, and the bridging mode of dppf unit.

In the crystal structures of the TMX complexes, the stronger N-coordination and weaker O coordination resulted in a trigonal planar geometry with a weakly interacting O donor in an approximately axial position to the PNPcCu plane (Figure 9.5). The copper-oxygen distances were found around a van-der-Waals sum. The distances were studied in three different complexes containing substituted phosphines, dppf, dippf and dchpf. The effect of phosphines on Cu-O binding has been discussed. The Cu-O binding is strongest when the metal fragment contains dippf as coligand. The study of $[Cu(dopf)]^+$ fragments binding to the substituted, lipophilized biomolecules have shown that the metal fragment interacts strongly to the N donor and weakly to the O donor site. It has been also observed that the O coordination depends on the heterocyclic ring systems and organometallic phosphine coligands. As a result the Cu-O distances varied from non-coordinated to the covalently bonded situation. The structural features, IR stretching frequencies of the carbonyl groups, UV-Vis absorption properties and the redox features of the ancillary ferrocenyldiphosphines were investigated for the complexes.

Chapter 4 describes the crystallographic characterization of both radical and non-radical states of a non-innocent ligand-bridged oligomeric complex. On electrolysis under argon the complex $[(\mu\text{-abcp})\{\text{Cu}(\text{dppf})_2\}_2](\text{BF}_4)_2$ produced the radical species $[(\mu\text{-abcp})\{\text{Cu}(\text{dppf})_2\}_2](\text{BF}_4)$. The abcp based radical centre was characterized by ligand centred spin with an isotropic EPR signal at $g = 2.0091$. The crystal structures of both complexes are distinguished by a significant change in the azo bond length. The N-N bond length was found at 1.308(9) Å in the non-radical complex and at 1.351(12) and 1.348(11) Å in the radical complex. The coordinations of $[\text{Cu}(\text{dppf})]^{+}$ units to a single bridging ligand occurred by sharing of a common edge by two five-membered rings. The differential pulse voltammogram of the non-radical complex revealed the oxidation of the iron centres at slightly different potentials, indicating the formation of a $\text{Fe}^{\text{II}}\text{Fe}^{\text{III}}$ mixed-valent intermediate during the electrochemical process (Figure 9.6). The iron-iron interaction at a very large distance of 12.8240(3) and 12.3462(3) Å in the paramagnetic complex, was observed for the first time in related complexes. In the radical-bridged copper complex, two copper centres exhibit a distance of 4.8016(1) and 4.8223(1) Å and in the non-radical complex the distance is 4.8013(3) Å. A broad, long-wavelength MLCT band at 910 nm is observed for the non-radical bridged complex (Figure 9.6). The spectroscopic characterization of both forms was carried out by UV-Vis-NIR spectroelectrochemistry. The effect of coligand on the azo-copper binding was studied employing dppf as another coligand in such systems.

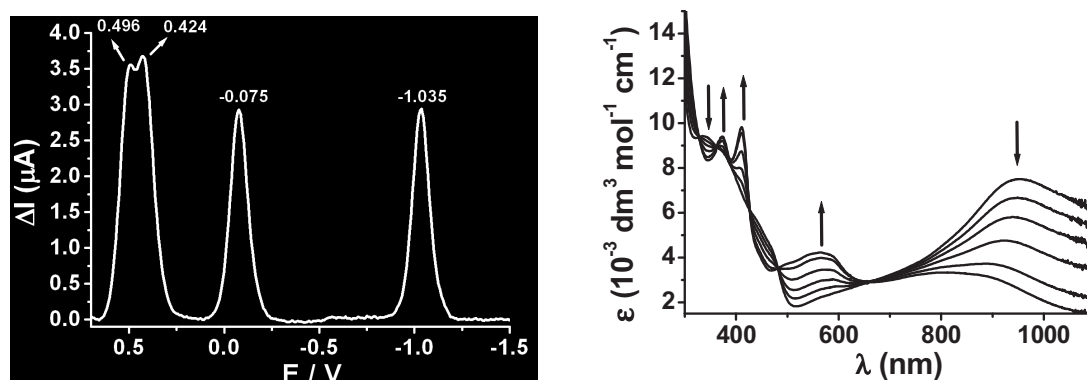


Figure 9.6. Differential pulse voltammogram of $\{(\mu\text{-abcp})[\text{Cu}(\text{dppf})_2]_2\}(\text{BF}_4)_2$ in CH_2Cl_2 / 0.1 M Bu_4NPF_6 with 70 mV/sec scan rate (left). UV-Vis-NIR spectroelectrochemistry for the reduction $\{(\mu\text{-abcp})[\text{Cu}(\text{dppf})_2]_2\}^{2+}$ to $\{(\mu\text{-abcp})[\text{Cu}(\text{dppf})_2]_2\}^{+}$ in CH_2Cl_2 / Bu_4NPF_6 in OTTLE cell (right).

In chapter 5, the tetraruthenium complex $\{[\text{Ru}(\text{NH}_3)_5]_4(\mu_4\text{-TCNQF}_4)\}(\text{PF}_6)_8$, $\text{TCNQF}_4 = 2,3,5,6\text{-tetrafluoro-7,7,8,8-tetracyano-}p\text{-benzoquinodimethane}$, was obtained and studied by cyclic voltammetry, IR, UV-VIS-NIR and EPR spectroelectrochemistry. Expectedly, the better π acceptor qualities of TCNQF_4 in comparison to TCNQ cause more accessible reduction to produce $\{[\text{Ru}(\text{NH}_3)_5]_4(\mu_4\text{-TCNQF}_4)\}^{7+}$ with enhanced metal contribution to the singly occupied MO and low-energy shifted IR vibrational and NIR electronic absorptions (Figure 9.7). However, the two-electron oxidation to the (10+) ion is also facilitated. The reason is seen in a more metal centered oxidation for the TCNQF_4 complex while the previously studied TCNQ analogue is assumed to undergo a higher degree of oxidation at the bridging ligand. As a result, the (8+) species has a redox potential range of only 0.51 V, indicating a significantly diminished HOMO-LUMO difference.

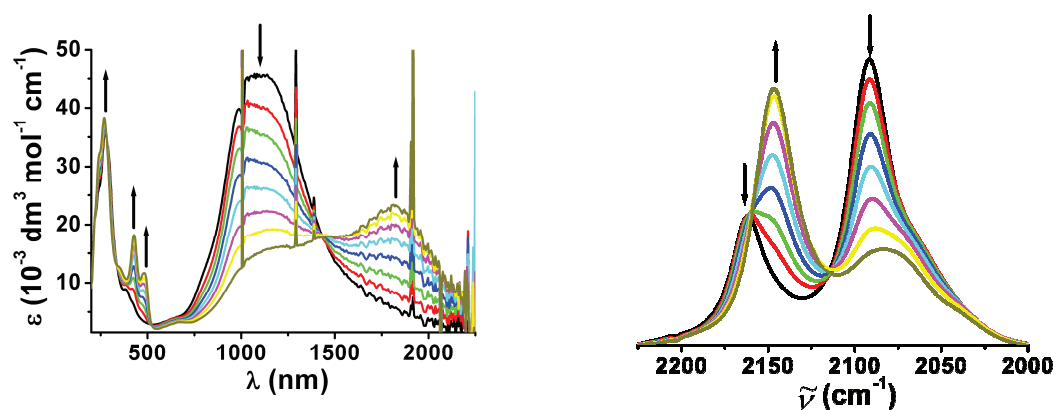


Figure 9.7. UV-Vis-NIR (left) and IR (right) spectroelectrochemistry for the reduction $\{[\text{Ru}(\text{NH}_3)_5]_4(\mu_4\text{-TCNQF}_4)\}^{8+}$ to $\{[\text{Ru}(\text{NH}_3)_5]_4(\mu_4\text{-TCNQF}_4)\}^{7+}$ in $\text{CH}_3\text{CN} / 0.1 \text{ M Bu}_4\text{NPF}_6$ at 298 K.

In chapter 6, I have explored various coordination modes of TCNB in discrete and polymeric complexes. It was possible to obtain the crystal structures of two complexes. All possible coordination modes of TCNB found also in related complexes from the literature were discussed. The 1,3 bridging mode was found here in a discrete complex $\{[\mu_2(1,3)\text{-TCNB}]\text{Cu}(\text{dppf})\}(\text{BF}_4)_2$ whereas the 1,4 bridging mode was found in a polymeric complex $\{[(\mu_2(1,4)\text{-TCNB})\text{Cu}(\text{dppf})]_2(\text{BF}_4)_2\}_n$. The 1,3 coordination of un-reduced TCNB to two $[\text{Cu}(\text{dppf})]^+$ fragments, leads to the formation of a 16-membered ring system containing two copper(I) ions. Two different organometallic fragments $[\text{Cu}(\text{dppf})]^+$ and $[\text{Cu}(\text{dchpf})]^+$ were used for the isolation of the complexes. The coordinatively saturated complex $[(\mu_4\text{-TCNB})\{\text{Cu}(\text{dchpf})\}_4](\text{BF}_4)_4$ produced single crystals of a polymeric product from the solution

equilibrium. The crystal structure showed that $\{[(\mu_2(1,4)\text{-TCNB})\text{Cu}(\text{dppf})]_2(\text{BF}_4)_2\}_n$ exhibits a 2D-polymeric network structure (Figure 9.8). The nitrile stretching of the reduced form of the complex $[(\mu_4\text{-TCNB})\{\text{Cu}(\text{dchpf})\}_4](\text{BF}_4)_4$ was observed at 2168 and 2160 cm^{-1} from one-electron IR spectroelectrochemical reduction (Figure 9.8). In addition to the structural characterization, spectroelectrochemistry and EPR spectroscopy were carried out with these complexes.

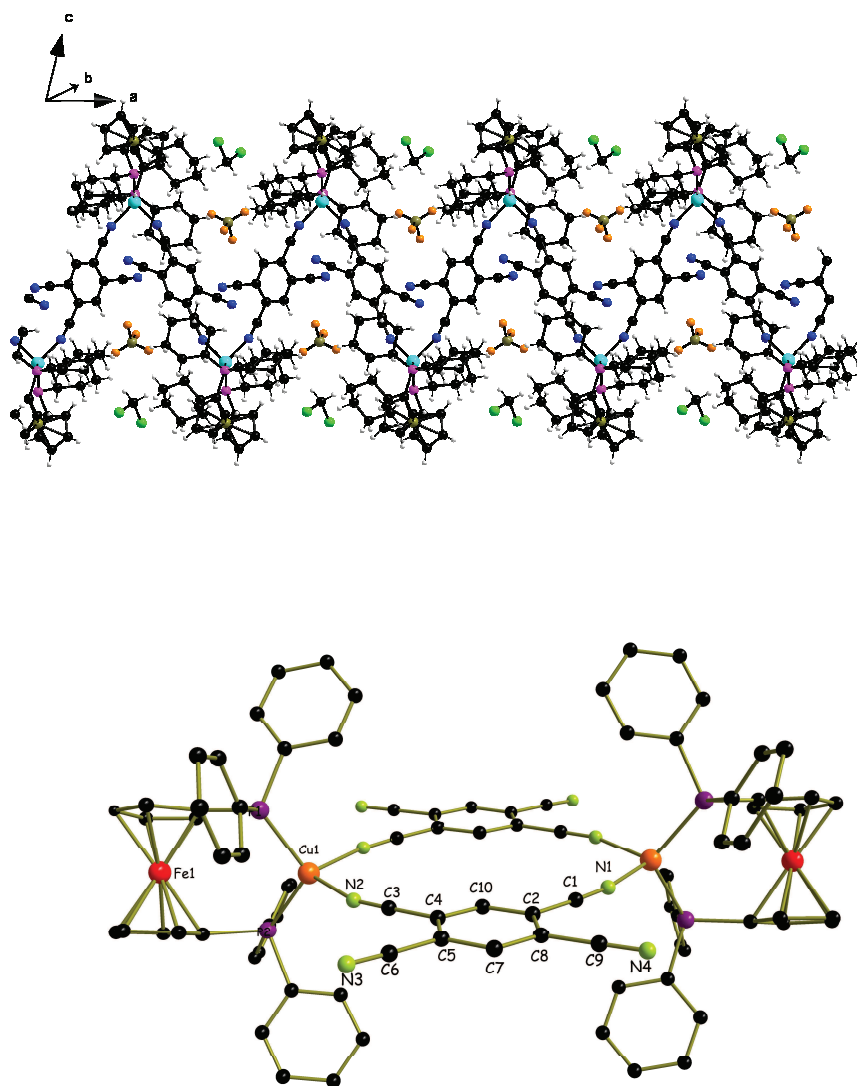


Figure 9.8. View of the 2D polymeric network structure in the crystal of $[(\mu_2(1,4)\text{-TCNB})\text{Cu}(\text{dchpf})]_n(\text{BF}_4)_n \times \text{CH}_2\text{Cl}_2$ (top). X-ray structure of the complex dication in the crystal of $\{[(\mu_2(1,3)\text{-TCNB})\text{Cu}(\text{dppf})](\text{BF}_4)\}_2 \cdot 3\text{CH}_2\text{Cl}_2 \cdot 3\text{H}_2\text{O}$. The counter anions and solvent molecules are omitted for clarity (bottom)

In chapter 7, I have discussed a Ru^{II}Ru^{III} mixed-valent intermediate via its EPR spectrum, spectroelectrochemistry and crystal structure determination (Figure 9.9). Reaction of Ru(bpy)₂Cl₂·2H₂O with 1,2-bis(trifluoroacetyl)hydrazine H₂(adc-CF₃) under basic conditions yields the dinuclear [(μ-adc-CF₃){Ru(bpy)₂}₂]²⁺ ion which was isolated and crystallized for structure determination in the *meso* diastereoisomer form as the bis(hexafluorophosphate). The Ru···Ru distance was determined at 5.029(1) Å, and the N-N bond length at 1.463(5) Å reveals a hydrazido(2-) form of the bridge, implying unchanged +II metal oxidation states.

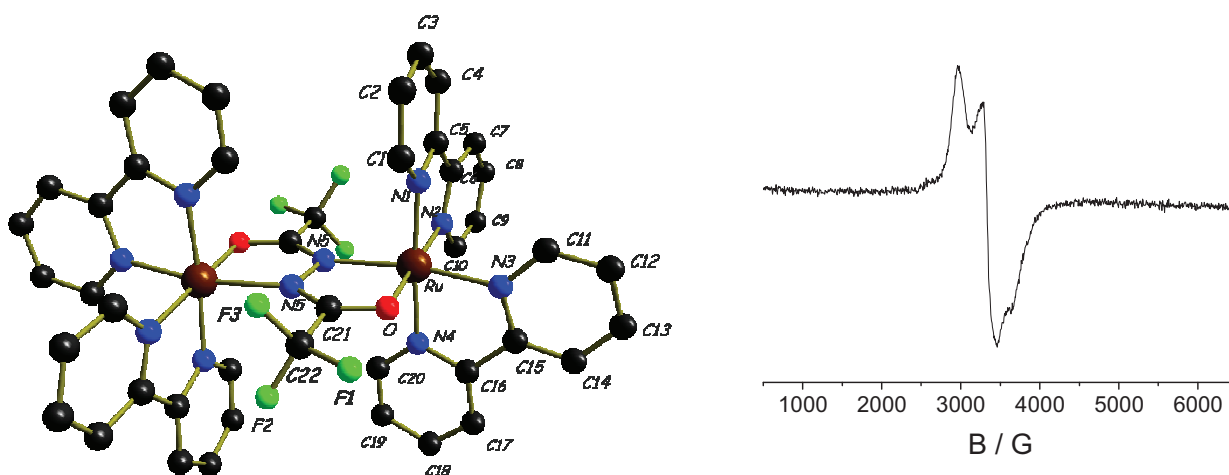


Figure 9.9. Molecular structure of the complex dication in the crystal of [(μ-adc-CF₃){Ru(bpy)₂}₂](PF₆)₂ × 2 (CH₃)₂CO (left). EPR spectrum of electrogenerated [(μ-adc-CF₃){Ru(bpy)₂}₂]³⁺ at 4 K in glassy frozen CH₃CN/0.1 M Bu₄NPF₆ solution (right).

Besides bpy-based reduction, the cyclic voltammetric analysis revealed two oxidation waves with a (3⁺) intermediate. Spectroelectrochemistry demonstrated that this intermediate [(μ-adc-CF₃){Ru(bpy)₂}₂]³⁺ with a comproportionation constant of $K_c = 10^{8.8}$ and an absorption at 1680 nm ($\epsilon = 9900 \text{ M}^{-1} \text{ cm}^{-1}$) is a mixed-valent species as evident most convincingly from the EPR parameters at $g_1 = 2.239$, $g_2 = 2.065$, $g_3 = 1.891$ ($g_{\text{av}} = 2.101$, $\Delta g = g_1 - g_3 = 0.348$).

Chapter 10

Zusammenfassung

Als Teil der vorliegenden Doktorarbeit wurden Kupferkomplexe biochemisch relevanter Liganden untersucht. Die Liganden 1,3-Dimethylumazin (DML), 1,3-Dimethylalloxazin (DMA), 1,3,7,8-Tetramethylalloxazin (TMA), 2-Pivaloylpterin (PP) (siehe Abschnitt 2.1.1), N2-Pivaloyl-9-methylguanin (P-9MG) und 1,3,9-Trimethylxanthin (TMX) (siehe Abschnitt 1.6) wurden verwendet, um Metallkomplexe mit interessanten Koordinationsmodi, elektrochemischem Verhalten und spektroskopischen Eigenschaften darzustellen. Die metallorganischen Fragmente $[\text{Cu}(\text{dppf})]^+$, $[\text{Cu}(\text{dippf})]^+$ und $[\text{Cu}(\text{dchpf})]^+$ wurden für die Metallkoordination benutzt (dppf = 1,1'-Bis(diphenylphosphino)ferrocen; dippf = 1,1'-Bis(diisopropylphosphino)ferrocen; dchpf = 1,1'-Bis(dicyclohexylphosphino)ferrocen). Andere Teile der Arbeit enthalten Untersuchungen der Ru-Ru-, Fe-Fe- und Cu-Cu-Wechselwirkungen über σ -Donor- und/oder π -Akzeptorbrücken. Die verbrückenden Liganden 2,2'-Azobispyridin (abpy), 2,2'-Azobis(chloropyrimidin) (abcp) (siehe Abschnitt 1.7), 2,3,5,6-Tetrafluoro-7,7,8,8-tetracyano-*p*-benzoquinodimethan (TCNQF₄) (Abschnitt 8.2.1), 1,2,4,5-Tetracyanobenzol (TCNB) (Abschnitt 1.8) und 1,2-Bis(trifluoroacetyl)-hydrazin (H₂adcCF₃) (Abschnitt 1.9) wurden zur Isolierung mehrkerniger Komplexe in radikalischer oder nicht-radikalischer Form eingesetzt.

In Kapitel 2 wurde die Koordination der metallorganischen Fragmente $[\text{Cu}(\text{dppf})]^+$ und $[\text{Cu}(\text{dippf})]^+$ an DML, DMA, TMA und PP in aprotischen Medien untersucht. Die Fragmente binden in nicht-reduzierter Form, wie durch die Carbonyl-Bindungslänge aus den Kristallstrukturen hervorgeht (Einige Biomoleküle tendieren dazu, bei Metallkoordination reduziert zu werden.). Die Kristallstrukturanalysen zeigten die unsymmetrische O,N-Chelatbindung in DML- und TMA-Komplexen (Abb. 9.1). Kupferfragmente binden stark an den Stickstoff- und schwach an den Sauerstoffdonor. Es wurde gefunden, dass die Kupferzentren eine stark verzerrte Geometrie mit unterschiedlichen Bisswinkeln einnehmen.

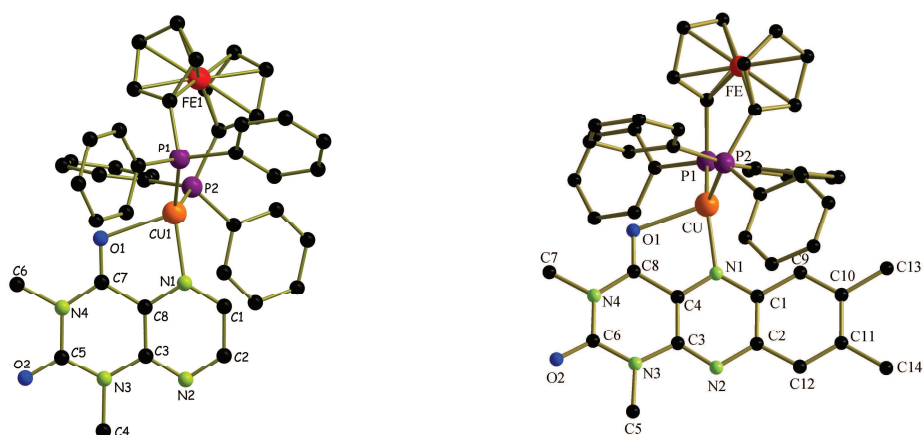


Abb. 9.1. Einkristall-Röntgenstruktur der Monokationen $[\text{Cu}(\text{dppf})(\text{DML})]^+$ (links) und $[\text{Cu}(\text{dppf})(\text{TMA})]^+$ (rechts) in den Kristallen von $[\text{Cu}(\text{dppf})(\text{DML})](\text{BF}_4)$ und $[\text{Cu}(\text{dppf})(\text{TMA})](\text{BF}_4) \times \text{CH}_2\text{Cl}_2$. Das Gegenanion und CH_2Cl_2 -Moleküle wurden zur Vereinfachung nicht eingezeichnet.

Die erhaltenen Metallkomplexe wurden mit Hilfe der IR-Spektroskopie untersucht. Durch die Metallkoordination ändern sich die Carbonylschwingungen nur sehr wenig, was auf eine relativ schwache Bindung des Metallfragments hinweist. Die reversible Elektronaufnahme dieser Komplexe wurde mit Hilfe der Zyklovoltammetrie erforscht (Abb. 9.2). Dabei wurde im Zyklovoltammogramm der Lumazinkomplexe ein interessantes Ergebnis gefunden. Zusätzlich zur ersten Reduktion wurde eine zweite weniger intensive Reduktionswelle bei stärker negativem Potential gefunden; diese wurde durch eine Vielzahl weiterer elektrochemischer Experimente in Zusammenarbeit mit Dr. Jan Fielder vom *J. Heyrovský Institute of Physical Chemistry, v.v.i., Academy of Sciences of the Czech Republic, Prague* genauer untersucht.

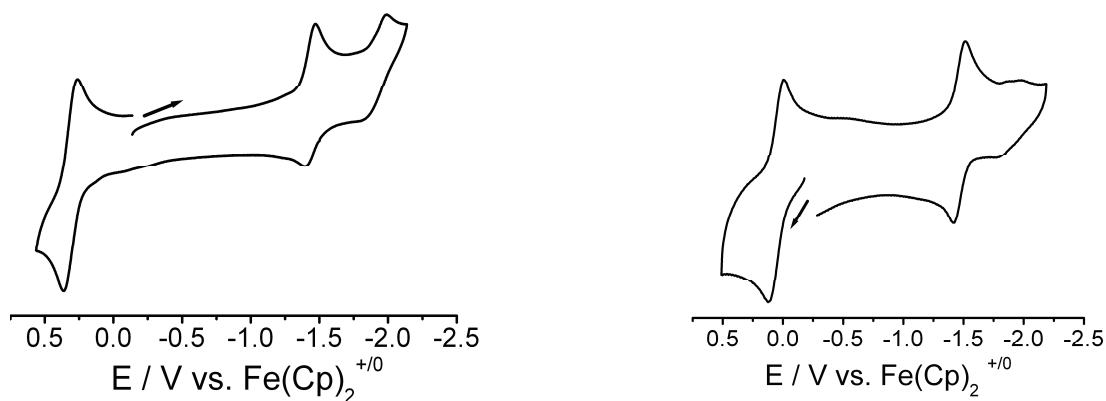


Abb 9.2. Zyklovoltammogramme von $[\text{Cu}(\text{dppf})(\text{DML})](\text{BF}_4)$ (links) und $[\text{Cu}(\text{dppf})(\text{DMA})](\text{BF}_4)$ (rechts) in $\text{CH}_2\text{Cl}_2 / \text{Bu}_4\text{NPF}_6$, Vorschubgeschwindigkeit 100 mV/s.

IR-spektroelektrochemische Experimente wurden ausgeführt, um die Carbonyl-Streckschwingungsfrequenzen in den oxidierten und reduzierten Komplexen zu bestimmen. Eine starke Verschiebung dieser Banden deutete auf ligandenzentrierte Reduktion hin (Abb. 9.3). Diese Beobachtung wurde durch ESR-Spektroskopie bestätigt. Die Metall-Ligand-Charge-Transfer-Absorption wurde aufgrund des radikalischen Zustands des reduzierten heterozyklischen Rings verringert.

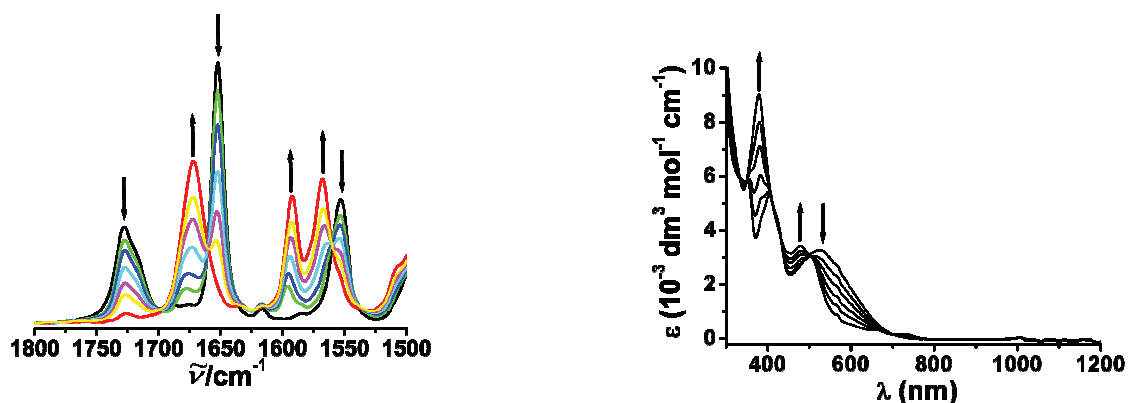


Abb 9.3. IR- (links) und UV-Vis- (rechts) Spektroelektrochemie für die Reduktion von $[\text{Cu}(\text{dppf})(\text{DMA})]^+$ zu $[\text{Cu}(\text{dppf})(\text{DMA}^-)]$ in $\text{CH}_2\text{Cl}_2 / \text{Bu}_4\text{NPF}_6$.

Die 2:1-Reaktion der Kupfervorstufe $[\text{Cu}(\text{dppf})(\text{CH}_3\text{CN})_2](\text{BF}_4)$ mit PP ergab einen pterinverbrückten heterovierkernigen Komplex $[\{\text{Cu}(\text{dppf})\}_2(\text{PP})](\text{BF}_4)_2$, welcher sich bei Kristallisation zu einem Aggregat mit sechs Kupfer- und vier Eisenzentren zusammenlagerte (Abb. 9.4). In dem isolierten Eisen-Kupfer-Pterin-Aggregat konnte Koordination durch alle Heteroatome mit Ausnahme des N^2 für die Pterinliganden beobachtet werden. Die gleichzeitige Koordination über N^1 , N^3 , N^5 , N^{10} und O^4 resultierte in interessanten strukturellen Eigenschaften, z.B. dem verbrückenden Modus eines Carbonyl-O-Donors, starken intra- und intermolekularen Wasserstoffbrücken, π - π -Wechselwirkungen und dem verbrückenden und chelatisierenden Bindungsverhalten der dppf-Einheit. Drei unterschiedliche Koordinationssphären CuP_2NO , CuPN_2O und CuPN_2O_2 wurden in einer verzerrt tetraedrischen und quadratisch-pyramidalen Geometrie gefunden. Die fünffach-kordinierten Kupferzentren sind an einer schwachen Koordination mit dem Carbonyl-Sauerstoff beteiligt, wobei der Abstand geringer ist als die Summe der van-der-Waals-Radien.

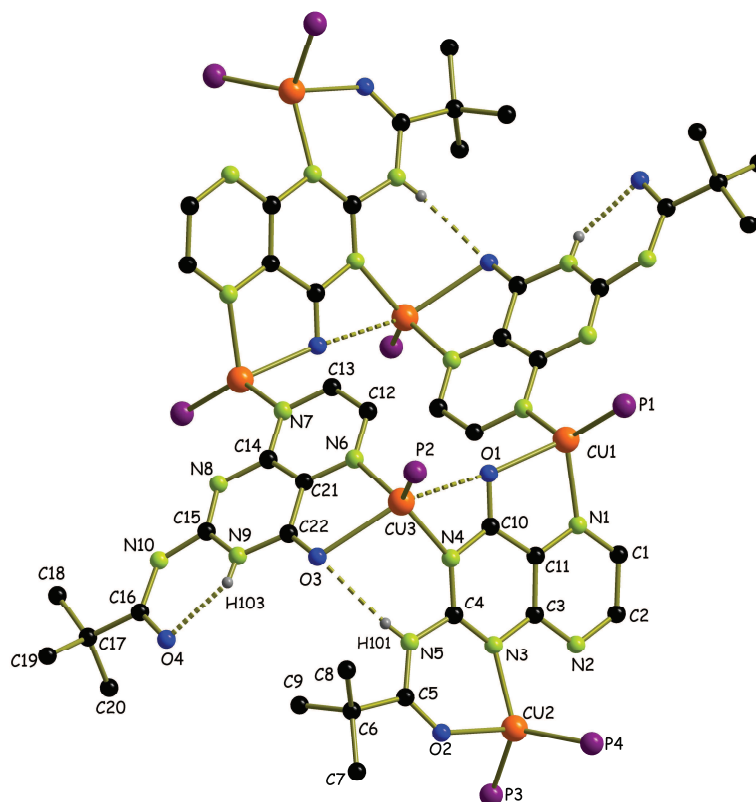


Abb 9.4. Einkristall-Röntgenstruktur des oligomeren $\text{Cu}^{\text{I}}\text{Fe}^{\text{II}}$ -PP-Komplex im Kristall von $[\text{Cu}_3(\text{dppf})(\mu_2\text{-dppf})(\text{PP})(\text{PP}')]_2(\text{BF}_4)_4 \times 5\text{CH}_2\text{Cl}_2$. Die BF_4^- -Gegenanionen und fünf CH_2Cl_2 -Moleküle wurden zur Vereinfachung nicht dargestellt.

In Kapitel 3 wurde das variable Bindungsverhalten von substituiertem Guanin (P-9MG) und Xanthin (TMX) an $[\text{Cu}(\text{dppf})]^+$, $[\text{Cu}(\text{dippf})]^+$ und $[\text{Cu}(\text{dchpf})]^+$ durch Kristallstrukturanalyse untersucht. Dabei wurde N^7 -monodentate Bindung von P-9MG in dem heterozweikernigen Eisen-Kupfer-Komplex $[\text{Cu}(\text{dppf})(\text{P-9MG})](\text{BF}_4)$ gefunden. Durch den großen Bisswinkel der α -Iminoketogruppe bindet P-9MG nicht-chelatisierend an das Metallzentrum. Das O^6 -Donoratom bleibt unkoordiniert in einem Abstand von $3.387(3) \text{ \AA}$, was in einer teilweise T-förmigen Geometrie um das dreifach koordinierte Kupferion resultiert (Abb. 9.5).

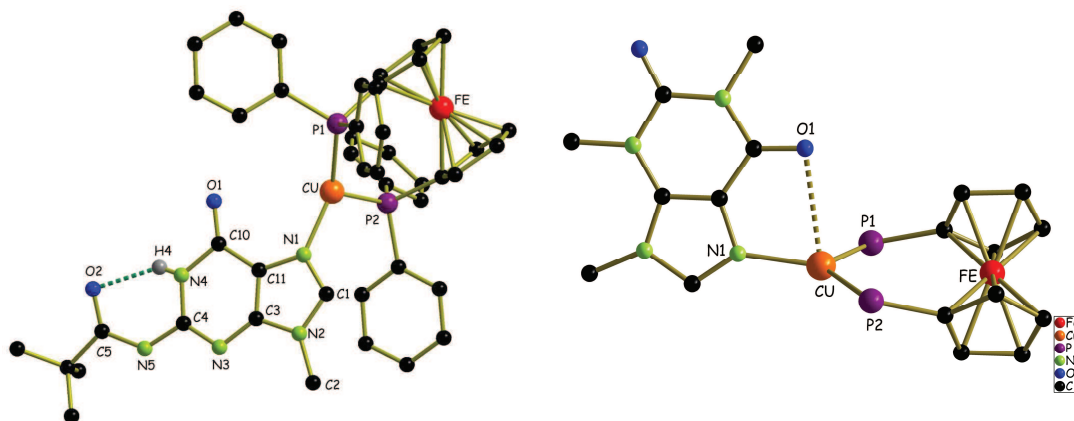


Abb. 9.5. Molekülstruktur des Monokations $[\text{Cu}(\text{dppf})(\text{P-9MG})]^+$ in den Kristallen von $[\text{Cu}(\text{dppf})(\text{P-9MG})](\text{BF}_4) \times 0.5 \text{CH}_2\text{Cl}_2$. Gegenanion, BF_4^- , und Lösungsmittelmoleküle, CH_2Cl_2 , wurden zur Vereinfachung nicht dargestellt (links). Darstellung der durchschnittlichen Geometrie um das Cu^+ -Ion in Kupfer-TMX-Komplexen (rechts).

Dreifach-Koordination des P-9MG über N^1 , N^7 und O^6 wurde in einem Eisen-Kupfer-P9MG-Clusterkomplex $[\text{Cu}_3(\text{P-9MG}^-)_2(\text{dppf})_2](\text{BF}_4)_2$ gefunden. Zu den strukturellen Eigenschaften gehören eine d^{10} - d^{10} -Wechselwirkung im Abstand von 2.763(1) Å, drei- und sechsfach-koordinierte Kupferionen und die verbrückende Koordination der dppf-Einheit.

In den Kristallstrukturen der TMX-Komplexe führten stärkere N- und schwächere O-Koordinationen zu einer trigonal-planaren Geometrie mit schwach wechselwirkenden O-Donorzentren in einer annäherungsweise axialen Position relativ zur PNPCu-Ebene (Abb. 9.5). Die Kupfer-Sauerstoff-Abstände entsprechen in etwa der Summe der van-der-Waals-Radien. Die Abstände wurden in drei verschiedenen Komplexen mit substituierten Phosphinen (dppf, dippf und dchpf) untersucht. Der Einfluss der Phosphine auf die Cu-O-Bindung wurde diskutiert. Die Cu-O-Bindung ist am stärksten, wenn das Metallfragment dippf als Coligand enthält. Die Untersuchung von $[\text{Cu}(\text{dopf})]^+$ -Fragmenten in Bezug auf ihre Bindung an die substituierten, lipophilisierten Biomoleküle hat ergeben, dass das Metallfragment am stärksten an den N- und schwach an den O-Donor bindet. Weiterhin wurde beobachtet, dass die O-Koordination vom heterozyklischen Ringsystem und den metallorganischen Phosphin-Coliganden abhängt. Als Ergebnis daraus variierten die Cu-O-Abstände von „nicht-koordiniert“ bis zu „kovalent gebunden“. Die strukturellen Eigenschaften, IR-Streckschwingungsfrequenzen der Carbonylgruppen, UV-Vis-Absorption und die Redox-Eigenschaften der zusätzlichen Ferrocenyldiphosphinliganden wurden für die Komplexe untersucht.

Kapitel 4 beschreibt die kristallographische Charakterisierung sowohl des radikalischen als auch des nicht-radikalischen Zustands eines ligandverbrückten, oligomeren Komplexes mit „non-innocent“ Liganden. Durch Elektrolyse unter Argon konnte aus dem Komplex $[(\mu\text{-abcp})\{\text{Cu}(\text{dppf})\}_2](\text{BF}_4)_2$ die radikalische Spezies $[(\mu\text{-abcp})\{\text{Cu}(\text{dppf})\}_2](\text{BF}_4)$ dargestellt werden. Das auf abcp basierende radikalische Zentrum wurde ESR-spektroskopisch durch einen ligandenzentrierten Spin mit einem isotropen Signal bei $g = 2.0091$ charakterisiert. Die Kristallstrukturen beider Komplexe unterscheiden sich durch eine signifikante Änderung der Länge der Azobindung. Die N-N-Bindungslänge wurde im nicht-radikalischen Komplex zu $1.308(9)$ Å, im radikalischen Komplex zu $1.351(12)$ und $1.348(11)$ Å bestimmt. Die Koordination von $[\text{Cu}(\text{dppf})]^+$ -Einheiten an einen einzelnen verbrückenden Liganden erfolgt dadurch, dass zwei fünfgliedrige Ringe sich eine gemeinsame Ecke teilen. Das Differentialpuls-Voltammogramm des nicht-radikalischen Komplexes zeigte die Oxidation der Eisen-Zentren bei leicht unterschiedlichen Potentialen, was auf die Bildung einer $\text{Fe}^{\text{II}}\text{Fe}^{\text{III}}$ gemischtvalenten Zwischenstufe während des elektrochemischen Prozesses hindeutet (Abb. 9.6). Eine Eisen-Eisen-Wechselwirkung mit dem extrem großen Abstand von $12.8240(3)$ und $12.3462(3)$ Å im paramagnetischen Komplex wurde zum ersten Mal in ähnlichen Komplexen beobachtet. In dem radikalverbrückten Kupferkomplex weisen die beiden Kupferzentren Abstände von $4.8016(1)$ und $4.8223(1)$ Å auf; im nicht-radikalischen Komplex beträgt der Abstand $4.8013(3)$ Å. Eine breite MLCT-Bande bei großen Wellenlängen um 910 nm wurde für den nicht-radikalverbrückten Komplex gefunden (Abb. 9.6). Die spektroskopische Charakterisierung beider Formen erfolgte mittels UV-Vis-NIR-Spektroelektrochemie. Der Effekt des Coliganden auf die Azo-Kupfer-Bindung wurde mit dippf als einem weiteren Coliganden in solchen Systemen untersucht.

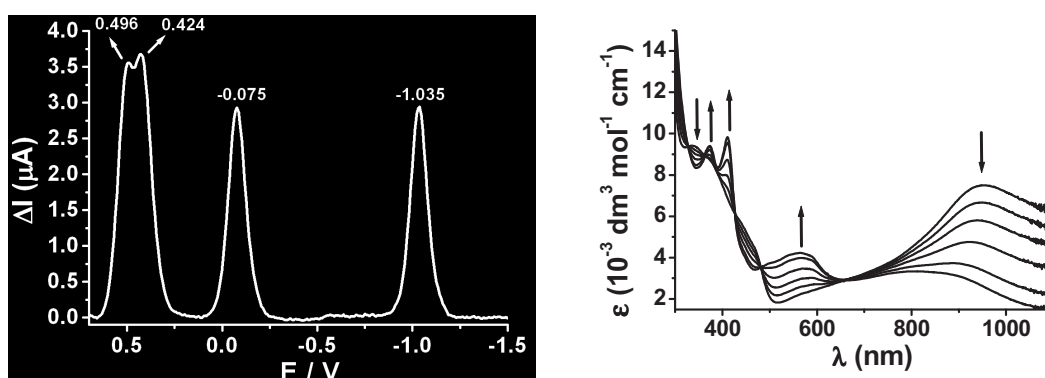


Abb. 9.6. Differentialpuls-Voltammogramm von $\{(\mu\text{-abcp})[\text{Cu}(\text{dppf})_2]_2\}(\text{BF}_4)_2$ in CH_2Cl_2 / $0.1 \text{ M Bu}_4\text{NPF}_6$ mit 70 mV/sec Vorschubgeschwindigkeit (links). UV-Vis-NIR-Spektroelektrochemie für die Reduktion von $\{(\mu\text{-abcp})[\text{Cu}(\text{dppf})_2]_2\}^{2+}$ zu $\{(\mu\text{-abcp})[\text{Cu}(\text{dppf})_2]_2\}^+$ in CH_2Cl_2 / Bu_4NPF_6 in einer OTTLE-Zelle (rechts).

In Kapitel 5 wurde der Tetrarutheniumkomplex $\{[\text{Ru}(\text{NH}_3)_5]_4(\mu_4\text{-TCNQF}_4)\}(\text{PF}_6)_8$, $\text{TCNQF}_4 = 2,3,5,6\text{-Tetrafluoro-7,7,8,8-tetracyano-}p\text{-benzochinodimethan}$ dargestellt und mit Hilfe von Zyklovoltammetrie, IR-, UV-VIS-NIR- und ESR-Spektroelektrochemie untersucht. Wie erwartet, ergeben die im Vergleich mit TCNQ besseren π -Akzeptor-Eigenschaften des TCNQF_4 eine erleichterte Reduktion zu $\{[\text{Ru}(\text{NH}_3)_5]_4(\mu_4\text{-TCNQF}_4)\}^{7+}$ mit stärkeren Metallanteilen am einfach besetzten MO und zu niedrigen Energien verschobenen IR- bzw. NIR-Absorptionen (Abb. 9.7). Die Zweielektronenoxidation zum (10+)-Ion ist jedoch ebenfalls erleichtert. Der Grund dafür liegt in einer stärker metallzentrierten Oxidation im Fall des TCNQF_4 -Komplexes, während beim zuvor untersuchten TCNQ-Analogen die Oxidation zu einem größeren Teil am verbrückenden Liganden abläuft. Als Resultat weist die (8+)-Spezies einen Redoxpotentialbereich von nur 0.51 V auf, was auf einen stark verminderten HOMO-LUMO-Abstand hinweist.

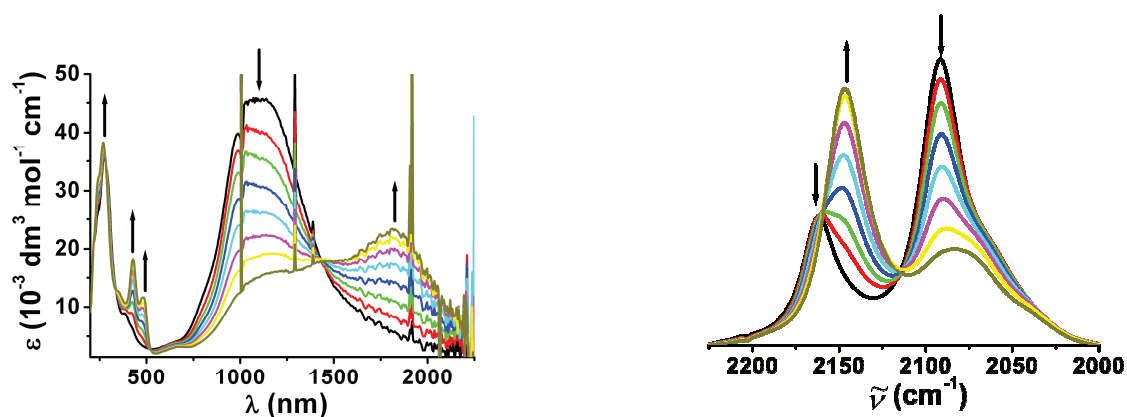


Abb 9.7. UV-Vis-NIR- (links) und IR- (rechts) Spektroelektrochemie für die Reduktion von $\{[\text{Ru}(\text{NH}_3)_5]_4(\mu_4\text{-TCNQF}_4)\}^{8+}$ zu $\{[\text{Ru}(\text{NH}_3)_5]_4(\mu_4\text{-TCNQF}_4)\}^{7+}$ in $\text{CH}_3\text{CN} / 0.1 \text{ M Bu}_4\text{NPF}_6$ bei 298 K.

In Kapitel 6 habe ich die verschiedenen Koordinationsmöglichkeiten von TCNB in mono- und polymeren Komplexen untersucht. Von zwei Komplexen konnten Kristallstrukturen erhalten werden. Alle Koordinationsmöglichkeiten des TCNB, auch solche aus literaturbekannten analogen Komplexen, wurden diskutiert. Die 1,3-Verbrückung wurde im vorliegenden Fall im monomeren Komplex $\{[\mu_2(1,3)\text{-TCNB}]\text{Cu}(\text{dppf})\}(\text{BF}_4)_2$ gefunden, während 1,4-Verbrückung in einem polymeren Komplex $\{[(\mu_2(1,4)\text{-TCNB})\text{Cu}(\text{dppf})]_2(\text{BF}_4)_2\}_n$ festgestellt wurde. Die 1,3-Koordination von nicht-reduziertem TCNB an zwei $[\text{Cu}(\text{dppf})]^+$ -Fragmente führt zur Bildung eines 16-gliedrigen Ringsystems mit

zwei Kupfer(I)-Ionen. Zwei unterschiedliche metallorganische Fragmente $[\text{Cu}(\text{dppf})]^+$ und $[\text{Cu}(\text{dchpf})]^+$ wurden zur Isolierung der Komplexe verwendet. Der koordinativ abgesättigte Komplex $[(\mu_4\text{-TCNB})\{\text{Cu}(\text{dchpf})\}_4](\text{BF}_4)_4$ führte zu Einkristallen eines polymeren Produkts aus dem Lösungsgleichgewicht. Die Kristallstruktur zeigt für $\{[(\mu_2(1,4)\text{-TCNB})\text{Cu}(\text{dppf})]_2(\text{BF}_4)_2\}_n$ ein zweidimensionales polymeres Netzwerk (Abb. 9.8). Die Nitril-Streckschwingungen der reduzierten Form des Komplexes $[(\mu_4\text{-TCNB})\{\text{Cu}(\text{dchpf})\}_4](\text{BF}_4)_4$ wurden nach Einelektronen-IR-spektroelektrochemischer Reduktion bei 2168 und 2160 cm^{-1} beobachtet (Abb. 9.8). Zusätzlich zur strukturellen Charakterisierung wurden mit diesen Komplexen spektroelektrochemische und ESR-spektroskopische Messungen durchgeführt.

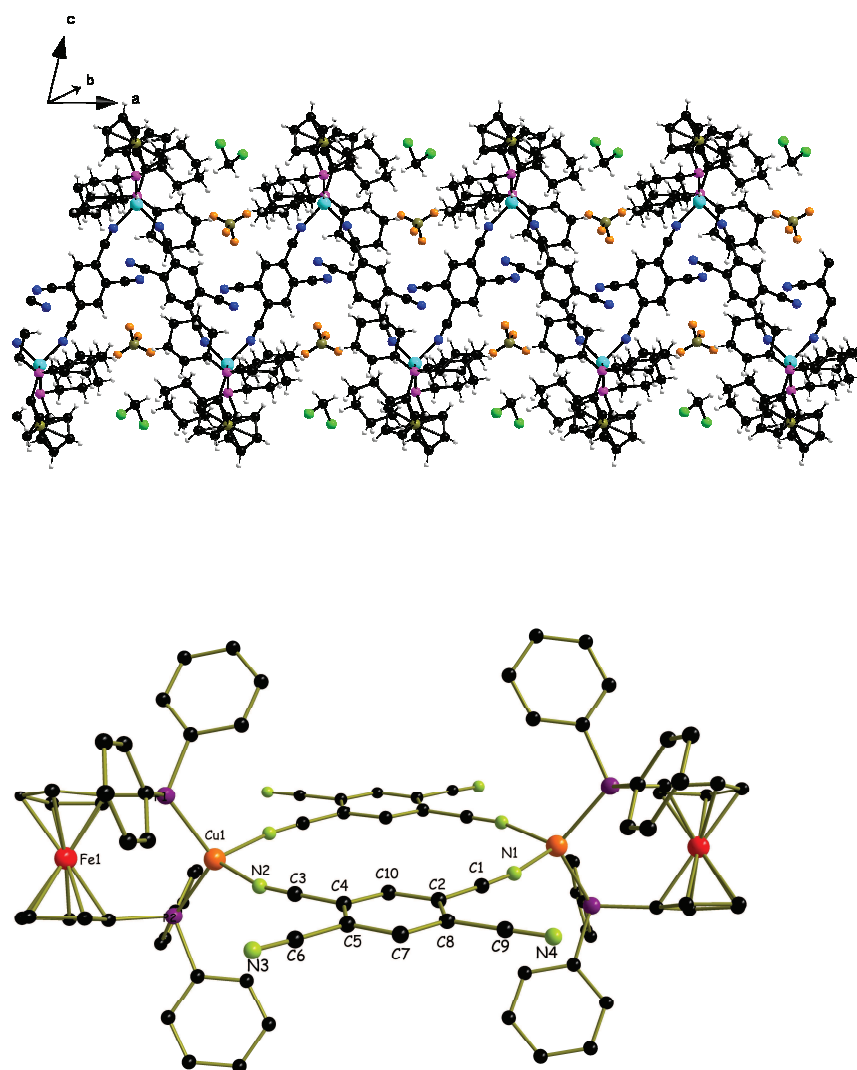


Abb 9.8. Ansicht des zweidimensionalen polymeren Netzwerks im Kristall von $[(\mu_2(1,4)\text{-TCNB})\text{Cu}(\text{dchpf})]_n(\text{BF}_4)_n \times \text{CH}_2\text{Cl}_2$ (oben). Röntgenstruktur des Dikations im Kristall von $\{[(\mu_2(1,3)\text{-TCNB})\text{Cu}(\text{dppf})]_2(\text{BF}_4)_2\}_n \cdot 3\text{CH}_2\text{Cl}_2 \cdot 3\text{H}_2\text{O}$. Die Gegenanionen und Lösungsmittelmoleküle sind zur Vereinfachung nicht dargestellt (unten).

In Kapitel 7 habe ich eine gemischtvalente $\text{Ru}^{\text{II}}\text{Ru}^{\text{III}}$ -Zwischenstufe durch ESR-Spektroskopie, Spektroelektrochemie und Kristallstrukturanalyse beschrieben (Abb. 9.9). Die Reaktion von $\text{Ru}(\text{bpy})_2\text{Cl}_2 \cdot 2\text{H}_2\text{O}$ mit 1,2-Bis(trifluoroacetyl)hydrazin $\text{H}_2(\text{adc}-\text{CF}_3)$ in Base ergibt das zweikernige $[(\mu\text{-adc}-\text{CF}_3)\{\text{Ru}(\text{bpy})_2\}_2]^{2+}$ -Ion, welches isoliert und für Strukturbestimmungen als Bis(hexafluorophosphate) in der *meso*-Form kristallisiert wurde. Der $\text{Ru}\cdots\text{Ru}$ -Abstand wurde zu $5.029(1) \text{ \AA}$ bestimmt, und die N-N-Bindungslänge von $1.463(5) \text{ \AA}$ weist auf die Hydrazido(2-)-Form der Brücke hin, wobei das Metall in der unveränderten Oxidationsstufe +II vorliegt.

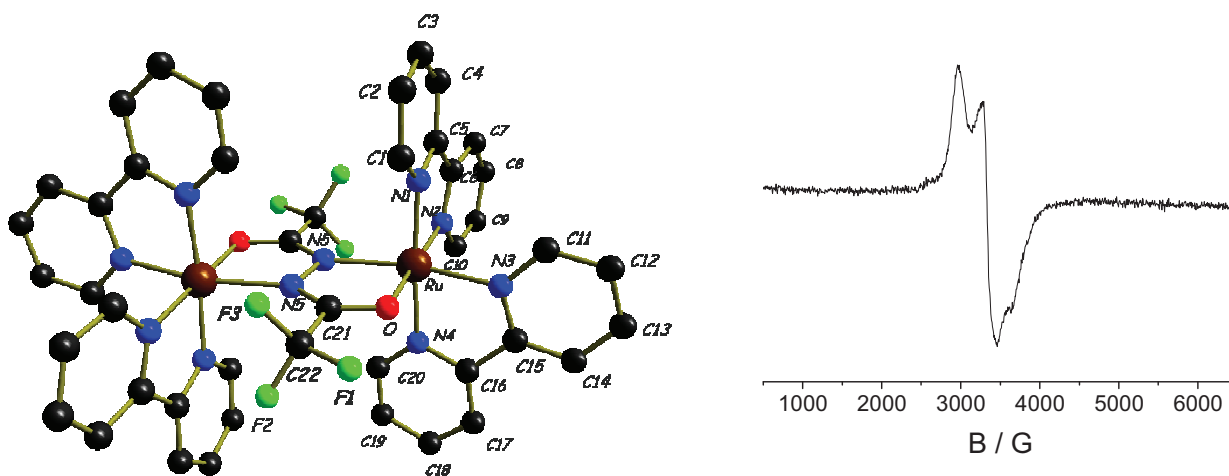


Abb 9.9. Molekulare Struktur des Dikations im Kristall von $[(\mu\text{-adc}-\text{CF}_3)\{\text{Ru}(\text{bpy})_2\}_2](\text{PF}_6)_2 \times 2 (\text{CH}_3)_2\text{CO}$ (links). ESR-Spektrum des elektrogenerierten $[(\mu\text{-adc}-\text{CF}_3)\{\text{Ru}(\text{bpy})_2\}_2]^{3+}$ bei 4 K in glasartig gefrorener $\text{CH}_3\text{CN}/0.1 \text{ M Bu}_4\text{NPF}_6$ -Lösung (rechts).

Neben der bpy-basierten Reduktion zeigt das Zyklovoltammogramm zwei Oxidationswellen mit einer (3+)-Zwischenstufe. Spektroelektrochemisch konnte nachgewiesen werden, dass diese Zwischenstufe $[(\mu\text{-adc}-\text{CF}_3)\{\text{Ru}(\text{bpy})_2\}_2]^{3+}$ eine gemischtvalente Spezies mit einer Komproportionierungskonstanten von $K_c = 10^{8.8}$ und einer Absorption bei 1680 nm ($\epsilon = 9900 \text{ M}^{-1} \text{ cm}^{-1}$) ist, was auch durch die ESR-Parameter $g_1 = 2.239$, $g_2 = 2.065$, $g_3 = 1.891$ ($g_{\text{av}} = 2.101$, $\Delta g = g_1 - g_3 = 0.348$) untermauert wird.

Bibilography

- [1] Kaim, W.; Schwederski, B. *Bioinorganic Chemistry*, Wiley, Chichester, **1994**
- [2] (a) Steffens, G. C. M.; Bielwald, R.; Buse, G. *Eur. J. Biochem.* **1987**, *164*, 295. (b) Steffens, G. C. M.; Soulimane, T.; Wolf, G.; Buse, G. *ibid.* **1993**, *213*, 1149.
- [3] Tainer, J. A.; Getzoff, E. D.; Richardson, J. S.; Richardson, D. C. *Nature (London United Kingdom)* **1983**, *306*, 284.
- [4] (a) Gartner, A.; Weser, U. *Top. Curr. Chem.* **1986**, *132*, 1. (b) A. E. G. Cass in *Metalloproteins, Part 1* (Ed.: P. Harrison), VCH, Weinheim, 1985, p. 121. (c) I. Fridovich, *J. Biol. Chem.* 1989, *264*, 7761.
- [5] (a) Kroneck, P. M. H.; Beuerle, J.; Schumacher, W. In *Metal Ions in Biological Systems*, Vol 28; Sigel, H.; Sigel, A.; Eds.; Dekker, New York, 1992, 28, pp 455. (b) Brittain, T.; Blackmore, R.; Greenwood, C.; Thomson, A. J. *Eur. J. Biochem.* **1992**, *209*, 793. (c) Zumft, W. G.; *Arch. Microbiol.* **1993**, *160*, 253.
- [6] (a) Godden, J. W.; Turley, S.; Teller, D. C.; Adman, E. T.; Liu, M. Y.; Payne, W. J. LeGall, J. *Science*, **1991**, *253*, 438. (b) Howes, B. D.; Abraham, Z. H. L.; Lowe, D. J.; Bruser, T.; Eady, R. R.; Smith, B. E. *Biochemistry*, **1994**, *33*, 3171.
- [7] Itoh, S.; Fukuzumi, S. *Acc. Chem. Res.* **2007**, *40*, 592.
- [8] (a) Vallee, B. L.; Williams, R. J. P. *Proc. Natl. Acad. Sci., USA.* **1968**, *59*, 498. (b) Williams, R. J. P. *J. Mol. Catal. (Review Issue)* **1986**, *1*. (c) Malmstrom, B. G. *Eur. J. Biochem.* **1994**, *223*, 711.
- [9] (a) Tolman, W. B. *Acc. Chem. Res.* **1997**, *30*, 227. (b) Cramer, C. J.; Tolman, W. B. *Acc. Chem. Res.* **2007**, *40*, 601.
- [10] Tyeklar, Z.; Karlin, K. D. *Acc. Chem. Res.* **1989**, *22*, 241.

- [11] Karlin, K. D.; Kaderli, S.; Zuberbühler, A. D. *Acc. Chem. Res.* **1997**, *30*, 139.
- [12] Kim, E.; Helton, M. E.; Wasser, I. M.; Karlin, K. D.; Huang, H-w; Moenne-Loccoz, P.; Incarvito, C. D.; Rheingold, A.; Honecker, M.; Kaderli, S.; Zuberbühler, A. D. *Proc. Nat. Acad. Sci.* **2003**, *100*, 3623.
- [13] Solomon, E. I; Sarangi, R.; Woertink, J. S.; Augustine, A. J.; Yoon, J.; Ghosh, S. *Acc. Chem. Res.* **2007**, *40*, 581.
- [14] Mirica, L. M.; Ottenwaelder, X.; Stack, T. D. P. *Chem. Rev.* **2004**, *104*, 1013.
- [15] (a) Collman, J. P.; Sunderland, C. J.; Berg, K. E.; Vance, M. A.; Solomon, E. I. *J. Am. Chem. Soc.* **2003**, *125*, 6648. (b) Collman, J. P.; Decreau, R. A.; Yan, Y.; Yoon, J.; Solomon, E. I. *J. Am. Chem. Soc.* **2007**, *129*, 5794.
- [16] (a) Benkovic, S. J. *Annu. Rev. Biochem.* 1980, *49*, 227. (a) Blakeley, R. L. In *The Biochemistry of Folic Acid and Related Pteridines*; Elsevier: New York, 1969.
- [17] J. W.; de Cock, R. M.; Vogels, G. D.; Guijt, W.; Haasnoot, C. A. G. *Biochemistry*, **1984**, *23*, 4448.
- [18] Gerdemann, C.; Eicken, C.; Krebs, B. *Acc. Chem. Res.* **2002**, *35*, 183.
- [19] Dolphin, D. *Adv. Chem. Ser.* **1980**, *191*, 65.
- [20] Massey, V. *Biochem. Soc. Trans.* **2000**, *28*, 283.
- [21] Purcell, E. B.; Crosson, S. *Curr. Opin. Microbiol.* **2008**, *11*, 168.
- [22] Demarsy, E.; Fankhauser, C. *Curr. Opin. Plant Biol.* **2009**, *12*, 69.
- [23] (a) Blakely, R. L.; Cocco, L. *Biochemistry*, **1985**, *24*, 4772. (b) In *Pteridine Chemistry*; Pfleiderer, W.; Taylor, E.; Eds.; Pergamon: Oxford, England, 1964.

- [24] Kaim, W.; Schwederski, B.; Heilmann, O.; Hornung, F. M. *Coord. Chem. Rev.* **1999**, *182*, 323.
- [25] (a) Rosenberg, B. In *Nucleic Acid-Metal Ion Interactions*, Vol. 1; T. G. Spiro, Ed. John Wiley & Sons, Inc.: New York, 1980, pp. 1-29. (b) Rosenberg, B.; VanCamp, L.; Trosko, J. E.; Mansour, V. H. *Nature*, **1969**, *222*, 385. (c) Choquesillo-Lazarte, D.; Maria del Pilar, B. – B.; Gracia-Santos, I.; Gonzalez-Perez, J. M.; Castineiras, A.; Niclos-Gutierrez, J. *Coord. Chem. Rev.* **2008**, *252*, 1241.
- [26] Lippert, B. *Coord. Chem. Rev.* **2000**, *200–202*, 487.
- [27] Kaim, W. *Coord. Chem. Rev.* **2001**, *219–221*, 463.
- [28] Doslik, N.; Sixt, T.; Kaim, W. *Angew. Chem. Int. Ed.* **1998**, *37*, 2403.
- [29] Sarkar, B.; Patra, S.; Fiedler, J.; Sunoj, R. B.; Janardanan, D.; Lahiri, G. K.; Kaim, W. *J. Am. Chem. Soc.* **2008**, *130*, 3532.
- [30] Kaim, W.; Doslik, N.; Frantz, S.; Sixt, T.; Wanner, M.; Baumann, F.; Denninger, G.; Kmmmerer, J. J.; Duboc-Toia, C.; Fiedler, J.; Zalis, S. *J. Mol. Str.*, **2003**, *656*, 183.
- [31] Vogler, A.; Kunkely, H. *Coord. Chem. Rev.* **2002**, *230*, 243.
- [32] Che, C. -M.; Mao, Z.; Miskowski, V. M.; Tse, M. -C.; Chan, C. -K.; Cheung, K. -K.; Phillips, D. L.; Leung, K.-H. *Angew. Chem. Int. Ed.* **2000**, *39*, 4084
- [33] Frausto da Silva, J. J. R.; Williams, R. J. P. In *The Biological Chemistry of the Elements*, *2nd edn.*; Oxford University Press, Oxford, 2001.
- [34] Kaim, W.; Moscherosch, M. *Coord. Chem. Rev.* **1994**, *129*, 157.
- [35] Miller, J. S.; Novoa, J. J. *Acc. Chem. Res.* **2007**, *40*, 189.

- [36] Moscherosch, M.; Waldhdr, E.; Binder, H.; Kaim, W.; Fiedler, J. *Inorg. Chem.* **1995**, *34*, 4326.
- [37] Miyasaka, H.; Izawa, T.; Takahashi, N.; Yamashita, M.; Dunbar, K. R. *J. Am. Chem. Soc.* **2006**, *128*, 11358.
- [38] (a) Silva, M. S. P.; Diogenes, I. C. N.; Lopes, L. G. F.; Moreira, I. S.; de Carvalho, I. M. M. *Polyhedron*, **2009**, *28*, 661. (b) Ward, M. D.; Johnson, D. C. *Inorg. Chem.* **1987**, *26*, 4213.
- [39] Baumann, F.; Kaim, W.; Olabe, J. A.; Parise, A. R.; Jordanov, J. *J. Chem. Soc. Dalton Trans.* **1997**, *22*, 4455.
- [40] Leirer, M.; Knor, G.; Volger, A. *Inorg. Chem. Commun.* **1999**, *1*, 110.
- [41] Maity, A. N.; Sarkar, B.; Niemeyer, M.; Sieger, M.; Duboc, C.; Zalis, S.; Kaim, W. *Dalton Trans.* **2008**, 5749.
- [42] Hartmann, H.; Kaim, W.; Wanner, M.; Klein, A.; Frantz, S.; Duboc-Toia, C.; Fiedler, J.; Zalis, S. *Inorg. Chem.* **2003**, *42*, 7018.
- [43] Olbrich-Deussner, B.; Kaim, W.; Gross-Lannert, R. *Inorg. Chem.* **1989**, *28*, 3115.
- [44] Maity, A. N.; Schwederski, B.; Sarkar, B.; Zalis, S.; Fiedler, J.; Kar, S.; Lahiri, G. K.; Duboc, C.; Grunert, M.; Gutlich, P.; Kaim, W. *Inorg. Chem.* **2007**, *46*, 7312.
- [45] Diaz, C.; Arancibia, A. *Polyhedron* **2000**, *19*, 137.
- [46] Berger, S.; Hartmann, H.; Wanner, M.; Fiedler, J.; Kaim, W. *Inorg. Chim. Acta.* **2001**, *314*, 22.
- [47] Munakata, M.; Ning, G. L.; Kuroda-Sowa, T.; Maekawa, M.; Suenaga, Y.; Horino, T. *Inorg. Chem.* **1998**, *37*, 5651.

- [48] Carlucci, L.; Ciani, G.; Gudenberg, D. W.v.; Proserpio, D. M. *New J. Chem.*, **1999**, *23*, 397.
- [49] Bunn, A. G.; Carroll, P. J.; Wayland, B. B. *Inorg. Chem.* **1992**, *31*, 1299.
- [50] Humphrey, D. G.; Fallon, G. D.; Murray, K. S. *J. Chem. Soc., Chem. Commun.*, **1988**, *20*, 1356.
- [51] Lopez, N.; Zhao, H.; Ota, A.; Prosvirin, A. V.; Reinheimer, E. W.; Dunbar, K. R. *Adv. Mater* **2010**, *22*, 986.
- [52] Harris, A. R.; Neufeld, A. K.; O'Mullane, A. P.; Bond, A. M. *J. Mater. Chem.* **2006**, *16*, 4397.
- [53] Taliaferro, M. L.; Thorum, M. S.; Miller, J. S. *Angew. Chem. Int. Ed.* **2006**, *45*, 5326.
- [54] Xun, S.; LeClair, G.; Zhang, J.; Chen, X.; Gao, J. P.; Wang, Z. Y. *Org. Lett.* **2006**, *8*, 1697.
- [55] Kasack, V.; Kaim, W.; Binder, H.; Jordanov, J.; Roth, E. *Inorg. Chem.* **1995**, *34*, 1924.
- [56] Kaim, W.; Kasack, V. *Inorg. Chem.* **1990**, *29*, 4696.
- [57] Kaim, W.; Lahiri, G. K. *Angew. Chem. Int. Ed.* **2007**, *46*, 1778.
- [58] Lee, J.; O'Kane, D. J.; Visser, A. J. W. G. *Biochemistry* **1985**, *24*, 1476.
- [59] Hemmerich, P.; Veeger, C. ; Wood, H. C. S. *Angew. Chem. Int. Ed. Engl.* **1965**, *4*, 671.
- [60] (a) Hemmerich, P.; Massey, V.; Michel, H.; Schug, C. *Struct. Bonding (Berlin)* **1982**, *48*, 93. (b) In *Chemistry and Biochemistry of Flavoenzymes*; Müller, F. Ed.; CRC Press, Boca Raton, 1991. (c) Ghisla, S.; Massey, V. *Eur. J. Biochem.* **1989**, *181*, 1. (d) Walsh, C. T. *Acc. Chem. Res.* **1980**, *13*, 148 and **1986**, *19*, 216.

- [61] Demarsy, E.; Fankhauser, C. *Curr. Opin. Plant Biol.* **2009**, *12*, 69.
- [62] Massey, V. *Biochem. Soc. Trans.* **2000**, *28*, 283.
- [63] Purcell, E. B.; Crosson, S. *Curr. Opin. Microbiol.* **2008**, *11*, 168 .
- [64] (a) Clarke, M. J. *Inorg. Chem.* **1984**, *3*, 133. (b) Clarke, M. J. *Rev. Inorg. Chem.* **1980**, *2*, 27.
- [65] Burgmayer, S. J. N. *Struct. Bonding (Berlin)* **1998**, 92.
- [66] Kaim, W.; Schulz, A.; Hilgers, F.; Hausen, H. D.; Moscherosch, M.; Lichtblau, A. *Res. Chem. Intermed.* **1993**, *19*, 603.
- [67] Shinkai, S.; Nakao, H.; Honda, N.; Manabe, O.; Mueller, F. *J. Chem. Soc. Perkin Trans.* **1986**, *1*, 1825.
- [68] (a) Hille, R. *Chem. Rev.* **1996**, *96*, 2757. (b) Collison, R.; Garner, C. D.; Joule, J. A. *Chem. Soc. Rev.* **1996**, *25*, 25. (c) Rees, D. C.; Hju, Y.; Kisker, C.; Schindelin, H. *J. Chem. Soc. Dalton Trans.* **1997**, 3909. (d) Stiefel, E. I. *J. Chem. Soc. Dalton Trans.* **1997**, 3915. (e) Davies, E. S.; Beddoes, R. L.; Collison, D.; Dinsmore, A.; Docrat, A.; Joule, J. A. *J. Chem. Soc. Dalton Trans.* **1997**, 3985. (f) Garton, S. D.; Hilton, J.; Oku, H.; Crouse, B. R.; Rajagopalan, K. V.; Johnson, M. K. *J. Am. Chem. Soc.* **1997**, *119*, 12906. (g) Westcott, B. L.; Gruhn, N. E.; Enemark, J. H. *J. Am. Chem. Soc.* **1998**, *120*, 3382.
- [69] (a) Perkinson, J.; Brodie, S.; Yoon, K.; Mosny, K.; Carroll, P. J.; Morgan, T. V.; Burgmayer, S. J. N. *Inorg. Chem.* **1991**, *30*, 719. (b) Mitsumi, M.; Toyoda, J.; Nakasuji, K. *Inorg. Chem.* **1995**, *34*, 3367. (c) Kohzuma, T.; Odani, A.; Morita, Y.; Takani, M.; Yamauchi, O. *Inorg. Chem.* **1988**, *27*, 3854. (d) Funahashi, Y.; Hara, Y.; Masuda, H.; Yamauchi, O. *Inorg. Chem.* **1997**, *36*, 3869. (e) Lee, D. H.; Murthy, N. N.; Lin, Y.; Nasir, N. S.; Karlin, K. D. *Inorg. Chem.* **1997**, *36*, 6328. (f) Nasir, M. S.; Karlin, K. D.; Chen, Q.; Zubieta, J. *J. Am. Chem. Soc.* **1992**, *114*, 1992. (g) Odani, A.; Masuda, H.; Inukai, K.; Yamauchi, O. *J. Am. Chem. Soc.* **1992**, *114*, 6294. (h) Kohzuma, T.; Masuda, H.; Yamauchi, O. *J. Am. Chem. Soc.* **1989**, *111*, 3431.

- [70] Heilmann, O.; Hornung, F. M.; Fiedler, J.; Kaim, W. *J. Organomet. Chem.* **1999**, *589*, 2.
- [71] Jimenez-Pulido, S. B.; Sieger, M.; Knodler, A.; Heilmann, O.; Wanner, M.; Schwederski, B.; Fiedler, J.; Moreno-Carretero, M. N.; Kaim, W. *Inorg. Chim. Acta* **2001**, *325*, 65.
- [72] Miyazaki, S.; Ohkubo, K.; Kojima, T.; Fukuzumi, S. *Angew. Chem. Int. Ed.* **2008**, *47*, 9669.
- [73] Abellera, A.; Galang, R. D.; Clarke, M. J. *Inorg. Chem.* **1990**, *29*, 633.
- [74] Glazer, E. C., Nguyen, Y. H. L.; Gray, H. B.; Goodwin, D. B. *Angew. Chem.* **2008**, *120*, 912. *Angew. Chem. Int. Ed.* **2008**, *47*, 898.
- [75] Hueso-Urena, F.; Illan-Cabeza, N. A.; Jimenez-Pulido S. B.; Moreno-Carretero, M. N. *Acta Cryst.* **2010**, *E66*, m145.
- [76] Picon-Ferrer, I.; Hueso-Urena, F.; Illan-Cabeza, N. A.; Jimenez-Pulido, S. B.; Martínez-Martos, J. M.; Ramirez-Exposito, M. J.; Moreno Carretero, M. N. *J. Inorg. Biochem.* **2009**, *103*, 94.
- [77] Jimenez-Pulido, S. B.; Linares-Ordonez, F. M.; Martinez-Martos, J. M.; Moreno-Carretero.; Quiros-Olozabal, M.; Ramirez-Exposito, M. J. *J. Inorg. Biochem.* **2008**, *102*, 1677.
- [78] Heilmann, O.; Hornung, F. M.; Kaim, W.; Fiedler, J. *J. Chem. Soc. Faraday Trans.* **1996**, *92*, 4233.
- [79] Cathey, C. J.; Constable, E. C.; Hannon, M. J.; Tocher, D. A.; Ward, M. D. *J. Chem. Soc. Chem. Commun.* **1990**, *8*, 621.
- [80] Bredereck, H.; Pfeleiderer, W. *Chem. Ber.* **1954**, *87*, 1119.
- [81] Russell, J. R.; David Garner, C.; Joule, J. A. *J. Chem. Soc. Perkin Trans.* **1992**, *1*, 1245.

- [82] Diaz, J.; Gamasa, M. P.; Gimeno, J.; Aguirre, A.; Gracia-Granda, S.; Holubova, J.; Falvello, L. R. *Organometallics*, **1999**, *18*, 662.
- [83] Bessenbacher, C.; Vogler, C.; Kaim, W. *Inorg. Chem.* **1989**, *28*, 1989.
- [84] Hornung, F. M.; Heilmann, O.; Kaim, W.; Zalis, S.; Fiedler, J. *Inorg. Chem.* **2000**, *39*, 4052.
- [85] Heilmann, O. *Ph.D. Thesis, University of Stuttgart*, **1997**
- [86] Hammarsten, E. *Biochem. Z.* **1924**, *144*, 383.
- [87] Werner, A. *Z. Anorg. Chem.* **1983**, *3*, 267.
- [88] Sletten, E. *J. Chem. Soc. Chem. Commun.* **1967**, *21*, 1119.
- [89] Bear, J. L.; Gray, H. B.; Rainen, L.; Chang, I. M.; Howard, R.; Serio, G.; Kimball, A. P. *Cancer. Chemother. Rep.* **1975**, *59*, 611.
- [90] Day, E. F.; Crawford, C. A.; Folting, K.; Dunbar, K. R.; Christou, G. *J. Am. Chem. Soc.* **1994**, *116*, 9339.
- [91] Catalan, K. V.; Mindiola, D. J.; Ward, D. L.; Dunbar, K. R. *Inorg. Chem.* **1997**, *36*, 2458.
- [92] Crawford, C. A.; Day, E. F.; Saharan, V. P.; Folting, K.; Huffman, J. C.; Dunbar, K. R.; Christou, G. *Chem. Commun.* **1996**, *10*, 1113.
- [93] Dunbar, K. R.; Matonic, J. H.; Saharan, V. P.; Crawford, C. A.; Christou, G. *J. Am. Chem. Soc.* **1994**, *116*, 2201.
- [94] Martin, R. B. In *Cisplatin: Chemistry and Biochemistry of a Leading Anticancer Drug*; Lippert, B. Ed.; VHCA Zürich and Wiley-VCH Weinheim, 1999, pp 183–133.

- [95] Sponer, J.; Leszczynski, J.; Hobza, P. *J. Phys. Chem.* **1996**, *100*, 1965.
- [96] Pullman, A.; Pullman, B. *Q. Rev. Biophys.* **1983**, *14*, 289.
- [97] Stiefel, E. J. *Prog. Inorg. Chem.* **1977**, *22*, 1.
- [98] Birdsall, W. J.; Pfennig, B. W.; Toto, J. L. *Polyhedron* **1986**, *5*, 1357.
- [99] Mikulski, C. M.; Gaul, M.; Bayne, M. L.; Grossman, S.; Renn, A.; Staley, D. L. *Transition Met. Chem.* **1989**, *14*, 336.
- [100] Mikulski, C. M.; Udell, K.; Staley, D. L. *Transition Met. Chem.* **1992**, *17*, 159.
- [101] Nonella, M.; Hlinggi, G.; Dubler, E. *J. Mol. Str. (Theochem)* **1993**, *219*, 173.
- [102] Kinjo, Y.; Maeda, M. *J. Inorg. Biochem.* **1991**, *43*, 51.
- [103] Dubler, E.; Hanggi, G. *Thermochimica Acta* **1994**, *234*, 201.
- [104] Dubler, E.; Hanggi, G.; Schmalle, H. *Inorg. Chem.* **1992**, *31*, 3728.
- [105] Lasocha, W.; Gawe, B.; Rafalska-Lasocha, A.; Pawłowski, M.; Talik, P.; Paszkowicz, W. *J. Appl. Cryst.* **2010**, *43*, 163.
- [106] Salas-Peregrin, J. M.; Colacia-Rodriguez, E.; Romero-Molina, M. A.; Sanchez-Sanchez M. P. *Thermochimica Acta* **1983**, *69*, 313.
- [107] Crowston, E. H.; Goodgame, D. M. L.; Hayman, P. B.; Slawin, A. M.; Williams, D. J. *Inorg. Chim. Acta* **1986**, *122*, 161.
- [108] Kaim, W.; Rall, J. *Angew. Chem. Int. Ed.* **1996**, *35*, 43.
- [109] Robins, R. K.; Revankar, G. R.; O'Brien, D. E.; Springer, R. H.; Novinson, T.; Albert, A.; Senga, K.; Miller, J. P.; Streeter, D. G. *J. Heterocycl. Chem.* **1985**, *22*, 601.

- [110] Frommer, G.; Mutikainen, I.; Pesch, F. J.; Hillgeris, E. C.; Preut, H.; Lippert, B. *Inorg. Chem.* **1992**, *31*, 2429.
- [111] (a) Abbott, D. W.; Woods, C. *Inorg. Chem.* **1983**, *22*, 2918. (b) Abbott, D. W.; Woods, C. *Inorg. Chem.* **1983**, *22*, 597.
- [112] (a) Frommer, G.; Schöllhorn, H.; Thewalt, U.; Lippert, B. *Inorg. Chem.* **1990**, *29*, 1417. (b) Longato, B.; Bandoli, G.; Trovo, G.; Marasciulo, E.; Valle, G. *Inorg. Chem.* **1995**, *24*, 1745.
- [113] Lippert, B. *Prog. Inorg. Chem.* **1989**, *37*, 1.
- [114] Raudaschl-Sieber, G.; Schöllhorn, H.; Thewalt, U.; Lippert, B. *J. Am. Chem. Soc.* **1985**, *107*, 3591.
- [115] Gellert, R. W.; Fischer, B. E.; Bau, R. *J. Am. Chem. Soc.* **1980**, *102*, 7812.
- [116] Lüth, M. S.; Freisinger, E.; Glahe, F.; Lippert, B. *Inorg. Chem.* **1998**, *37*, 5044.
- [117] Tian, Y. Q.; Xu, H. J.; Weng, L. H.; Chen, Z. X.; Zhao, D. Y.; You, X. Z. *Eur. J. Inorg. Chem.* **2004**, 1813.
- [118] Pyykkö, P. *Chem. Rev.* **1997**, *97*, 597.
- [119] Dunbar, K. R.; Matonic, J. H.; Saharan, V. P.; Crawford, C. A.; Christou, G. *J. Am. Chem. Soc.* **1994**, *116*, 2201. (b) Crawford, C. A.; Day, E. F.; Saharan, V. P.; Folting, K.; Huffman, J. C.; Dunbar, K. R.; Christou, G. *Chem. Commun.* **1996**, 1113.
- [120] (a) Kang, C.; Zhang, X.; Moyzis, R.; Rich, A. *Nature* **1992**, *356*, 126. (b) Laughlan, G.; Murchie, I. H.; Norman, D. G.; Moore, M. H.; Moody, P. C. E.; Lilley, D. M. J.; Luisi, B. *Science* **1994**, *265*, 520.

[121] (a) Abbott, D. W.; Woods, C. *Inorg. Chem.* **1983**, *22*, 2918. (b) Abbott, D. W.; Woods, C. *Inorg. Chem.* **1983**, *22*, 597.

[122] Labib, L.; El-Essawi, M.; Massa, W.; Lorberth, J. *Angew. Chem. Int. Ed. Engl.* **1998**, *27*, 1160.

[123] Shivakumar, M.; Pramanik, K.; Ghosh, P.; Chakravorty, A. *Inorg. Chem.* **1998**, *37*, 5968.

[124] Roy, S. *Ph.D. Thesis, University of Stuttgart*, **2009**.

[125] Roy, S. *Unpublished Work*.

[126] Bock, H.; Dienelt, R.; Schodel, H.; Van, T. T. H. *Struct. Chem.* **1998**, *9*, 279.

[127] Kaim, W.; Kohlmann, S.; Jordanov, J.; Fenske, D. *Z. Anorg. Allg. Chem.* **1991**, *217*, 598.

[128] Krejcik, M.; Zalis, S.; Klima, J.; Sykora, D.; Matheis, W.; Klein, A.; Kaim, W. *Inorg. Chem.* **1993**, *32*, 3362.

[129] Vickers, E. B.; Giles, I. D.; Miller, J. S. *Chemistry of Materials* **2005**, *17*, 1667.

[130] Taliaferro, M. L.; Palacio, F.; Miller, J. S. *J. Materials Chem.* **2006**, *16*, 2677.

[131] Reis, A. H., Jr.; Preston, L. D.; Williams, J. M.; Peterson, S. W.; Candela, G. A.; Swartzendruber, L. J.; Miller, J. S. *J. Am. Chem. Soc.* **1979**, *101*, 2756.

[132] Candela, G. A.; Swartzendruber, L. J.; Miller, J. S.; Rice, M. J. *J. Am. Chem. Soc.* **1979**, *101*, 2755.

[133] O'Kane, S. A.; Clerac, R.; Zhao, H.; Ouyang, X.; Galan-Mascaros, J. R.; Heintz, R.; Dunbar, K. R. *J. Solid State Chem.* **2000**, *152*, 159.

- [134] Zhao, H.; Heintz, R. A.; Ouyang, X.; Dunbar, K. R.; Campana, C. F.; Rogers, R. D. *Chemistry of Materials* **1999**, *11*, 736.
- [135] Heintz, R. A.; Zhao, H.; Ouyang, X.; Grandinetti, G.; Cowen, J.; Dunbar, K. R. *Inorg. Chem.* **1999**, *38*, 144.
- [136] Zhao, H.; Heintz, R. A.; Dunbar, K. R.; Rogers, R. D. *J. Am. Chem. Soc.* **1996**, *118*, 12844.
- [137] Campana, C.; Dunbar, K. R.; Ouyang, X. *Chem. Commun.* **1996**, *21*, 2427.
- [138] Goldberg, S. Z.; Spivack, B.; Stanley, G.; Eisenberg, R.; Braitsch, D. M.; Miller, J. S.; Abkowitz, M. *J. Am. Chem. Soc.* **1977**, *99*, 110.
- [139] Moscherosch, M.; Kaim, W. *Inorg. Chim. Acta* **1993**, *206*, 229.
- [140] Berger, S.; Hartmann, H.; Wanner, M.; Fiedler, J.; Kaim, W. *Inorg. Chim. Acta* **2001**, *314*, 22.
- [141] Waldhoer, E.; Kaim, W.; Lawson, M.; Jordanov, J. *Inorg. Chem.* **1997**, *36*, 3248.
- [142] Baumann, F.; Kaim, W.; Olabe, J. A.; Parise, A. R.; Jordanov, J. *J. Chem. Soc. Dalton Trans: Inorg. Chem.* **1997**, *22*, 4455.
- [143] Maity, A. N.; Schwederski, B.; Sarkar, B.; Zalis, S.; Fiedler, J.; Kar, S.; Lahiri, G. K.; Duboc, C.; Grunert, M.; Guetlich, P.; Kaim, W. *Inorg. Chem.* **2007**, *46*, 7312.
- [144] Maity, A. N.; Sarkar, B.; Niemeyer, M.; Sieger, M.; Duboc, C.; Zalis, S.; Kaim, W. *Dalton Trans.* **2008**, *42*, 5749.
- [145] Hartmann, H.; Kaim, W.; Wanner, M.; Klein, A.; Frantz, S.; Duboc-Toia, C.; Fiedler, J.; Zalis, S. *Inorg. Chem.* **2003**, *42*, 7018.
- [146] Bozio, R.; Girlando, A.; Pecile, C. *J. Chem. Soc. Faraday Trans.* **1975**, *71*, 1237.

- [147] Khoo, S. B.; Foley, J. F.; Korzeniewski, C.; Pons, S. *J. Electroanal. Chem.* **1987**, *233*, 223.
- [148] Gross-Lannert, R.; Kaim, W.; Olbrich-Deussner, B. *Inorg. Chem.* **1990**, *29*, 5046.
- [149] Gross, R.; Kaim, W. *Angew. Chem.* **1987**, *99*, 257.
- [150] Novoa, J. J.; Stephens, P. W.; Weerasekare, M.; Shum, W. W.; Miller, J. S. *J. Am. Chem. Soc.* **2009**, *131*, 9070.
- [151] Trifonov, A. A.; Gudilenkov, I. D.; Fukin, G. K.; Cherkasov, A. V.; Larionova, J. *Organometallics* **2009**, *28*, 3421.
- [152] Roy, S.; Sieger, M.; Singh, P.; Niemeyer, M.; Fiedler, J.; Duboc, C.; Kaim, W. *Inor. Chim. Acta* **2008**, *361*, 1699.
- [153] Roy, S.; Sieger, M.; Duboc, C.; Denninger, G.; Kümmerer, H. J.; Kaim, W. *J. Mol. Str.* **2008**, *890*, 133.
- [154] Roy, S.; Sieger, M.; Sarkar, B.; Schwederski, B.; Lissner, F.; Schleid, T.; Fiedler, J.; Kaim, W. *Angew. Chem. Int. Ed.* **2008**, *47*, 6192.
- [155] Roy, S.; Sarkar, B.; Bubrin, D.; Niemeyer, M.; Zalis, S.; Lahiri, G. K.; Kaim, W. *J. Am. Chem. Soc.* **2008**, *130*, 15230.
- [156] (a) Xun, S.; Zhang, J.; Li, X.; Ma, D.; Wang, Z. Y. *Synth. Met.* **2008**, *158*, 484. (b) Wang, S.; Li, X.; Xun, S.; Wan, X.; Wang, Z. Y. *Macromolecules* **2006**, *39*, 7502. (c) Rastegar, M. F.; Todd, E. K.; Tang, H.; Wang, Z. Y. *Org. Lett.* **2004**, *6*, 4519.
- [157] Kao, C. K. *Sand from Centuries Past; Send Future Voices Fast, Nobel Prize Lecture*, December 8th, **2009**.
- [158] LeClair, G.; Wang, Z. Y. *J. Solid State Electrochem.* **2009**, *13*, 365.

- [159] Mayerhoeffler, U.; Deing, K.; Gruss, K.; Braunschweig, H.; Meerholz, K.; Wuerthner, F. *Angew. Chem.* **2009**, *121*, 8934. *Angew. Chem. Int. Ed.* **2009**, *48*, 8776.
- [160] (a) Qi, Y.; Desjardins, P.; Wang, Z. Y. *J. Opt. A: Pure Appl. Opt.* **2002**, *4*, S273. (b) Qi, Y.; Wang, Z. Y. *Macromolecules* **2003**, *36*, 3146. (c) Xun, S.; LeClair, G.; Zhang, J.; Chen, X.; Gao, J. P.; Wang, Z. Y. *Org. Lett.* **2006**, *8*, 1697.
- [161] Maji, S.; Sarkar, B.; Patra, S.; Fiedler, J.; Mobin, S. M.; Puranik, V. G.; Kaim, W.; Lahiri, G. K. *Inorg. Chem.* **2006**, *45*, 1316.
- [162] Moscherosch, M.; Field, J. S.; Kaim, W.; Kohlmann, S.; Krejcik, M. *J. Chem. Soc. Dalton Trans.: Inorg. Chem. (1972-1999)* **1993**, *2*, 211.
- [163] (a) Chen, K. S.; Wan, J. K. S. *J. Am. Chem. Soc.* **1978**, *100*, 6051. (b) Creber, K. A. M.; Ho, T. I.; Depew, M. C.; Weir, D.; Wan, J. K. S. *Can. J. Chem.* **1982**, *60*, 1504.
- [164] Knödler, A.; Fiedler, J.; Kaim, W. *Polyhedron* **2004**, *23*, 701.
- [165] Reitz, D. B.; Finkes, M. J. *J. Heterocyclic Chem.* **1989**, *26*, 225.
- [166] (a) Ernst, S.; Kasack, V.; Kaim, W. *Inorg. Chem.* **1988**, *27*, 1146. (b) Keene, F. R. *Chem. Soc. Rev.* **1998**, *27*, 185. (c) Sarkar, B.; Patra, S.; Fiedler, J.; Sunoj, R.; Janardanan, D.; Mobin, M. S.; Niemeyer, M.; Lahiri, G. K.; Kaim, W. *Angew. Chem.* **2005**, *117*, 5800. *Angew. Chem. Int. Ed.* **2005**, *44*, 5655.
- [167] Ye, S.; Sarkar, B.; Duboc, C.; Fiedler, J.; Kaim, W. *Inorg. Chem.* **2005**, *44*, 2843.
- [168] Kaim, W.; Ernst, S.; Kasack, V. *J. Am. Chem. Soc.* **1990**, *112*, 173.
- [169] Krejcik, M.; Danek, M.; Hartl, F. *J. Electroanal. Chem.* **1991**, *317*, 179.
- [170] Baldwin, D. A.; Lever, A. B. P.; Parish, R. V. *Inorg. Chem.* **1969**, *8*, 107.

[171] *CrysAlis*, version 1.171; Oxford Diffraction: Wroclaw, Poland, **2007**.

[172] Sheldrick, G. M. *Programme SHELXS*: Göttingen, **1997**.

[173] Sheldrick, G. M. *Programme SHELXL*: Göttingen, **1997**.

[174] Herrendorf, W.; Bärnighausen, H. *Programme HABITUS*: Giessen, Karlsruhe, **1993**,
Giessen, **1996**.

[175] CRYSTAL IMPACT *Programme DAIMOND, Version 2.1e*: Bonn, **2001**.

Abbreviations

A	ampere
A.C.	alternating current
abb.	Abbildung
abcp	azo bis(5-chloropyrimidine)
abpy	2,2'-azobispyridine
av	average
b	broad (IR band)
B	magnetic field
bpy	2,2'-bipyridine
Bu ₄ NBF ₄	tetrabutylammonium tetrafluoroborate
Bu ₄ NClO ₄	tetrabutylammonium perchlorate
Bu ₄ NPF ₆	tetrabutylammonium hexafluorophosphate
calc.	calculated
cm	centimetre
Cl	chloro
Cp	cyclopentadienyl
Ch	cyclohexyl
d	doublet / bond length
dd	doublet of a doublet
δ	chemical shift
Δg	g anisotropy
Δv _{1/2}	band width at half height
DCM	dichloromethane
dm	decimetre
DMA	1,3-dimethylalloxazine
DML	1,3-dimethylumazine
dppf	1,1'-bis(diphenylphosphino)ferrocene
dippf	1,1'-bis(di-isopropylphosphino)ferrocene
dchpf	1,1'-bis(dicyclohexylphosphino)ferrocene
E	potential
E _{pa}	anodic peak potential
E _{pc}	cathodic peak potential
ε	molar extinction coefficient

EPR	electron paramagnetic resonance
exp	experimental
ESI	Electrospray ionization
$\text{Fe}(\text{Cp}_2)^{+/0}$	ferrocenium / ferrocene
FT	Fourier Transform
G	gauss / guanine
g	gram
g_e	free electron g value
GHz	gigahertz
HOMO	highest occupied molecular orbital
Hz	hertz
$\text{H}_2\text{-adcCF}_3$	1,2-bis(trifluoroacetyl)-hydrazine
IR	infrared
irr	irreversible
iso	isotropic
i_{pa}	anodic peak current
i_{pc}	cathodic peak current
i_{Pr}	isopropyl
IVCT	inter valence charge transfer
k	rate constant
K	Kelvin
K_c	comproportionation constant
KPF_6	potassium hexafluorophosphate
L	ligand
LiClO_4	lithium perchlorate
λ	wavelength
LLCT	ligand to ligand charge transfer
LMCT	ligand to metal charge transfer
LUMO	lowest unoccupied molecular orbital
M	mole / multiplet
M	molar / metal
max	maximum
Me	methyl
Mg	milligram

MHz	megahertz
mL	millilitre
MLCT	metal to ligand charge transfer
mm	millimeter
mmol	millimole
MO	molecular orbital
mol	mole
MS	mass spectrum
mT	militesla
mV	milivolt
v	wavenumbers
n	natural number
n.a.	not applicable
n.d.	not detemined
n.o.	not observed
NIR	near infrared
nm	nanometer
NMR	nuclear magnetic resonance
°	degree
°C	degree centigrade
OTTLE cell	optically transparent thin layer electrochemical cell
Ox	oxidized
Ph	phenyl
PP	2-pivaloylpterin
ppm	parts per million
P-9MG	N2-pivaloyl-9-methylguanine
red	reduced
RT	room temperature
s	strong (IR band) / singlet / second
S	electron spin
SCE	standard calomel electrode
sh	shoulder
SOMO	singly occupied molecular orbital
t	triplet

T	temperature / Tesla
Tab	table
TCNB	1,2,4,5-tetracyanobenzene
TCNQ	7,7,8,8,-Tetracyano- <i>p</i> -benzoquinodimethane
TCNQF ₄	2,3,5,6-tetrafluoro-7,7,8,8-tetracyano- <i>p</i> -quinodimethane
TMA	1,3,7,8-tetramethylalloxazine
TMX	1,3,9-trimethylxanthine
UV	ultra violet
V	volt
Vdw	van-der-Waals
vs	very strong (IR band)
vs.	versus
vis	visible
Z	atomic number

Curriculum Vitae

Personal profile:

Name: Rajkumar Jana
Sex: Male
Date of Birth: 04-05-1985
Nationality: Indian
Marital Status: Single
Languages known: English, Bengali, Hindi
Address: Rajkumar Jana
C/O Prof. Dr. Wolfgang Kaim
Institut für Anorganische Chemie
Universität Stuttgart
Pfaffenwaldring 55
70569 Stuttgart
Germany

Studies:

1999 to 2003: Baradongal R. N. Institution, West Bengal, India

2003 to 2006: *University of Calcutta*, Kolkata, West Bengal
Degree obtained: Bachelor of Science in Chemistry

2006 to 2008: *Indian Institute of Technology, Delhi*, India
Degree obtained: Master of Science in Chemistry
Master Thesis was titled as 'Exploring the chemistry of cobalt sandwich compounds: Reactions of η^5 -CpCoC₄Ph₄, η^5 -(MeCp)CoC₄Ph₄ and their derivatives' under the supervision of Prof. Anil Jacob Elias.

September 2008 to January 2011: Doctoral work at the *Institut für Anorganische Chemie, Stuttgart* under the guidance of Prof. Dr. Wolfgang Kaim.

Title: Study of metal interactions with biomolecules and π -acceptor systems: A detailed investigation of structural aspects, electrochemical properties and spectroscopic features

Position held:

September 2008 to November 2008:
Wissenschaftliche Hilfskraft at the Institut für Anorganische Chemie
der Universität Stuttgart

December 2008 to January 2011:
Wissenschaftlicher Angestellter at the Institut für Anorganische Chemie
der Universität Stuttgart